UNIVERSITÀ
DEGLI STUDI
DI PADOVA

Head Office: Università degli Studi di Padova

Centro di Ateneo di Studi e Attività Spaziali (CISAS)

Ph.D. COURSE IN: Scienze, Tecnologie e Misure Spaziali (STMS)
CURRICULUM: Sciences and Technologies for Aeronautics and Satellite Applications (STASA)
SERIES 35

SPACE SYSTEMS FOR OPTICAL COMMUNICATIONS

Thesis written with the financial contribution of Stellar Project.

Coordinator: Prof. Francesco Picano
Supervisor: Prof. Alessandro Francesconi
Co-supervisor: Dr. Francesco Sansone

Ph.D. student :Andrea Vettor

“Be the person you needed when you were younger”

ACKNOWLEDGMENTS

I would like to thank Stellar Project and Centro di Ateneo di Studi e Attività Spaziali "Giuseppe Colombo" (CISAS) for supporting this research work. I would like to thank in particular Prof. Alessandro Francesconi, which has represented an important point of reference for both my personal and professional growth. I would also like to thank the ASI and eGeos researchers and personnel at Matera Laser Ranging Observatory for welcoming me and providing an unvaluable support and a constant source of knowledge and experience.

Ma soprattutto ringrazio i miei genitori, che mi hanno supportato nell’unica ricerca che in fondo per me conta veramente: grazie a loro scorgo il senso autentico della parola “gratitudine”.

ABSTRACT

The rapid development and miniaturization of technologies has progressively allowed for the integration of spaceborne applications in the context of privately led scientific and commercial activities. This groundbreaking trend has recently caused the emergence of a new approach commonly referred to as "New Space", which aims at providing a faster and more cost-effective access to space technologies and services for small and medium businesses. This necessarily requires the further development of a variety of new satellite technologies, among which telecommunications will play a decisive role. Satellite telecommunication has been historically dominated by Radio Frequency (RF) transmission. Although this technology has shown remarkable improvements, at this point a considerable increase in data rate can only be obtained at the expense of an increase in transmitted RF power. Free Space Optical Communication (FSOC) is a technology that promises to increase the available data rate by at least one order of magnitude at the same transmitted power, thanks to the small width of the transmitted beam translating into a high antenna gain. The narrow beam also guarantees extreme directivity of transmission, which represents a crucial advantage in terms of band regulation flexibility and data security. Although satellite optical communication feasibility has been widely proven during in-orbit demonstrations carried out on larger satellites during the last decades, several challenges remain open to make this technology reliable, cost-effective and available at large scale.

The research presented in this work has specifically aimed at advancing the technological state of the art of satellite optical communications, focusing on small size satellites. The work has been carried out in the context of the activities related to the development of LaserCube, an optical communication terminal compatible with CubeSat standards developed by Stellar Project. After a preliminary survey of the applications that will benefit the most from increased satellite communications capabilities and of the state of the art of optical communication technologies (Chapter 2), the research has been focused on the development of the main building blocks that will enable the large scale adoption of space optical communications: the analysis and design of innovative applications based on satellite network configurations supported by optical communications (Chapter 3); and the design and development of the optical communications space segment (Chapter 4) and ground segment (Chapter 5). The general context of these developments is the in-orbit demonstration of LaserCube, whose launch has taken place on 30th June 2021. The activities specifically related to the preparation and operations management of the in-orbit demonstration mission are presented in Chapter 6: these include the space qualification of the system, a preliminary ground-to-ground test performed to assess system functional compliance, the description of the planned orbital operations and the detailed orbital determination analysis required for the link acquisition procedure.

Table of Contents

1. INTRODUCTION

In this chapter a preliminary introduction to the thesis work is provided. The chapter is divided into three sections: in Section 1.1 the motivations driving the work are presented, both in terms of market needs and technological challenges to be overcome; in Section 1.2 the scope and objectives of the work deriving from the motivations are described in detail; in Section 1.3 the methodological approach and the structure of the thesis are presented.

1.1 Motivation

The introduction of novel space technologies and the rapid development of the existing ones has allowed in the last years to make important progresses in the direction of the miniaturization of the satellites and payloads to be launched in orbit. Since launch mass constitutes one of the main costs of space missions, these innovations pave the way for the access of private actors in the world of space activities, oriented to an exploitation of the opportunities offered by space both scientifically and commercially. This process, often referred to as "New Space Economy", consists in the gradual integration of space technologies and services in economically growing sectors, such as: meteorological and climate monitoring, agriculture management, forest and biodiversity conservation, maritime traffic management, satellite internet services, just to mention a few [1] [2].

These premises, supported by numerous market and technical analyses (see Section 2.1), allow to understand how the volume of data generated in space will most likely require a fast increase in the available data rate in the short and medium term. To this should also be added the forthcoming implementation on large scale of novel satellite configurations, such as satellite formations and constellations, which will require powerful and reliable intersatellite communication systems, for the transmission of both payload and satellite management data.

Satellite communications are currently based almost exclusively on the transmission of radio frequency signals. The state of the art of this technology is substantially consolidated and typically guarantees data rate values which, even in the most favorable case, do not exceed 500 Mbps. Moreover, these values refer to large satellites with abundant resources in terms of available power and mass and decrease considerably in the case of small and nano satellites. Today, nanosatellites typically exploit telecommunication subsystems based on Ultra High Frequency (UHF), S or X band to transmit data towards ground stations, with bitrates bounded from few kbps to some tens of Mbps. Bitrates up to 220Mbps have been achieved using proprietary X–band systems in conjunction with several-meter ground antennas. Ka–band is an emerging technology which is not a standard in the nanosatellite community yet [3] [4]. As regards intersatellite links between nanosatellites, there have been some recent developments using S–band systems, but the in-flight performance in terms of bitrate is not sufficient for commercial purposes (1Kbps over few hundred km).

Despite the ongoing research to improve and optimize RF systems, it is however clear that it will not be possible to obtain substantial data rate increase without simultaneously increasing the mass of the system and the required electrical power. On the contrary, optical communication systems promise to offer, at similar mass and power, a strong increase of the available telecom performance (tens of Gbps for nanosatellites and hundreds of Gbps for large satellites) [5].

Moreover, even assuming that the technological advancement will allow to obtain similar performance using RF systems, the latter present strong limitations in terms of bandwidth saturation. This represents a further advantage of optical communication systems, as the main characteristic of this type of technology is the extremely reduced divergence of the transmitted beam, which translates into extremely high values of the optical antenna gain. The high directivity of the transmission then constitutes a major advantage in applications such as intelligence and data traffic management, namely in all the situations in which it is of vital importance to eliminate problems related to (licit or illicit) interference and interception of the signal.

If on one hand optical communications present a series of important advantages with respect to radio frequency systems, on the other hand several challenges remain open on the road to make this technology performing, secure and feasible on large scale. The reduced angle of divergence requires an extremely precise pointing system, capable of facing the high distances and the vibrational disturbances of the satellite platform. Moreover, the high relative speed of the communicating terminals requires a point ahead system for the compensation of velocity aberration due to the finite nature of the speed of light, which in turn translates into excellent orbital and attitude determination capabilities. Another major criticality emerging in case one or more of the involved terminals is within the atmosphere is related to atmospheric disturbances: in addition to the problem of absorption, the atmospheric medium introduces complex phenomena of beam deviation and distortion due to turbulences and thermal gradients. Optical beam transmission is also very dependent on atmospheric humidity which, in the limit case of cloud coverage, can completely prevent link acquisition and require mitigation strategies based on techniques like spatial diversification of the receiving platforms.

It is then clear that additional effort in terms of research and development is fundamental to make optical communications a secure and reliable technology, capable of providing the “New Space Economy” with the performance that has so far proven to be able to guarantee during the numerous in orbit demonstrations. Solving or mitigating the mentioned challenges would allow to obtain a remarkably higher space-to-ground and space-to-space data transmission speed, promoting the development of space activities with an unprecedented scientific and commercial return. It would also allow to implement a robust backhaul network for the diffusion of new generation mobile data services, in the context of innovative internet solutions, such as Internet of Things (IoT), Automatic Identification System (AIS) and Machine-to-Machine (M2M). These improvements would be even more important for small satellites, as lower costs would further widen the access to satellite services.

1.2 Thesis scope and objectives

The research has been carried out in collaboration with Stellar Project, a start-up company founded in 2015 focusing on the development of optical communication technologies. At the beginning of the research project LaserCube, Stellar Project's flagship product, was already at an advanced stage of development. LaserCube is an optical communication terminal compliant with CubeSat standards which specifically targets small and nano satellites and guarantees considerably higher performance with respect to the state of the art of small satellite communications.

A first phase of the research work has been dedicated to a preliminary investigation of the current market requirements, aimed at identifying the applications which could benefit the most from the introduction of satellite optical communications from which useful design indications could be derived. Moreover, a survey of the state of the art of optical communications system has been carried out to set a starting point for the doctoral work. Based on this investigation and on the already solid competence of Stellar Project in the field, the research has then been oriented to the development of hardware and software solutions for satellite optical communications, eventually concretizing in the prototyping and flight test of a fully functional optical communication terminal. The main objective of the work has been the optimization of the system's design and the further improvement of the elements necessary to compose a complete commercial offer, both for space-to-ground and space-to-space telecommunications.

Due to the promising role assumed by global communications based on satellite networks highlighted by the preliminary market investigation, a consistent part of the first year of doctoral activities has been dedicated to the development of a software tool in support of satellite networks analysis. The developed software allows to analyze satellite constellations dedicated to global communication in terms of latency and throughput performance, with the aim to offer a valuable support to the design phase both at network and system level. In order to assess the potential of the software, three case studies have been performed, showing the potential of satellite optical communications in several applications and highlighting the challenges to be addressed.

Given the high complexity of a satellite optical communication system and the already advanced stage of development of LaserCube, a complete detailed design from scratch of the space segment could not be the scope of the doctoral work. A preliminary LaserCube system analysis was then performed to identify specific aspects for which a further development was required, in the scope of the final in-orbit demonstration of the system. The work package concerning LaserCube's design optimization was extensively interdisciplinary and included activities ranging from the structural analysis of the system to assess its capability to withstand launch loads to the structural and thermal analysis of a launch lock mechanism. In addition to the design development and testing of LaserCube in the perspective of an in-orbit demonstration of the system, the study of specific solutions for a version of the terminal dedicated to inter-satellite communication was carried out. Although inter-satellite optical communication is based on similar principles and technologies with respect to space-to-ground communications, some specific challenges must be faced, mainly related to the relative position of the communicating terminals and the constraints in terms of mass and power. In this context, the doctoral work has specifically focused on the intersatellite link budget analysis and on the functional verification of the system's telecommunications performance.

Concerning space-to-ground and ground-to-space communications, a further major step for the development of an end-to-end telecommunication service consists in the development of a dedicated

Optical Ground Station, to be used both for the support of the satellite optical terminal demonstration and during nominal operations. As anticipated, the areas of development that promise to drastically improve the performance are numerous and are distributed on the different operational phase of the telecommunication: pointing, acquisition and tracking. The current work has primarily focused on the upgrade of an existing facility (Matera Laser Ranging Observatory) to make it compatible with space optical communications. In a first phase, the existing facility has been studied at system level to identify which subsystems had to be integrated. This translated into the design of the optomechanical subsystem dedicated to the reception of the telecom signal from the satellite and the transmission of the required reference beacon beam and the uplink telecommunication signal. This work required an extensive understanding of an intrinsically multidisciplinary problem, including the challenges related to the atmospheric medium turbulences. The design has led to the selection, procurement and installation of the final components through an iterative design process that ensured the compatibility of system and application requirements.

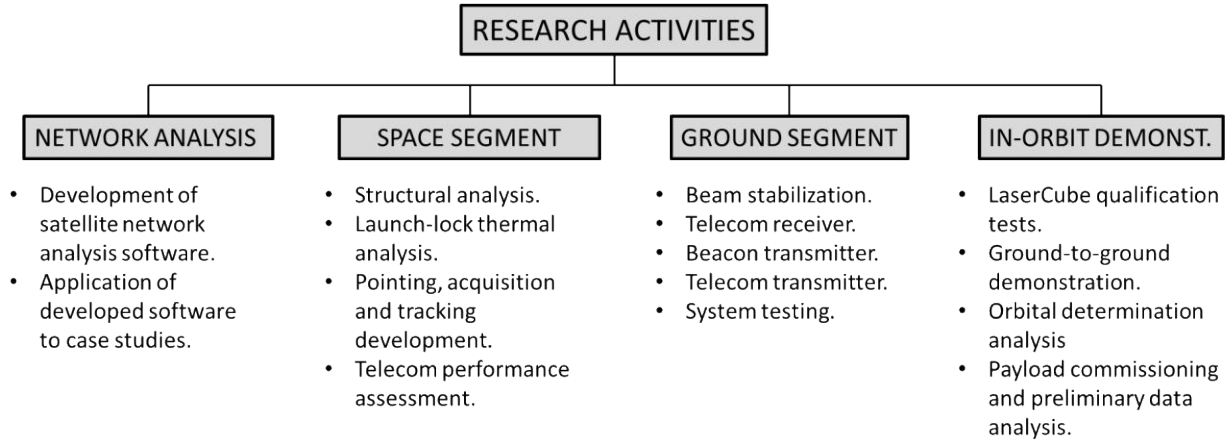

Figure 1-1: schematic description of the research activities.

A consistent part of the work has finally been dedicated to the support of the activities specifically related to ensure the successful in-orbit demonstration of the developed telecommunications terminal. First, the correct establishment of the link and the minimization of the acquisition time had to be ensured. For this purpose, a preliminary ground-to-ground test was conducted to familiarize with the specific challenges related to the link acquisition and assess the functional performance of the system in a representative environment. The adoption of techniques for the accurate determination of the satellite position was also necessary and has been implemented through the development of advanced orbital determination and propagation algorithms and the application of existing ones to the challenges of optical communications. A numerical analysis of signal acquisition strategies has also been performed for the identification and optimization of the solution most suitable to the developed system. The project has culminated with the activities related to the actual in-orbit launch of the system, namely: space qualification tests, integration on the host satellite, support to the operation management and system commissioning.

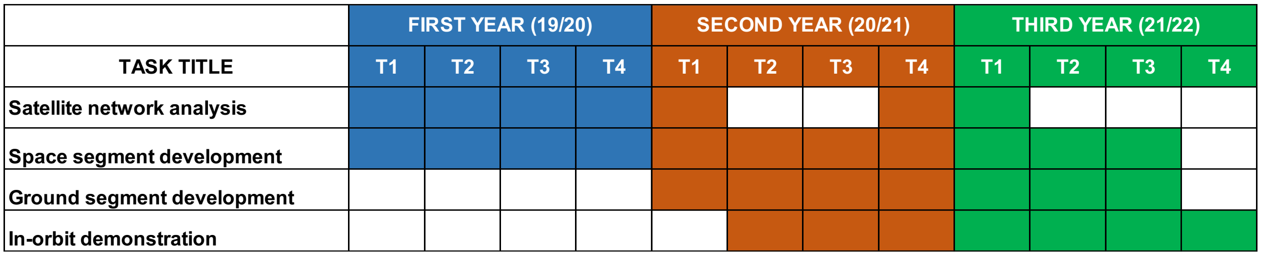

	FIRST YEAR (19/20)				SECOND YEAR (20/21)				THIRD YEAR (21/22)			
TASK TITLE	T1	T2	T3	T4	T1	T2	T3	T4	T1	T2	T3	T4
Satellite network analysis	🟦	🟦	🟦	🟦	🟧			🟧	🟩			
Space segment development	🟦	🟦	🟦	🟦	🟧	🟧	🟧	🟧	🟩	🟩	🟩	
Ground segment development					🟧	🟧	🟧	🟧	🟩	🟩	🟩	
In-orbit demonstration						🟧	🟧	🟧	🟩	🟩	🟩	🟩

Figure 1-2: Synthetic Gantt chart of the performed activities.

1.3 Research approach and thesis structure

The conduction of the doctoral work in the context of a space mission leading to an in-orbit launch has requested a profoundly multidisciplinary approach and allowed the candidate to work on all the phases of a space system development, from the preliminary design of the system to the final commissioning of a satellite payload. The theoretical understanding of the challenges specifically related to space systems and optical communication applications was obtained through the analysis of the state of the art, the individual study of bibliography and the educational activities and resources offered by the doctoral course. The theoretical study has been of constant support to the activities related to system and subsystems analysis and design, which was carried out both with analytical and numerical tools. A consistent part of the work has included the manufacturing, assembly, integration and testing of the designed systems and the writing of the relative documentation and reports.

The results achieved by the research are numerous, both in terms of scientific and technical achievements and of professional education of the candidate. From a technical-scientific point of view, the followed approach has allowed to deeply investigate the challenges relative to optical communications, contributing to a substantial strengthening of the already existing competences of the start-up company in which the project has been carried out. Moreover, the start-up context has allowed to combine the acquisition of a solid research method with the peculiar competences of an industrial environment, such as the effective interaction with clients, partners and suppliers.

The main activities carried out during the three years are documented in this thesis, which is structured as following:

- Chapter 1: introduction to the project motivation, scopes and methodology.
- Chapter 2: overview of satellite optical communications, in terms of market prospects, relevant applications and technical state of the art.
- Chapter 3: description of the developed optical satellite networks analysis tool and case studies description.

- Chapter 4: description of the main activities related to the space segment development.
- Chapter 5: description of the main activities related to the ground segment development.
- Chapter 6: description of the main activities related to LaserCube’s in-orbit demonstration.
- Chapter 7: conclusions and future work.
- Appendix I: description of optical link budget design principles.
- Appendix II: description of link acquisition analysis.

2. SATELLITE OPTICAL COMMUNICATIONS OVERVIEW

In this chapter an introduction to the current trends of satellite optical telecommunications is provided, with a specific attention to small satellites. The chapter has been divided into three sections, corresponding to the following purposes:

- Provide market context to support the motivations at the base of the work carried out during the doctoral project (Section 2.1)
- Present promising applications that can help to identify design requirements and to perform trade-off analyses at system level (Section 2.2)
- Describe the state of the art to establish a benchmark and a starting point for the technological developments reported in the rest of the work (Section 2.3).

2.1 Market prospects

The small-satellite market is in a phase of fast growth. The 2019 Euroconsult “Prospects for the Small Satellite Market” report [6] anticipates that around 8600 smallsats will be launched within 2029, with an average of 880 sats/year by the end of the decade and an increase of 22% with respect to previous estimates. These figures are in line with the estimates provided by other analysis companies, such as Northern Sky Research ([7], see Figure 2-1). The increase in the number of satellites launched is associated with a strong economic growth, with forecasts on the small-satellite market Compound Annual Growth Rate (CAGR) ranging from 12% to 18% for the next years ([8], [9], [10]). This growth leverages the emergence of a wider trend often referred to as New Space Economy, consisting in the integration of spaceborne applications in the context of privately led scientific and commercial activities.

Four major services driving the development of small-satellite market are commonly reported (see e.g. [11]):

- Earth Observation imagery and analytics
- LEO broadband constellations
- Situational awareness
- In-orbit servicing, assembly, and manufacturing

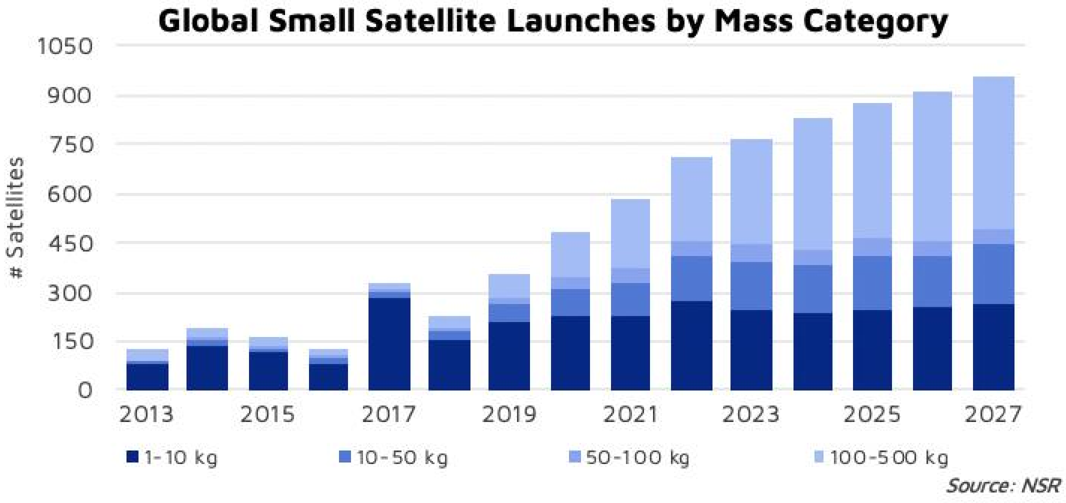

Figure 2-1: NSR’s Small Satellite Markets 5th Edition report

The use of Earth Observation data for terrestrial applications is having increasing success, thanks also to the cost reduction of space access allowed by technological developments, which is reflected in lower costs of satellite data services. The progressive consolidation of the applied technologies and the professional training of specialized personnel is expected to further support the growth of this sector, with an estimated CAGR around 7% from 2022 to 2031 [[12], [13]]. The estimated evolution of the EO global market in the next years is presented in Figure 2-2. A particular boost is expected to be offered by the insurance and finance sector [13], once the value of EO data for financial forecasts and risk assessment will be fully recognized and integrated in the decision-making process.

The increasing demand of data generated in space, which is progressively leading to discuss EO in terms of *big data*, is automatically reflected in the technological developments that are necessary to effectively bring these data to relevant users and stakeholder. This implies that, besides the remarkable opportunities that *big data* can provide in terms of increase in information value [14], the challenges that derive from this approach to data collection and processing must be taken into account, both in terms of storage ([15], [16]) and telecommunication system requirements ([17]). This means that fast and reliable telecommunication systems will be needed, with available data rates in the order of 10s or 100s of Mbps, a performance which can hardly be obtained with traditional RF-based technologies. The adoption of satellite optical communications can then guarantee to meet the technological requirements that will enable the development of faster and effective EO services.

Besides representing an enabling technology for the diffusion of EO services and the delivery of space-generated data back to Earth (the so-called “From Space” paradigm), satellite optical communications are obtaining growing interest as a means to transfer data generated on ground to other locations on Earth (“Through Space” paradigm). According to NSR’s 2021 Space Traffic Study ([18]), space data volumes are expected to grow by a factor 14 over the next few years, with a volume passing from 8900 petabytes in 2020 to more than 125000 petabytes by 2030 [18]. Among the many advantages provided by satellite optical communications with respect to traditional ground and space telecommunication services, the most

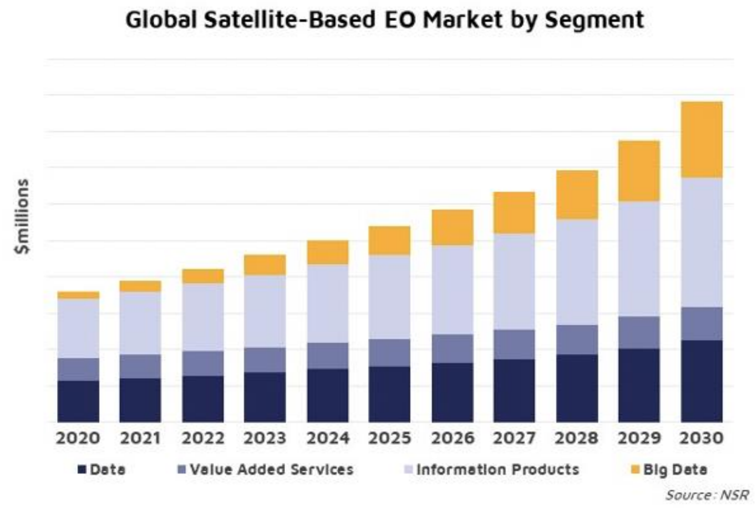

Figure 2-2: *Satellite-Based Earth Observation, 13th Edition* (EO13)

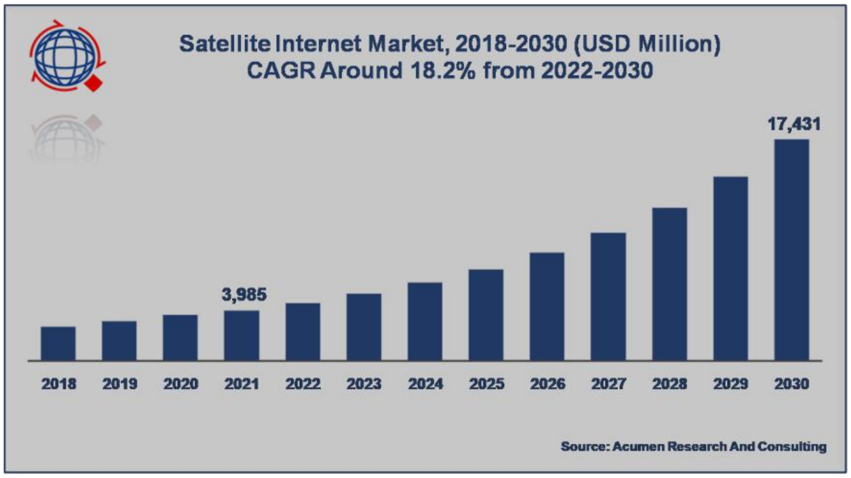

Figure 2-3: Satellite internet market forecasts by Acumen Research and Consulting.

promising from a market point of view are the higher bandwidth, the service security guaranteed by extreme beam directivity and the possibility to provide connection to remote areas where recurring to classical land infrastructure is expensive and complicated. Satellite internet is expected to represent a solid resource for both private and public economy in the next years, with an estimated CAGR of 18.2% between 2022 and 2030 (Figure 2-3, [19]).

A further field that will strongly benefit from the development of satellite optical communications is situational awareness. Leveraging the opportunity offered by satellite networks to transfer high volumes of data anywhere on Earth in real-time, applications such as ship traffic monitoring and mining facilities management are expected to complement the role of EO and satellite internet for a fast and effective integration of satellite services into day-to-day activities.

The considerations developed in this paragraph have aimed at providing a sound context to understand the rapid increase in the research and development efforts for satellite communication technologies. This appears to be consistent with a remarkable 59.3% estimate of laser communication terminals CAGR between 2022 and 2030, taking the expected size of this market from just above 20 million USD in 2021 to more than 700 million USD in 2030 [20].

2.2 Applications and services

In this Section an introduction to the main applications of satellite optical communications related to the market trends described in Section 2.1 are presented.
From a technical point of view, satellite optical communications offer two main advantages:

- High throughput, also for small spacecraft
- Possibility of near-real-time delivery thanks to ISL connectivity

The implementation of inter-satellite connectivity to small satellite constellations in Low Earh Orbit (LEO) could allow to achieve quasi-global coverage and quasi-real-time satellite data access at the same time. This would represent an invaluable resource in applications in which real-time data are specifically required, generated either in space or on ground.
For what concerns data generated in space, traditional Earth Observation systems are usually based on few large spacecrafts, such as the European Space Agency (ESA) Sentinel program satellites. This implies that an excessive amount of time can be needed from the request of data access to the communication of the requested data back to Earth, which translates into potentially inadequate Age of Information (AoI) performance. More recently, small satellite LEO constellations are being deployed, allowing for an increased revisit rate at comparable performances. Two remarkable examples are Planet, which put in orbit two different constellations of satellites, one with more than 150 3U satellites and one with 21 satellites of 110 kg, and Iceye that has 10 satellites of 85 kg in orbit, and plans to launch 8 new satellites within 2022 [21] [22]. An application of Earth Observation which is receiving increasing interest, also in relation to the emerging issue of climate change and global warming, is agriculture monitoring for crop yields preservation and optimization. The capability to track changes in soil and vegetation and the availability of up-to-date remote sensing data is a valuable resource in the direction of a more efficient and sustainable food chain, effectively contributing to the decision-making process both at private and government level. ESA is paying strong attention in this direction [23], in parallel with an ever-increasing awareness of hydrological and hydrogeological issues affecting the global food system. In this regard, private companies are already starting to provide groundwater monitoring services leveraging the capabilities offered by satellite communications, both in terms of the relay of data collected in-situ [24] and data collection by satellite-based remote-sensing instruments. The growing availability of up-to-date data is also supporting the adoption of traditional financial instruments, such as index-based insurances, to users located in remote areas and developing countries, where the absence of a widespread ground based crop monitoring infrastructure represent a discouraging factor both for insurance companies (due to the higher probability of frauds) and farmers (due to the high premium costs that derive from the difficulty to build a risk history and assess losses and damages). In-depth analyses of the potential of satellite remote sensing for agricultural insurances can be found in [25] [26] [27] [28].Other commercial examples for which frequent

remote sensing data could provide a valid support is asset monitoring for business and stock health assessment ([29], [30]) and geological monitoring to support real estate management, improve quality of dwelling and support city planning ([31], [32]).

Besides having a strong economic relevance, the near-real-time delivery of remote sensing data could even more importantly represent a game changer for climatic disaster response. The use of data collected in-situ is a typical choice in case of disaster response operations, but it requires the presence of a pre-existing infrastructure, preventing interventions in remote or developing areas. Satellite data are a valuable alternative, as they provide information from any point on Earth regardless of the ground equipment availability. Besides providing complementary data in support of disaster response management, the implementation of satellite network based on inter-satellite connectivity would give access to up-to-date information: the access to real-time data for disaster response can make a difference in saving human lives and preserving the environment [33], but it has also an important economic impact [34]. An in-depth analysis of the potential benefits of inter-satellite connectivity for disaster response is provided in Section 3.3.

If on one hand satellite optical communications promise to address a wide variety of civil and commercial needs, several challenges remain open to make satellite telecommunications payloads capable of providing a reliable and high-performance service. A crucial step to effectively achieve high throughput real-time data delivery across the globe is the development of satellite communication networks, either in terms of intra-constellation connection or of single satellite-to-satellite data relay. This process concurs to the wider trend of integration of satellite platforms in the global internet network. Impressive efforts are being made in this direction by the private sector, with the progressive deployment of the Starlink constellation by SpaceX being just the most outstanding example. Nevertheless, the current state-of-the-art of satellite optical communications cannot guarantee the throughput performance requested to implement a fully integrated satellite internet network based on small-satellite LEO constellations: a challenge that requires to put additional effort in the next years in terms of network-, system- and component-level technological research and development. Satellite internet networks would also be crucial for technologies such as IoT and M2M, specifically for applications involving the communication with remote systems, for example in the context of mining plant monitoring or crop management. An in-depth analysis showing the potential benefits of the integration of optical communications on constellations already devoted global connection through space is presented in Section 3.2.

One final scope in which optical communications could offer an outstanding contribution is that of secure communications, an area which is having increasing relevance as a consequence of the growing presence of digitally-based systems in daily activities. One characteristic of optical communications that constitutes a direct advantage for secure communications is the extremely low divergence of the transmitted beams, which allows for a very precise selection of the telecommunication targets. A second characteristic that will indirectly contribute to the security of telecommunications is the capability of implementing fully autonomous satellite-based networks, which are intrinsically more immune to jamming and sabotage. Moreover, the adoption of optical wavelengths introduces the possibility to implement quantum communications, an opportunity that is raising growing interest [35] and that was previously unavailable, mainly due to the difficulty of building RF single photon detectors. Besides opening a series of opportunities for civil applications, this will represent a crucial edge in defense and intelligence applications, also considering the increasing importance of telecommunication technologies in general for modern warfare operations [36].

More in-depth surveys of the potential of satellite optical communications for commercial and civil applications can be found for example in [13], [37], [38].

2.3 Technical overview and state of the art

In this section an introduction of satellite optical communication systems state of the art is given. Most of the theoretical content reported in this Section has been derived from [5] and [39]. The first three paragraphs will provide an overview of the state of the art of the main aspects of a satellite communication system: network architecture, space segment and ground segment. Two additional paragraphs have been included to address two cutting edge applications on telecommunications systems based on optical wavelengths: quantum communications and deep-space communications. A brief mention to optical communication systems recently developed by government and private actors is also included in each paragraph.

2.3.1 Satellite networks

A satellite network is a global access network relying on a global transport network that is formed in space by ISLs. Traditional satellite networks are based on large Geostationary Earth Orbit (GEO) spacecraft addressing mainly broadcasting applications. A trend towards satellite networks based on Non-Geostationary Orbits (NGSO) constellations has emerged lately. The main reasons for the increasing interest in NGSO broadband satellite networks are:

- The possibility to provide global coverage, compared to single-satellite-based systems
- The possibility to implement fully autonomous satellite communications systems.
- The ability to adopt frequency reuse using multi-spot beams thanks to low beam divergence.
- Very low latency compared to GEO (due to reduced overall link distances) and terrestrial optical fibre (due to higher speed of light in vacuum) networks.
- Easier implementation of redundancy, since each spacecraft of a small satellite constellation is much less expensive.

Optical satellite networks design is typically based on satellite constellations. Two traditional constellations architectures have consolidated, the so-called Walker Star and Walker Delta constellations (Figure 2-4), whose geometry is in the first place defined by:

- The total number of satellites
- The number of satellites per plane (which automatically defines the number of planes)
- The phasing factor between homologous satellites in adjacent planes

In these types of constellations, the network topology is typically derived from the classical Manhattan mesh, where each node of the network can communicate with four adjacent nodes, overall forming a chessboard-like structure (Figure 2-5).

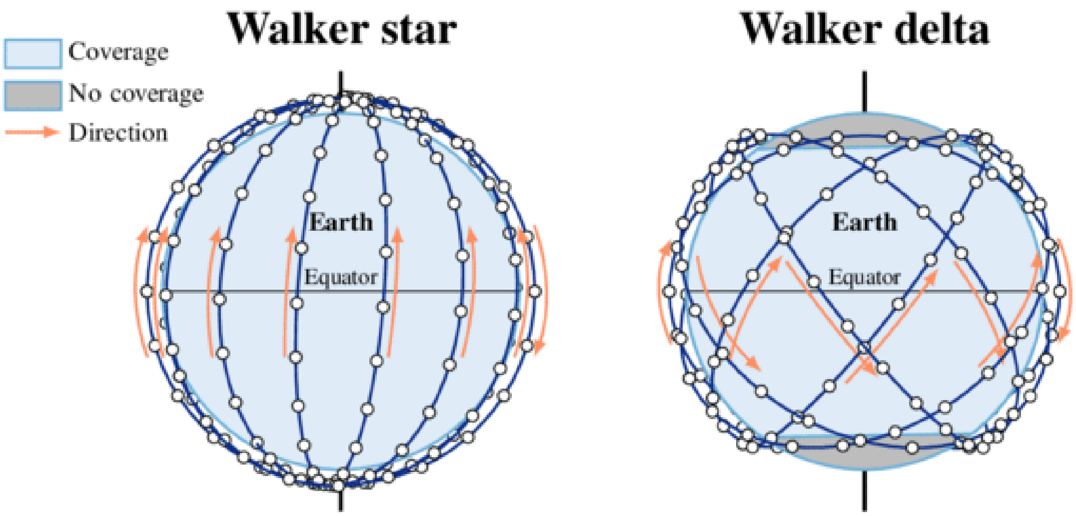

Figure 2-4: schematic representation of Walker star and Walker delta constellations.

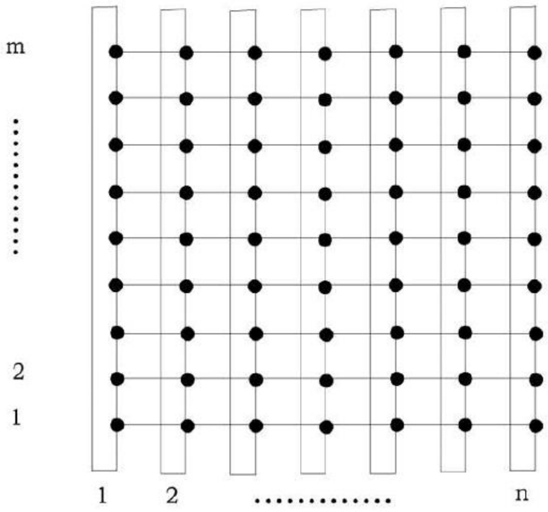

Figure 2-5: schematic representation of Walker Star constellation mesh topology.

In designing the space segment of an optical satellite network, SW&P constraints must be considered carefully, as both electrical consumption for driving the transmitted laser and running the onboard processing for routing management must be taken into account.

The main components of an optical satellite network payload are:

- Laser transmission hardware (see Paragraph 2.3.2).
- The electro-optical components necessary for routing.
- Harness for connecting the laser transmission and routing components.

Data capacity requirements for the design of the space segment terminal, which directly reflect on SW&P requirements, are based on traffic demand statistics. Two main types of traffic can be addressed by a satellite network, based on the origin of the generated data:

- Satellite-sourced, which typically refers to applications requiring downlink of remote sensing data generated by either the same satellite, another satellite of the constellation or an external satellite for which the constellation serves as data relay provider.
- Source-to-destination, which addresses applications requiring global data transport.

The data traffic passing through a node of the network depends on the dynamically changing connections with the ground stations connecting the network to the terrestrial network: it can be shown that average traffic through each node of the network is typically much lower than the peak traffic, since satellites are above areas with low user density for most of their orbit. While optical communications intrinsically allow to reach higher bitrates with respect to RF systems at comparable SW&P specs, the performance of these systems can be further improved to reach Tbps uplink/downlink capacity using Wavelength Division Multiplexing (WDM), a technique that consists in establishing several channels for each terminal, where at each channel is associated a specific wavelength. This approach basically allows to multiply the terminal capacity by the number of available wavelengths at a relatively low increase in the system's SW&P requirements. Moreover, this approach allows to adopt very efficient network routing techniques such as wavelength routing, a consolidated approach for terrestrial fibre networks: this approach is based on the concept of *lightpath*, which consists in the establishment of a fully optical communication channel between the source and the destination. The terminals representing the nodes of a network where wavelength routing is adopted are often referred to as "transparent", as no electro-optical conversion is needed. Routing decisions are ultimately based on a tradeoff between minimizing the number of lightpaths, minimizing the total distance of the lightpath and maximizing the overall throughput of the constellation.

Although optical satellite networks promise to represent a turning point in terms of global communications capabilities, the insufficient Technology Readiness Level (TRL) of several fundamental components of such networks have so far prevented a large scale spread of this type of infrastructure. Nevertheless, the rapid technological developments in the space field of the last decades have recently led private actors to heavily invest in this sector, making satellite networks deployment in the short/medium term a concrete possibility.

The private company SpaceX from USA has worked in the last years at the development of Starlink, a constellation which aims to provide a global broadband internet access service. The constellation is expected to comprise thousands of satellites in LEO, in order to achieve complete global coverage and minimize telecommunication latency. The constellation deployment has begun in 2018 and as of September 2022 it counts over 700000 subscribers and 2300 functioning satellites in orbit, with a deployment rate of about 50 satellites per Falcon 9 flight. The company has announced in August 2021 that all future Starlink satellites will be provided with optical communications terminals for ISL capability [40]. A visual representation of the thousands of satellites planned to be deployed at regime is shown in Figure 2-6.

Telesat is developing Lightspeed, a satellite global network comprising 188 satellites in hybrid (polar and inclined) LEO orbits. The constellation will feature phased array antennas for space-to-ground telecom and optical terminals for intersatellite connectivity. The integration of high throughput telecommunication payloads and state-of-the-art in-space modulation, demodulation and routing capabilities will allow the constellation to achieve Gbps data capacity and Tbps overall constellation throughput. The constellation is planned to target mainly aeronautical, maritime, enterprise, telecom and government applications [41].

Oneweb is a space telecommunications enterprise headquartered in London that plans to operate a constellation of 648 satellites in LEO (1200 km). The 150 kg class spacecraft will feature RF feeder links to provide backhaul and mobile broadband connections to remote and unserved users from around the globe. The performance target is an available datarate up to 50 Mbps, with latency as low as 50 ms [42].

Astrocast is a Swiss company which aims to deploy a satellite constellation of nanosatellites based on the CubeSat standards. The constellation will target IoT applications and will be comprised of approximately 100 satellites. The constellation will provide bidirectional communication and an expected latency below 15 minutes [43]. Although it will likely not comprise optical communication terminals, it will serve as a test bench for the development of satellite networking solutions.

ESA has recently started funding for a Phase A study for Hydron (High Throughput Optical Newtork). The tender aims to investigate end-to-end system architecture to extend terrestrial networks based on optical fibres into space. The funded studies will analyse the main enabling elements of a high throughput optical network based on optical communications, such as optical feeder links, high datarate WDM, optical ISL, onboard routing, integration with terrestrial networks etc. The final goal of the programme is the launch of a series of in-orbit missions for the feasibility demonstration of a Tbps rated satellite optical network and the definition of a plausible roadmap to full network deployment taking into account costs and scheduling constraints.

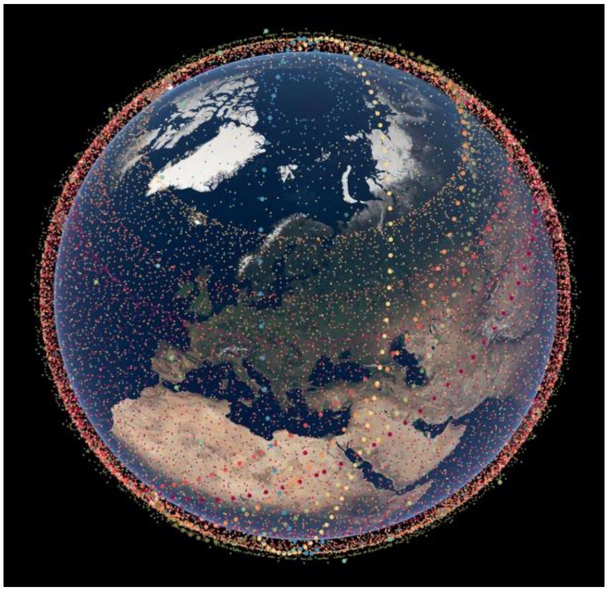

Figure 2-6: Visualisation of the 30000 planned satellites from the Starlink Generation 2 constellation as of 2022. Different sub-constellations are illustrated with a different colour. (Credits: European Southern Observatory, ESO).

2.3.2 Space segment

The space segment is the fundamental building block of any kind of optical satellite network. Optical communication payloads are dedicated to the transmission of the laser signal for space-to-space or space-to-ground telecommunication. They are typically provided with a Pointing, Acquisition and Tracking (PAT) system that ensures that the narrow transmitted beam reaches the target terminal with minimum pointing losses. The transmitted and received optical beams are shaped by a focal plane array which ensures the required quality of the transmit beam and the optimal coupling of the incoming signal with an optical fiber or directly to the photosensitive detector.

From a functional architecture point of view, laser communication terminals typically consist of:

- A flight optomechanical assembly
- TX beam generation and modulation electronics
- RX beam demodulation electronics

The flight optomechanical assembly is the part of the system mainly dedicated to the accurate pointing of the system's optical axis for receive and transmit purposes and the correct shaping of the incoming and outcoming light beams. A flight optomechanical assembly is typically composed of the following main parts:

- Transmit and receive aperture optics
- Beam path routing optics
- Acquisition and tracking sensors and fine pointing actuators
- Mechanical structure
- Coarse-pointing mechanism (in alternative/integration to spacecraft attitude pointing)

Due to the extreme beam pointing accuracy requirements, the optomechanical assembly design must confer to the system high levels of thermo-mechanical stability, in order for the payload to withstand launch vibrational loads and orbital thermal cycles. Beam divergence and/or focus control mechanisms may be included to increase system versatility and ensure margin with respect to potential misalignments during launch. Moreover, active and/or passive isolation systems may be integrated in the structural design to decrease the requirements severity on coarse/fine pointing mechanisms, which are strictly dependent on the residual spacecraft jitter spectrum (typically in the 0.1 to 100s Hz range).

Three main high-level layouts can be adopted for the optomechanical assembly:

- Gimbaled telescope and optical bench.
- Gimbaled telescope with coudé path to fixed optical bench.
- Gimbaled flat mirror to fixed telescope and optical bench.

The selection of the architecture is based, among other factors, on Field of View (FoV) and Field of Regard (FoR) requirements, which are in turn dictated by mission requirements.

PAT is one of the main functions of the optomechanical assembly. The main requirements in terms of PAT capabilities are:

- Rapid link acquisition with high probability of success.
- Tracking of opposite platform with (sub-)microradian accuracy to minimize pointing losses.
- Provide sufficient FoR.

- Compensate for residual jitter from host platform and/or active/passive isolation system.

Specific attention must be paid to the phenomenon of velocity aberration, which may require the implementation of a Point-Ahead Angle (PAA) mechanism.

The ultimate functional requirement for an optical communication terminal is to transmit data at high speed and with few errors. Two main detection approaches can be adopted:

- Direct detection: this type of detection is based on a corpuscular representation of light, as the information content is basically related to the number of photons arriving at the photosensitive detector and translated into an electrical signal by means of photon-electron conversion; typical modulation formats are On-Off Keying (OOK) and Pulse Position Modulation (PPM)
- Coherent detection: this type of detection is based on an electromagnetic wave representation of light; in this case information can be encoded in several properties of the transmitted light, such as amplitude, frequency, phase, polarization and combinations therof. In order to perform coherent detection, the received light electromagnetic field is coherently superimposed to the electromagnetic field of a light source generated by a local oscillator; the intrinsic non-linearity of the photodetector with respect to electric field amplitude allows to amplify nominal optical frequency only and filter out unwanted frequencies. This theoretically allows to achieve shot-noise-limited performance (See Appendix A), regardless of the limits imposed by the detector itself. Typical modulation formats that can be adopted are Binary Phase Shift Keying (BPSK), Quadrature Phase Shift Keying (QPSK), n-Quadrature Amplitude Modulation (n-QAM), and PPM.

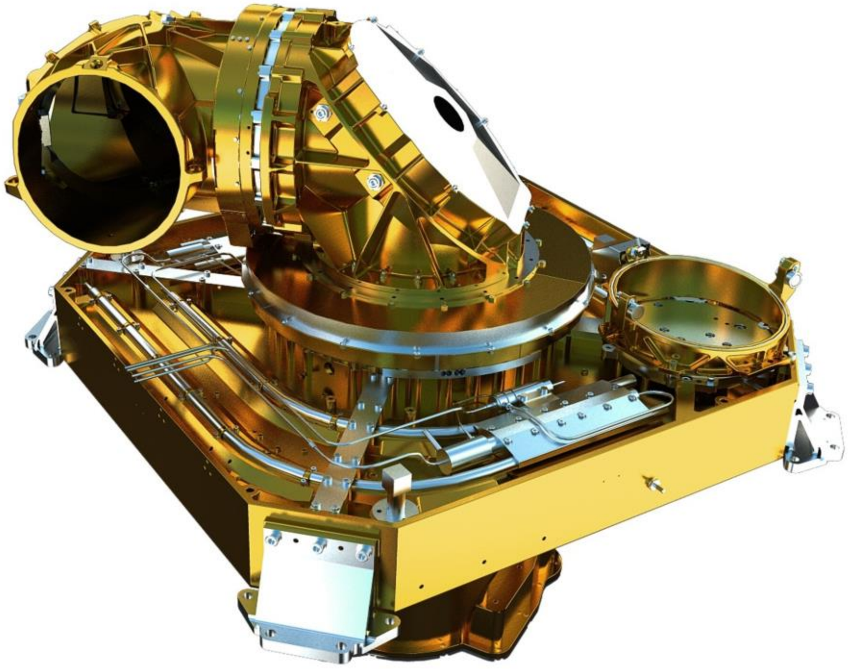

Figure 2-7: European Data Relay System Laser Communication Terminal (LCT). (Credits: ESA).

The selection of the detection approach has a direct impact on both the receiver and transmitter system architecture, reflecting in system complexity and achievable performance. Better performances can typically be obtained with a system based on coherent detection, at the expense of considerably higher system complexity and development/operational cost.

The detection approach has also a direct impact on the laser modulation architecture. The first option is the direct modulation of low-power lasers driving current: this approach is relatively simple, inexpensive and compact, but can only applied to direct-detection-based systems. The second option is the external modulation (e.g., by means of electro-optical modulation or electroabsorption) of a CW (Continuous Wave) laser: besides being compatible with both direct and coherent detection formats, this approach allows for much higher speeds (typically 10s GHz), larger extinction ratios, lower chirp, and lower modulation distortion; nevertheless, a higher insertion loss (typically > 6 dB) must be considered in the link budget.

A consolidated history of optical communication terminal in-orbit demonstrations based on large satellite platforms can be found in literature. Japan has been a pioneer in this sense with the first downlink demonstration between the Japan Aerospace Exploration Agency (JAXA) RTS-VI GEO satellite and a telescope of the National Institute of Communications Technology (NICT) in 1995. JAXA's work in this field has continued with the demonstration of the first LEO-to-ground optical downlink from the OICETS satellite. Further experiments have been conducted by ESA to assess the feasibility of inter-satellite connectivity, which resulted in the in-orbit demonstration of the first optical ISL between Artemis satellite and the SPOT 4 satellite from the French National Centre for Space Studies (NICT). A second fundamental test has been performed by ESA in 2008, when an ISL was established between two satellites 40000 km apart by means of Tesat-Spacecom's Laser Communication terminal (LCT, Figure 2-7), achieving a remarkable bitrate of 1.8 Gbps. Several experiments have also been conducted by private companies, like the demonstration of a downlink connection from the International Space Station (ISS) with the SOLISS by Sony and KSAT and the recent development of LCT135, a high throughput terminal by Tesat. Further technological demonstrations are planned for the near future: see for example NASA's Laser Communication Relay Demonstration (LCRD) and Terabit Infrared Delivery (TBIRD) and ESA's funding of numerous research projects by means of the ARTES programme.

Besides the solid history of technology demonstrator with large satellites by governmental actors, the development of more compact systems small satellites has recently gained importance, paving the way for the deployment of fast satellite communication networks. Germany is among the countries that have invested the most in this direction, both from government and private actors, with Mynaric and Tesat being at the forefront of space systems for optical communication. German Aerospace Center (DLR) has consolidated a strong expertise in this field, with the development of systems such as Optel-µ, OSIRIS and PIXL 1, all below the 5 kg payload class. Finally, a remarkable effort for the development of optical communication terminals compatible with platforms observing the CubeSat standard has been made by the private sector: see for example Tesat's CubeLCT, AAC Clyde Space's CubeCat and Stellar Project's LaserCUbe. A synthesis of the performance of some currently available or planned terminals is presented in Table 2-1. The performance presented in the table has been derived from publicly available information and should represent a mere indication of performance orders of magnitude, since system specifications declared by providers are subject to frequent changes.

Table 2-1: Synthesis of demonstrated/declared terminals specs and performances.

Terminal	Provider	Application	Mass [kg]	Power [W]	Bitrate	Max link range [km]
µLCT	Space Micro	DL/ISL	25	150	100 Gbps	8000
Alphasat LCT	ESA	ISL	53	160	1.8 Gbps	45000
Click A	NASA	DL	<5	NA	10 Mbps	400
Click B/C	NASA	ISL	<5	NA	>20 Mbps	15-360
CONDOR	Mynaric	ISL	NA	NA	2.5 Gbps	10000
Cube4ISL	DLR	ISL	NA	NA	100 Mbps	1500
CubeCat	AAC Clyde Space	DL	<1.5	15	100-1000 Mbps	1000
CubeLCT	Tesat	DL	0.4	10	100 Mbps	1500
LaserCube DL	Stellar Project	DL	< 2.5 kg	<30	1 Gbps	1500
LaserCube ISL	Stellar Project	ISL	< 2.5 kg	<30	100 Mbps	1000
LCRD	NASA	LC/DL	69	130	1.2 Gbps	36000
LCT135	Tesat	ISL	53	120	1.8 Gbps	80000
Lucas	NICT	ISL	NA	NA	1.8 Gbps	40000
O2O	NASA	DL	NA	NA	250 Mbps	400000
OCSD	NASA	DL	3	NA	200 Mbps	LEO-to-ground
OICETS	JAXA	ISL	570 (overall satellite)	1200	50 Mbps	45000
Optel-µ	DLR	DL	< 5	<45	2 Gbps	LEO-to-ground
OSIRIS	DLR	DL	5	50	10-100 Gbps	LEO-to-ground
PIXL 1	DLR	DL	0.35	8.5	100 Mbps	LEO-to-ground
Silex	ESA	ISL	150	130	50 Mbps	40000
SmartLCT	Tesat	ISL	30	150	1.8 Gbps	45000
SOLISS	Sony, KSAT	DL	NA	NA	100 Mbps	LEO-to-ground
SOTA	NICT	DL	6	<40	10 Mbps	1000
TBIRD	NASA	DL	2.3	120	200 Gbps	LEO-to-ground
TOSIRIS	Tesat	DL	9	130	Up to 10 Gbps	LEO-to-ground

2.3.3 Ground segment

The ground segment is the part of the satellite communication network dedicated to the connection of the orbital and the terrestrial subsections of the network. The connection established between the ground segment and the space segment is commonly named *feeder link*. The ground segment Optical Ground Station (OGS) typically includes an optical aperture to collect the light coming from the satellite during downlink operations and an uplink beacon to provide the space segment with a reference beam for link acquisition and tracking. The OGS may also include a telecom laser transmission subsystem in case of uplink capability requirements. The collected beam is routed to a focal plane array to couple it with an optical fiber or directly into a photosensitive detector, which converts the optical signal into an electrical signal that can then be demodulated by dedicated electronic components.

As opposed to inter-satellite connectivity, the communication between an OGS and a spaceborne terminal is intrinsically affected by phenomena related to the atmospheric medium. These may include reduced visibility, attenuation, atmospheric turbulence, scattering etc. Atmospheric turbulence is particularly critical for coherent detection links, as it introduces phase fluctuations. Another critical phenomenon related to atmospheric turbulence is scintillation, which consists in the fluctuation of the signal irradiance, similarly to what can be observed with twinkling stars; increasing the aperture area typically results in lower scintillation (aperture averaging) but at the cost of higher system complexity. Two additional atmospheric phenomena, affecting in particular uplink transmitted beams, are beam spreading and beam wander. These two phenomena typically result in a lower average beam irradiance at the target satellite and are generally mitigated by a larger aperture at the receiver. The design of the OGS must then be performed carefully to effectively take into account the several criticalities imposed by the atmospheric medium. Atmospheric effects can be studied both analytically and numerically. The selection of the OGS site must also be performed carefully. The mitigation of atmospheric effects is typically facilitated by high altitude locations, in the same way as they represent optimal sites for astronomical observations; on the other hand, these locations are typically isolated and lack the necessary infrastructure. A tradeoff between these two requirements must be carried out.

If high focusing resolution and preservation of phase information are required, like in the case of coherent detection, adaptive optics can be used to mitigate the effect of turbulence and bring the system near to diffraction limit. Simpler systems only include tip-tilt compensation, while more advanced system allow to compensate for higher-order distortions of the beam wavefront as well. These systems are typically based on spatially deformable mirrors controlled in closed loop based on the feedback from a wavefront sensor.

Figure 2-8: ESA’s OGS in Tenerife sending a laser beacon during optical communications experiment.

Although a lack of OGS facilities is still an obstacle for the fast development of satellite terminals and the future deployment of fully integrated satellite networks, a consistent effort has been made in the last years to provide an adequate infrastructure for technological demonstrations and future commercial exploitation.

ESA has built and regularly operates an OGS in Tenerife, Spain (Figure 2-8). The OGS is provided with a 1-meter telescope and serves as a test bench for optical communications experiments. Update activities have recently been carried out on ASI's Matera Laser Ranging Observatory (MLRO) to make it compatible with space-to-ground and ground-to-space optical communications experiments; a consistent part of the work presented in this thesis has been dedicated to this very activity and is described in Chapter 5. The Aristarchos telescope at Helmos Observatory (Greece) has been selected in 2020 to be first OGS of the Scylight programme. Australia is particularly active in this direction and is establishing an optical communications infrastructure named Australian Optical Ground Station Network (AOGSN): the Defence Science and Technology Group (DSTG) is currently developing an OGS near Adelaide and upgrade activities are currently underway to realize the Mount Stromlo Optical Communication Ground Station. DLR's has developed an OGS in Oberpfaffenhofen specifically dedicated to acquiring measurement during optical communication experiments (Figure 2-9). Several other ground systems are under development around the globe, like DLR's Transportable Optical Ground Station (TOGS) and Onera's FEELING OGS. Even more ambitious projects are under evaluation to achieve Tbps class feeder link capability thanks to adaptive optics, like the Terabit Optical Communication Adaptive Terminal (TOmCAT), ESA's Optical Ground Station for Terabit Feeder Link (OGS-OFL) the Advanced Laser Guide Star Adaptive Optics for Satellite Communication Assessments (ALASCA). The direct intervention of private actors has recently reaffirmed the commercial potential of optical ground station development: see for example Officina Stellare's supply of an OGS to the Indian Space Research Organisation (ISRO), KSAT's contribution on the deployment of the European Optical Nucleus Network (EONN), and Tesat's Transportable Adaptive Optics Ground Station (T-AOGS).

Figure 2-9: DLR's OGS in Oberpfaffenhofen.

2.3.4 Quantum communications

Besides the intrinsic advantages of using optical wavelengths described in this chapter, the use of laser-based systems will be an enabler factor for the implementation of quantum communications, an extremely promising technology in the frame of secure communications. Satellite quantum communications cannot be implemented with traditional telecommunication systems, due to difficulties related to single photon detection using RF wavelengths. One of the greatest advantages provided by quantum communications is the capability to identify communication eavesdropping, thanks to intrinsic properties of quantum physics. This allows to adopt robust cryptographic schemes, such as Quantum Key Distribution (QKD), for which unconditional security is virtually guaranteed by the very laws of physics [44]. The most ambitious programmes are investigating the feasibility to develop secure end-to-end satellite communications leveraging entangled quantum systems. The integration of quantum communications and the deployment of satellite networks could represent a paradigm shift in the management of data security at civil, military and commercial level.

Several projects have been funded to investigate the potential of satellite quantum communications. The Chinese Quantum Experiments at Space Scale (QUESS) onboard the Micius satellite operated by the Chinese Academy of Sciences is performing a series of experiments to test quantum-based satellite communications [45]. Canadian government is planning to verify the possibility to create a quantum communication infrastructure with the Quantum Encryption and Science Satellite (QEYSSat) [46]. NASA has funded the development of a payload, the Space Entanglement and Annealing QUantum Experiment (SEAQUE), to be mounted onboard the ISS to test three of the most promising technologies related to quantum communications: quantum computing, quantum sensors, and free-space optical communications. A fully integrated European Quantum Communications Network (EuroQCI) is under development thanks to an agreement between the European Commission, which will be in charge of the ground infrastructure, and ESA, which will develop the space segment through the Security and crytoGrAphic (SAGA) mission [47]. Other technology development and demonstration projects have been funded in Europe by the European Commission, such as the cubesat for QUANtum and 5G cOmmunications (QUANGO), a project in which Stellar Project has provided a consistent contribution. Padua is at the forefront of quantum communication technology development, with experiments like GaliQEye by the Department of Information Engineering (DEI) and the University of Padua's spin-off start-up ThinkQuantum.

2.3.5 Deep space optical communications

Although the technological developments presented in this work are mainly focused on small satellites in LEO, a brief description of optical communications peculiarities for deep-space missions shall be provided. One major characteristic of Deep-Space Optical Communications (DSOC) is the extreme distance at which links are established, which can be in the order of billions of kilometers in case of the farthest bodies like Pluto. This translates into huge space propagation losses, which can reduce the available bitrate of 10 orders of magnitude with respect to GEO-to-earth RF links at comparable system SW&P. Moreover, this imposes remarkable requirements on the ground segment infrastructure: NASA's Deep Space Network (DSN) antennas, for example, feature diameters up to 70 meters. Besides involving enormous technical complexity in terms of design and management of both space and ground segments, limits on the RF have represented a bottleneck for the potential scientific data return for several deep-space missions, with telecommunications performance falling short of the actual data collection capabilities of scientific payloads. All this considered, optical communications represent a valid solution to provide orders-of-magnitude higher data return from deep-space missions with respect to traditional RF systems and reduce the burden both on the space segment and the ground segment. Optical communications in deep space are affected by very specific challenges, like the strong stray light disturbance from sun for deep-space-to-earth communications, due to the low Sun-Probe-Earth angles (typically < 2). This requires to perform in-depth analysis of straylight disturbance and to design adequate mitigation solutions, like baffling, field-stops and Lyot stops. Moreover, extreme levels of cleanliness may be required to limit as much as possible unwanted scattering and reflections. Pointing based on star trackers may be a viable option to avoid particularly intense background noise from the sun (beaconless tracking). Tracking based on Earth imaging is also a valid option for relatively near bodies (Mars, Jupiter). As a final remark, particular attention should also be paid to the radiation environment on systems with strong magnetic fields (like Jupiter), an issue affecting both electronic components and optics coatings.

Figure 2-10: artistic depiction of NASA's Psyche mission.

Several projects and missions have been funded by agencies to develop deep-space optical communication capabilities. Between 2013 and 2014, NASA has demonstrated the first Moon-to-Earth optical link with the Lunar Laser Communication Demonstration (LLCD), achieving a remarkable 622 Mbps bitrate [48]. DLR is currently developing a miniatured system for Moon-to-Earth communication, SelenIRIS, based on the heritage obtained through near-earth optical communication systems like OSIRIS4Cubesat (O4C) [49] [50]. A series of Mars-to-Earth optical communication missions have also been proposed by NASA, starting from the Mars Telecommunications Orbiter (MTO) [51], but have been so far delayed due to shift in the Agency's priorities. Two important missions will demonstrate technological capability to perform laser communication from extreme deep-space distances: the Asteroid Impact Mission (AIM), developed by ESA, will transmit back to Earth the data collected during the investigation of the Didymos asteroid from a distance of 75 million km using laser communication [52]; while NASA will include a DSOC package to retrieve data collected by the PSYCHE mission, investigating a metal-rich asteroid orbiting the Sun between Mars and Jupiter [53].

3. OPTICAL SATELLITE NETWORKS ANALYSIS

In this chapter the activity related to the analysis and development of novel solutions for optical satellite networks is presented. This includes the development of a dedicated software for the analysis of telecommunication constellations performance in terms of latency and throughput, which has then been applied to the main applications of satellite telecommunication services, such as global internet connection, Internet of Things and earth observation data delivery. The chapter ends with a brief discussion of the results in terms of system level design implications.

3.1 Development of satellite network analysis software

Due to the promising role assumed in the near future by global communications based on satellite networks highlighted by the preliminary market investigation, a consistent part of the first year of doctoral activities has been dedicated to the development of a software tool in the Matlab environment in support of satellite networks analysis. The candidate has been the main contributor to the development of the described software, with the valuable support of Stellar Project's team. The time-based software allows to perform simulations and analysis of satellite network performance in terms of latency and throughput, in scenarios in which data is generated either on ground or in space, and retrieve the source-to-destination capacity at each time-step based on the current routing configuration. The software is based on the modelling of satellite constellations for optical communications based on classical network theory, in which the network is mainly characterized by:

- The network nodes, representing the satellites of the constellation
- The capacity of the data source, which can be located either on ground or in space
- The capacity of ISL connections in terms of available bps

A synthetic functional flowchart of the developed software is presented in Figure 3-1. As can be seen, a modular approach has been followed during the development of the software for the sake of higher flexibility. Starting from the definition of the fundamental simulation parameters (such as physical constants, constellation parameters, telecommunication parameters, simulation interval, etc.) the simulation proceeds with the definition of the location of the ground nodes (i.e. the ground stations) and the constellation network structure (Figure 3-2, left). The orbit of each satellite of the constellation is then propagated with a simplified geometrical model for simulation time reduction, with the assumption that this does not have a significant impact on the results. At each propagation time-step, the network connections are updated mainly based on the relative position of the network nodes (both on ground and in space) and a new traffic matrix is defined. The telecom performance at each time step is then computed in terms of connection latency and overall network throughput. Results are then saved in the form of numerical arrays and synthetic graphs. An animation of the constellation evolution can also be generated (Figure 3-2, right), an option that has turned out to be very useful both for the visualization of the modelled scenario and for code debugging purposes, as it immediately allows to identify macroscopic errors in the definition of network connections.

The main goal of the development of this software has been to derive valuable guidelines, both for constellation and payload design decisions and for the analysis of promising applications of satellite optical communications applied to global data transport infrastructures.

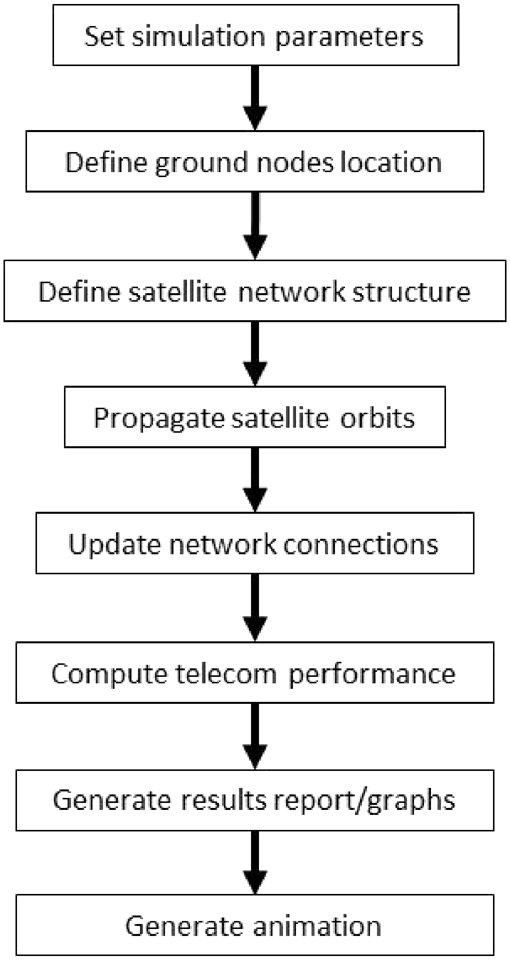

Figure 3-1: Software functional flowchart.

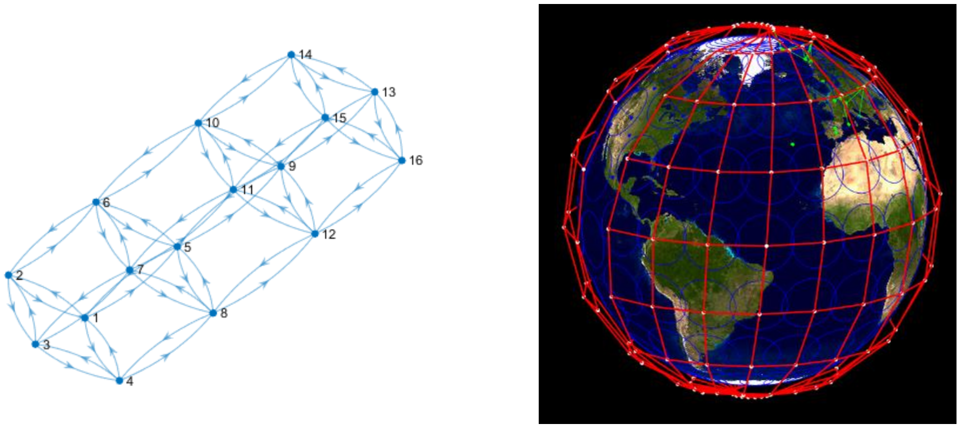

Figure 3-2: Left: example of satellite network structure defined by the connections (edges) between the constellation node. Right: example of Walker star satellite constellation provided with ISL capability; available connections between satellites are shown in red; the typical seam of a satellite network based on Walker star constellation can be seen on the left side of the picture.

3.2 Case study: latency in satellite backhaul networks

Among the many applications enabled by the possibility to connect through space using small satellites, the implementation of services for which broadband is not strictly necessary has raised particular attention. These applications include M2M, IoT, AIS and Automatic Dependent Surveillance-Broadcast (ADS-B). While broadband connectivity is not a strict requirement for these applications, low latency and high reliability constitute a major edge for these technologies. Moreover, for applications such as AIS and ADS-B low latency (few minutes down to real time) could be not only beneficial but actually essential. Given the rising interest in efficient and integrated systems, these applications could constitute a fundamental breakthrough in the context of production automation and Industry 4.0.

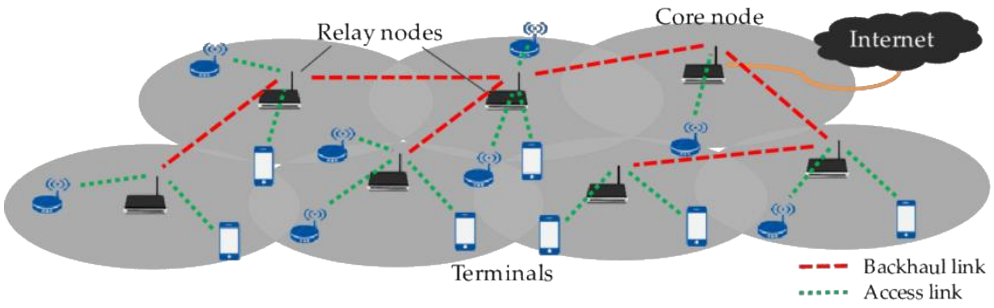

Figure 3-3: Representation of a typical network hierarchy (Maruta): the user terminals are connected to the core (Internet) through relays that constitute the nodes of the backhaul segment of the network. In this work, the relays are represented by the constellations satellites, the terminals are represented by the users and the core nodes are represented by the ground stations.

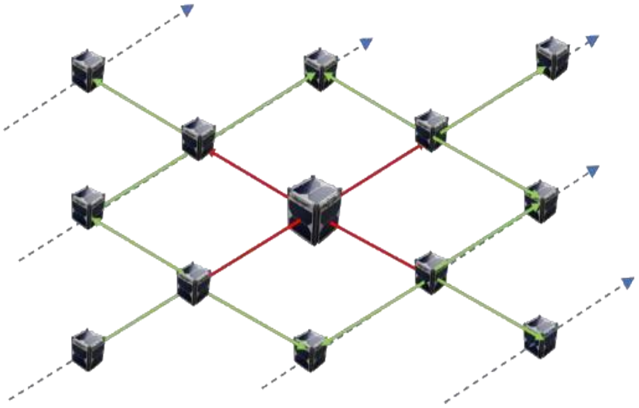

Figure 3-4: Visual representation of a meshed-type constellation based on small satellites. The first available hops from the central satellite are shown in red. The second hops are shown in green.

For this reasons, the impact of ISLs (Inter-Satellite Links) on the capacity of satellite telecommunications networks to enhance ground infrastructure performance has been quantitatively investigated, in order to assess its potential and pinpoint the settings for which a technological development would be particularly beneficial. The candidate has been the main contributor to this case study, with the constant support of Stellar Project's team. The content of this work has been published on the International Astronautical Congress (IAC) 2020 proceedings [54]. A particular focus is put on the capacity to support systems that do not necessarily require high throughput but which could highly benefit from a low latency service, such as IoT, M2M, AIS, ADS-B, etc. For this reason, traditional satellite communications systems are compared with networks provided with ISL capabilities and their performances in terms of wait time between data transmission and data reception are evaluated.

The structure of the work performed for this case study is the following. First, the general scenario under analysis is described. Then, the methodology proposed for the evaluation of the systems performance is presented. Then, the results of the analysis are shown and discussed. Finally, the main conclusions of the analysis and some final observations are presented.

Scenario

The general scenario under evaluation is that of a satellite backhaul network, which is the portion of a network that connects the core network to the subnetworks at the edge or directly to the end user (See Figure 3-3).This type of satellite service would be particularly suitable to connect users for which a direct access to the core network is currently arduous, due for example to the difficulty to lay cables in certain areas of the world or the virtual impossibility to do so, for example in the case of off-shore maritime applications.

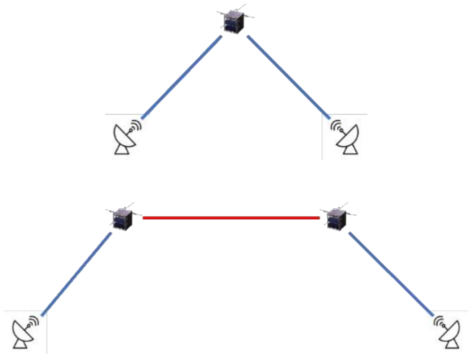

Figure 3-5: Graphical representation of a transmission between a user and a ground station using a satellite network. Top: no ISL hop is used; bottom: 1 ISL hop is used.

In Figure 3-4 and Figure 3-5 the adopted data transmission scheme is shown. From now on, we will refer to user as any device which has the necessity to connect to the core network and the potential to communicate with LEO satellites. We refer to GS (Ground Station) as the facility that receives the data from the satellite and routes it to the core network. In this configuration, the user is assumed not to have direct access to the core network. Data generated by the user is thus transmitted to the nearest spacecraft of the satellite backhaul constellation, which has the task to connect the otherwise permanently or temporarily isolated user. The assumption of complete coverage of the user distribution area by the constellation is made, so that each user has at least one satellite in sight at every moment. Although this hypothesis is relatively stringent, the progressive deployment of LEO telecommunications constellations in the near future could soon make this hypothesis a reality. Moreover, this is equivalent to neglect the wait time between the data generation and the access to the backhaul network by the user. The present analysis can then be easily extended to include the more general case.

Once the data has been received by one of the satellites in the constellation, different possibilities can appear depending on the availability of ISL. In this analysis, ISL availability only depends on the presence of a communication module onboard the spacecraft and not on specific constraints such as distance between neighbouring satellites. If no ISL is available, the satellite can directly transmit the data to the backbone network only if a GS is in direct sight. A store-and-forward approach is followed otherwise, meaning that the satellite stores the data received from the user until a GS is in sight. If ISL is available, each satellite can transmit the data received from the user to a set of reachable satellites of the constellation. The number of reachable satellites depends on the number of available hops. We then assume that as soon as at least one of the reachable satellites is in sight of a GS the data can be transmitted to ground, even if the very satellite that received the data from the user has no downlink possibility at that moment (Figure 3-5, bottom). In case none of the reachable satellites is in sight of a GS, a store-and-forward approach is again adopted, until the link condition is met. Since routing considerations are not the focus of this work, we assume that every reachable satellite is always available, thus neglecting problems such as link saturation.

The variables considered in the present analysis are described in the next section. We should highlight that, in a real scenario, the number of reachable satellites at a specific time depends on several other factors that have not been considered in this work, such as: the maximum ISL distance, the constellation architecture, the number of available ISL hops, routing constraints due to node saturation, etc. Moreover, the impact of cloud coverage has not been considered.

Satellites/constellation

A particular focus has been put on the use of constellations with a relatively high number of small satellites located in LEO orbits, as opposed to traditional systems which are usually based on large GEO satellites. The latter allow for an almost complete coverage of the Earth's surface with a limited number of satellites, but they require considerably more expensive spacecraft and can hardly rely on network redundancy. On the contrary, small satellites constellations obtain wide surface coverage through the deployment of a larger number of units. This allows for a highly flexible network architecture and reduces the development and launch costs, at the expense of relatively strict constraints on system mass and complexity and on the available electrical power. Three potential constellations are considered, named respectively Constellation A, Constellation B and Constellation C. They are shaped on existing, or under development, constellations, for which public data are available (see Section 2.3.1). In Table 3-1 the main parameters considered for these constellations are summarised.

Since an evaluation of the performances in terms of throughput is not directly included in this case study, no particular quantitative hypothesis concerning the specific telecommunication system capability (e.g. available bitrate) aboard the satellite has been made. However, in order to base the analysis on a consolidated ground infrastructure, we assume a standard RF system for data downlink. For this paper's objectives, the only relevant parameter of the specific telecom system adopted is the minimum elevation angle at which a link can be established between a satellite and a GS, which we assume as 20° for all the constellations.

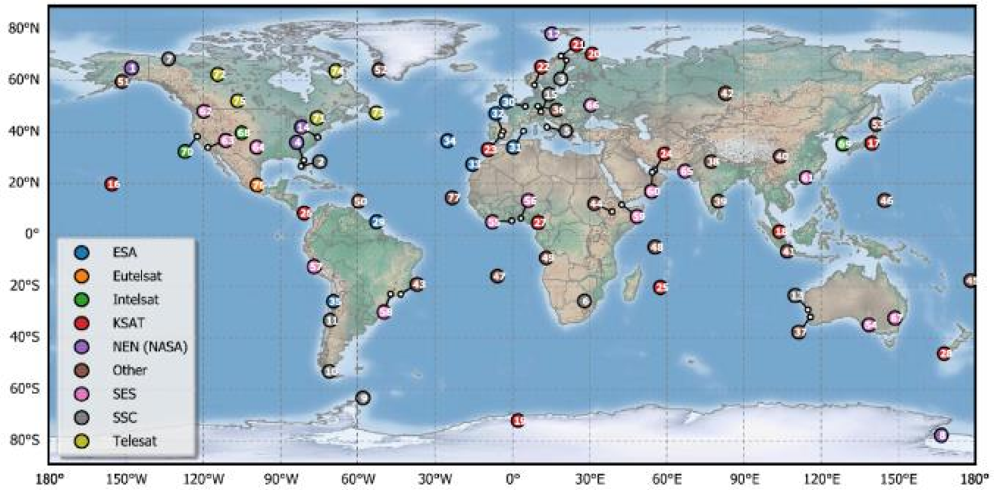

Figure 3-6: Ground stations distribution considered for this analysis. The same locations assumed in **[55]** have been used.

Conversely, state-of-the-art RF technology does not seem to provide the sufficient throughput and distance range while meeting mass and power requirements imposed by small satellites. For this reason, an optical telecommunication system is assumed for ISLs, as this appears to be the most promising way to obtain intersatellite data exchange with sufficient performances while maintaining low mass and power.

Table 3-1: Main parameters of the analysed constellations.

	Const. A	Const. B	Const. C
Height [km]	1000	600	1200
Inclination [°]	99.5	97	87.9
No. Of planes	6	8	12
Satellites per planes	12	8	40
Total number of satellites	72	64	480

Ground stations distribution

As large-scale telecommunications based on small satellite constellations are still at an initial phase of development, a solid infrastructure specifically dedicated to this kind of service has not been deployed yet, although several efforts are being made by private and public organizations to expand the available capability to communicate between the ground and small satellites in LEO orbits in an efficient way [56].
A thorough work has been made by Del Portillo [55] to evaluate the optimal location of ground stations used as feeder links for large LEO constellations. In [57] the author has selected a list of 77 GS locations taken from the International Telecommunication Union (ITU) Space Network List database. The same choice of GS distribution has been made in this paper, in order for the analysed scenarios to be consistent with previous works. The distribution of the available GS considered in this paper is shown in Figure 3-6.

Users distribution

As mentioned in Section 2.2, the use of satellite constellations could enhance telecommunications performance in a large range of applications. Nevertheless, one of the fundamental advantages of satellite connectivity is the possibility to reach users that are otherwise unable to access the network, regardless of their physical proximity to ground infrastructure.

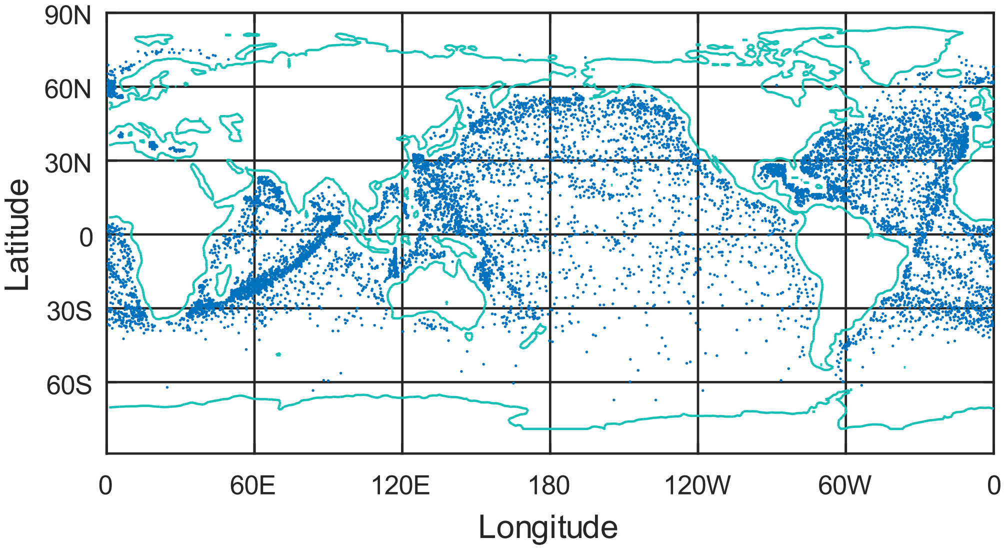

Figure 3-7: Example of a 10000-point user distribution sample space generated starting from a density map. In this example the distribution related to off-shore ships density provided in **[57]** was used.

One major focus of this case study is thus the quantitative evaluation of the performance enhancement allowed by advanced satellite communications architectures, specifically for applications for which access to standard backbone network gates is arduous. One example of such an application is the connection of maritime users, such as cargo vessels or offshore platforms, for which high distance from ground infrastructure is an intrinsic feature. The access to maritime traffic distribution information necessary for this analysis is not trivial, as few comprehensive and publicly available surveys of vessel routes on a global scale have been carried out. In this paper, we refer to the work of Wu [57], in which shipping density maps were derived from AIS data provided by the China Transport Telecommunications and Information Centre (CTTIC) for the period August 2012 to April 2015. A 1° x 1° resolution map directly provided by the authors has been used. A filtering has been applied in order to eliminate all the ships within approximately 60 miles from the coast, since it is assumed that closer to the coast the vessels can directly access the ground network.

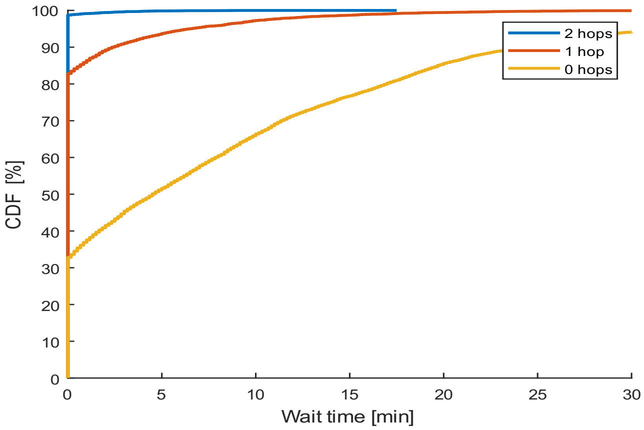

Figure 3-8: Example of Cumulative Distribution Fucntion (CDF) distribution generated from the simulation of 10000 items of the sample space. In this specific example, an off-shore user distribution using Constellation A as backhaul link provider has been considered. We can observe that increasing the number of hops moves us closer to the ideal situation, i.e. with null wait time for all items in the sample space.

In order to compare the results with a case in which access to the network is assumed to be less problematic, an instant messaging application has also been considered. Similarly to the previous case, messaging services are not based on the transmission of large data volumes but require low latency between transmission and reception. As opposed to the maritime case, though, a spatial correlation is expected to exist between land users and GSs, as they are both situated on land. We assume a direct proportionality between user density and population density, as the analysed application is highly non-specific and widespread among the population. For this purpose, the Gridded Population of the World density map provided by NASA Socioeconomic Data and Applications Center (SEDAC) [58] has been used, describing the estimated global population density for 2020. A 1° x 1° resolution map has been used in this case as well.
Besides providing information regarding the impact of ISL availability for specific applications, the choice of these two cases will allow us to quantitatively assess how this impact is influenced by the distribution of the target users.

<u>Simulation</u>

In the definition of the general scenario carried out in previous sections, a set of categorical variables have been defined:

- Constellation structure
- ISL availability (0, 1, 2 hops)
- Number of GS (5, 20 or 50)
- User distribution (maritime, population density)

Each combination of the specific values for each of these variables will be referred to as *specific scenario* (e.g. the combination 'Constellation A, 1 available hop, 50 GS, maritime distribution' constitutes a specific scenario). The analysis is then based on a Monte-Carlo-like approach. For each of the specific scenarios, a sample space is randomly generated based on the assumed user distribution. The sample space is composed of 10000 orbital locations in which the satellite is expected to receive data from a ground user, assuming for simplicity that the satellite is directly above the user at the time of receipt. An example of satellite location sample space is shown in Figure 3-7. For each element of the generated sample space a complete simulation of the data transmission procedure described in previous sections is carried out.

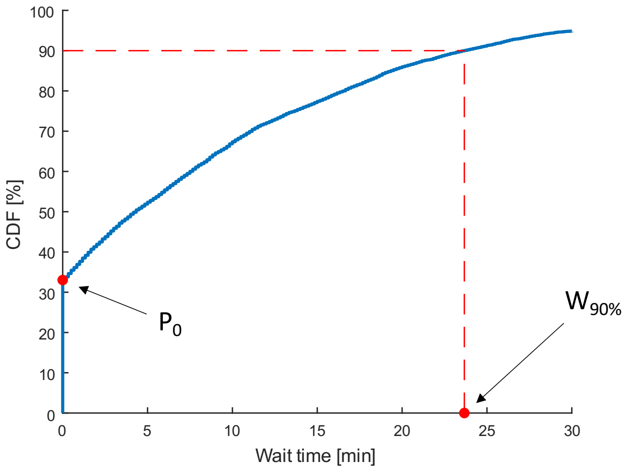

Figure 3-9: A visual representation of the relationship between the CDF and the metrics used in this works is presented. P_0 represents the probability to have a null wait time, while $W_{90\%}$ is the 90th percentile of the distribution.

The next step is the definition of the available 5, 20 or 50 GS subset. The focus of the present work in this regard is the mere number of available GSs belonging to the selected list; no specific selection criteria have been considered. For this reason, in order to decorrelate the results from the specific selection criterion, *n* GSs are randomly selected from the list at each simulation, where *n* is the number of GS considered in the specific scenario under analysis.

The following step is the orbit propagation until the link condition is met. A simple kinematic orbital model is considered both for the central and reachable satellites, with orbital parameters derived from the constellation characteristics. Perfectly circular orbits are assumed.

The elapsed time from data reception to data downlink is then stored and determines the wait time for the current simulation. This sequence is repeated for each of the 10000 elements of the sample space, i.e. all the generated orbital positions in the specific scenario under analysis. These stored results allow to define a CDF of the wait time for the specific scenario, from which statistical information can be analytically and visually derived (see Figure 3-8 and Figure 3-9). Based on the computed CDF, two main metrics have been selected to represent the overall performance for the specific scenario:

- $W_{90\%}$: the 90th percentile of the wait time distribution.
- P_0: the probability to have a null wait time, computed as the relative frequency of occurrence expressed as percentage.

Results

The results of the current analysis will contribute to quantitatively assess the convenience of the implementation of ISLs in a telecommunication constellation and to establish in which scenarios it constitutes a crucial feature.

The first step of the analysis is the creation of the software that generates a CDF database for each of the specific scenarios considered. An example of resulting CDF is shown in Figure 3-8. Some significant results will be described in this section.

In Table 3-2 the $W_{90\%}$ value for different GS and hop numbers are shown. The values are computed as an average of the results of alle the three constellations. We can see that a strong reduction in wait time can be obtained regardless of the number of ground stations. For example, a reduction of a factor of almost 10 can be observed passing from 0 to 2 hops in the case of 5 available ground stations.

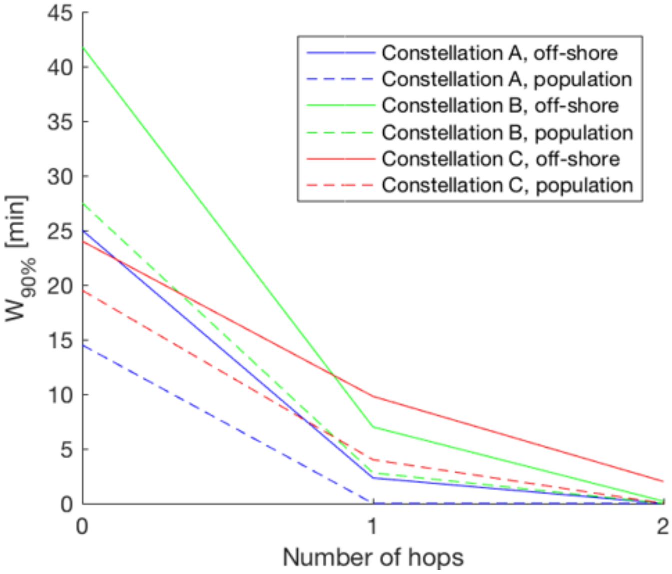

Figure 3-10: $W_{90\%}$ value for the three constellations (A, B and C) as a function of hops number, considering 20 available GSs. Both results of population (dashed lines) and off-shore maritime (solid lines) user distributions are presented.

Table 3-2: $W_{90\%}$ averaged among constellations expressed in minutes.

#GS	0 hop	1 hop	2 hops
5	159.19	47.00	18.03
20	25.39	4.33	0.36
50	7.08	0.02	0.00

Table 3-3: P_0 averaged among constellations, expressed as percentage.

#GS	0 hop	1 hop	2 hops
5	12.44	34.31	57.74
20	39.81	78.02	93.93
50	69.30	96.33	99.61

More specific results relative to the wait time percentage reduction due to the implementation of ISLs can be found in Table 3-4. Here, the results of the single constellations are presented together with the results averaged among all the constellations. Let us consider for example the case of 20 available GSs, which is a likely number to be obtained in the medium-term for a typical large-scale constellation. We can see that a reduction of wait time in terms of $W_{90\%}$ greater than 95% can be obtained for all the constellations by implementing 2 ISL hops, with an average value of 98.85%.

Another important advantage of the implementation of ISLs is the possibility to reduce the number of GS while maintaining a low wait time value. Observing Table 3-2 for example, we can see that a lower $W_{90\%}$ value (18.03 minutes) can be obtained by using 2 ISL hops with 5 available GS than by establishing a link with no ISL and 20 available GSs (25.39 minutes). This could be particularly important to reduce the costs of the constellation in terms of ground segment building and maintenance and to make the telecommunication infrastructure less vulnerable to potential attacks, e.g. in case of governmental or defence use of the constellation.

In Table 3-4 the $W_{90\%}$ value for the three constellations (A, B and C) as a function of hops number is presented, considering the availability of 20 GSs. Both results of population and offshore maritime user distributions are shown. The graph confirms the initial thesis that the correlation between the GS distribution and the user distribution is crucial in terms of wait time. Indeed, considering the single constellations the $W_{90\%}$ values are always higher for the maritime case (solid lines) with respect to the population distribution case (dashed lines). From Table 3-4 we can also see that, while the difference in wait time between offshore and population density is remarkable when no hops are available, this difference is substantially reduced when ISL hops are introduced. We then infer that ISLs have the potential to reduce the gap in communication wait time between users far from the GSs and users with an easier access to ground infrastructure.

Results relative to P_0, the second metric used in this work to assess the constellation performance, follow the trend seen for $W_{90\%}$ results, confirming the potential of ISLs to reduce communication wait time. Results averaged among constellations can be found in Table 3-3. We can observe in particular that with a sufficient number of GSs and as few as 2 ISL hops the probability of a null link wait time can be brought to almost 100%.In Table 3-5 the P_0 increase allowed by the implementation of ISLs is shown, expressed as increase factor. The results show that ISLs are particularly helpful when a smaller number of GS are available. For example, the P_0 allowed by the implementation of 2 ISL hops for Constellation 2 with 5 available GS is greater than 8.

Table 3-4: $W_{90\%}$ reduction with respect to 0 hops, expressed as percentage. The value is averaged between maritime and population results.

	Constellation A		Constellation B		Constellation C		Averaged	
# GS	**1 hop**	**2 hops**	**1 hop**	**2 hops**	**1 hop**	**2 hops**	**1 hop**	**2 hops**
5	77.63	94.51	75.62	93.28	53.68	74.26	70.48	88.68
20	94.09	100	85.82	99.76	68.20	95.40	82.93	98.58
50	100	100	99.35	100	100	100	99.61	100

Table 3-5: P_0 increase factor with respect to 0 hops. The value is averaged between maritime and population results.

	Constellation A		Constellation B		Constellation C		Averaged	
# GS	**1 hop**	**2 hops**	**1 hop**	**2 hops**	**1 hop**	**2 hops**	**1 hop**	**2 hops**
5	3.51	6.10	4.14	8.07	1.86	2.77	3.17	5.65
20	2.22	2.53	2.86	3.95	1.49	1.77	2.19	2.75
50	1.36	1.38	1.97	2.12	1.18	1.22	1.50	1.57

Conclusions

This work has allowed to carry out a preliminary analysis of the impact of ISLs on the performance of backhaul satellite networks in terms of wait time between data reception by the satellite and data transmission to the first available GS. Several categorical variables have been considered for this analysis, namely: constellation architecture, number of available ground stations, user distribution and number of available ISL hops. Results show that ISL implementation is crucial in terms of wait time reduction for all the specific scenarios taken into account. The greatest improvement offered by ISL implementation seems to appear especially for remote users applications, such as off-shore vessels, with wait time reduction above 90% with as few as 2 ISL hops. Moreover, ISLs allow to compensate for the lack of an extensive ground station network, allowing for example to maintain wait time below 20 minutes with as few as 2 ISL hops. This translates into a potential cost reduction and an increase in network resilience to potential attacks.

3.3 Case study: satellite networks for disaster response operations

Another application that could strongly benefit from the availability of opical communication is disaster response (see Section 2.2). A typical metric used to define how recent is the information relative to an observed target is the Age of Information (AoI), which represents the time elapsed since the latest useful piece of information that reached its intended destination has been generated at its source [59]. The use of data collected in-situ is a typical choice in case of disaster response situations, but it requires the presence of a pre-existing infrastructure, preventing interventions in remote or developing areas. Satellite data are a valuable alternative, as they provide information from any point on Earth regardless of the ground equipment availability.

Current space infrastructures do not provide real-time access to the acquired data. The deployment of relatively large constellations of small satellites supplied with inter-satellite connectivity could allow quasi-global coverage and real-time data access at the same time. With the integration of intersatellite connectivity within a constellation, single satellites become nodes of a communication network; this way, they are not bound to store optical observation data until they pass over a Ground Station (GS) but, instead, are able to transmit data to other platforms until one of them is in sight of a ground station. Therefore, latency of critical data can be dramatically reduced from hours to few minutes.

The integration of remote sensing data collected by space-borne instruments for disaster response operations has followed the technological advancement of satellite payloads, which are able to collect an ever-increasing quantity of Earth Observation data. The most commonly used remote sensing systems for wildfire research are multispectral sensors. The Sea and Land Surface Temperature Radiometer (SLSTR) instrument of Sentinel-3, for example, is employed to detect active fires measuring the changes in earth surface temperature. The SLSTR images consist of 9 bands with a spatial resolution of 1000 m in Mid-wave Infrared (MWIR) and Thermal Infrared (TIR) bands. The radiometric resolution is 10 bit saved using unsigned integer 16 bit. Assuming a pixel spacing equal to the spatial resolution then the uncompressed data volume results in 0.18 MB/10000 km^2. The time frame for delivery of products in case of Near Real-Time (NRT) applications is typically 3 hours after acquisition of data by the sensor and the downlink data rate is 2 Mbit/s [60].

MultiSpectral Instrument (MSI) of Sentinel-2 can be used to provide information that facilitates the mitigation of and response to many types of disasters or crises including floods and fires. Near Infrared (NIR) and Short Wave Infrared (SWIR) bands are used to to calculate, among others: the Normalized Difference Water Index (NDWI), used in floods since it is the best performing for surface water detection [61]; and the differential Normalized Burn Ratio (dNBR), which identifies the burned areas and its severity burn index [62].

In Figure 3-11 an example of differential Normalized Burn Ratio (dNBR) analysis is reported. A pair of Sentinel-2 images are used to detect the impact of the Sardinia wildfire that occurred on 25 July 2021. The MSI products consist of 13 bands with a spatial resolution that ranges in 10/20/60 m in Visible (VIS), NIR (Near InfraRed) and SWIR (Short Wavelength InfraRed) bands. The radiometric resolution is 12 bit saved using unsigned integer 16 bit. Assuming a pixel spacing equal to 20 m then the uncompressed data volume results in 650 MB/10000 km^2. The data delivery time is 100 minutes in Near Real Time areas and the downlink data rate is 500 Mbit/s [63].

Table 3-6: Sample Earth Observation images and their application and data volume

	Scenario	Pixel Resolution [m]	Data Volume per 10000 km^2 [MB]
SLSTR	Active fires	1000	0.18
MSI	Burned areas, floods	20	650
SAR	Oil spills, floods	10	800

The last considered satellite image typology is the Synthetic Aperture Radar (SAR). SAR instruments can obtain high-resolution remote sensing data independent of both weather conditions and illumination, so that it can operate day and night, even with cloud complete cloud coverage. Sentinel-1 is equipped with a SAR instrument, which produces data suitable for monitoring floods and oil spills. Sentinel-1 products consist of 2 bands, one for each polarization mode with 32 bit per pixel and spatial resolution in the best case below 10 m. The uncompressed data volume is about 800 MB/10000 km^2. The data delivery time is 1h in Near Real Time areas and the downlink data rate is 500 Mbit/s. Table 3-6 summarizes the data volume of the satellite images for managing the considered hazard scenarios.

Objectives

In this case study, the performance of Earth observation constellations based on small satellites provided with inter-satellite link (ISL) connectivity is analysed from a data communication point of view. In particular, performance is evaluated in terms of availability of connection, AoI and throughput of the constellation, depending on several parameters such as the data rate of ISL, the constellation parameters and the availability of ground stations. Scenarios in which real-time data are specifically required have been considered, focusing on disaster response applications in which a fast action is vital, such as floods, fires and oil spills. The candidate has been the main contributor to this case study, with the valuable contribution of Stellar Project's team support. The content of this work has been published on IAC 2021 proceedings [64].

Besides providing useful guidelines for optical inter-satellite link terminals, the analysis contributes to develop an approach to assess the increase in Value of Information (VoI) of Earth observation data offered by the implementation of inter-satellite connectivity.

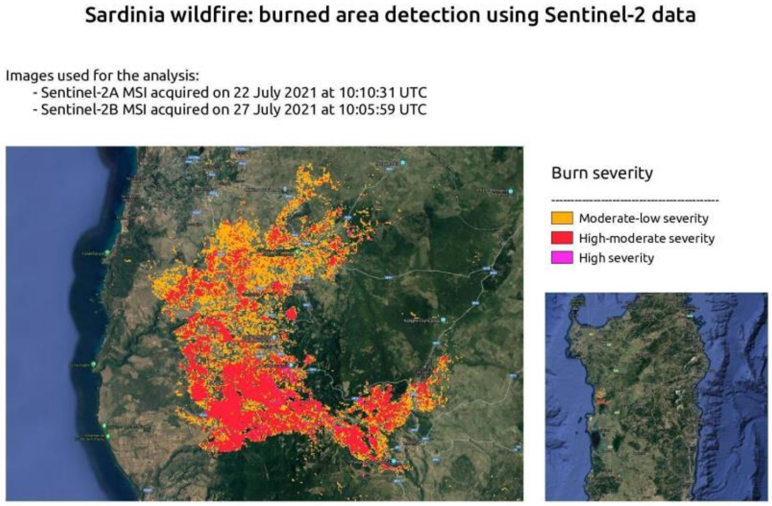

Figure 3-11: Example of differential Normalized Burn Ratio (dNBR) analysis. A pair of Sentinel-2 products at the turn of the wildfire are used to detect the impact of the Sardinia wildfire that occurred on 25 July 2021.

Scenarios

Three cases from the last 20 years were analyzed:

The first case concerns the oil spill taken place on the 16th of January 2001 on the coasts of Galapagos islands, one of the United Nations Educational, Scientific and Cultural Organization (UNESCO) world heritage sites [65]. A massive oil tanker ran aground at the port of Puerto of Baquerizo Moreno, the capital of Galapagos province, located on the southwestern coast of San Cristobal Island, and from the 20th started to spill diesel and fuel oil into the sea for a total of 660 thousands of liters. Hundreds of animals, including protected species, were affected by the oil spill. During the crisis, it was necessary to map the area to understand how to contain slicks, so twice daily flights were used.

The second case considers floods and mudslides that occurred, on the 23rd of November 2019, in West Pokot County, a region in the north west of Kenya where agriculture and livestock farming are the main sources of income [66]. Unluckily, this kind of phenomena are recurrent in this area of Africa and they cause death and displacement of thousands of people as well as houses destructions, so it would be fundamental to have a continuous coverage of the zone to better manage rescues and to assure communications, but in this case first satellite images of the area were available five days after.

The last case is about the fires that occurred in the west area of Sardinia in July 2021, an island and Italian region where more than 20 thousand hectares were destroyed and thousands of people were forced to leave their homes. Figure 3-11 shows the identified burned area obtained through the processing of two pictures collected by Sentinel 2 with five days of difference. Continuous images would be useful to predict how flames advance and to limit damages.

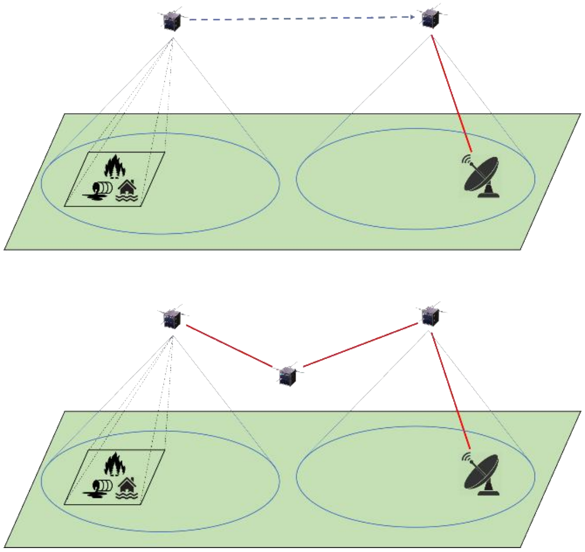

Figure 3-12: Schematic representation of satellite connectivity architecture. Top: a satellite not provided with inter-satellite link acquires images of the target area and waits to be in view of a GS to transmit the collected data. Bottom: inter-satellite links allow the satellite to immediately transmit the collected data using the other satellites in the constellation as relays.

Satellite connectivity architecture

Traditional EO spacecraft are bound to store optical observation data until they pass over a ground station, a technique usually referred to as store-and-forward (Figure 3-12, top). This puts a strong limit on the achievable AoI performance since several hours could be necessary for a satellite to establish a connection with a GS, unless a diffuse network of several hundred (or even thousand) GSs is available.

With the integration of intersatellite connectivity within a constellation, single satellites become nodes of a communication network. This allows to transmit the EO data of the disaster area under observation acquired by the satellite to the nodes of the constellation network, which in turn relay it to the nearest GS (Figure 3-12, bottom). This can enable real-time data acquisition of an area under observation.

In this case study we analyse the performance of an ISL-provided constellation and compare the results with the performance of state-of-the-art space-based EO systems lacking ISL connectivity.

Ground Stations

A remarkable advantage of ISL implementation is that it can potentially guarantee real-time connectivity between space and ground even with a small number of GS with respect to the number required by a traditional system. A crucial parameter is the bitrate that a GS is capable to receive.

Figure 3-13: Ground station distribution of the ATLAS antenna network.

For this study, ATLAS Antenna network (see Figure 3-13), was chosen because it has 11 globally distributed active antennas (more antennas are planned to be operational soon) and bitrate ranging from 100 Mbps to 1.5 Gbps [67]. The size of the antennas varies between 3 and 11 meters and they operate on S-, X-, Ka-, Ku-bands. Since the potential ISL data rate considered in this work is of several hundreds of Mbps, we will assume here that the ground stations are capable of receiving any datarate ≤ 1.5 Gbps.

Preliminary constellation design

Various constellation designs have been proposed during the last 50 years for small satellites in LEO. In this work we have decided to adopt the Walker delta pattern constellation, as it is the most widely used because of its simplicity [68]. This constellation architecture includes T satellites distributed on P orbital planes evenly spaced in node with the same inclination. The ascending node of each orbit is distributed around the equator at intervals of 360°/P, while satellites on the same orbital plane are distributed at intervals of 360°/S, where S = T/P is the number of satellites for each orbital plane. The last parameter that defines a Walker delta constellation is the relative spacing F between satellites on adjacent planes. F is an integer number between 0 and P-1 and multiplied for 360°/T provides the phase difference between satellites on adjacent planes. In this analysis, orbits are considered circular and inclination fixed at 65° because the majority of the disasters considered (fires, floods, oil spills) happened at low/middle latitudes. Furthermore, we decided to give priority to areas with higher population density. The study considered the Walker constellations that are allowed by the free parameters shown in Table 3-7, and 3 constellations have been selected for producing the results. A revisit time lower than 15 minutes has been selected as requirement.

Table 3-7: Range of parameters considered for the selection of case-study of Walker constellations.

Height of orbit	500 to 1000 km
Total number of satellites (T)	up to 200
Total number of orbital planes (P)	up to 25

Link budget

The achievable datarate is strongly dependent on the distance between two communicating terminals, which is in turn influenced by the architecture of the constellation.

In order to relate the specific constellation geometry to the achievable datarate, a link budget analysis has been carried out.

Table 3-8: Main parameters of the optical inter-satellite communication used for the link budget analysis.

Parameter	Value
Transmitted power [W]	1
Wavelength [nm]	1550
Beamwidth [µrad]	50
Receiver aperture [mm]	50
Receiver NEP [W/√Hz	10^{-12}
Spectral efficiency [bps/Hz]	1
Required BER	$\leq 10^{-6}$

The required link distance for each of the selected constellation geometry has been determined by imposing that each satellite must have ISL mediated connection to a GS for at least 95% of the time. Given the other main assumptions regarding the optical communication listed in Table 3-8, the expected optical power at the receiver terminal has been computed. The link budget has then been defined computing the maximum allowable bandwidth dependent-noise resulting in a SNR that guarantees a Bit Error Ratio (BER) $\leq 10^{-6}$ (see Appendix A for link budget details). Considering a Non-return to Zero On-Off Keying (NRZ-OOK) modulation scheme, a spectral efficiency of 1 bps/Hz can be assumed [69].The available datarate can then immediately be obtained.

This allows to assign a typical datarate to each constellation based on its geometry.

Constellation network analysis

Once the constellation and telecommunication parameters are chosen, a dynamic simulation of the actual data transmission operations spanning a defined time interval is carried out using the Matlab code based on the satellite network analysis software described in Section 3.1. At each timestep of the simulation, the code proceeds with the following main steps:

1. Define the GS locations in Earth Centered Earth Fixed (ECEF) coordinates;
2. Propagate the orbit of each satellite and define their position in ECEF coordinates;

3. Define the constellation network structure based on the relative position of the satellites at current time, assuming that two nodes (satellites) of the network are connected if their distance is lower than the maximum optical link distance (see Section 3.2);
4. Define available connection between satellites and GSs;
5. Verify coverage of the target area by a satellite of the constellation and, if so, compute the shortest network path between that satellite and the nearest GS;
6. Compute performance metrics (coverage, link availability, AoI).

In Figure 3-14 an example of a network connection between a satellite acquiring data over Sardinia and a GS in Florida is shown. It is immediately evident that many orbits would be necessary to transfer data to the ground if ISL (red lines) were not available, unless a very dense network of GS were deployed.

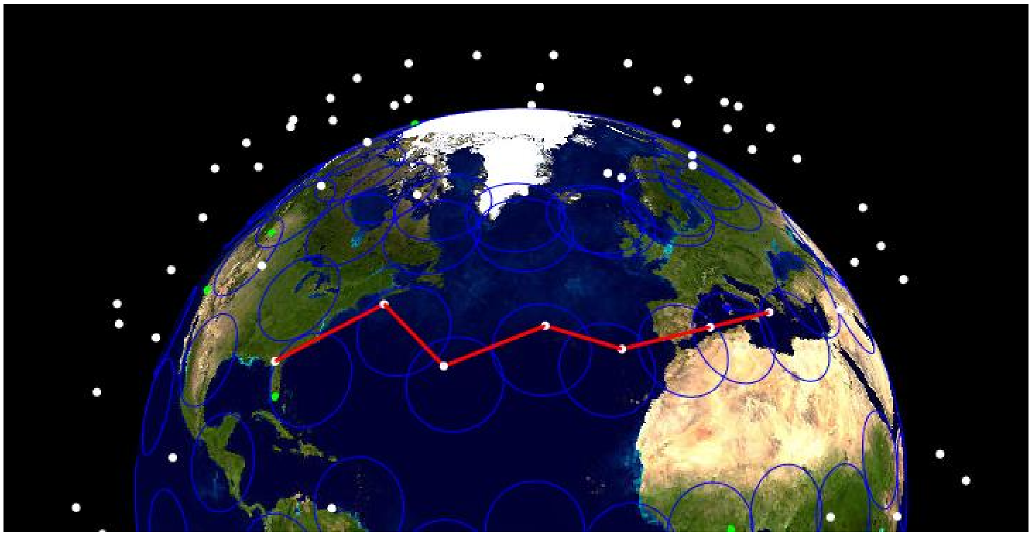

Figure 3-14: Example of real-time data transmission of images acquired in Sardinia (Italy) to a remote ground station in Florida (USA) using the constellation satellites as nodes relays. Red lines represent optical ISL between the involved satellites.

Deliverable data products

The last part of the analysis is dedicated to the determination of the actual performance in terms of derivable data products, based on the constellation network analysis. The purpose is:

- to quantify the performance in terms of data delivery time, AoI and imaging data volume;
- to define image requirements for the inter-satellite constellation needed to produce useful analysis in fires, floods and oil spill detection and monitoring.

In order to obtain a quantitative analysis of Earth observation images produced by a satellite constellation, a simplified model of the AoI trend of a target area is considered. As depicted in Figure 3-15, after the acquisition of the image ACQ 1, the AoI starts to linearly increase over time. The AoI resets to zero when a new image ACQ 2 is acquired, which takes the place of ACQ 1 as the most recent image of the considered hazard area. Let us call the time between the two acquisitions Inter Acquisition Time (IAT). The most recent acquired image is transmitted to the ground station during the IAT. This period of time is twice the average of AoI, as can be seen in Figure 3-15. The data volume relative to an imaging product deliverable by the ISL constellation for a specific acquisition is obtained by multiplying the average downlink data rate of the satellite constellation times IAT.

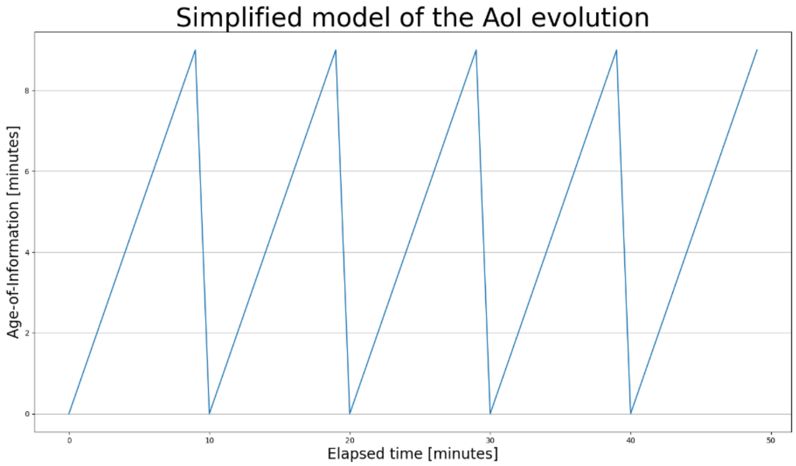

Figure 3-15: Simplified model of the Age of Information evolution. The time between two minimum peak is the Inter Acquisition Time, which is twice the average of AoI.

Preliminary constellation design results

For the choice of the constellation architecture, the main requirement was to limit the maximum revisit time to 15 minutes in a 1-day simulation.

Table 3-9: Main parameters of the constellations emerging from the preliminary design. T is the number of satellites and P the number of orbital planes.

H [km]	T	P	F	Max revisit time
500	200	25	0	11’
700	175	25	0	12’
1000	150	25	2	10’

Moreover, if at the same height multiple architectures were possible, the one with the lower number of satellites and orbital planes was chosen. So, 3 possible designs of constellations emerged, which are presented in Table 3-9.

When the height increases the number of satellites and orbital planes decreases (Table 3-9), but at the same time the distance between satellites increases, reducing the available ISL datarate. Considerations related to telecommunications performance in relation to constellation design will be presented in the next paragraph.

Link budget results

A series of simulations has been performed for each constellation geometry in order the determine the required link distance to guarantee that each satellite has ISL mediated connection to a GS for at least 95% of the time. The results are presented in the second column of Table 3-10, showing that the required link distance increases rapidly with the orbital height, also due to the lower number of satellites used for higher altitude constellations.

Table 3-10: Main results of the link budget analysis, in terms of required link distance and achievable datarate.

Constellation number	Required link distance [km]	Achievable datarate [Mbps]
1 (500 km)	1500	300
2 (700 km)	1800	150
3 (1000 km)	2400	50

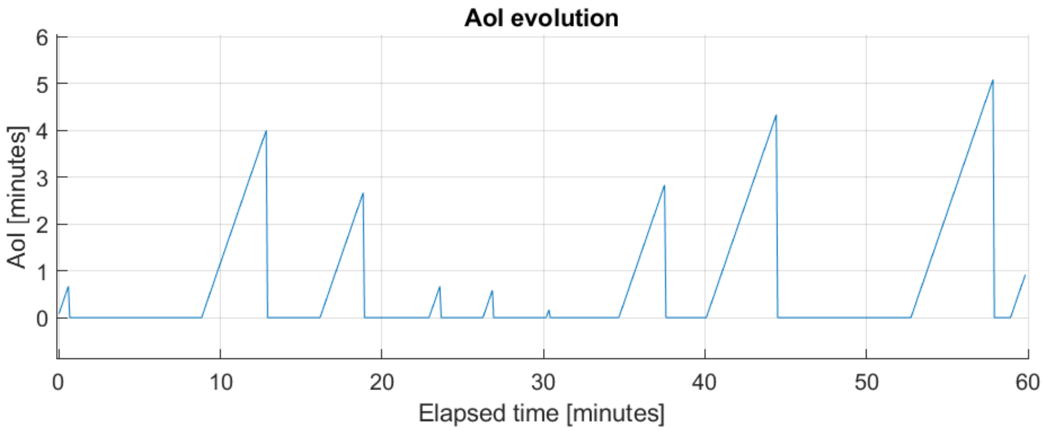

Figure 3-16: Example of the AoI evolution simulated over a 1-hour time period.

The, the required link distance has been related to the achievable datarate (Table 3-10, 3rd column) by means of the link budget analysis described in Paragraph 3.2. The achievable datarate decreases approximately with the 4th power of the link distance.

Constellation network performance

The dynamical simulation of the acquired data transmission to the nearest GS has then been run in order to compute the performance metrics of the selected constellations for each of the three cases under analysis (wildfire, flood, oil spill). The simulation covers a period of 24 hours, with a timestep of 1 minute.

Table 3-11: Fraction of time the target is covered [%]

	Const 1	Const 2	Const 3
Case 1 (lat)	17.3	27.8	42.2
Case 2	17.2	27.9	43.7
Case 3	18.9	40.2	62.9

In Table 3-11 the fraction of time the selected target is covered by at least one satellite is presented for each case study. The results highlight how time coverage increases with increasing orbit height, since the footprint of the single satellite is wider at higher altitudes.

Results relative to Case 1 and Case 2 are very similar, while Case 3 results are significantly better. This suggests that the result has scarce dependence on the targets longitude, while a better time coverage can be obtained at higher latitudes, where the satellite density in the constellation is higher.

In Table 3-14 the evolution of the AoI simulated over a 1-hour interval is shown. In Table 3-12 the results relative to the AoI of the acquired data is presented, both in terms of average and maximum values. Similar considerations to the ones exposed for the time coverage results can be made. Most notably, a very low average value of 1.1 minutes can be reached in the case of a 1000 km altitude constellation targeting Sardinia (Constellation 3, Case 3), improving the state-of-the-art of more than two orders of magnitude.
Finally, in Table 3-13 the average achievable data rate is presented for each constellation and target area. The results reaffirm the results of the previous tables, as performance appears to depend only on latitude and not longitude. We can also observe a general decrease in performance with the increase of constellation altitude. This suggests that the increase in time coverage allowed by higher altitude does not compensate for the decrease in available data rate due to the increased average distance between satellites.

Table 3-12: AoI: average/maximum [minutes]

	Const 1	Const 2	Const 3
Case 1	4.5/11	3.2/12	2.1/10
Case 2	4.5/11	3.2/12	2.1/10
Case 3	4.3/10	2.3/9	1.1/10

Table 3-13: Average data rate [Mbps]

	Const 1	Const 2	Const 3
Case 1	51.9	41.7	21.1
Case 2	51.7	41.9	21.9
Case 3	56.7	60.25	31.4

Deliverable data products

The actual performance in terms of derivable data products is obtained by supplying the proposed AoI model with the constellation network performance results. As mentioned before, the Inter-Acquisition Time (IAT) is calculated by doubling the average AoI. By multiplying IAT by the corresponding average available data rate, the total amount of earth observation data deliverable from the satellite constellation during the

IAT is obtained. Table 3-14 shows the amount of deliverable data volume per IAT. Let us consider the data volume of Earth observation images with a standard coverage of 100 x 100 km^2 presented in Table 3-6. The maximum number of data products collected per IAT is reported in Table 3-15. As an example, looking at the first row and first column of Table 3-15, that is the case of oil spills monitored with the SAR inter-satellite constellation number 1. Every 9 minutes the constellation is able to downlink 35 SAR images to the ground station.

Table 3-14: Deliverable data volume per IAT [MB] (IAT) [minutes]

	Const 1	Const 2	Const 3
Case 1	28026 (9)	16012 (6.4)	5317 (4.2)
Case 2	27918 (9)	16089 (6.4)	5518 (4.2)
Case 3	29257 (8.6)	16629 (4.6)	4144 (2.2)

Table 3-15: Deliverable EO images per IAT [#images] (IAT) [minutes]

	Const 1	Const 2	Const 3
Case 1 with SAR	35 (9)	20 (6.4)	7 (4.2)
Case 2 with MSI	43 (9)	25 (6.4)	8 (4.2)
Case 2 with SAR	35 (9)	20 (6.4)	7 (4.2)
Case 3 with MSI	45 (8.6)	26 (4.6)	6 (2.2)

Conclusions

This work investigates the potential performance enhancement allowed by the implementation of optical ISL connectivity in the context of disaster response applications. Three promising constellation architectures at 500, 700 and 1000 km altitude have been identified, with 200, 175 and 150 satellites respectively. The results of the optical link budget analysis show that ISL data rates ranging from 50 to 300 Mbps can be obtained with reasonable assumptions regarding optical telecommunication terminals compatible with small satellite requirements.

The constellation network analysis shows that increasing the constellation altitude on one hand improves the AoI performance but, on the other hand, decreases the average available data rate due to increase of intersatellite distance.

In terms of derivable data products, this translates into a decreasing number of Earth observation images when the constellation altitude increases. It should be noted that, when the constellation altitude is less than or equal to 700 km (Const 1, Const 2), the designed ISL constellation is able to provide to the ground stations tens of images every few minutes. Constellation altitude may then be selected as a trade-off between AoI and data volume requirements provided by actors involved in disaster response operations.

3.4 Case study: LaserCube ISL for satellite networks

The third case study has been carried out to evaluate the use of LaserCube ISL model for in-plane and out-of-plane intersatellite links, considering four LEO constellations based on small satellites as key cases. For this case study, the candidate has specifically contributed to the generation of numerical results; the candidate has also supported Stellar Project's team on the analysis of the generated results.

The analysis has been performed in two steps:

- calculation of relative position and velocity between spacecraft belonging to the selected constellation, considering both in-plane and out-of-plane links;
- determination of conditions that allow for ISLs acquisition and comparison with the expected performance of the LaserCube system.

Key Cases

The small satellites constellations that have been studied are summarized in Table 3-16, considering publicly available information.

Table 3-16: Parameters of the constellations considered for this analysis.

Constellation	Application	Altitude	Inclination	No. of Planes	No. of sats/plane	No. of sats
Astrocast	IoT / M2M	600 km	97 deg	8	8	64
OneWeb	Global telecom and Internet	1200 km	87.9 deg	12	40	480
SSG	Telecom for low latitude countries	650 km	0 deg 10 deg	1 4	200	200
Telesat	Global Internet	1000 km	99.5 deg	6	12	72

Model

The developed software has been used to calculate the relative position and velocity between satellites belonging to the same LEO constellation, placed on the same orbital plane or on adjacent orbital planes. The "Star Shape" ISL mesh link configuration has been considered, as shown in Figure 3-17: a central satellite is equipped with four LaserCube units, pointing forward, backward and laterally (left and right). The central satellite is labelled as 1; the two satellites on the same orbital plane, placed ahead and behind satellite 1 are labelled as 4 and 5; the two satellites placed on the two adjacent orbital planes are labelled as 2 and 3. The front and back LaserCube terminals are used for in-plane ISLs with satellites 4 and 5, while the lateral terminals are used for ISLs with the satellites on adjacent planes.

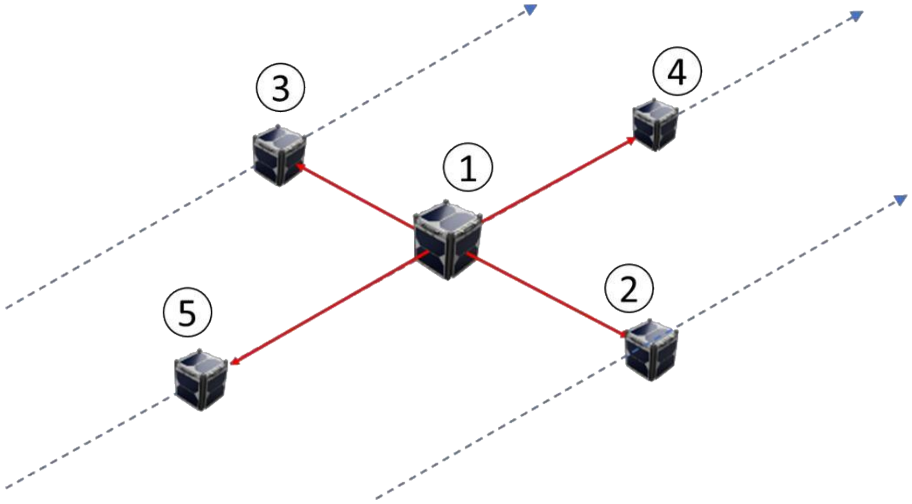

Figure 3-17: Satellite configuration considered for the ISL analysis.

Table 3-17: LaserCube main figures relevant to the ISL analysis.

Parameter	Value	Unit
Maximum ISL range	2000	[km]
Coarse pointing angular range	±10	[deg]
Pointing system maximum angular rate	0.5	[deg/s]

LaserCube ISL terminal main features are summarized in Table 3-17. As shown in Table 3-16, there are situations where inter-satellite links might be established between satellites in different orbits/orbital planes. This section reports a preliminary analysis to identify the maximum orbits separation that makes a laser connection between two LaserCube ISL units possible, taking into consideration the performance of LaserCube pointing, acquisition and tracking capabilities. This analysis might also be used to point out possible directions for future improvements of LaserCube-ISL.

Results for in-plane ISLs

Table 3-18 summarizes the results of the analysis considering in-plane ISLs for the four small satellite constellations considered. According to the results, the most critical parameter for in-plane ISLs is the distance between satellites, which is much larger than the actual maximum range of LaserCube in two out of four cases (Astrocast and Telesat). Pointing angle, calculated as the angle between the line connecting satellite 1 and 4 and the velocity vector of satellite 1, is also beyond the current LaserCube capability; however, since the pointing angle is basically a constant for in-plane ISLs, this is not a show-stopper since it can be compensated by a mounting offset of the LaserCube terminals (see Figure 3-18). We can conclude that the most critical parameter for the realization of in-plane ISLs is the intersatellite range.

Table 3-18: Results from the in-plane ISL analysis.

Constellation	In-plane ISL range	In-plane ISL pointing angle
Astrocast	5795 km	22.5 deg
OneWeb	1187 km	4.5 deg
SSG	1101 km	4.5 deg
Telesat	3809 km	15.0 deg

Results for out-of-plane ISLs

The results of the out-of-plane ISL analysis are shown in Figure 3-19, Figure 3-20, Figure 3-21 and Figure 3-22, for the four constellations respectively. Each chart shows (1) the range between satellite 1 and satellite 2, (2) the pointing angle and (3) the pointing angular velocity that the LaserCube pointing system shall satisfy in order to maintain line of sight between satellite 1 and 2. The pointing angle is calculated as the angle between the y-axis (out-of-plane axis) of the central satellite and the line connecting the central satellite to satellite 2, which starts at the right side of the central satellite. Thus, pointing angle of 0 deg means satellite 2 is exactly at the right side of satellite 1 and pointing angle of 180 deg means satellite 2 is exactly at the left side of satellite 1.

Three constellations (Astrocast, OneWeb and Telesat) are based on high-inclination orbits which cause the satellite 2 to cross the path of satellite 1 twice per orbit, causing the pointing angle to shift from ≈0 deg to ≈180 deg and the pointing angular velocity to increase significantly during the crossing. For the same reason, the satellite distance varies between a minimum and a maximum value. In these conditions, laser terminals on the right and left side of satellite 1 are used to perform ISLs, each one with a 10 deg offset with respect the y-axis. The resulting pointing angle ranges are 0-20 deg (i.e. 10 ±10 deg) and 160-180 deg (i.e. 170 ±10 deg), as shown in Figure 3-18, left. Such ranges are represented by the horizontal lines in the second plot of Figure 3-19 to Figure 3-22.

As regards the SSG constellation, out-of-plane ISL has been considered between satellites belonging to the equatorial orbit (satellites 1, 4 and 5) and satellites on one low-inclination orbit (satellites 2 and 3). The pointing ranges of the LaserCube terminals placed on the lateral sides of satellite 1 are 20-40 deg (i.e. 30 ±10 deg) and 140-160 deg (i.e. 150 ±10 deg), as shown in Figure 3-18, right.

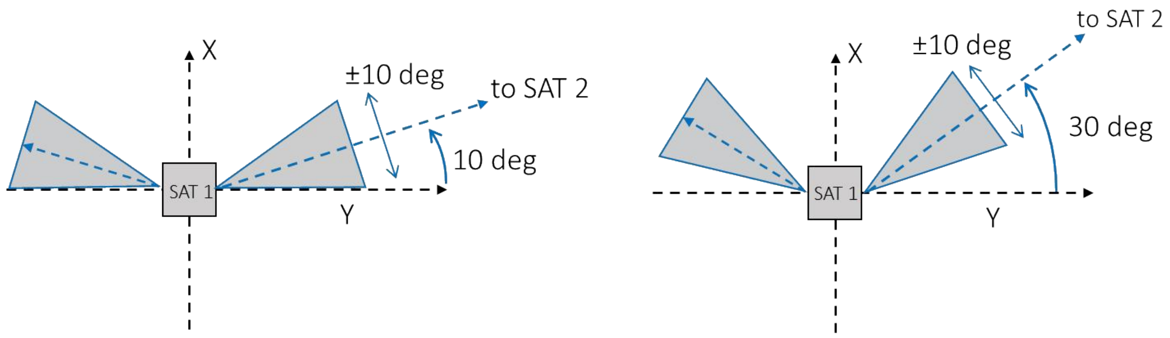

Astrocast, OneWeb, Telesat

SSG

Figure 3-18: Orientation of the LaserCube terminals for out-of-plane ISLs. Left: envisaged configuration for Astrocast, OneWeb and Telesat cases. Right: envisaged configuration for SSG.

In Figure 3-19 to Figure 3-22, the green parts of each plot indicate the parts of one orbit during which the parameter (range, pointing angle, pointing angular rate) is within the capabilities of the LaserCube ISL system; the boxed areas represent the intersection between the green areas, i.e. the areas where all parameters are within the LaserCube system capabilities and thus ISL can be performed. Table 3-19 summarizes the orbit percentage where out-of-plane ISLs can be performed.

Table 3-19: LaserCube main figures relevant to the ISL analysis.

Constellation	% of orbit available to ISL
Astrocast	45 %
OneWeb	88 %
SSG	62 %
Telesat	18 %

We can conclude that the actual LaserCube ISL configuration is already capable to realise data transmission during a significant part of the orbital period of every constellation we considered (especially OneWeb). However, it is worth to underline that the most impeding parameter for the implementation of out-of-plane ISLs is again the intersatellite range, which cuts off most of the orbit for the Astrocast case and, especially, the Telesat case.

This confirms that the most important future developments of LaserCube-ISL shall be focused on the increase of the workable ISL range or, in other words, on the increase of the bitrate performance for a given range.

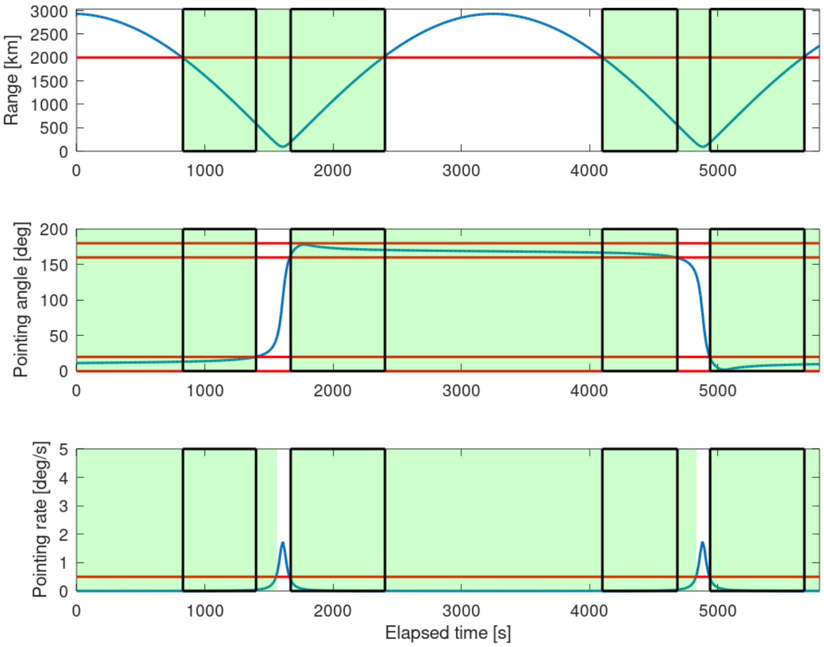

Figure 3-19: Results of the ISL analysis for the Astrocast constellation. Green shadows indicate the areas where the parameters are within the LaserCube ISL system performance (represented by the red lines). Areas within rectangles indicate the green areas intersection, i.e. when ISL can be performed.

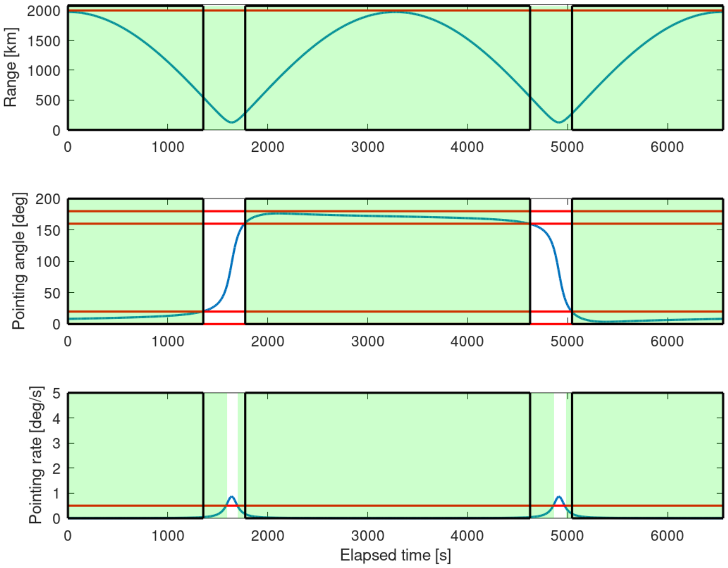

Figure 3-20: Results of the ISL analysis for the OneWeb constellation. Green shadows indicate the areas where the parameters are within the LaserCube ISL system performance (represented by the red lines). Areas within rectangles indicate the green areas intersection, i.e. when ISL can be performed.

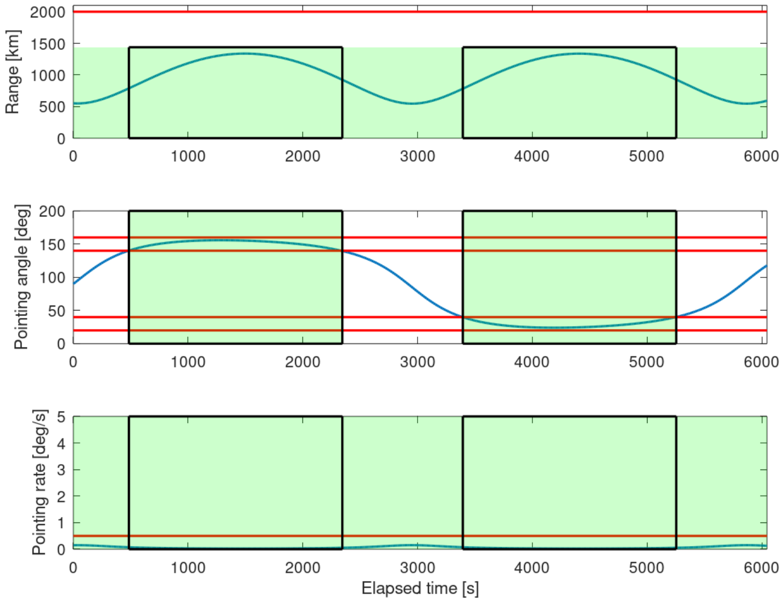

Figure 3-21: Results of the ISL analysis for the SSG constellation. Green shadows indicate the areas where the parameters are within the LaserCube ISL system performance (represented by the red lines). Areas within rectangles indicate the green areas intersection, i.e. when ISL can be performed.

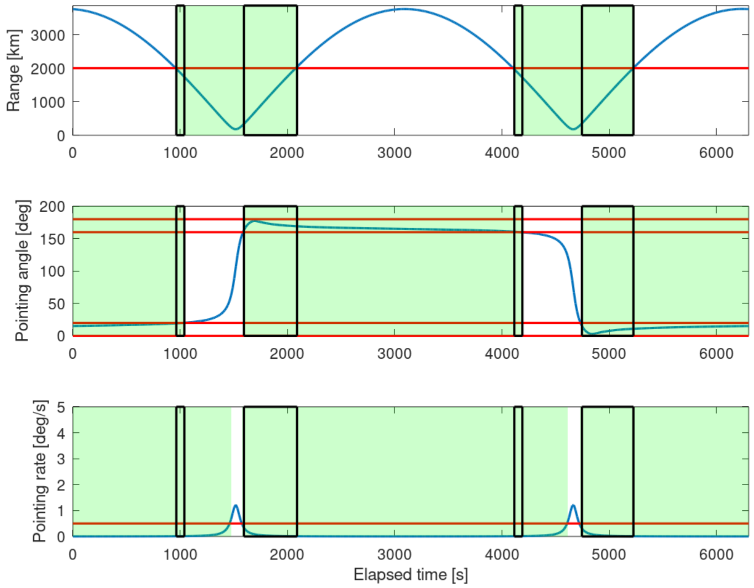

Figure 3-22: Results of the ISL analysis for the Telesat constellation. Green shadows indicate the areas where the parameters are within the LaserCube ISL system performance (represented by the red lines). Areas within rectangles indicate the green areas intersection, i.e. when ISL can be performed

3.5 Design guidelines

The application of the developed software to a series of case studies has allowed to derive valuable guidelines for future design tradeoffs at network and telecommunication payload level and for the selection of promising applications to which satellite optical communications could provide important support.

The results of the investigations have allowed to show in a quantitative fashion that ISL connectivity is particularly useful for applications targeting users for which the deployment of traditional terrestrial infrastructure is arduous due to their remote location, such as ships or remote mining plants. In this regard, ISL show the potential to partially compensate for the lack of a widespread ground station network, an advantage that could turn out to be extremely strategic in the frame of intelligence and defence operations.

For what concerns constellation design, the altitude of the satellite orbits should be carefully selected by means of a trade off considering both the Age of Information and data volume requirements. The selection of the number of satellites is influenced by both coverage requirements and link range performance, as increasing the number of satellites typically decreases their average relative distance. An aspect that should also be included in the simulation, which has not been considered in the described works, is the resolution requirement of the acquired images, which could favour the selection of lower orbits.

In terms of system design guidelines, an urgent need to increase the available connection range has clearly emerged from the case studies, in order to maximize link availability without excessively increasing the number of satellites and/or the number of hops.

4. SPACE SEGMENT DEVELOPMENT

In this chapter the activities related to the development of the space segment of an optical communications system is presented. A substantial part of the work described has been carried out in the context of the development of LaserCube, an optical communication terminal developed by Stellar Project. A specific focus on the contribution provided by the author to the advancement of LaserCube design is described here.

4.1 LaserCube overview

LaserCube (Figure 4-1) is a miniature optical communication system developed by Stellar Project. The system is compatible with CubeSat standards and mainly targets nano, micro and mini satellites. The objective of LaserCube project has been the development of telecommunication systems providing small satellite platforms with high-capacity downlink and intersatellite link capabilities. The system is designed to support LEO constellation networks for both space-generated and ground-generated fast data transport. The fundamental goal of the program has been to increase performance with respect to the state of the art, at comparable SW&P and without imposing additional constraints on the host platform.

LaserCube is a 2U system composed of two main units (Figure 4-2): the Opto-Mechanical Unit (OMU), in which the main optical components and mechanical actuators used for coarse and fine pointing are located; and the Electronic Unit (ELU), in which the electronic boards are located. The two units are independent from a structural point of view. The OMU is divided into a Miniature Pointing and Stabilization Subsystem (MPSS) and a Miniature Optical Syubsystem (MOS). The MPSS is a dedicated coarse pointing mechanical system that (1) relieves the host satellite attitude control system of this task, allowing the satellite to execute other operations that may require a different attitude, and (2) permits to achieve laser coarse pointing accuracy better than 100 µrad, which is much better than the attitude pointing accuracy that can be achieved by nano and micro satellites equipped with star trackers (2 mrad). This allows to use Commercial Off-The-Shelf (COTS) components for CubeSat Attitude Determination and Control System (ADCS) without dedicated star trackers. The MOS is in charge of collecting and transmitting both the beacon and telecom laser light necessary for link establishment; it also comprises a Fast Steering Mirror for fine pointing capabilities. The ELU comprises the electronic boards and relative

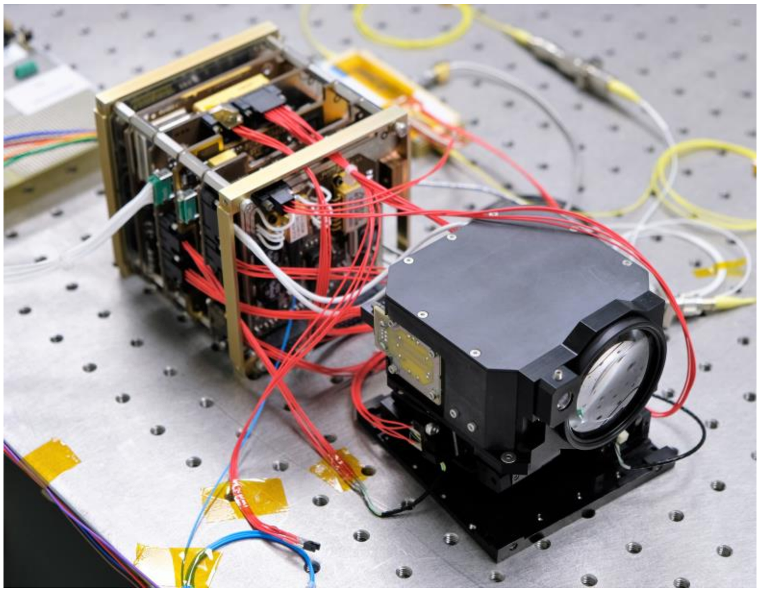

Figure 4-1: LaserCube.

interfaces necessary to generate and modulate the optical carrier; it also includes the electronic components for power distribution, coarse and fine pointing control and actuation, on-board data handling and interface with the host platform.

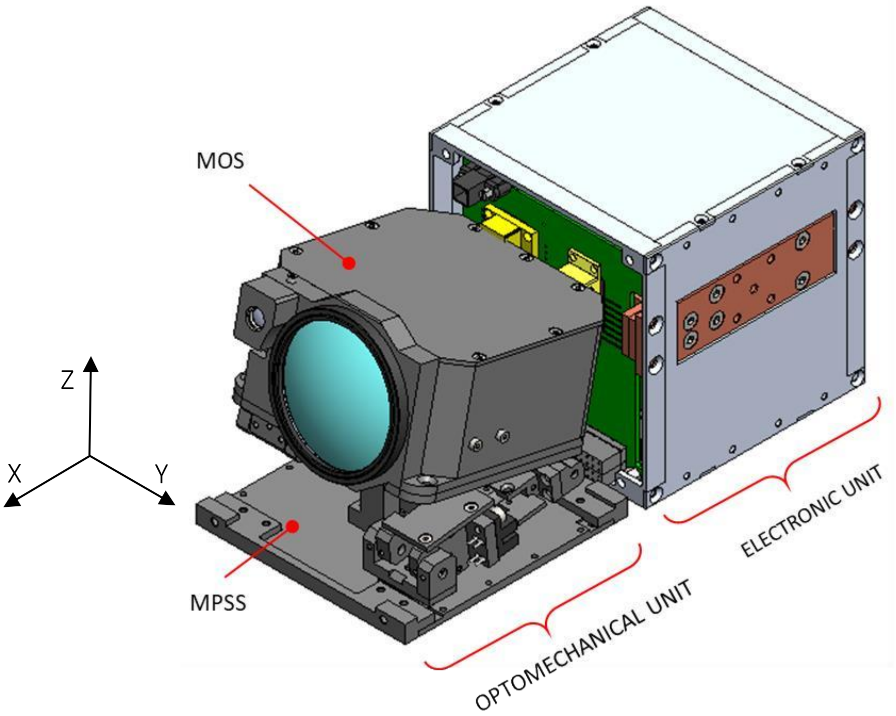

Figure 4-2: CAD view of the LaserCube Downlink terminal with indication of main parts.

Two main versions of LaserCube have been designed:

- LaserCube DL, specifically intended for high capacity space-to-ground optical communications
- LaserCube ISL, which is designed to perform inter-satellite communications and is thus also provided with a telecom receiver.

Given that LaserCube achieves its PAT capabilities by means of an actuated mechanism, a mechanical Launch Lock (LL) is necessary to lock the degrees of freedom of the mechanism and provide additional stiffness to the system during launch, in order to guarantee its resistance during this critical phase of the mission.

More details of LaserCube can be found in [70].

4.2 Structural analysis

This section describes the development and validation of the Finite Elements Model (FEM) and the verification of the stresses on the components of the OMU when the system is subjected to qualification loads. The candidate has been the main contributor to the described FEM model development and has supported Stellar Project's team with laboratory tests design, tests completion and analysis of results.

4.2.1 FEM Model Description

In this section the OMU structural model is described. Two main FEM models have been created for the current analysis:

- EM-FEM: used to simulate the behaviour of the Engineering Model (EM), on which the vibration tests have been performed, and to tune the LL stiffness parameters accordingly.
- FM-FEM: used to retrieve the expected behaviour of the Flight Model (FM), once the LL stiffness tuning has been carried out.

A representation of the EM-FEM and FM-FEM meshes can be found respectively in Figure 4-3 and Figure 4-4, with the coarse pointing system in its stowed configuration for launch.

The software used for the simulations is Ansys Workbench. Both EM-FEM and FM-FEM comprise a *system level structural model*, used to simulate the behaviour of the entire OMU. In this model all the components of the OMU are directly represented by their CAD geometry, except for the actuators (which are neglected due to their low expected contribution in terms of structural stiffness) and the LL, which is represented by a 6 degrees-of-freedom (3 translations, 3 rotations) stiffness matrix. A separate *LL dedicated model* has been used to derive the 6 stiffness values to be assigned to the LL stiffness matrix. These values have then been tuned according to the vibration test results, as presented in Section 4.2.3. Although the use of a single model for the entire analysis would have been preferred, the intrinsic non-linear behaviour of the LL due to its contact surfaces cannot be directly represented by the eigenvalues modal analysis tool provided by Ansys. The main properties of the materials involved in this analysis are listed in Table 4-1. The components with respective materials are shown in

Table 4-2.

Table 4-1: Material properties.

#	Material	Density [kg/m^3]	Young modulus [Gpa]	Yield stress [Mpa]
1	Ti-6Al-4V	4429	114	830
2	Aluminium 7075 T6	2800	73	503
3	Stainless steel AISI 410	7749	213	1225
4	Peek	1100	3.85	90.9
5	Glass	2460	70	32.6
6	Ti AMS 4965	4429	114	1100

Table 4-2: List of components and respective material

Components	Material
Launch Lock	1
Central joint supports	2
MPSS bottom plate	2
MPSS top plate	2
Flexural pivots	3
MOS supports	2
MOS cover	4
Lens and mirrors	5
PI316	3
LL Screw	6

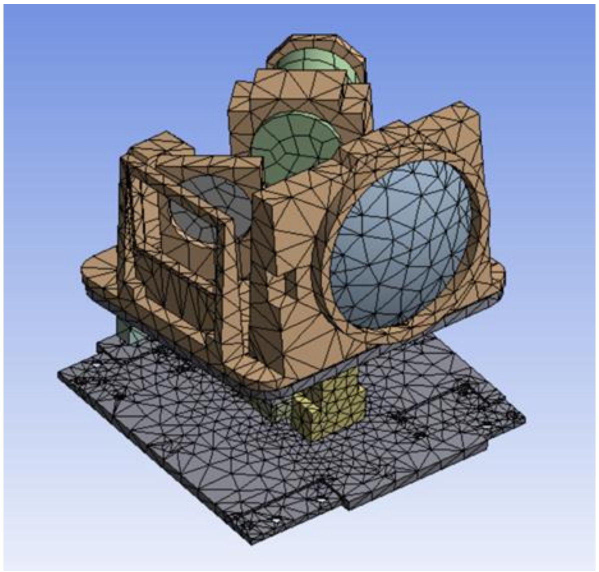

Figure 4-3. EM-FEM mesh.

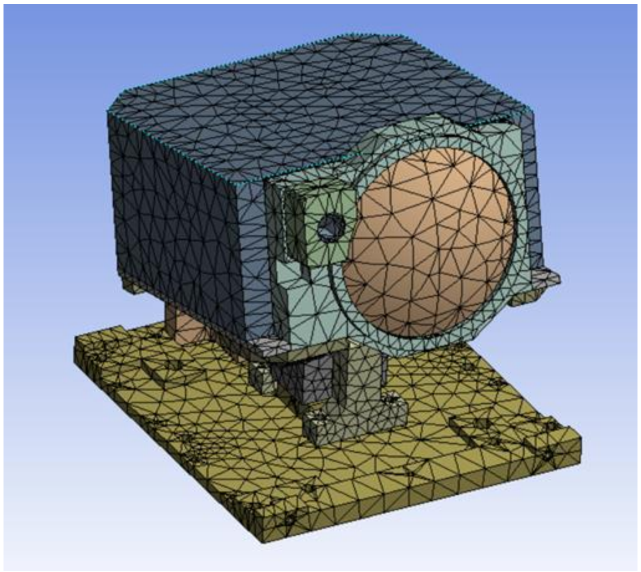

Figure 4-4. FM-FEM mesh.

MOS

The MOS models used for these simulations (Figure 4-3 and Figure 4-4) are slightly simplified versions of the EM and FM configuration, respectively. Although some minor details have been excluded for the sake of computational simplicity, the location of the masses is expected to result in a representative inertia tensor. The overall mass of the EM and FM MOS are 400 and 295 g, respectively.

Flexural Pivots

A consistent part of the system stiffness is expected to depend on the mechanical properties of flexural pivots, which are used in all the rotative joints of the MPSS mechanism. A number was assigned to each flexural pivot in order to relate it to the specific loads emerging from the analysis. The numbering is illustrated in Figure 4-5.

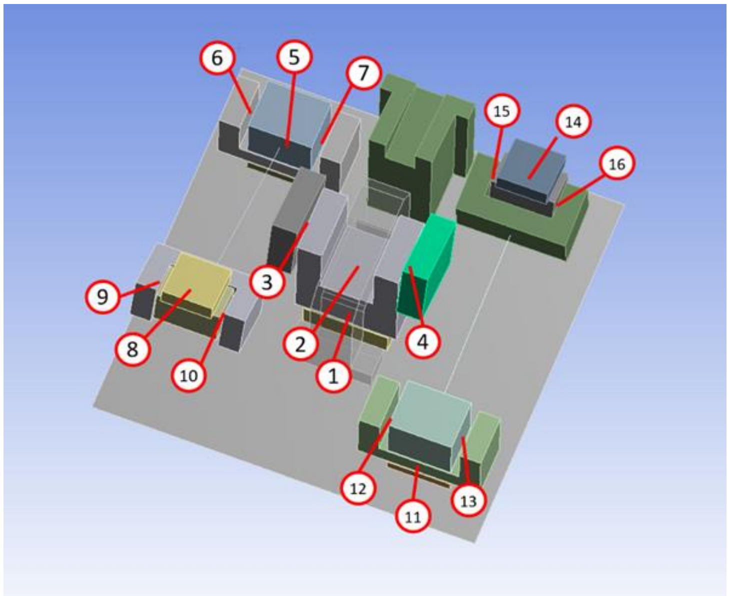

Figure 4-5: Flexural pivots numbering.

A major goal of the LL development has been to guarantee that the stresses induced on the flexural pivots during launch do not exceed the yield stress of the material.

The flexural pivots considered for this analysis are supplied by Riverhawk, which also provided the CAD used for the simulations. The material used for the simulation is AISI 410, as specified by supplier.

The CAD model of the flexural pivots has been directly used in the FEM of the system, as opposed to previous analyses in which they were characterized separately and only their stiffness matrix was included in the *system level structural model*. The surfaces of the pivots have been considered as bonded to the respective supports. An example of the pivot in its support and of a meshed pivot is show Figure 4-6.

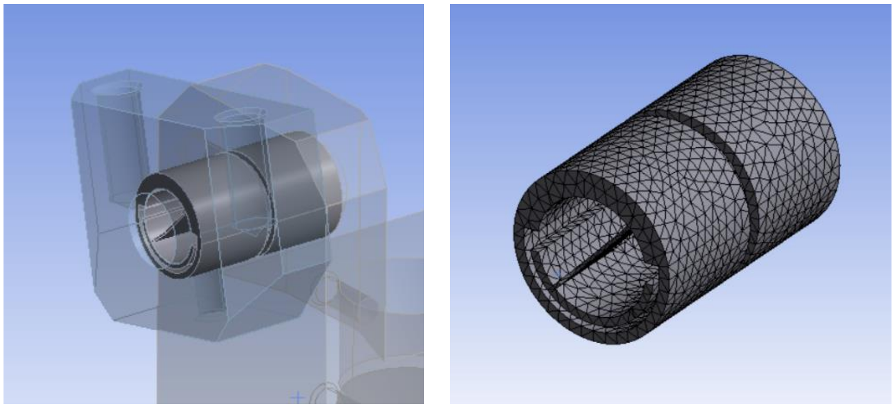

Figure 4-6: A flexural pivot in its supports (left) and its mesh (right).

Actuators

Considering the mechanical complexity of the actuator assemblies, a detailed representation of these elements is particularly demanding in terms of computational complexity and not relevant to the objectives of this analysis. Moreover, results of previous analyses suggest that their influence on the system's stiffness is negligible and that loads on actuators should be very low as they are intrinsically compliant to the system's degrees of freedom. For these reasons they were not included in the LL development model. Further analyses could assess the impact of resulting loads on the actuators.

Central Joint

The central joint geometry was directly taken from the design CADs, with some minor simplifications. As opposed to previous analyses in which flexural pivots were modelled separately, their CAD geometry has been directly included in the FEM model.

Launch Lock

In the architecture considered for this analysis, the LL is composed of two pieces rigidly connected respectively to the MPSS base and the MOS base. The two pieces are in turn bolted together by means of an M2 titanium notched screw, which guarantees the adherence of the two pieces and the overall stiffness of the LL during the launch phase.

In the *system level structural model* the two elements of the LL have been maintained in order to include their inertia, but the connection between them is represented by a stiffness matrix and the bolt is not directly included in this model. In particular, the rotational stiffnesses are represented by a bushing joint and the translational stiffnesses are represented by springs. The use of springs has been chosen to be able to retrieve the axial and shear loads on the screw. The initial stiffness values of both bushing joint and springs are derived from the characterization carried out using the *LL specific model* and are listed in Table 4-5. These values are the main object of the model tuning. The joints are applied to the upper surface of the top element and to the lower surface of the bottom element.

The final version of the LL used for this analysis is shown in Figure 4-7. A specific FEM model is dedicated to the characterization of the LL stiffness matrix, here assumed diagonal. This is necessary to adequately represent the intrinsic non-linear nature of the surface contact between the two pieces. This also allows us to have a direct feedback of the design changes on the LL stiffness and to have a reference for the LL stiffness values derived from the tuning.

In this model, all the structural components of the LL are directly represented by their CAD geometry, except for the screw, which is represented by a set of 3 springs which model its axial and shear stiffness. The screw stiffness is derived from a specific FEM characterization.

The stiffness values have been derived for two values of friction coefficients between the LL components: 0 and 0.4. Two series of results have thus been produced, corresponding to the two friction values.

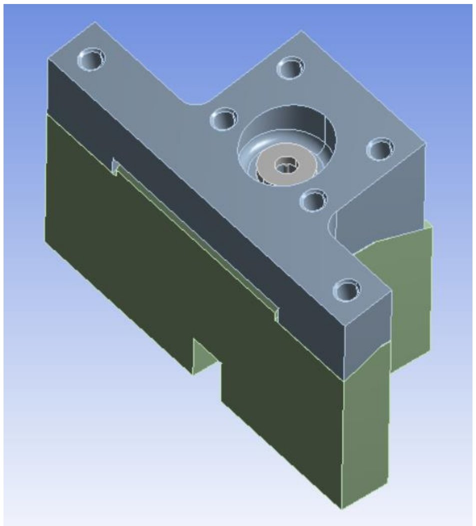

Figure 4-7: Selected LL geometry.

The LL characterization process consists in imposing a displacement (translation/rotation) of the top element corresponding to the investigated degree of freedom and measuring the resulting reaction (force/moment). The displacement is applied at the upper surface of the top element. The reaction is measured at the lower surface of the bottom element, which is the fixed support of the model. The stiffness is then computed as the ratio between the reaction and the imposed displacement.

The resulting stiffness values are shown in Table 4-5. These values are the ones used as initial parameters for the simulations and have been modified during the tuning process to match the results of the resonance search tests.

<u>ELU</u>

For the modelling of Electronic Unit (ELU), a slightly simplified version of its actual geometry was taken into account, excluding very small components which are not expected to have any structural function or to be directly subjected to significant loads. This simplification has been made to limit computational cost and numerical artifacts. The density of the Printed Circuit Boards (PCB) was artificially increased in order to represent the additional mass added by electronic components, which are not modelled in detail in the present analysis.

In order to have a clearer presentation of the analysis results, the components have been grouped into five categories (see Figure 4-8), namely:

- Aluminium structure (frames and panels)
- Steel spacers
- Connectors
- Electronic boards
- Thermal straps

The analysis has been performed both on the DL and ISL versions of the ELU. From a structural point of view, the major difference between the two versions is represented by the additional optical components required for the optical signal reception (see Figure 4-9), which are housed between the electronic boards and the OMU. The geometry of the additional ISL optical component has been slightly simplified for the simulation, while the geometry of the frame housing them has been left unchanged. The material considered for these components is aluminium and their results are included into the aluminium structure group.

Table 4-3: Material properties.

#	Material	Density [kg/m^3]	Young modulus [Gpa]	Yield stress [Mpa]
1	Aluminium 7075 T6	2800	73	503
2	Stainless steel AISI 410	7749	213	1225
3	Copper	8940	131	247
4	Polyamide	4250	24.9	249

Table 4-4: List of components and respective material.

Components	Material
Aluminium structure	1
Spacers	2
Connectors	1
Boards	4
Thermal straps	3

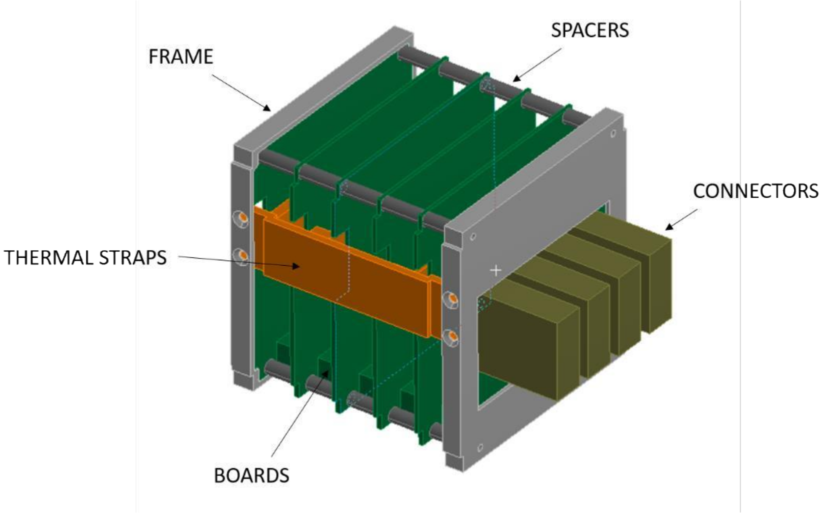

Figure 4-8: ELU model used for the simulations. The components have been grouped in order to present the results in a clearer way. Side panels are not shown here.

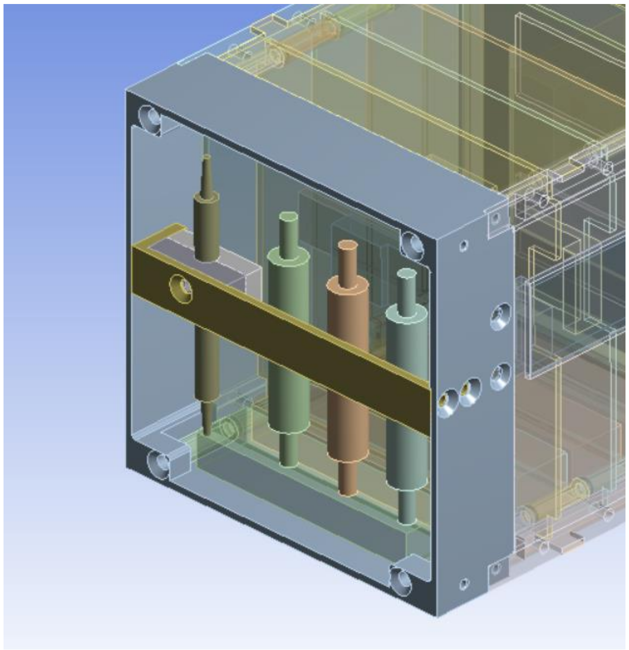

Figure 4-9: CAD model of the additional optical components for the ISL version of LaserCube's ELU.

4.2.2 Experimental resonance search

A resonance search has been performed on the EM in order to retrieve the first natural frequencies of the system and tune the FEM model. The tests have been conducted at CISAS premises using electromechanical shaker and monitoring accelerations in several unit locations using piezo-electric accelerometers. The set up for mechanical test implies the use of an electrodynamic shaker and 9 accelerometers to be used for monitoring levels (Figure 4-10).

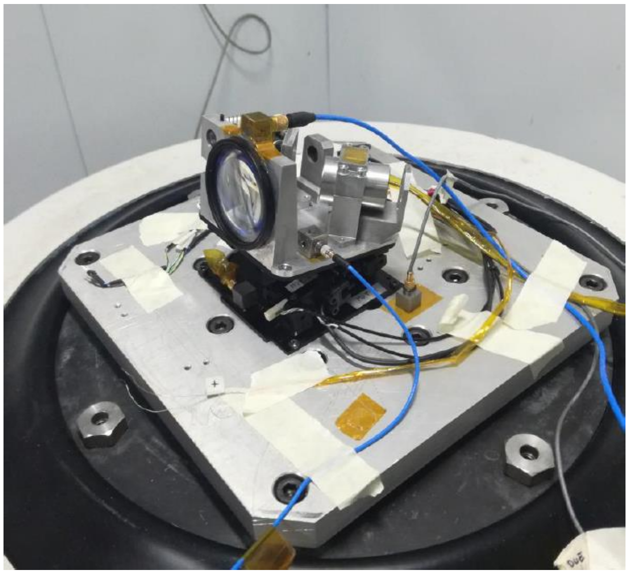

Figure 4-10: resonance search test setup on shaker table at CISAS facilities.

The results of the experimental resonance search on the EM model are shown in Figure 4-11 and Figure 4-12. See Figure 4-2 for the definition of the frame of reference. Two main modes have been identified from the X-axis excitation results, respectively at 200 Hz and 370 Hz. From a qualitative analysis of the difference in amplification among the accelerometers, the first mode seems to be predominantly associated to a roll motion of the MOS with respect to the MPSS central joint (rotation along X-axis), while the second mode to a pitch motion (rotation along Y-axis). This is consistent with the FEM simulations results. Similar results have been found for Y-axis, with both frequencies shifted up of about 10 Hz (i.e. respectively 210 Hz and 380 Hz).

We assume that results of X-axis and Y-axis refer to the same modes of vibration, and that the frequency shift is due to non-linear phenomena. We use the lower values (200 and 370 Hz) for the tuning process.

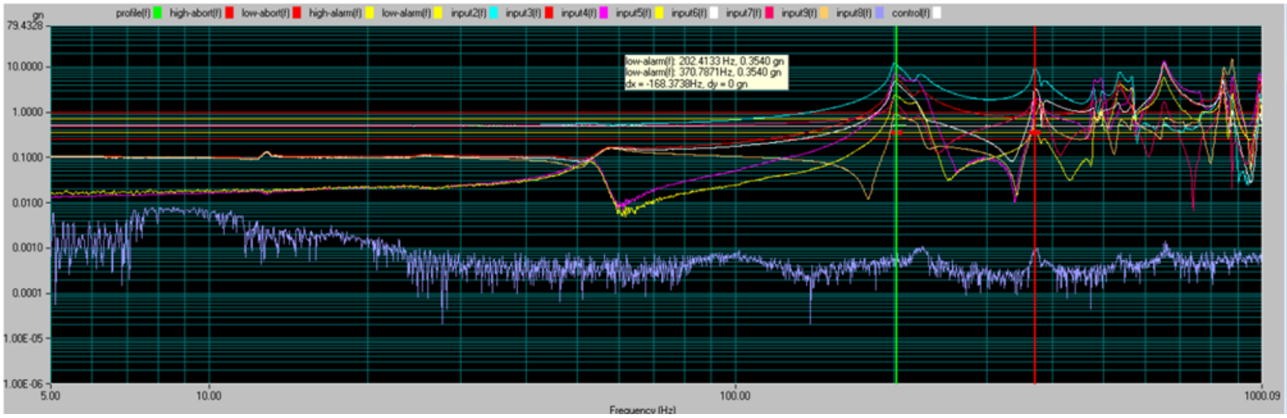

Figure 4-11: results of the resonance search, X-axis excitation. The peaks at 200 Hz and 370 Hz can be observed.

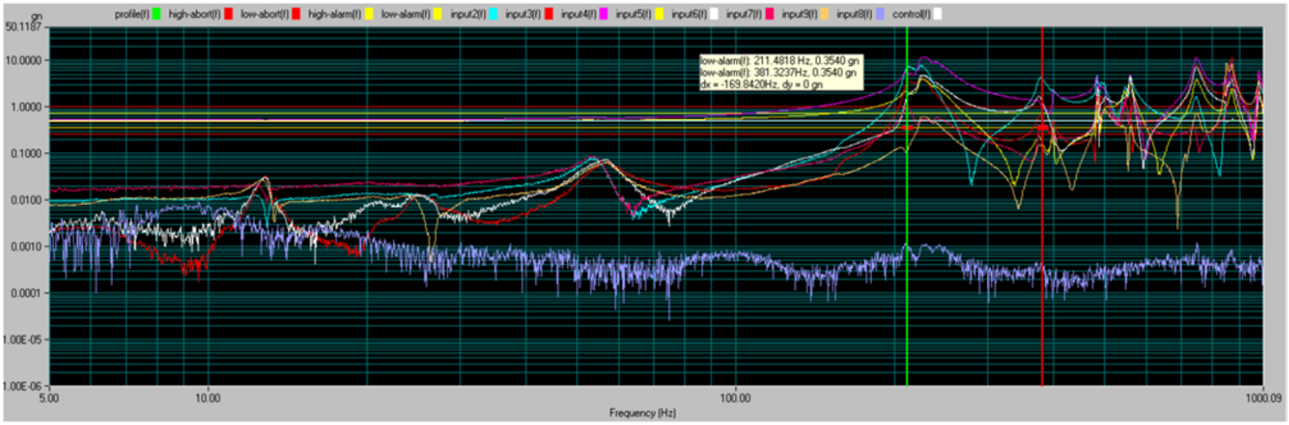

Figure 4-12: results of the resonance search, Y-axis excitation. The peaks at 210 Hz and 380 Hz can be observed.

4.2.3 Model tuning

For the tuning of the model we assumed that the estimated stiffness properties of the flexural pivots are correct, as their geometry is directly included in the *system level structural model*. We therefore only acted on the stiffness of the EM-FEM LL, modifying the stiffness matrix values until the resulting first two frequencies matched the ones found during the laboratory test. The stiffness matrices of the LL are shown in Table 4-5, respectively for the original and tuned cases.

Table 4-5: Stiffness matrices of the LL. Top: from LL FEM characterization; Bottom: adapted.

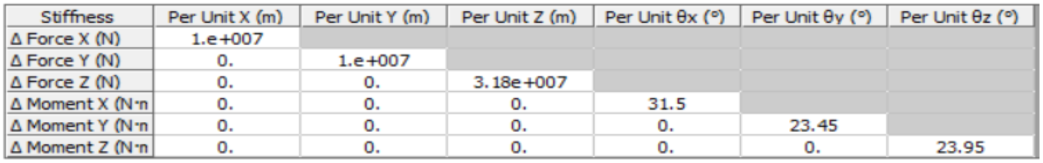

Stiffness	Per Unit X (m)	Per Unit Y (m)	Per Unit Z (m)	Per Unit θx (°)	Per Unit θy (°)	Per Unit θz (°)
Δ Force X (N)	1.e+007					
Δ Force Y (N)	0.	1.e+007				
Δ Force Z (N)	0.	0.	3.18e+007			
Δ Moment X (N·n	0.	0.	0.	31.5		
Δ Moment Y (N·n	0.	0.	0.	0.	23.45	
Δ Moment Z (N·n	0.	0.	0.	0.	0.	23.95

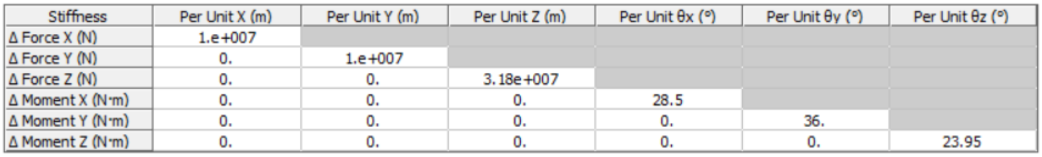

Stiffness	Per Unit X (m)	Per Unit Y (m)	Per Unit Z (m)	Per Unit θx (°)	Per Unit θy (°)	Per Unit θz (°)
Δ Force X (N)	1.e+007					
Δ Force Y (N)	0.	1.e+007				
Δ Force Z (N)	0.	0.	3.18e+007			
Δ Moment X (N·m)	0.	0.	0.	28.5		
Δ Moment Y (N·m)	0.	0.	0.	0.	36.	
Δ Moment Z (N·m)	0.	0.	0.	0.	0.	23.95

4.2.4 Simulations and loads definition

The stiffness values derived from the tuning process have been used for the FM-FEM simulations, in order to retrieve the stresses and loads on the most critical components and to assess that they do not exceed their limit strength. The loads used for the simulations are in any case higher than the expected qualification levels.

Static

A steady-state acceleration of 16 g has been applied to each axis independently, to simulate the loads induced by the quasi-static accelerations during launch.

Modal

Ansys Modal tool has been used to analyse the modal behaviour of the system. The main output of this analysis are the first 6 modes of vibration of the assembly, with the associated modal frequencies and modal shapes. In particular, this is used to assess that the first frequency exceeds the reference frequency specified by launch requirements (200 Hz).

Sine

A harmonic analysis has been performed to simulate the sine sweep test. The frequency range considered in this analysis is 5 to 125 Hz. An acceleration of 25 g has been applied to each axis throughout the frequency range.

Random

Random vibration simulations were performed in order to retrieve the stress on critical elements arising from qualification random vibration load levels.

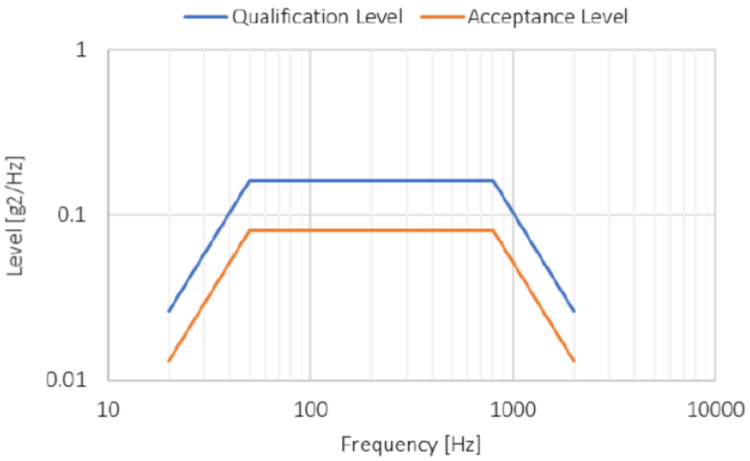

Figure 4-13: Random load spectrum corresponding to acceptance and qualification levels

Table 4-6: Random load spectrum corresponding to acceptance and qualification levels.

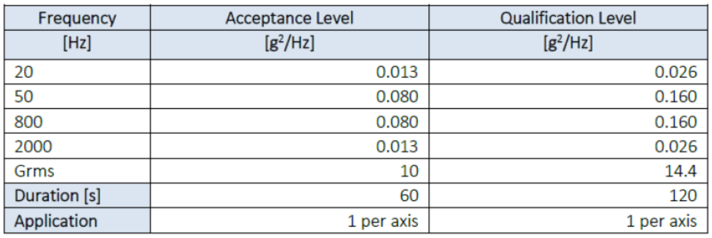

Frequency	Acceptance Level	Qualification Level
[Hz]	[g^2/Hz]	[g^2/Hz]
20	0.013	0.026
50	0.080	0.160
800	0.080	0.160
2000	0.013	0.026
Grms	10	14.4
Duration [s]	60	120
Application	1 per axis	1 per axis

The load profiles used for the simulations (see Figure 4-13 and Table 4-6) are the same that have been used for the qualification tests, i.e. the vibration levels specified by NASA General Environmental Verification Specification (GEVS), [AD3]. 2σ results have always been considered.

4.2.5 Results

The results of the FM-FEM simulations have been computed both in terms of natural frequencies and of stress on the components and associated Margins of Safety (MoS), defined as:

$$MoS = \frac{\sigma_y}{\sigma} - 1$$

where σ_y is the yield stress of the material and σ is the stress resulting from the simulations.
For what concerns the OMU, the results of the simulation show that the expected first natural frequency is 240 Hz, above the requirement (200 Hz). Moreover, neither quasi-static loads, sine loads nor random vibrations are expected to induce stresses that could represent a critical condition for the system, with MoS>0 in all conditions. For what concerns the ELU, similar results have been obtained for both DL and ISL versions. The first natural frequency (299 Hz) is well-above the requirement. Neither quasi-static loads, sine loads nor random vibrations are expected to induce critical stresses on any component and high MoS values have been obtained for every item and loading condition.
A further analysis has been performed to assess that the loads on the LL screw do not exceed the limit values specified by the supplier (1269 N). Loads are indirectly computed using the following equation:

$$L = P + L_m + L_b$$

which considers the contribution of the preload P, the output load directly retrieved from the simulation along the screw axis L_m, and the load due to the LL bending L_b. L_b has been indirectly obtained from the computed rotation of the upper part of the LL and the rotational stiffness of the LL. This further assessment confirms the robustness of the system, with MoS>0 in all conditions (in this case MoS has been computed with respect to the limit load of the screw).
In conclusion, the work described in this section has allowed to define a FEM mechanical and vibrational model of LaserCube, from which we have retrieved their first natural frequencies and the expected

displacements, loads and stresses on critical elements due to load levels to which the system has been subsequently submitted during structural qualification tests. Moreover, a laboratory shaker table test has been performed, through which the actual natural frequencies of the EM have been measured and compared with the simulated results. In this way, the model's parameters have been tuned and a validated FEM model of the system has been obtained.

4.3 Launch-lock thermal analysis

This section presents the development of the lumped-model thermal analysis of the LL mechanism. Paragraph 4.3.1 is dedicated to the description of the thermal model and of the main parameters involved. In Paragraph 4.3.2 the validation and calibration of the model is presented. In Paragraph 4.3.3 the most relevant results of the analysis are presented, aiming at illustrating the impact of some major design parameters on the performance of the LL mechanism. The candidate has been the main contributor to the described model development and has supported Stellar Project's team with laboratory tests design, tests completion and analysis of results.

4.3.1 Lumped-element model description

The LL unlock is based on the heating of a Shape Memory Alloy (SMA) actuator until activation temperature by means of an electric resistor. The constraint on the supply voltage is 5 V, with the electric resistance depending on temperature according to:

$$R = R_0 \cdot \left[1 + \alpha\left(T - T_{ref}\right)\right]$$

Where the values provided by supplier are R0 = 4.1 Ω, α = 0.0024, Tref = 25°C.

In order to simulate the thermal behaviour of the LL mechanism during its activation, a 5-node lumped-element model was developed. The model has been developed in Matlab and the thermal evolution of the system is computed by solving the characteristic differential equations through the ode45 function.

The elements into which the system was divided and the derived heat transfer model are shown respectively in Figure 4-15 and Figure 4-16. The SMA actuator (1) is made of a NiTi alloy, the notched bolt (2) is made of titanium while the supports (3, 4 and 5) material can be selected between aluminium and titanium. Washers are made of titanium and are treated as pure thermal resistances. The properties of materials are described in Table 4-7.

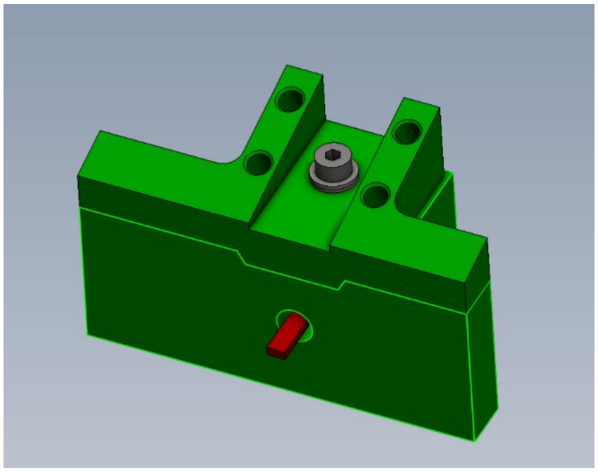

Figure 4-14: Launch lock geometry.

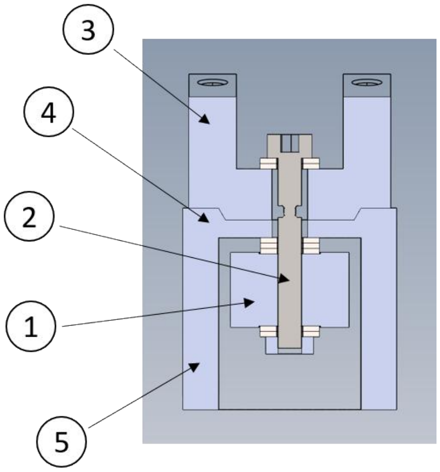

Figure 4-15 Section view of the LL mechanism, with indication of the model's lumped elements. 1) SMA actuator; 2) notched screw; 3) upper support; 4) lower support, upper part; 5) lower support, lower part.

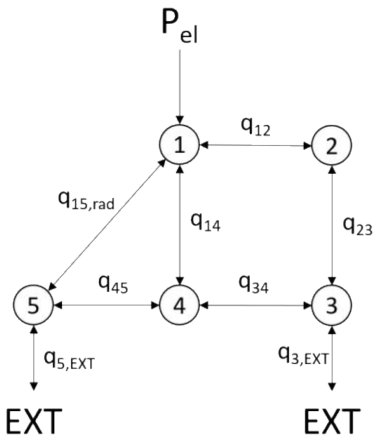

Figure 4-16 Heat transfer model. P_{el}: heat provided by electric resistance; q_{abs}: heat absorbed by SMA actuator at activation; q_{ij}: heat transferred from node i to node j; EXT: external environment (fixed temperature).

Parameter	Value	Unit
λ_{Al}	230	W/mK
λ_{NiTi}	10	-
λ_{Ti}	6.7	-
ρ_{Al}	2.7	g/cm³
ρ_{NiTi}	/	-
ρ_{Ti}	4.5	-
c_{Al}	880	J/kgK
c_{NiTi}	320	-
c_{Ti}	526	-

Table 4-7 Properties of materials: thermal conductivity (⍰), density (⍰) and heat capacity (c).

Thermal resistances between nodes have been computed by considering both the pure resistance of washers and the resistance of the components. This is the most critical phase of the simulation, as several assumptions regarding heat exchange areas and resistance thickness were needed, due to the relative complexity of the system's geometry. For this reason, the model has been experimentally verified to assess its ability to predict the system's behaviour. The radiation between element 1 and 4 has been included in the analysis; radiation between case and environment has been neglected, since their temperature difference remains very small (<1°C) throughout the operation.

After few exploratory simulations, the main design parameters resulted to be the supporting elements material (aluminium *vs* titanium), the number of washers (2 to 5, M2, 0.45 mm thick) between element 1 and 4 and the SMA activation temperature (140°C to 220°C). For what concerns the supports material, aluminium has been quickly discarded for its low thermal performance and titanium has been selected.

The environmental temperature is expected to vary between -25 and 50 °C. Several simulations have been produced varying these parameters and the results will be shown and commented in the following sections.

4.3.2 Model validation and calibration

In order to assess that the simulations can suitably predict the behaviour of the system, a validation and calibration of the model was performed. For this purpose, a test campaign was carried out with the aim of comparing the system's temperature evolution with the model predictions and to calibrate the model accordingly.

The first step was the calibration of the resistance model, by fitting the resistance values derived by acquired data as a function of temperature. In Figure 4-17 the original and calibrated resistance model are shown in comparison with acquired data. Error bars have been computed and added, considering a 0.1 V error on measured voltage and 0.01 A on measured current.

The values found from curve fitting are R0 = 4.6 Ω, α = 0.0012 at Tref = 25°C.

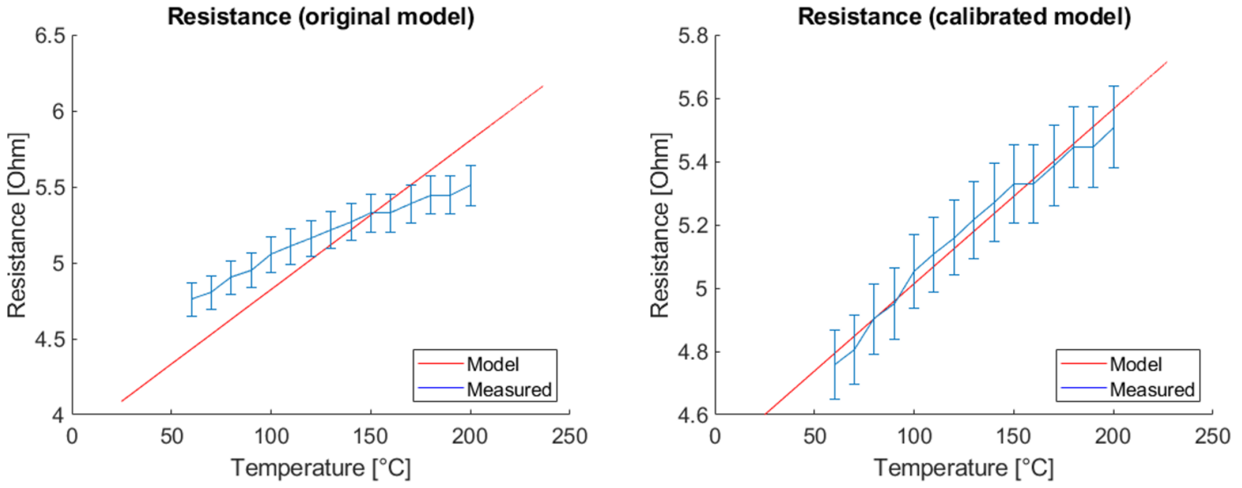

Figure 4-17: original and calibrated resistance model, superimposed to resistance derived from measurements.

For the tuning of the model, the assumed thermal resistance between the elements of the system has been rescaled. The comparison of the temperature evolution profiles acquired during test and predicted by the calibrated model is shown in Figure 4-18. What we observe is that the model cannot accurately predict the behaviour of the system in the first seconds of activation, while the temperature trend is followed as the system reaches the equilibrium temperature. For this reason, and since the behaviour of the system at higher temperatures is our main focus, the model was tuned so that the temperature predictions for all acquisitions remain within ± 10 °C from the acquired data starting from 20 s after activation.

In Figure 4-19 the same comparison has been performed, but different cases have been separated in order to include a 10°C error bar for each data acquisition. This allows to assess the correct matching of the model within a ± 10 °C tolerance.

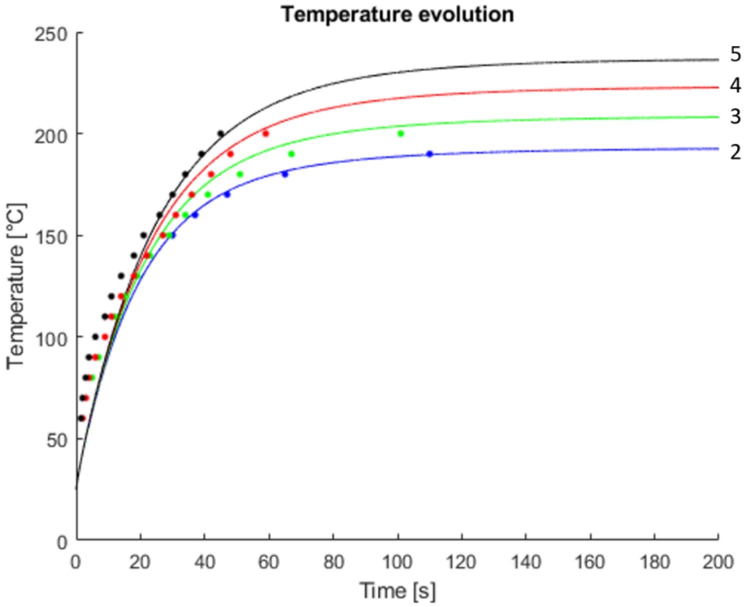

Figure 4-18: Temperature evolution, parametric in the number of washers. Solid lines represent simulated evolutions, dots represent data acquired during validation tests.

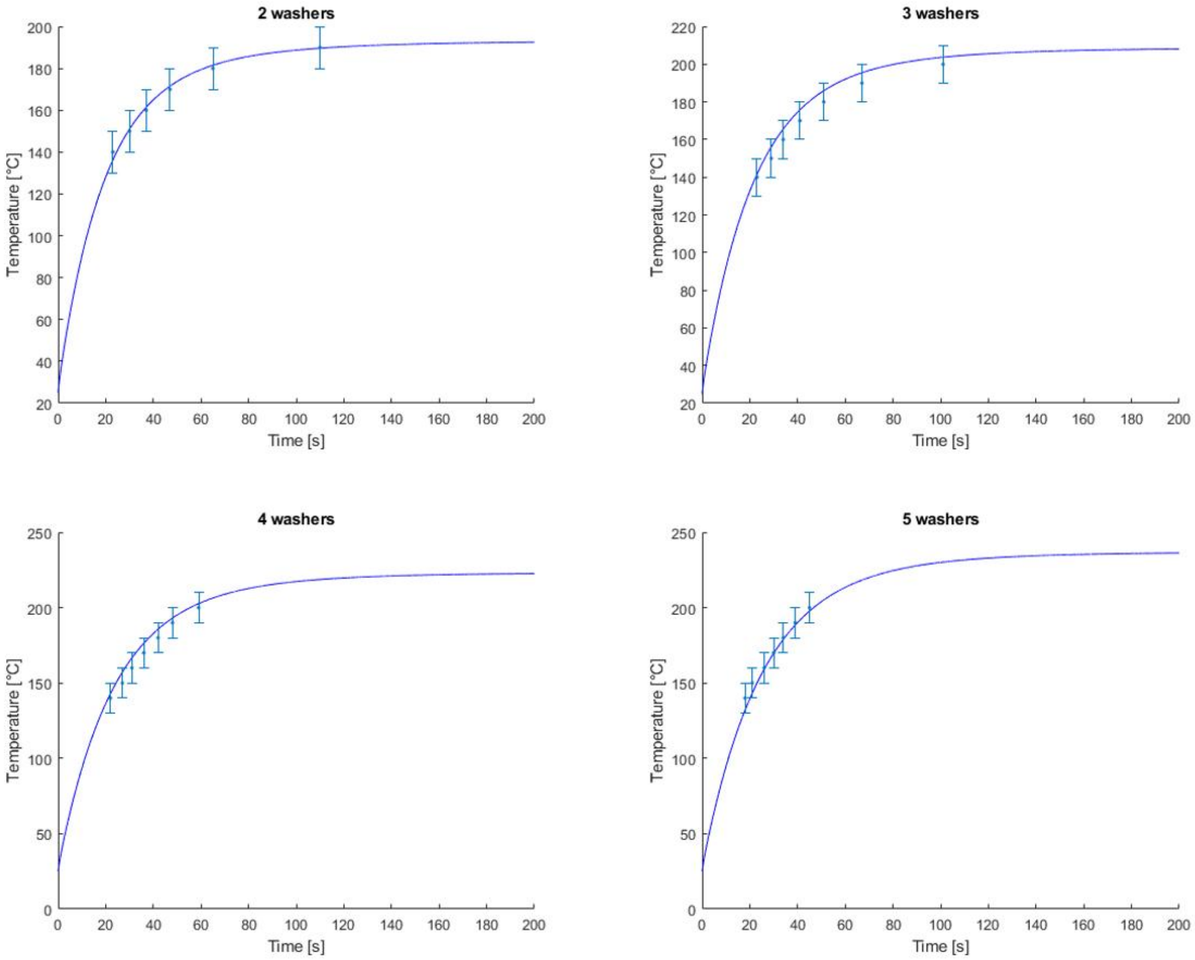

Figure 4-19: Error bar plots.

4.3.3 Results

In order to clearly show the performance of the system as a function of design parameters, a number of representative quantities has been selected to produce useful parametric diagrams. In Figure 4-20 the maximum temperature that the SMA actuator will reach (assumed to be the temperature after 180 s) as a function of environmental temperature is shown. The graphs are parametric in the number of washers between element 1 and 4. We can observe that for worst case conditions (T_{env} = -25 °C), T_{max} ranges between 150°C and 200°C according to the number of washers. These correspond to the maximum activation temperatures of the SMA actuator for the system to work correctly throughout the expected temperature range. The cases in which the system is expected to activate for all environmental conditions taken into account is with 4 and 5 washers (considering a 180 °C activation temperature).

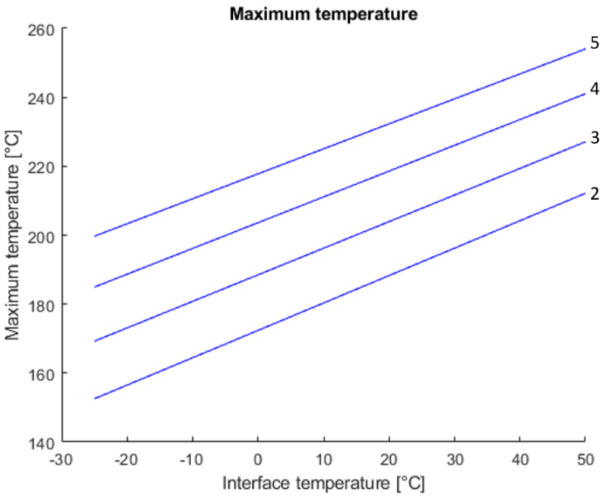

Figure 4-20: Maximum temperature that can be reached as a function of the envirnomental temperature, parametric in the number of washers between SMA actuator and support (titanium case).

In Figure 4-21 the SMA actuator activation time as a function of environmental temperature is shown, parametric in the number of washers. Activation temperature is here fixed at 180°C. We can clearly see that in the case of 2 and 3 washers there is an environmental temperature below which it is not possible to reach activation.

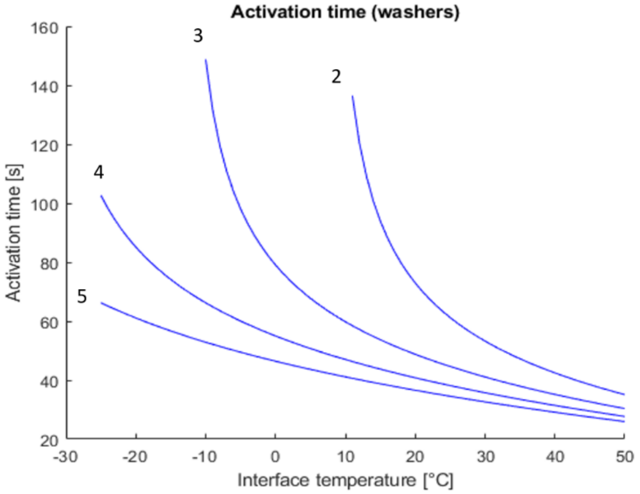

Figure 4-21: Activation time as a function of the environmental temperature, parametric in the number of washers between SMA actuator and support.

In Figure 4-22 the SMA actuator activation time as a function of environmental temperature is shown again, but this time parametric in the activation temperature. The number of washers is fixed at 5.

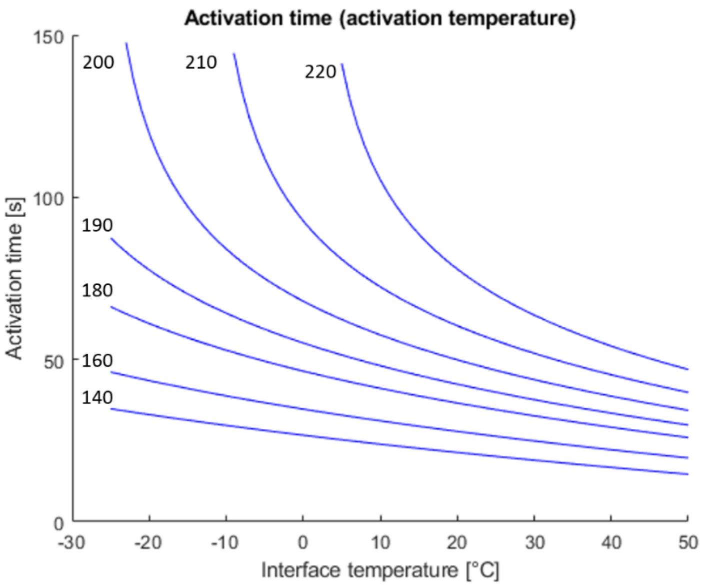

Figure 4-22: Activation time as a function of the environmental temperature, parametric in the SMA activation temperature.

Although the activation temperature range considered for these simulations (140°C to 220°C) is well above the expected working conditions of the mechanism, keeping a higher temperature could help avoiding any unwanted activations. For this reason, an intermediate activation temperature seems to be appropriate, i.e. a temperature that is difficult to reach accidentally but that still guarantees activation for the titanium solution even with two washers only.

It is also suggested to use the highest number of washers compatible with geometrical constraints, in order to assure activation at all environmental conditions and to maximize temperature margins. It is also necessary to experimentally assess that the SMA expansion is sufficient to break the notched screw, as the load on this element will decrease with the increase of washers number.

Finally, a substantial difference has been observed with respect to information provided by supplier, in terms of electrical resistance variation as a function of temperature and of SMA activation temperature (220 vs 210 °C). For this reason, a better characterization of the SMA actuator assembly is suggested, in terms of electrical resistance variation with temperature and of activation temperature.

4.4 LaserCube pointing, acquisition and tracking performance

The tests performed to assess LaserCube's combined coarse and fine pointing system performance (see Section 4.1) are presented in this Section. These tests represent the result of Stellar Project's team technological development activities since its foundation and are the outcome of several peoples' collaboration. The candidate has mainly contributed by supporting Stellar Project's team with laboratory tests design and tests completion and has also provided a partial support to the analysis of results; a specific contribution has been provided by the candidate with the identification of an optimal voltage supply configuration, which has allowed to improve system's performance by reducing sensor noise.

4.4.1 Test setup

The test setup is shown in the figure below and consisted in:

- LC-ISL Qualification Model (QM) (OMU+ELU)
- Pan/tilt platform and dedicated controller
- Beam expander with beacon laser source (see Figure 4-23)
- External Position Sensitive Detector (PSD) sensitive at 1550 nm
- Electrical Ground Support Equipment (EGSE)
- Optical table with vibration control
- Power supplies
- Laptop

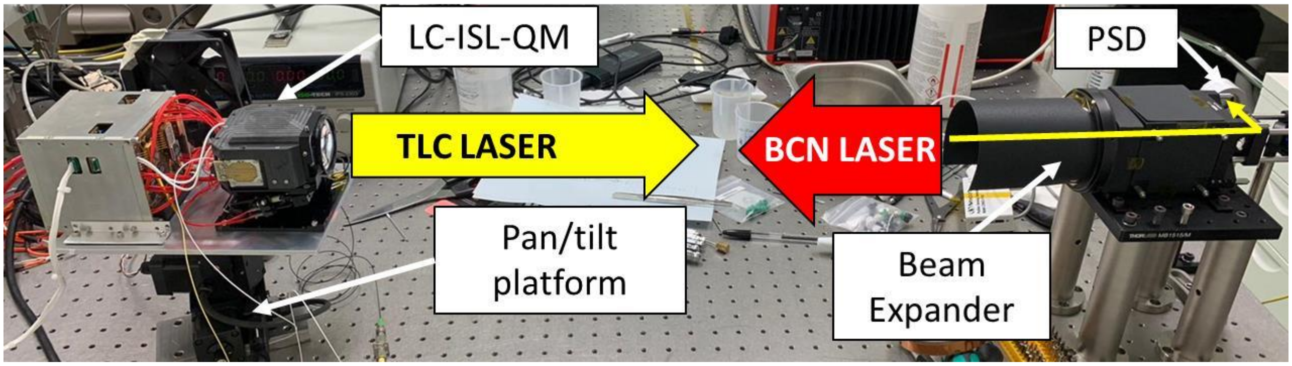

Figure 4-23. Test setup for test T1, including LaserCube-ISL QM on pan-tilt platform (on the left) and the beam expander with the PSD (on the right).

4.4.2 Test procedure

First, a system calibration process has been carried out. The goal of this calibration process is to determine experimentally the relationship between the beacon sensor output voltages to the measured direction of the incoming beacon beam in terms of elevation and azimuth angles (θ, ψ) and (2) the fine pointing systems calibration factors.

After that, the execution of the spiral trajectory to be followed during the seeking procedure was tested, as well as the transition from Seeking to Tracking when the beacon beam coming from the remote terminal is detected. To perform this test, LaserCube is mounted on the pan/tilt platform and the laser beam transmitted by the beam expander is initially turned off. The execution of the spiral trajectory is commanded to LaserCube, whose coarse pointing system starts following the spiral trajectory. After an arbitrary amount of time in the order of few minutes, the beacon laser is turned on. Upon beacon detection, the system automatically switches from seeking to tracking and centres the received beacon beam on the beacon sensor, minimizing the alignment error.

Once the system is in tracking mode, the LaserCube telecom laser is turned on and detected by the PSD, whose outputs are measures and give an estimate of the pointing error. During this phase, the pan/tilt platform may be used to impose a jitter motion at the payload base to simulate the host platform attitude jitter, which is a disturbance to the pointing system.

4.4.3 Test Results

Figure 4-24 presents the results of the seeking procedure test. In Figure 4-24 left, the spiral trajectory calculated from the elongation of the MPSS linear motors is shown in terms of orientation (ψ_{MPSS}, θ_{MPSS}) of the MPSS upper platform with respect to its base. The blue path represents the spiral trajectory while the red path represents the motion performed after beacon detection in order to align the optical unit to the beacon laser direction. In Figure 4-24 right, the beacon laser decentre with respect to the beacon sensor is shown in terms of angles (ψ_{QD}, θ_{QD}), which represent the angular pointing error. The latter is minimized and stabilized close to zero after a transient phase. ψ_{QD} is minimized in a shorter time since its initial value is lower than the initial θ_{QD}; indeed, θ_{QD} at the moment of beacon detection is outside the linear range of the beacon sensor; in fact, it seems that its value does not change within the first seconds of tracking. When the pointing error on θ_{QD} enters the linear range of the beacon sensor, θ_{QD} values decrease to zero. This is because the linear range of the beacon sensor is lower than its FoV.

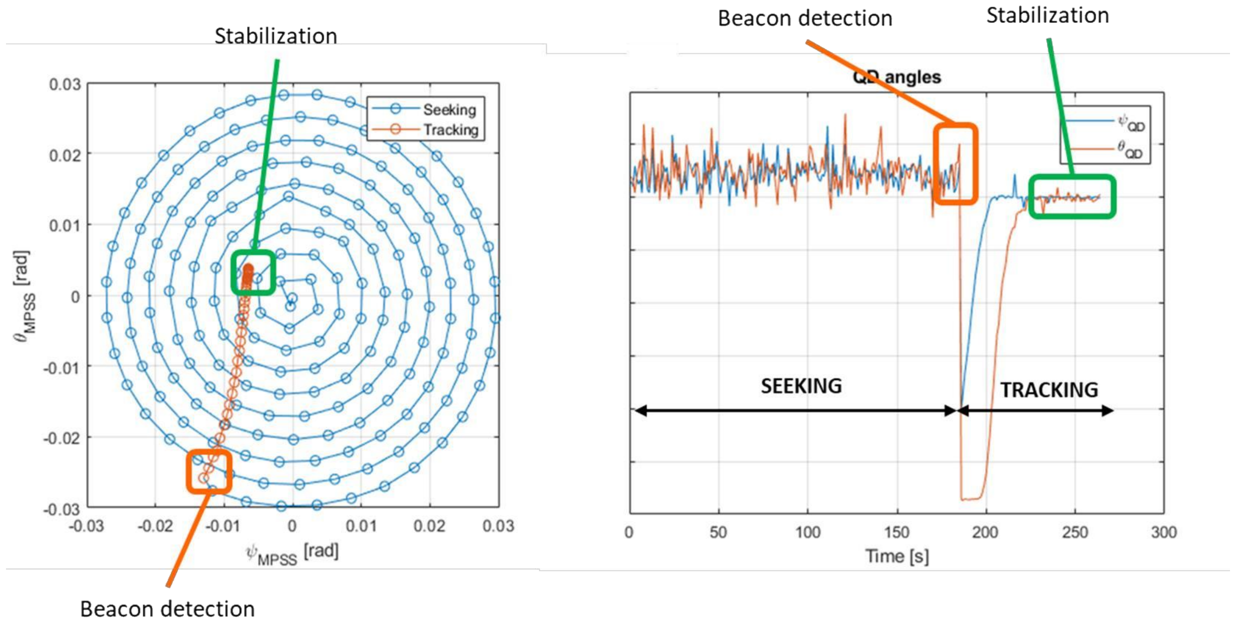

Figure 4-24. Left: measured spiral trajectory in azimuth ψ and elevation θ inferred by the elongation of the MPSS linear actuators. Right: beacon beam decentring measured by the beacon sensor inside the MOS (values of the y-axis have been omitted for intellectual property reasons).

Examples of results from tracking tests are shown in Figure 4-25 left (static tracking) and Figure 4-25 right (dynamic tracking, i.e., with jitter imposed by the pan/tilt platform). Values of the y-axis and tracking error standard deviations have been omitted for intellectual property reasons

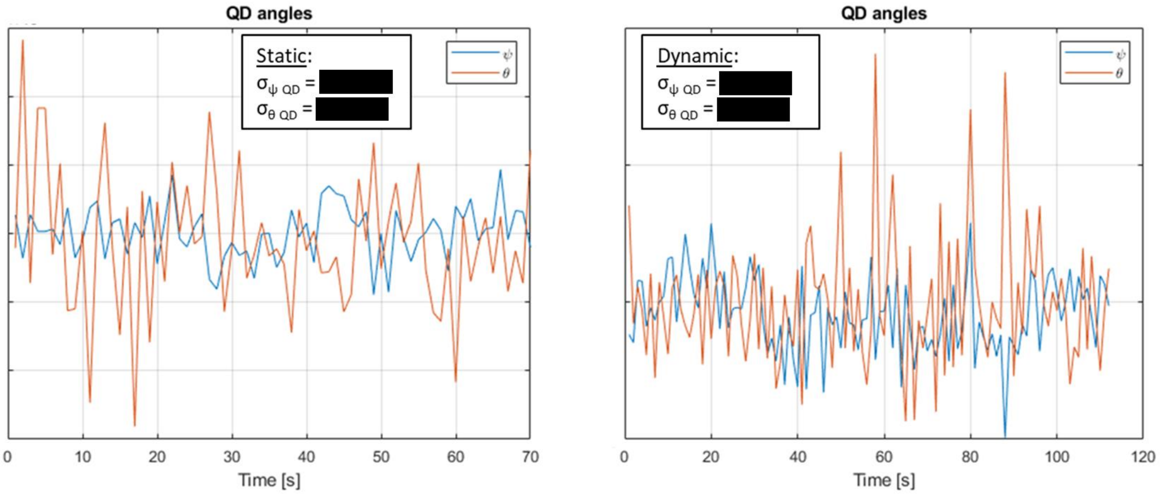

Figure 4-25. Left: example of pointing error during static tracking; right: example of pointing error during dynamic tracking. Values of the y-axis and tracking error standard deviations have been omitted for intellectual property reasons.

A second test campaign has been carried out with reduction of beacon sensor noise and tuning of parameters of the algorithms. These two adjustments have allowed to consistently improve the system's performance. Results show that tracking performance is partially compliant with requirements; however, results are not representative of the current system performance; full system compliance is expected with the optimization of control software implementation and further reduction of sensor noise.

4.5 LaserCube ISL telecom performance

A specific version of LaserCube, referred to as LaserCube ISL, has been designed by Stellar Project's team to perform inter-satellite communication (see Section 4.1). A test campaign has been carried out to assess LaserCube ISL's telecom performance. The candidate is the main contributor to the test plan definition; a consistent contribution has also been offered by the candidate to test completion and analysis of results. The description and results of the tests performed are presented in this Section. Please notice that results are in general not representative of the current system performance due to successive developments.

4.5.1 Bit sequence generation

A first test has been performed to verify the transmission of the correct bitrate. In particular, the frequency of the generated RF signal used for laser modulation should match the target Pseudo-Random Bit Sequence (PRBS) bitrate with a ±5% tolerance.

Test setup

Test setup consists in:

- ELU-ISL
- Oscilloscope

The ISL versione of the Telecom Management Unit (TMU) is used to generate a clock signal at modulation rate in the 5-200 MHz range and the consequent TLC TX RF modulation signal, which is analysed by means of an oscilloscope. Frequency of the TLC TX RF signal is measured and compared with target modulation frequency.

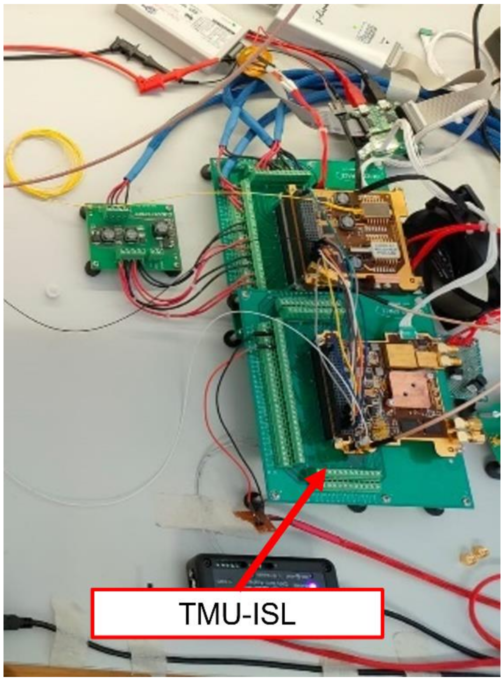

Figure 4-26: T-2.1 test setup: TMU ISL on test board.

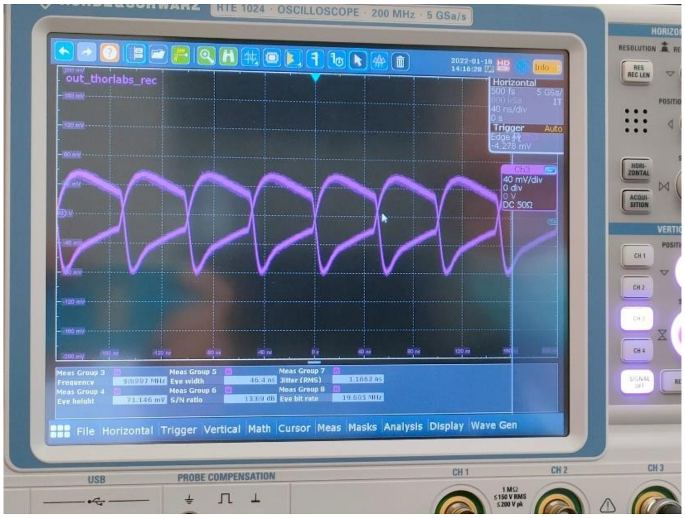

Figure 4-27: Example of eye-diagram measurement by means of oscilloscope acquired during test campaign.

<u>Test results</u>

Oscilloscope measurements at different modulation frequencies are shown in Figure 4-28. We can observe that the generated RF signal frequency is compliant with the target frequency. Results also show a SNR > 25 dB (2 V eye width, < 0.1 V noise floor) in all test cases, which translates into a theoretical BER < 10E-12. We can also observe that the clock peak-to-peak signal reaches its nominal value (2V) for all operational modulation frequencies (i.e. ≤ 100 MHz). The generated RF signal is then compliatn with requirements.

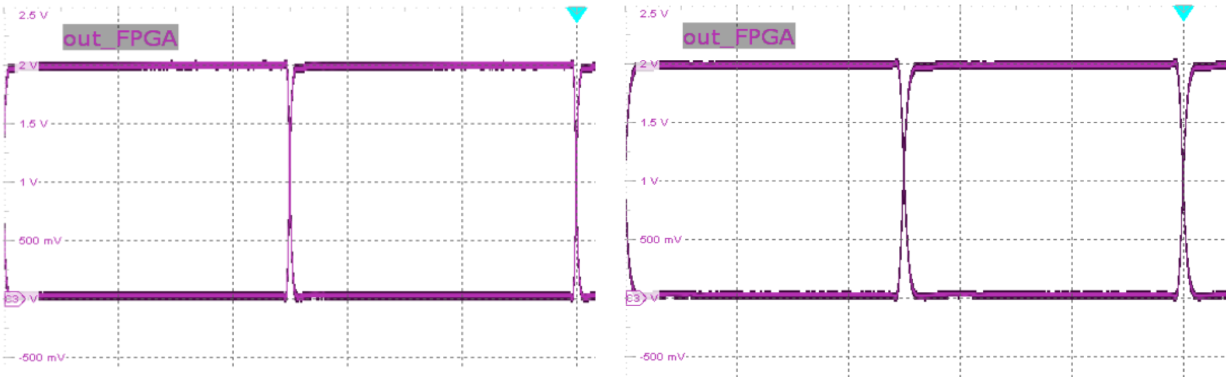

5 MHz, 40 ns time division

10 MHz, 20 ns time division

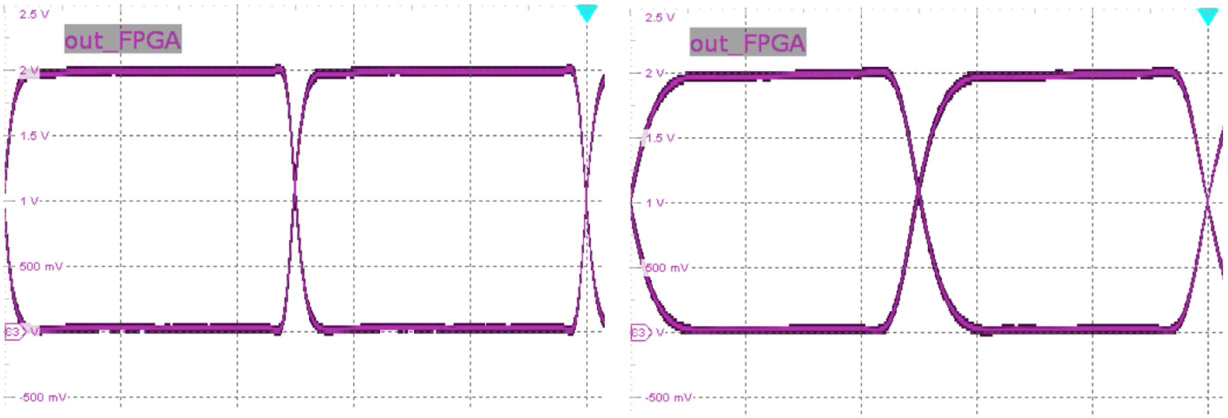

20 MHz, 10 ns time division

50 MHz, 4 ns time division

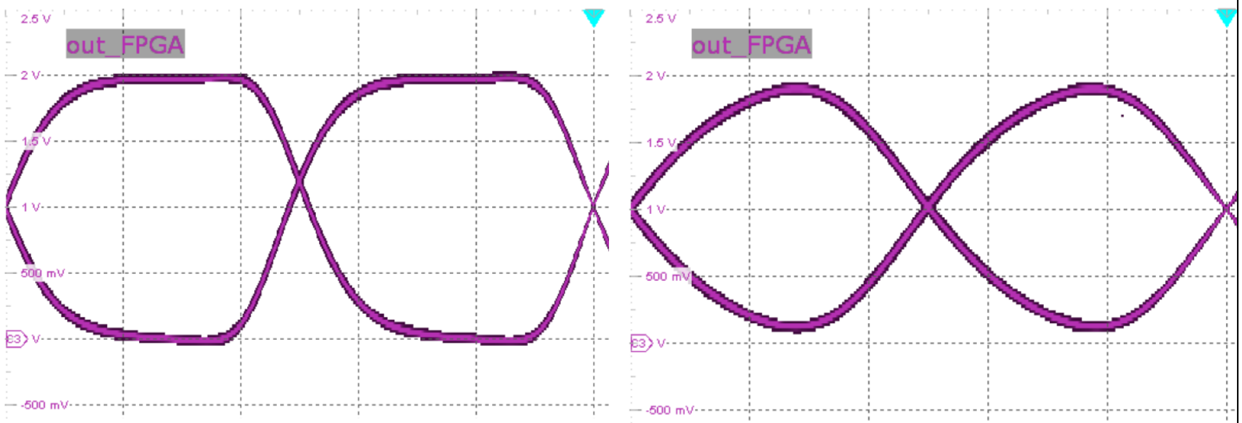

100 MHz, 2 ns time division

200 MHz, 1 ns time division

Figure 4-28: Eye-diagrams of RF square-wave clock signals acquired at different frequencies.

4.5.2 Optical signal modulation

A second test has been carried out to assess the compliance of the modulated optical signal. The goal of the test was to show a theoretical BER (from eye diagram) ≤ 10^{-6}.

Test setup

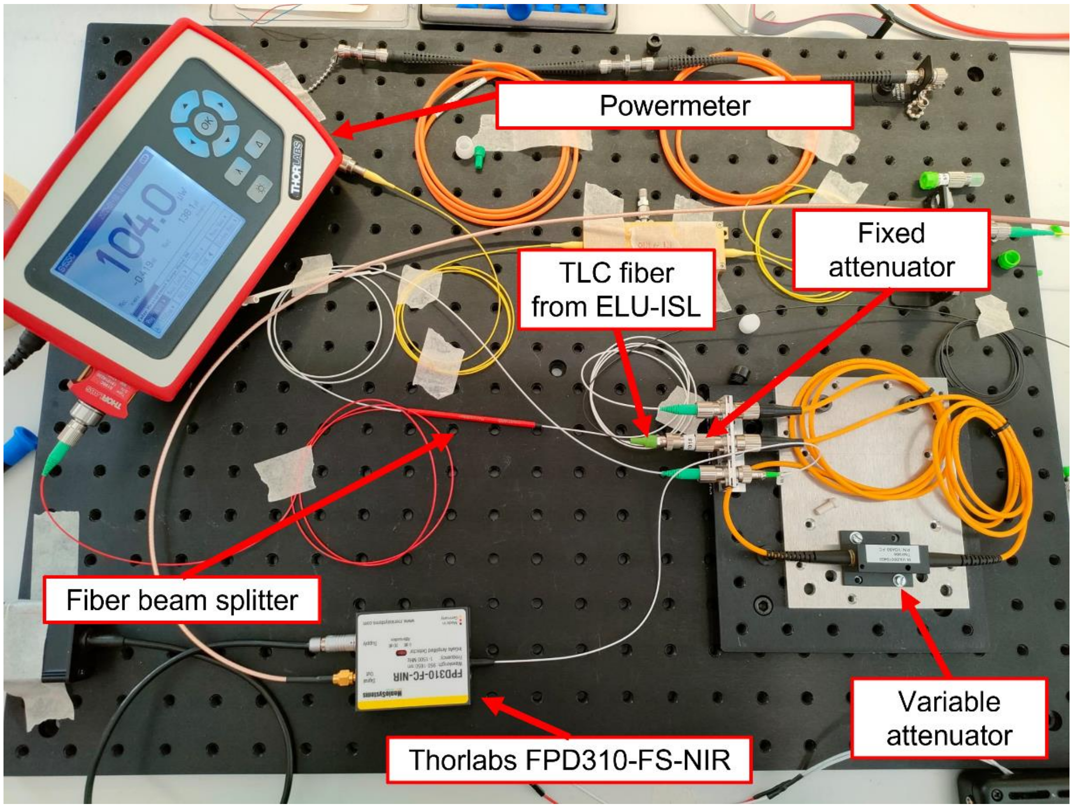

Figure 4-29: T-2.2 test setup: optical table.

Test setup consists in:

- ELU-ISL
- Fibre optical attenuators
- Photoreceiver (Thorlabs FPD310-FS-NIR, TMU breadboard)
- Oscilloscope

Test Procedure

The first part of the test consists in the measurement of the laser driving current generated by the laser Driver Unit (LDU). A square wave clock signal at different frequencies is generated by the TMU and is used by the LDU to generate the laser driving current. Please notice that a 1 MHz square wave signal corresponds to 2 bit switches in 1 µs, i.e. 2 Mbps bitrate.

The second part of the test consists in the measurement of the optical signal transmitted by the LDU-ISL modulated by means of the RF signal generated by the TMU-ISL. To perform the measurement, the output optical signal is attenuated and converted into an electrical signal by means of the commercial laboratory photoreceiver (Thorlabs FPD310-FS-NIR). The attenuation level was selected in order to send on the detector a power level that was well above the instrument sensitivity, in order to minimize effects due to noise of the detector itself. The converted electrical signal is measured with an oscilloscope and the resulting eye pattern is analysed to assess signal compliance. The same measurements have been repeated using the TMU breadboard instead of the commercial laboratory photoreceiver. The test has been performed at the nominal TMU modulation rates, namely 10-25-50-100 Mbps.

Test results

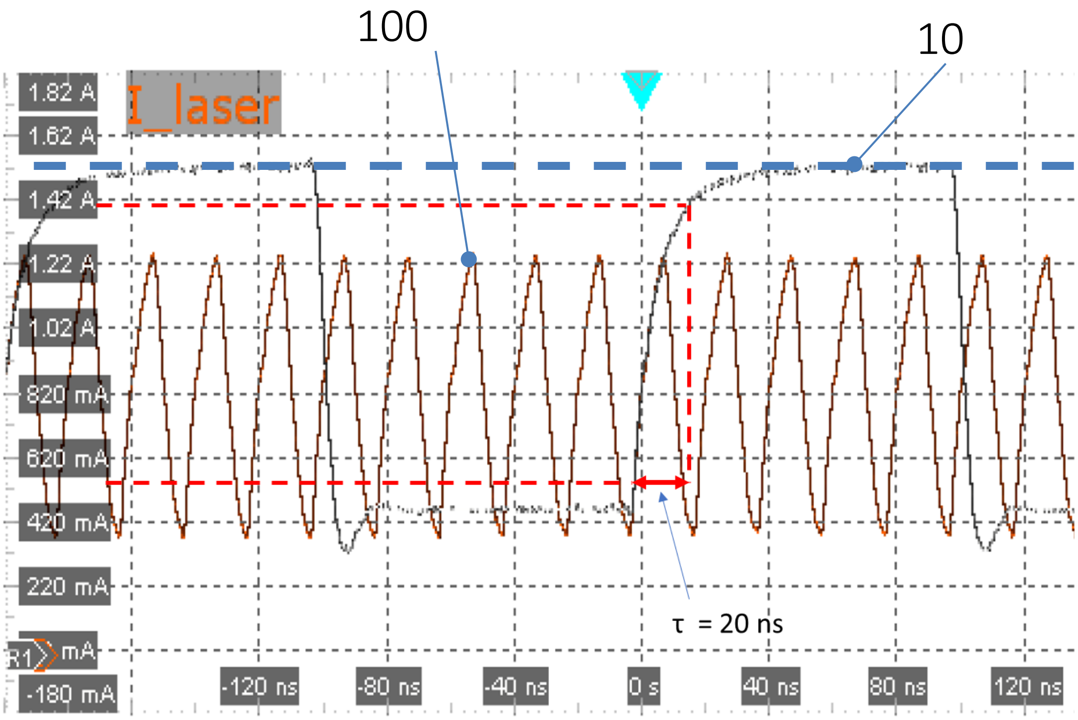

Figure 4-30: Laser driving current obtained with a 5 MHz (10 Mbps) and 50 MHz (100 Mbps) square wave modulating signal respectively. The 10%-90% rise time ($\boldsymbol{\tau = 20\,ns}$) is shown.

In Figure 4-30 the measurements performed during the first part of the test are presented. The results show that the laser driving current response can be modelled by a first order system with a time constant $\tau = 20\ ns$. This translates into a substantially reduced peak-to-peak response for modulation frequencies > 50 MHz. This attenuation may be attributed to the pins of the laser butterfly package.

The impact of this peak-to-peak attenuation of the laser driving current on the output optical signal has been investigated in the second part of the test, by measuring the modulated optical output at several modulation frequencies, namely 10 MHz, 25 MHz, 50 MHz, 100 MHz. Results are presented in Figure 4-31. A substantial decrease in peak-to-peak amplitude can be observed starting from the 50 MHz modulation acquisition. In Figure 4-33 the measured peak-to-peak loss as a function of modulation frequency has been superimposed to a second order low pass filter model with a 50 MHz cut-off frequency, showing good compatibility.

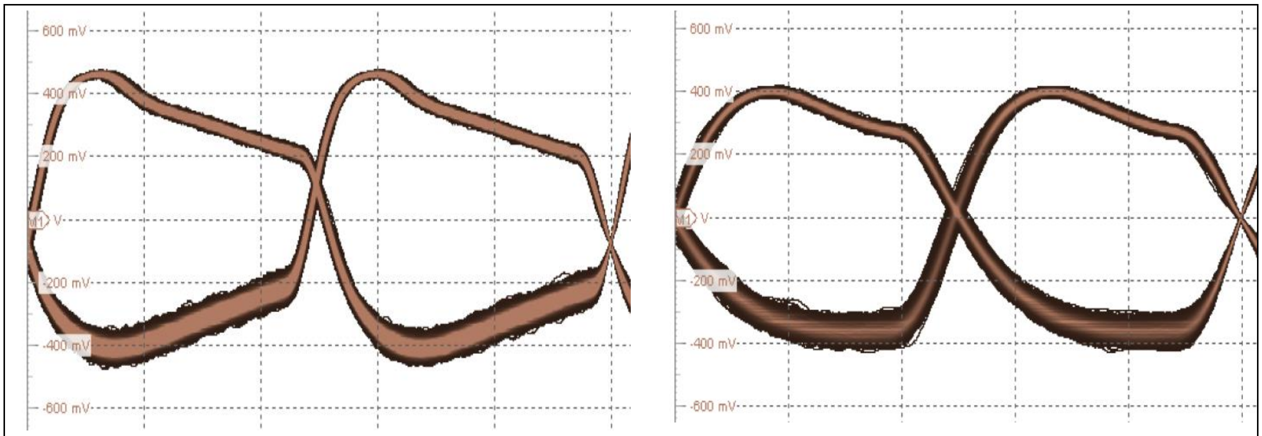

10 MHz (20 Mbps), 20 ns time division

20 MHz (40 Mbps), 10 ns time division

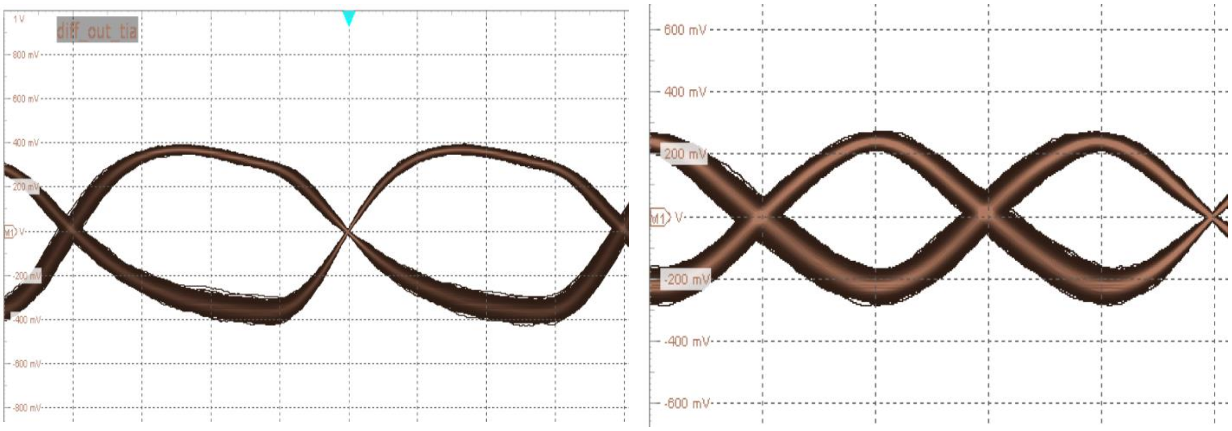

25 MHz (50 Mbps), 8 ns time division

50 MHz (100 Mbps), 4 ns time division

Figure 4-31: Acquired eye-diagrams at different modulation frequencies (TMU breadboard receiver).

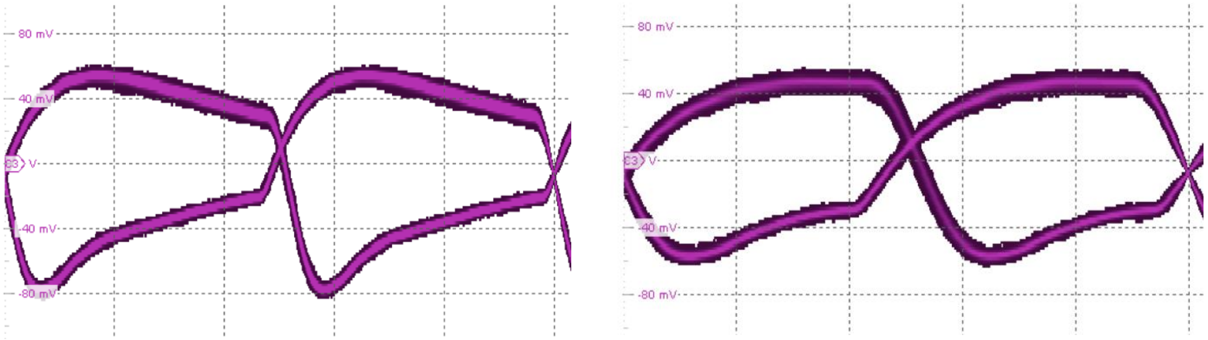

10 MHz (20 Mbps), 20 ns time division

20 MHz (40 Mbps), 10 ns time division

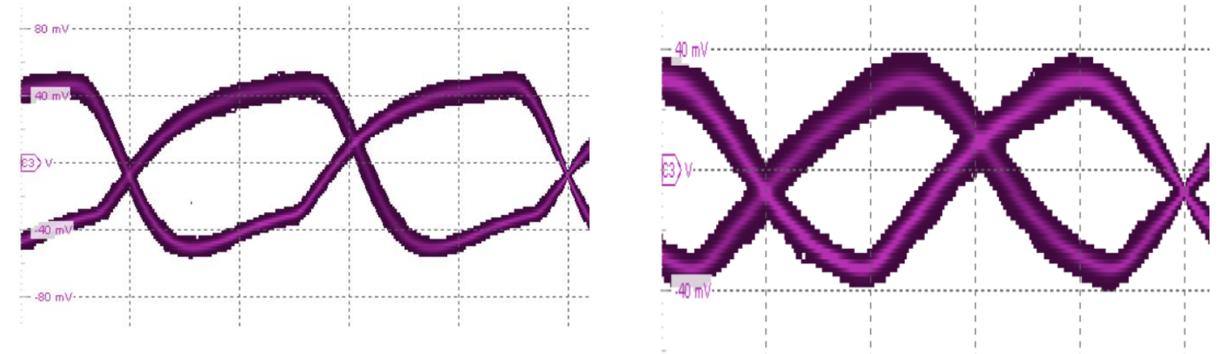

25 MHz (50 Mbps), 10 ns time division

50 MHz (100 Mbps), 5 ns time division

Figure 4-32: Acquired eye-diagrams at different modulation frequencies (Thorlabs receiver).

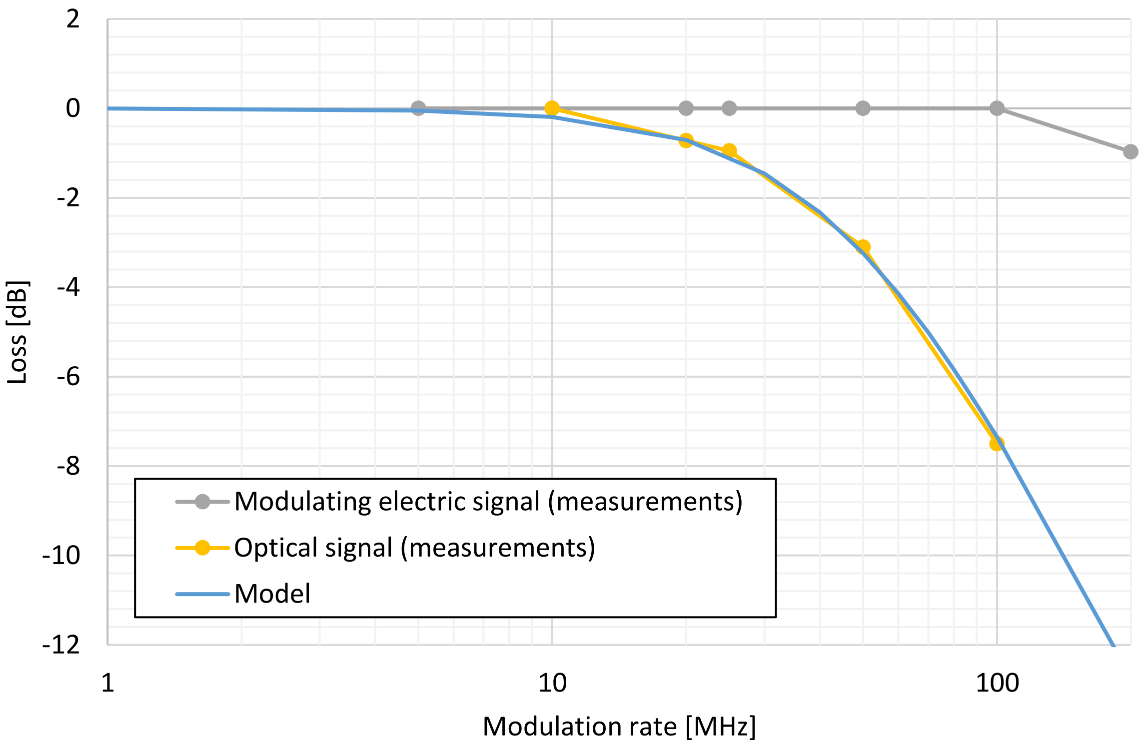

Figure 4-33: Laser modulation loss as a function of modulation rate, calculated as peak-to-peak attenuation with respect to 5 MHz case. Yellow line: measurements (average of the results obtained with the two detectors); blue: second order low-pass filter model, 50 MHz cut-off frequency.

SNR values have been measured for each modulation frequency, from which resulting theoretical BER values have been derived. Results show BER values ≤ 10^{-6} in all test cases. Detailed quantitative results have been omitted for intellectual property reasons.

4.5.3 End-to-end test

A final test campaign was carried out to assess the system end-to-end performance. The main goal of this test was to demonstrate that the system could achieve a BER ≤ 10^{-5} in operational conditions.

Test setup

Test setup consists in:

- TMU-ISL breadboard model
- LDU-ISL engineering model
- Fibre optical attenuators
- Oscilloscope

The test consists in an end-to-end transmission of a reference PRBS (Pseudo-Random Binary Sequence), representative of a typical transmitted/received bit sequence in nominal operations. The signal goes through the following steps: RF signal generation by the TMU, generation of modulated optical signal by the LDU, optical attenuation, detection and conversion to electrical signal by TMU breadboard receiver, demodulation by TMU. A direct measurement of the BER is performed. The test has been performed at 25-50-100 Mbps bitrates. The test has been performed at different received power values corresponding to operational conditions.

Test results

Two test campaigns were performed. Several acquisitions have been taken for each bitrate and power combination to optimize the bias voltage to be supplied to the receiver APD.
Quantitative results have been omitted for intellectual property reasons. Results of the first test campaign showed that a BER ≤ 10^{-5} could be obtained both at 50 and 100 Mbps. Nevertheless, the optical powers necessary to reach this performance were associated to expected link distances lower than requirement.
Two main factors have been identified as the cause of performance reduction with respect to the expected performance:

- As emerged from the results of test T-2.2, laser modulation electronics present a low pass filter behaviour which causes a reduction of peak-to-peak amplitude of the optical signal at increasing modulation frequencies.
- As the design link budget showed a safe link margin, the bandwidth of the receiver had not been limited to a 100 Mbps bitrate, to allow for the possibility of higher bitrate transmissions.

In order to improve the performance of the system, two possible solutions can then be adopted in parallel:

1. Substitute the laser with a component that allows for lower rise times, in order to eliminate the low pass filter behaviour observed during previous tests (see 4.5.2). This solution could not be adopted at that moment, as it implies consistent modifications of the system design, but can be considered for future improvements.
2. Limit the receiver bandwidth to reduce noise and reach a 100 Mbps optimized configuration.

Modifications to the receiver section have then been performed to implement solution n. 2, i.e., limit the bandwidth of the receiver to 100 MHz. Results of the second test campaign show a performance improvement due to the implementation of solution n. 2. In the final configuration (after modifications), a BER ≤ 10^{-5} can be obtained at target operational distances.

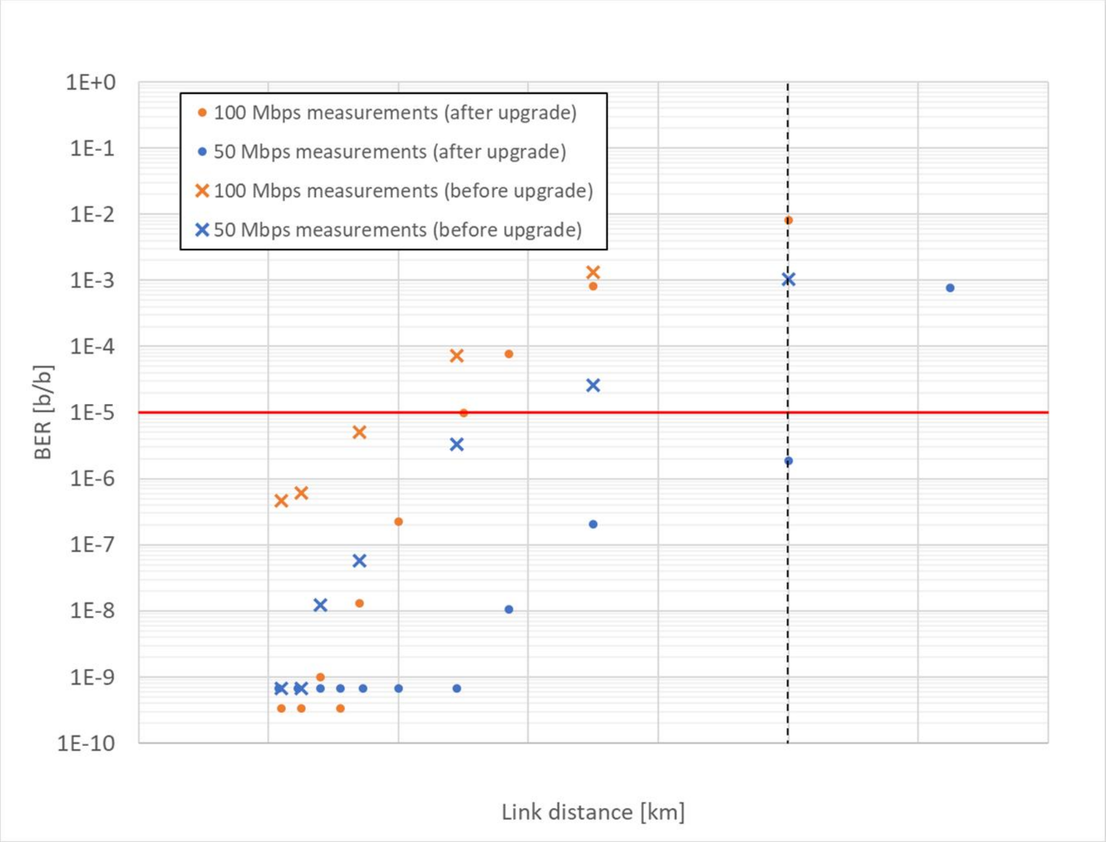

Figure 4-34: results obtained during first test campaign (before upgrade) and second test campaign (after upgrade). X-axis values have been omitted for intellectual property reasons.

5. GROUND SEGMENT DEVELOPMENT

The content of this section refers to the activities related to development of the optical ground segment. The design of the system has been guided primarily by the requirements dictated by LaserCube's IOD, consisting in the demonstration of the capability to transmit a telecom signal from LaserCube to the Optical Ground Station (OGS) of the Matera Laser Ranging Observatory (MLRO) during a passage of the satellite above the site.

During IOD operations LC-DL sends both a beacon and telecom beam. The beacon beam allows the ground station to detect the satellite's position and to have a reference for the compensation of the telescope's vibration. The telecom beam will carry the actual data to be transmitted from LC-DL to the OGS.

A beacon signal from the OGS is also needed for LC-DL to track the OGS position and transmit the telecom beacon in the correct direction. For these reasons the development of both a receiver section, a telecom transmitter section and beacon transmission section are required at the OGS.

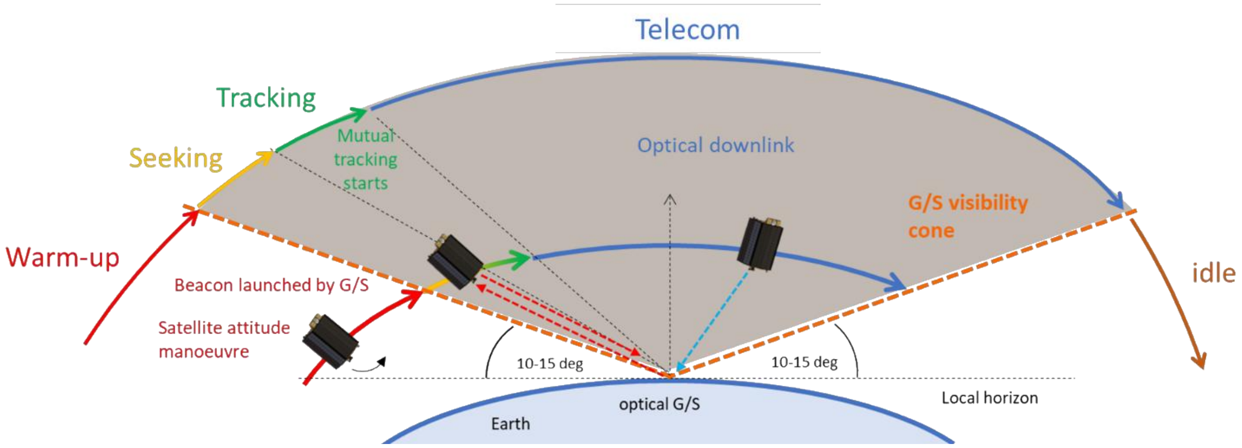

Figure 5-1: Schematic illustration of the planned IOD operations. In this document the design of the OGS development design is presented.

5.1 Functional architecture

Matera's facility is equipped with a 1.5 m telescope (Figure 5-2) with automatic pointing capabilities. The incoming beam is routed in the form of a collimated beam to an optical table in an underlying room by means of a coudé path (Figure 5-3). Due to the very high required beam diameter reduction factor (250), the deviation of the incoming beam with respect to the telescope optical axis is highly magnified. This requires the implementation of a Fine Pointing Assembly (FPA) to compensate for the telescope's vibrations due to the motors actuation during the tracking phase, in order to minimize beam coupling losses. The stabilized beam is then coupled with the Telecom Receiver (TLC-RX), which is composed of a photodetection stage (which translates the optical signal into an appropriate electrical signal) and the Transmitter-Receiver Electronic Unit (TREU) for analog signal demodulation and digital bitstream generation and storage. The output of the Telecom Transmitter (TLC-TX) follows the same path in the opposite direction.

A beacon transmission section has been developed to transmit a beacon to the satellite for tracking purposes. The optical beam generated by the Laser Source Unit (LSU) is transmitted to the Uplink Beacon Collimator (UBC) mounted externally on the telescope tube (Figure 5-2) via optical fiber. A Collimator Adjustable Mount (CAM) mechanically connects the UBC to the telescope interface plate in order to be able to precisely align the beacon optical axis with the telescope optical axis, to ensure that the transmitted beacon is actually illuminating the satellite when the received beacon is at the center of the telescope Field of View (FoV). The LSU activation is managed by a Laser Control Unit (LCU). A telecom transmission section has also been included.

A schematic representation of the system's functional layout is presented in Figure 5-4.

Figure 5-2: 1.5 m telescope at the Matera Laser Ranging Observatory (MLRO).

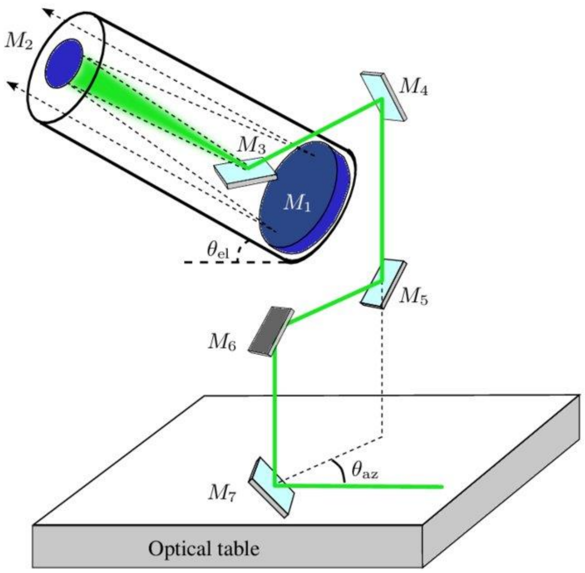

Figure 5-3: Representation of the optical path of the incoming beam, including the telescope tube path and the coudé path that routes the beam to the optical table in the underlying room.

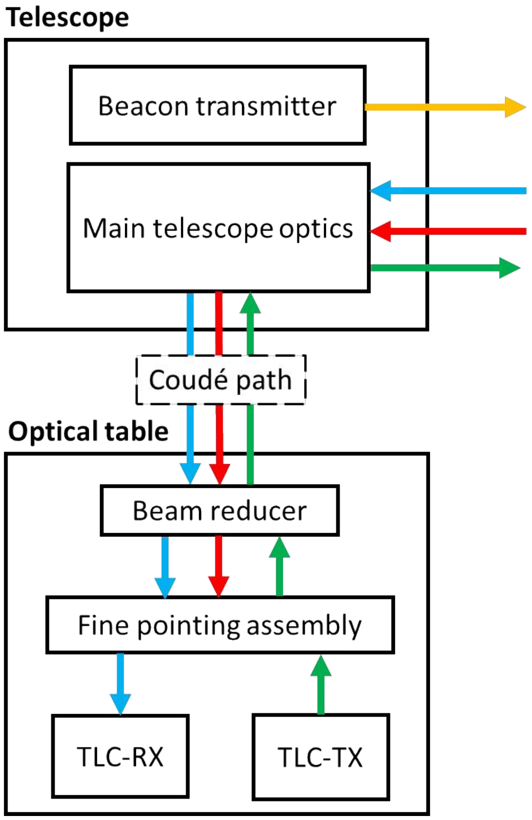

Figure 5-4: Block diagram of the system's functional layout. Yellow: transmitted beacon, blue: received telecom, red: received beacon, green: transmitted telecom.

5.2 System design description

In this section the detailed design of the developed systems is described. The specific contribution of the candidate to each work package of the design activities is made explicit at the beginning of each paragraph.

5.2.1 Optical bench layout

As briefly mentioned in Section 5.1, the optical bench is divided into a beam reduction stage, a FPA for beam stabilization, a TLC-RX section for telecom signal detection and demodulation, a TLC-TX section for telecom signal transmission and an auxiliary line for alignment purposes (Figure 5-5 and Figure 5-6). The overall system layout has been partially inherited from previous activities performed by researchers of the DEI's Quantum Future group at the University of Padua. The candidate has mainly contributed to the adaptation of the inherited optical table layout to specific requirements of the project, with the constant support of ASI researchers, eGeos personnel and Stellar Project's team. A specific contribution of the candidate consisted in the design activities related to the integration of the TLC-RX and TLC-TX sections and of the auxiliary alignment line with the rest of the system.

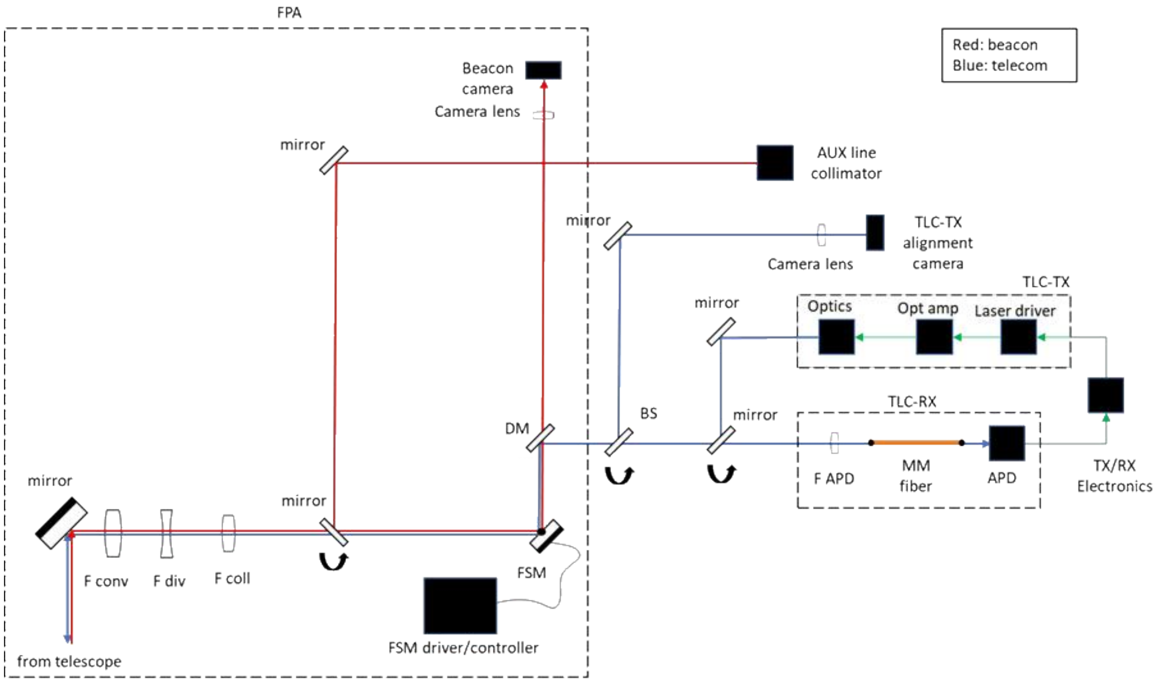

Figure 5-5: Schematic representation of the optical table layout. Red line is received beacon laser, blue one is telecom laser (transmitted and received).

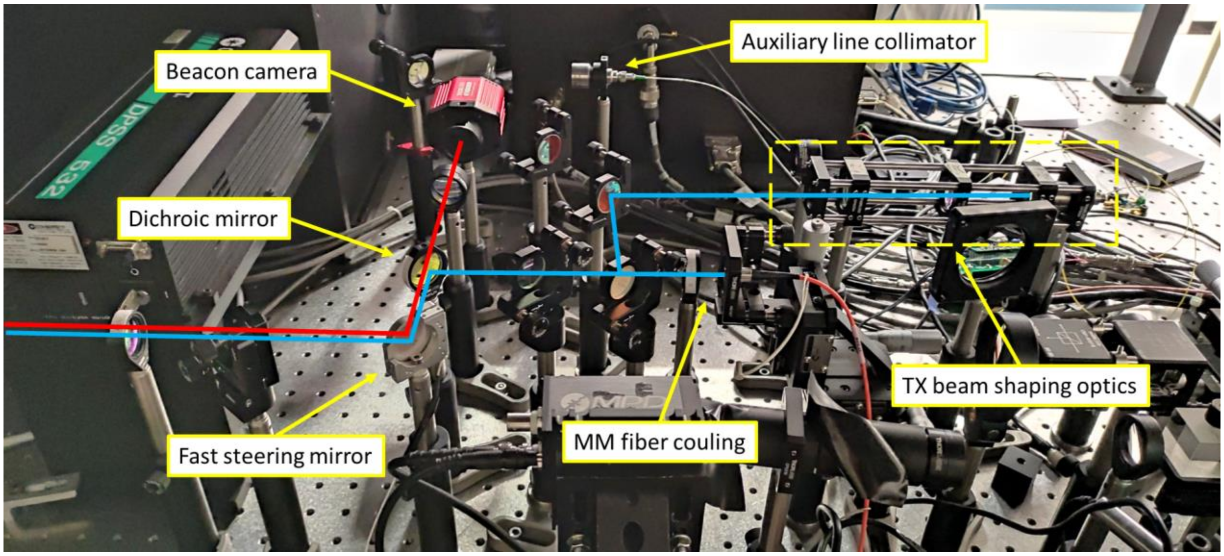

Figure 5-6: Main elements of the optical bench. Beacon light path (808 nm) is shown in red; RX and TX telecom ligh path (1550 nm) is shown in light blue.

5.2.2 Power budgets

A power budget analysis has been performed to select the appropriate components of the receiving section system, ensuring that the beacon and telecom power received at the telescope aperture are sufficient. The candidate is the main contributor to the power budget definition and assessment, with the constant support of ASI researchers, eGeos personnel and Stellar Project team. Previous experience at Matera telescope with a 532 nm beacon has shown that the required fine pointing stability can be obtained with a received power at the telescope aperture as low as 50 nW. Considering that the camera sensitivity at 808 nm is approximately 25% the sensitivity at 532 nm (see Figure 5-7), the requirement for the 808 nm is 200 nW. In Table 5-1 the power budget computed for the satellite at 15° elevation over horizon (1500 km distance) is presented, showing an optical power at telescope aperture > 300 nW. Notice that this is the worst expected condition in terms of received power. See Appendix A for link budget computation details. A Complementary Metal-Oxide Semiconductor (CMOS) camera compatible with these figures has been selected accordingly (see Section 5.2.3).

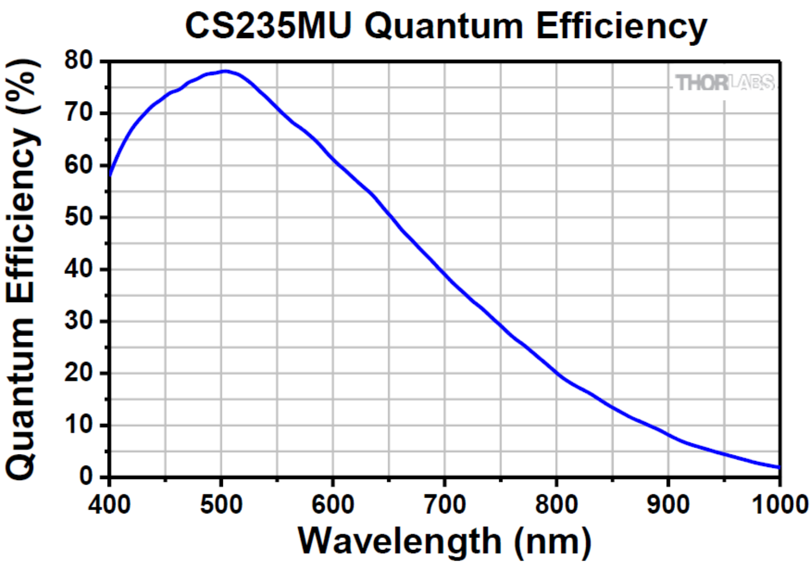

Figure 5-7: FPA camera sensitivity as a function of wavelength expressed in terms of quantum efficiency.

Table 5-1: Downlink beacon link budget relative to satellite 15° over horizon (worst condition).

	Description	Unit	Value
Physical constants	Boltzmann constant	J/K	1.38E-23
	Planck constant	J/Hz	6.63E-34
	Electron charge	C	1.60E-19
	Speed of light	m/s	3.00E+08
Space terminal	TLC transmitted optical power	W	2
	TLC transmitted optical power	dBm	33
	Wavelength	m	8.08E-07
	Optical frequency	Hz	3.71E+14
	Beamwidth	μrad	1000
	Solid angle	sr	7.9E-07
	Transmitter gain	dB	72.0
	Pointing accuracy	μrad	100
	Pointing loss	dB	-1.92
Free space propagation	Link distance	km	1500
	Spatial loss	dB	-267.4
	Atmospheric loss	dB	-5
	Space segment line losses	dB	-1
Ground receiver	Receiver aperture	m	1.5
	Receiver gain	dB	135.3
	Received optical power	dBm	-35
	Optical power at telescope aperture	W	3.2E-07

A similar link budget has been calculated for the received telecom signal, considering the receiver elements described in the following sections. The results of the link budget for a distance of 1500 km (worst case, 15° elevation) is summarized in Table 5-2 and shows a link margin of 4.2 dB. A link margin of 18.5 dB has been computed at 590 km distance (best case, 70° elevation).

Table 5-2: Downlink budget.

Description	Unit	Value
TLC transmitted optical power	W	0.1
Wavelength	m	1.55E-06
Beamwidth	µrad	100
Transmitter gain	dB	92
Pointing accuracy	µrad	10
Pointing loss	dB	-1.92
Link distance	km	1500
Spatial loss	dB	-262
Atmospheric loss	dB	-5
Space segment line losses	dB	-1
Receiver aperture	m	1.5
Receiver gain	dB	130
Received optical power	W	1.61E-06
Telescope line losses	dB	-3
Coupling losses	dB	-2
Optical power @ APD sensor	W	5.11E-07
Shot noise limited SNR	dB	33
Shot noise equivalent power @ APD	W	1.14E-08
APD overall sensitivity	V/W	4.50E+04
NEP density	W/Hz^0.5	1.1E-12
Bandwidth	Hz	1.00E+09
Detector dark current NEP	W	3.47851E-08
Load resistance	Ω	50
Temperature	°C	20
Receiver bandwidth	Hz	1E+09
RF amplifier gain	dB	20
RF amplifier noise figure	dB	5
Useful signal @ FPGA	mV	230
Shot noise signal @ FPGA	mV	5.2
Thermal noise signal @ FPGA	mV	0.5
Detector dark current signal @ FPGA	mV	15.7
Overall noise @ FPGA	mV	16.5
Amplified SNR	dB	22.9
Required SNR (BER = 10^{-5})	dB	18.7
Spectral efficiency	bps/Hz	1
Datarate @ BER = 10^{-5}	Mbps	1000
Link margin	dB	4.2

5.2.3 Beam reduction and Fine Pointing Assembly

The design of the beam reduction and FPA stages has been almost entirely inherited from a work carried out by DEI's researchers of the University of Padova. The candidate has specifically contributed to the optimization of the system for the requirements of the project and assessment of design compliance at system level. A picture with the main components of the FPA can be found in Figure 5-8. The FPA is preceded by a beam reduction stage, composed of three coated lenses that reduce the beams (beacon and telecom) from 50 mm at the input to 6 mm at the output. The 6 mm beams are then reflected on a Fast-Steering Mirror (FSM) (Smaract STT-25.4, Figure 5-9) which corrects the incoming beam deviation due to the telescope's vibrations. Both beams follow the same optical path until a Dichroic Mirror (DM), where the beacon beam is transmitted and focused on a CMOS camera (Thorlabs CS235MU, Figure 5-10) and the telecom beam is reflected towards the TLC-RX. The FSM is controlled in closed loop by means of the FSM driver, which commands the FSM actuation according to the position of the beacon spot position on the CMOS camera sensor. This design ensures that, once a preliminary alignment of the TLC-RX is performed correctly, while the control loop maintains the beacon spot at the center of the CMOS camera the telecom beam is coupled with the APD receiver. The main parameters of the FPA are presented in Table 5-3.

Preliminary tests performed at MLRO with a 200 mm lens focusing the beam on the camera sensor show a pointing error in far-field of 6 urad. Considering the beam reduction factor, this is equivalent to 1.5 mrad on the camera, which corresponds to about 50 pixels. This suggests that the camera resolution is not the limiting factor. If the 200 mm lens is substituted with a 125 mm lens, the pointing error of 6 urad in far-field would correspond to 30 pixels, meaning that pixel resolution remains far better than the overall system resolution. For this reason, no performance degradation is expected with the 125 mm. The use of a 125 mm lens allows to extend the far-field FoV in order to cover the maximum expected pointing error. Variation of the single pixel angular resolution across the camera FoV has been estimated to be < 1%; thus, it is considered negligible, also considering that single pixel resolution is not the limiting factor. The maximum travel of the FSM (+/- 2.5° mechanical, +/- 5° optical) translates into a far field range of +/- 350 µrad. This is well above the camera FoV both with 200 mm (+/- 70 µrad FoV) and 125 mm (+/- 110 µrad FoV) focal length.

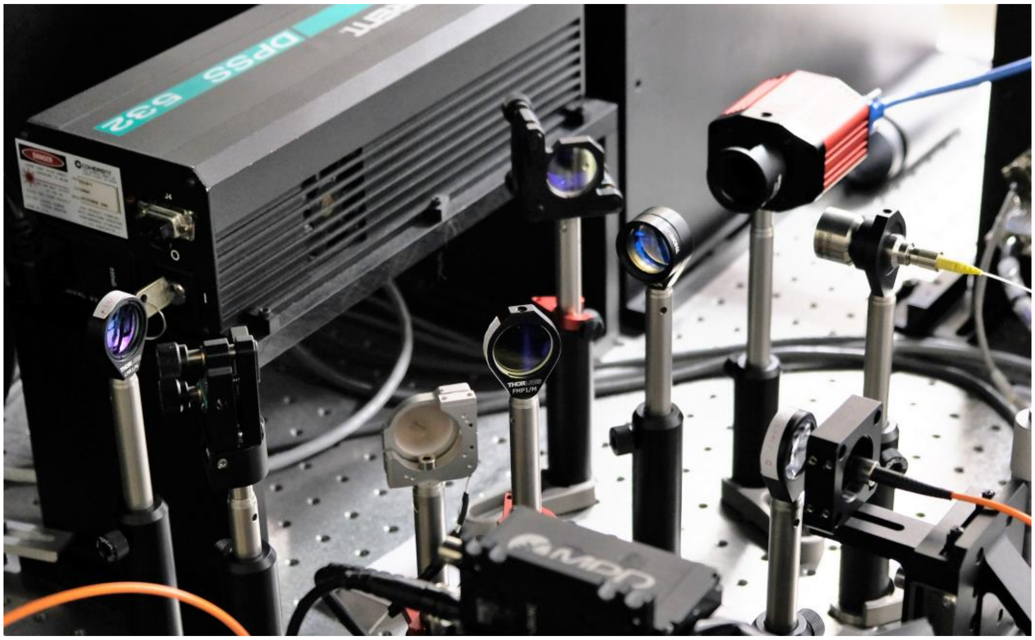

Figure 5-8: Fine pointing assembly optical elements placed on the optical table.

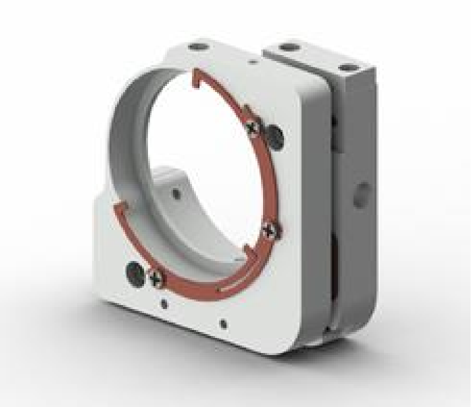

Figure 5-9: Smaract STT-25.4 FSM.

Figure 5-10: Thorlabs CS235MU CMOS camera.

Table 5-3: Main specifications of the FPA components.

FPA input beam diameter [mm]	50
FPA input beam convergence [mrad]	7
F conv focal length [mm]	500
F div focal length [mm]	-150
F coll focal length [mm]	200
Dichroic mirror cutoff [nm]	1000
F camera focal length [mm]	125-200
CMOS camera pixel size [µm]	4.8 x 4.8
Camera angular resolution in far-field [µrad]	0.12 with 200 mm lens 0.19 with 125 mm lens
Variation of resolution across FoV [%]	<1
CMOS minimum required power [nW]	~10
FPA output beam diameter [mm]	6
FPA output beam divergence [mrad]	≤ 1
Output beam deviation std [mrad]	1.5

5.2.4 Telecom receiver

The candidate is the main contributor to the design definition of the telecom receiver, with the constant support of ASI researchers, eGeos personnel and Stellar Project team. Optical analysis based on numerical simulators is a contribution of Stellar Project team and has not been directly performed by the candidate. A dedicated modulation/demodulation and telecom analysis electronics has been provided by a third-party supplier. A schematic drawing and picture of the telecom receiver can be found in Figure 5-5 and Figure 5-6 respectively.

Fiber Coupling

The nominal layout of the system requires the injection of the received telecom signal into a multimode fiber: this can be achieved by placing a focusing lens right before a multimode fiber tip to focus the beam with the smallest spot possible with respect to the core diameter, compatibly with the fiber numerical aperture.

The optical layout of the beam reducer and focusing lens is shown in Figure 5-11:

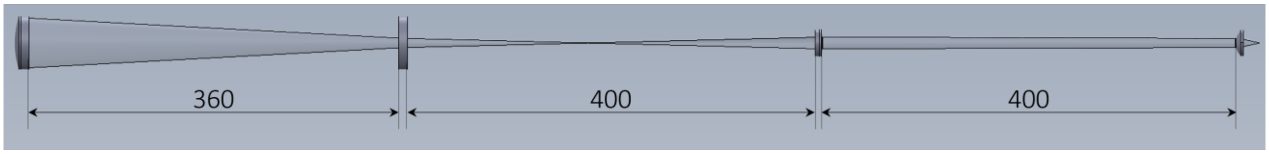

Figure 5-11: Optical layout of the beam reducer followed by a 20 mm focal length aspheric lens (Thorlabs AL2520).

The optical alignment of the system has been performed by observing a bright star (e.g. Vega, Sirius) with the MLRO telescope. Due to the stars' typical emission spectrum, the light component around 1550 nm is too weak to be used as a reference for the alignment. Moreover, the telescope mirrors coating will mainly reflect a relatively narrow band of the incoming light centered around 532 nm. For this reason, an optical analysis using Zemax has been performed to assess that the system performance at 1550 nm is adequate even though a 532 nm source is used for the alignment.

Figure 5-12 shows the spot diagram of the 532 nm beam after optimizing distances between elements. In Figure 5-13 the spot diagram of the 1550 nm beam with the lenses and fiber position optimized for a 532 beam is shown. From this configuration, fiber position can be slightly modified to minimize spot diameter at 1550 nm (see Figure 5-14). In Table 5-4 the results of this analysis are summarized.

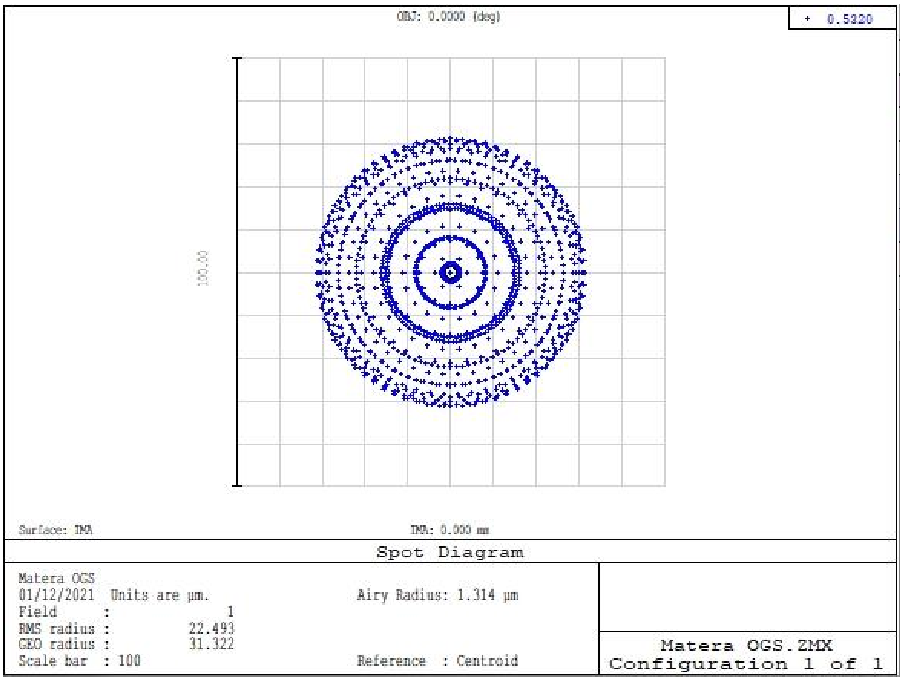

```
Matera OGS
01/12/2021  Units are µm.                     Airy Radius: 1.314 µm
Field      :             1
RMS radius :        22.493
GEO radius :        31.322                                              Matera OGS.ZMX
Scale bar  : 100                              Reference  : Centroid   Configuration 1 of 1
```

Figure 5-12: Spot diagram of a 532 nm beam passing through the layout presented.

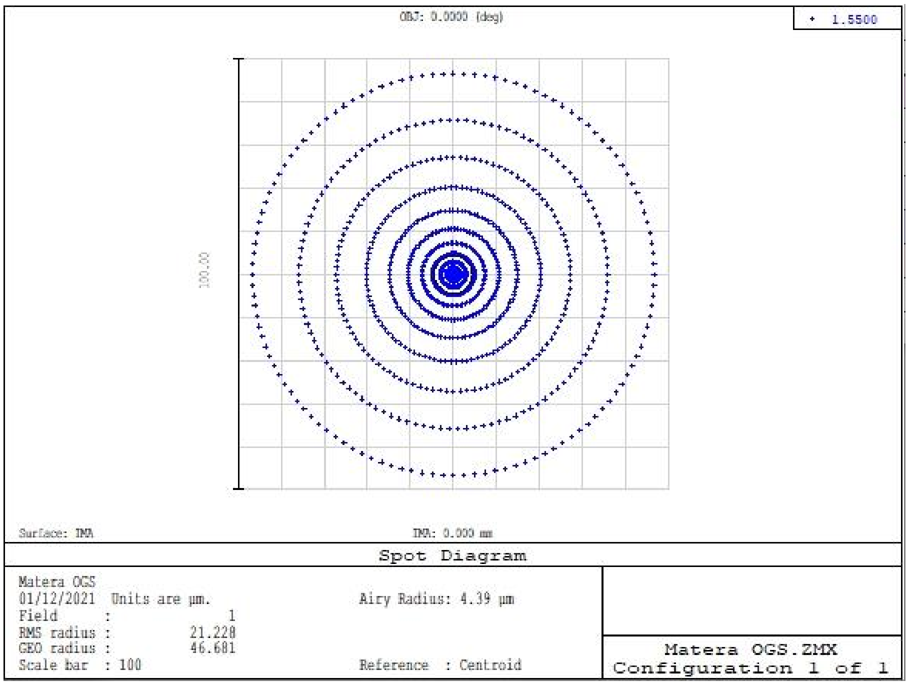

```
Matera OGS
01/12/2021  Units are µm.                     Airy Radius: 4.39 µm
Field      :             1
RMS radius :        21.228
GEO radius :        46.681                                              Matera OGS.ZMX
Scale bar  : 100                              Reference  : Centroid   Configuration 1 of 1
```

Figure 5-13: Spot diagram of a 1550 nm beam passing through the layout presented.

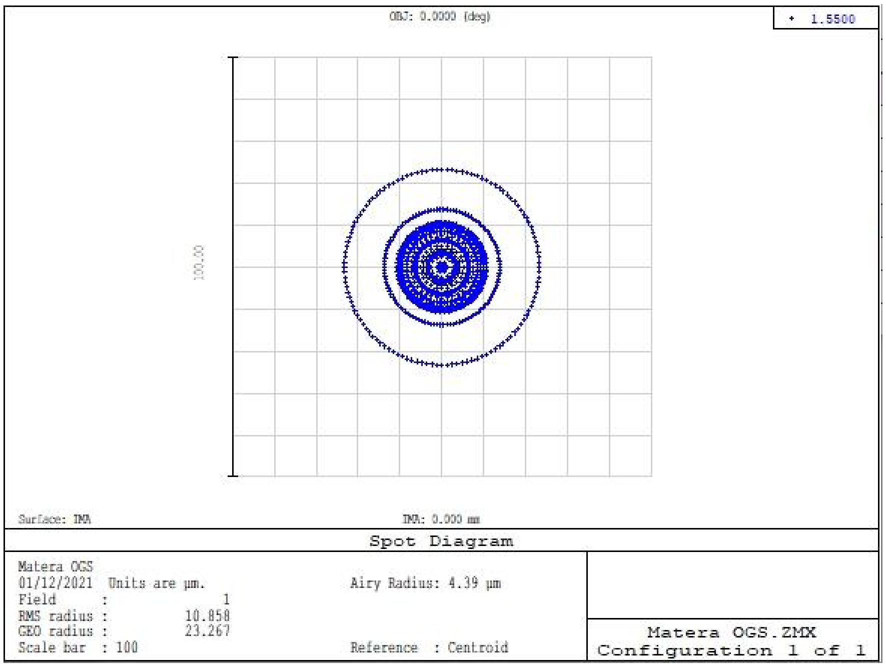

Figure 5-14: Spot diagram of a 1550 nm beam passing through the layout presented after adjusting fiber position.

Table 5-4: Spot sizes at different wavelengths/ fiber positions.

Case	Wavelength [nm]	Fiber distance from focusing lens [mm]	RMS diameter [µm]	86 % power diameter [µm]
1	532	15.62 (532 nm optimized)	44.98	36.64
2	1550	15.62 (532 nm optimized)	42.46	60.20
3	1550	15.73 (1550 nm optimized)	21.36	22.20

The analysis shows that a minimum fiber diameter of 50 µm should be selected in all cases. A slight increase in the 86% encircled power diameter is present in case 2 with respect to case 1. The selection of the multimode fiber diameter is ultimately driven by a tradeoff analysis between coupling efficiency at the fiber input (higher diameter is preferred) and coupling efficiency at the APD detector (lower diameter is preferred). See Paragraph 5.3.4 for fiber coupling verification.

APD receiver

The incoming beam from the FPA is coupled into a multimode fiber by means of a focusing lens (see Figure 5-15). The optical signal is then routed to an optical assembly (Figure 5-16) that focuses the beam on the free-space window of the selected APD receiver (Thorlabs APD450C, Figure 5-17). The window is provided with a 1.5 mm ball lens. The APD converts the incoming optical power into an electrical signal.

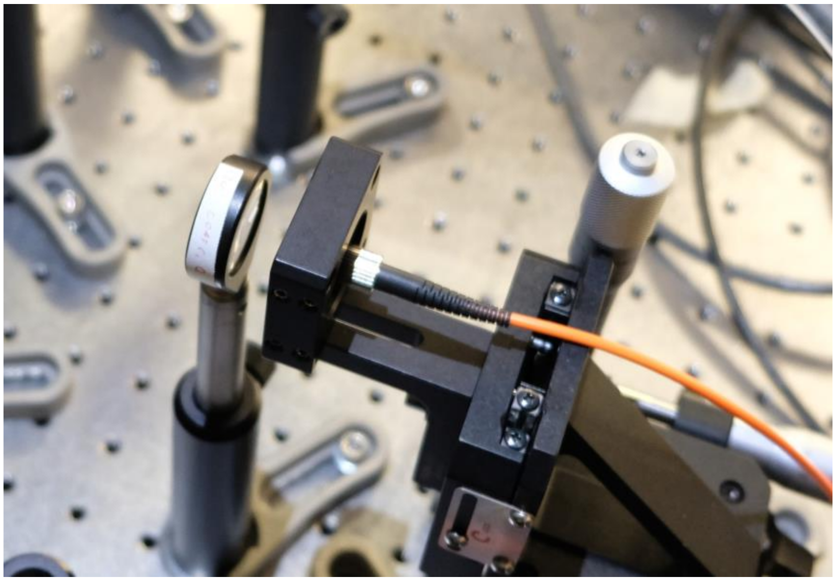

Figure 5-15: MM fiber coupling elements.

Figure 5-16: MM fiber coupled to optical assembly that focuses the received light into APD receiver sensor.

Figure 5-17: Thorlabs APD450C APD receiver.

An electrical amplification stage (Minicircuits ZFL-2000+, Figure 5-18) can be used optionally to amplify the APD output to reach the voltage level required by the Ground Station Transmitter-Receiver Electronic Unit.

Figure 5-18: Minicircuits ZFL-2000+ electrical amplifier.

Table 5-5: main specifics of APD receiver from datasheet.

F APD focal length [mm]	20
APD wavelength range [nm]	1260 - 1620
APD sensitivity [V/W]	$4.5 \cdot 10^4$
APD bandwidth [MHz]	0.3 - 1600
Electrical amplifier gain	20 dB

Ground Station Transmitter-Receiver Electronic Unit

A dedicated electronic component (from now on: TX/RX electronics) has been designed and developed by a third-party supplier for the demodulation of the received optical signal and the generation of the modulated RF signal for the transmitter laser driver (see Paragraph 5.2.5). The candidate has contributed to the assessment of interface requirements between the electronic component and the rest of the system.

The design of the TX/RX electronics has been performed to be able to receive the modulated analogue signal at different bit rates (the same ones that can be set on LaserCube DL) and to store the demodulated signal to making it available for post processing activities and analysis. Moreover, the transmitting section can deliver a modulated signal to a laser driver for a ground-to-space telecom transmission. The following block diagram shows the signal flow between the optical bench components and the TX/RX electronics. When the telecom operations are completed, the stored data is sent to an external PC (for example to a laptop locally or remotely connected) for data analysis and BER statistics.

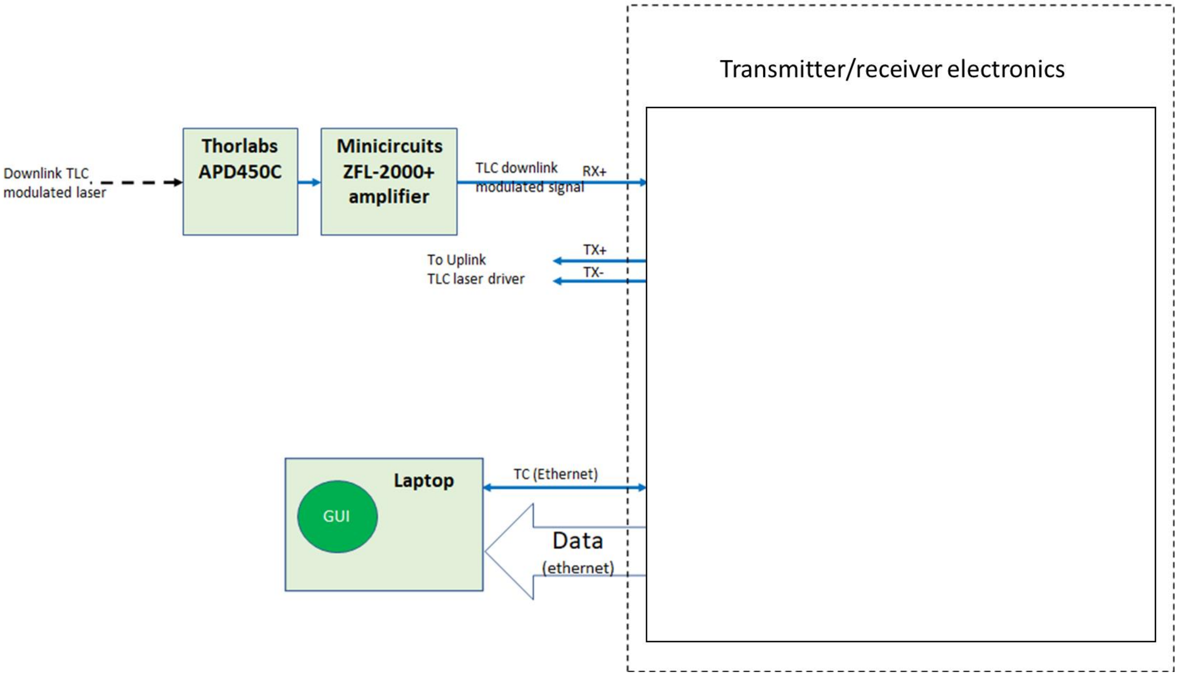

Figure 5-19: OGS transceiver electronics architecture and data flux.

5.2.5 Telecom transmission

The instrumentation installed at the MLRO focal plane assembly has been augmented with the addition of an uplink telecom transmission subsystem (TLC-TX). The subsystem is composed by:

- The TX section of the transceiver electronic unit developed within this activity
- A unit comprising a seed laser and its driver unit, which receives as input modulation signals from the transceiver electronic unit in order to impose OOK modulation to the seed laser by current modulation, with bitrates ranging from 25 to 100 Mbps. The laser wavelength is 1550 nm.
- An optical amplifier unit to increase the optical output power to 10-20 W.
- An optical system used to shape the transmit beam.
- A 1550 nm TLC-TX camera for alignment purposes.

The candidate is the main contributor to the TLC-TX optics design and optical alignment procedure definition, with the constant support of ASI researchers, eGeos personnel and Stellar Project team. The candidate has also supported the assessment of subsystem compliance with system requirements and the selection of the laser source and driver unit. A detail of the optical bench elements showing the TLC-TX subsystem can be seen in Figure 5-20 (the TLC-TX camera had not been installed yet when the picture was taken).

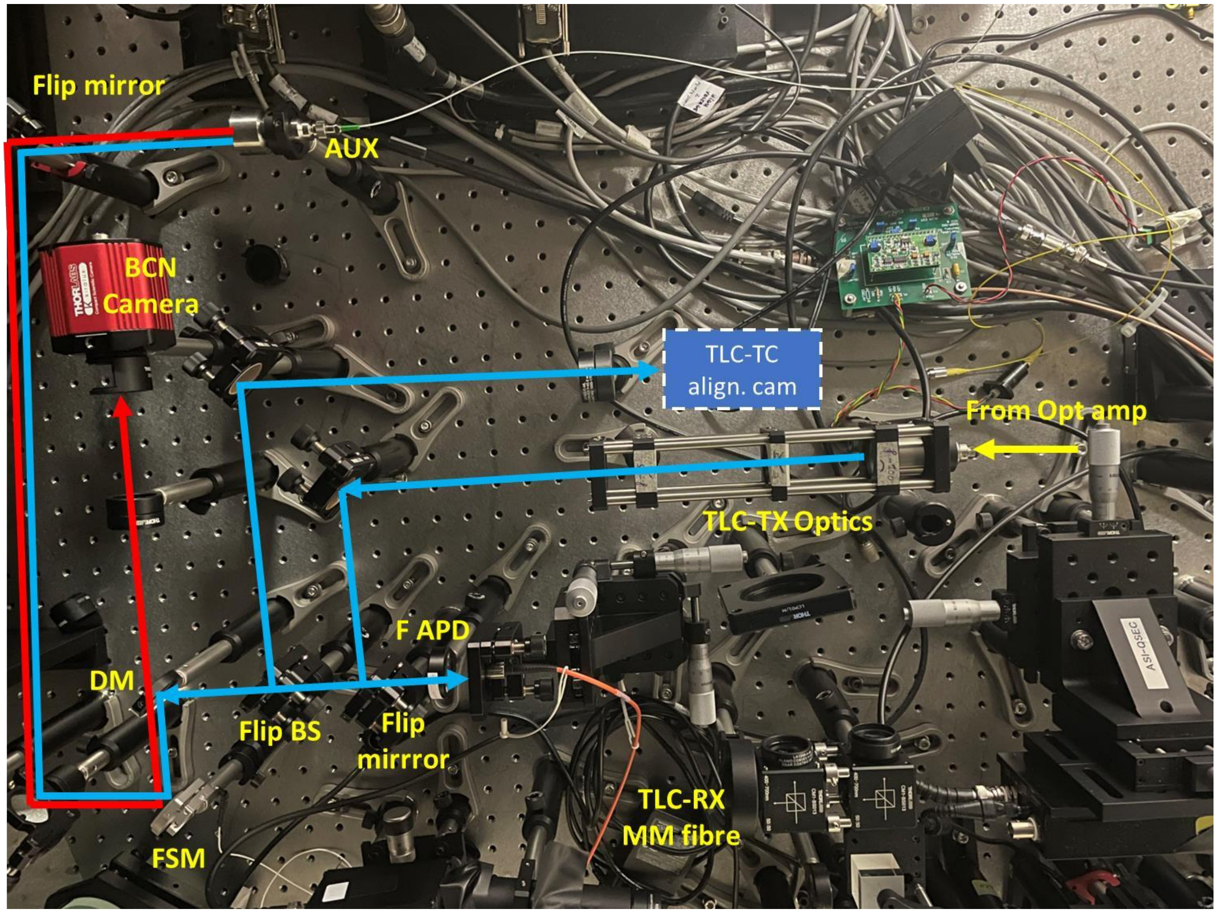

Figure 5-20: FPA with the addition of the TLC-TX optical section.

The selected laser driver unit is a 100 mW Aerodiode laser source with integrated driver (Figure 5-21). This unit can deliver a 1550 nm, 100 mW modulated signal at 100 MHz. The unit has a SMA input that received modulation RF signals from the transceiver unit, compatible with both Low-Voltage Transistor-Transistor Logic (LVTTL) and Transistor-Transistor Logic (TTL) (2.2V to 5V) signals. The driver is driven by the Transceiver Unit (see Section 5.2.4) which delivers a LVTTL modulation signal.

Figure 5-21: Aerodiode 100 mW laser source with integrated driver.

5.2.6 Beacon transmission

The design of the beacon transmitter section is reported in this section. The candidate has consistently contributed to the design at system level and the assessment of subsystem compliance with system and mission requirements. The candidate has also had a primary role in the completion and supervision of the hardware installation activities, with the constant support of ASI researchers, eGeos personnel and Stellar Project team.

Uplink error budget

A link budget analysis has been performed to select the correct combination of uplink beacon power and beam divergence, ensuring compatibility between the power received at LC-DL aperture and the sensitivity of the Quadrant Detector (QD) on board LC-DL. First, a beam full divergence of 200 µrad has been selected to safely cover the uncertainty cone related to the uncertainty in the orbital position of the satellite. The main results of the analysis have been obtained assuming the selected beamwidth and an orbit altitude of 550 km and are presented in Figure 5-22 and Table 5-6. They show that a minimum received power of 0.5 µW can be obtained for a 3 minutes time interval during a passage with a 50 W beacon power. In order to guarantee a better link margin and to make up for potential increase in atmospheric losses due to weather conditions, a laser with the capability to generate a power of up to 100 W has been selected.

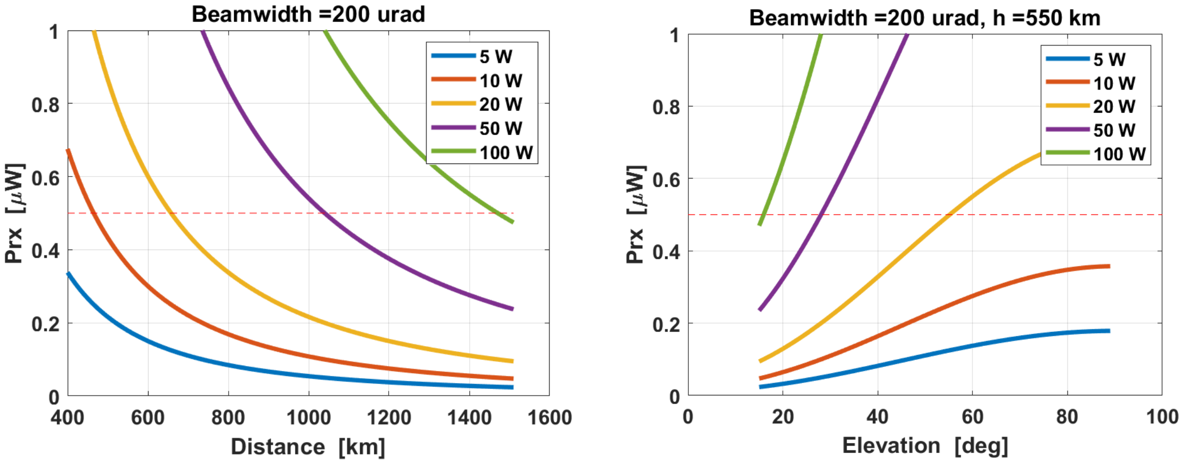

Figure 5-22: Received power at LC-DL QD as a function of distance from OGS and elevation above OGS local horizon, parametric with respect to transmitted optical power.

Table 5-6: Duration of link availability depending on transmitted optical power (50 W, 100 W) and minimum required power at LC-DL QD (0.5 µW, 1 µW) for 90° and 45° maximum elevation during pass over the OGS. In case of 45°, the elevation between brackets is the elevation at which the required optical power is received.

	90° elevation		45° elevation	
RX power	BCN 50 W	BCN 100 W	BCN 50 W	BCN 100 W
0.5 uW	192 s	324 s	202 s (28°)	354 s (16 °)
1 uW	84 s	192 s	0 s (46°)	202 s (28°)

A detailed pointing error budget analysis for the uplink beacon during LaserCube IOD has been performed. Details of the analysis can be found in Section 6.2.

LSU

The LSU (BKtel THFL-1040, Figure 5-23) is dedicated to the generation of the required optical power derived from the link budget design. The main specifications of the LSU are presented in Table 5-7. The 6 mm output armored fiber cable is directly connected to the UBC, which is fixed to the telescope tube by means of a dedicated support. The fiber support is fixed to the telescope by means of a rotary junction (Figure 5-25), to be compliant with the telescope elevation movement. The LSU is provided with an interlock connector that allows to remotely switch off the laser for safety reasons.

Figure 5-23: BKtel THFL2-1040 laser source.

T**able 5-7.** The main specifications of the LSU.

Wavelength [nm]	1040
Output Power [W]	100
Output power tunability [%]	1 - 100
Beam diameter @ output [mm]	10
Beam full divergence [μrad]	< 200
Auxiliary beam: wavelength [nm]	650
Auxiliary beam: power [mW]	> 10
Output fiber	6 mm armored cable, 3 meters
Dimensions	3U 19”

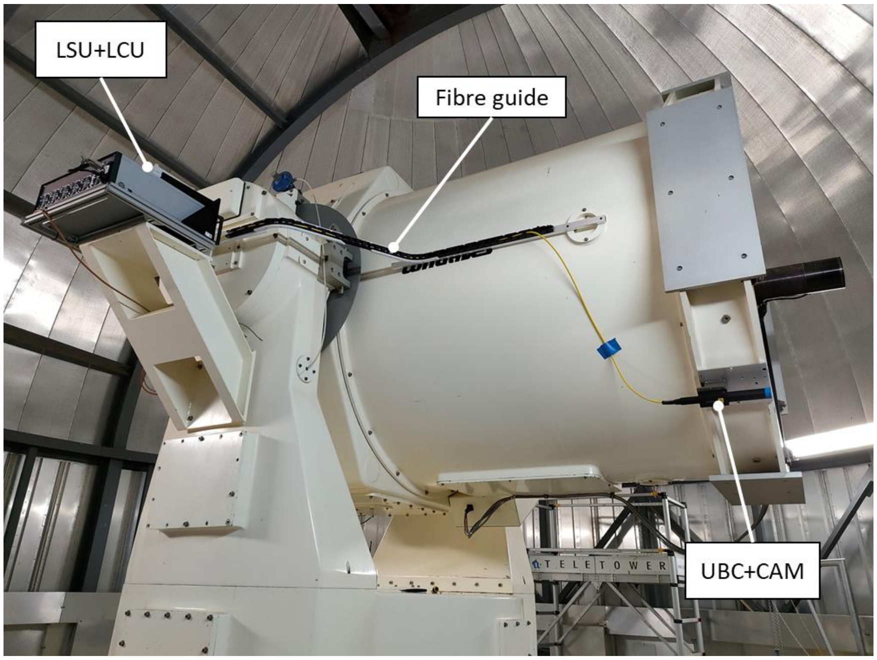

Figure 5-24: Fiber guide fixed to the telescope tube.

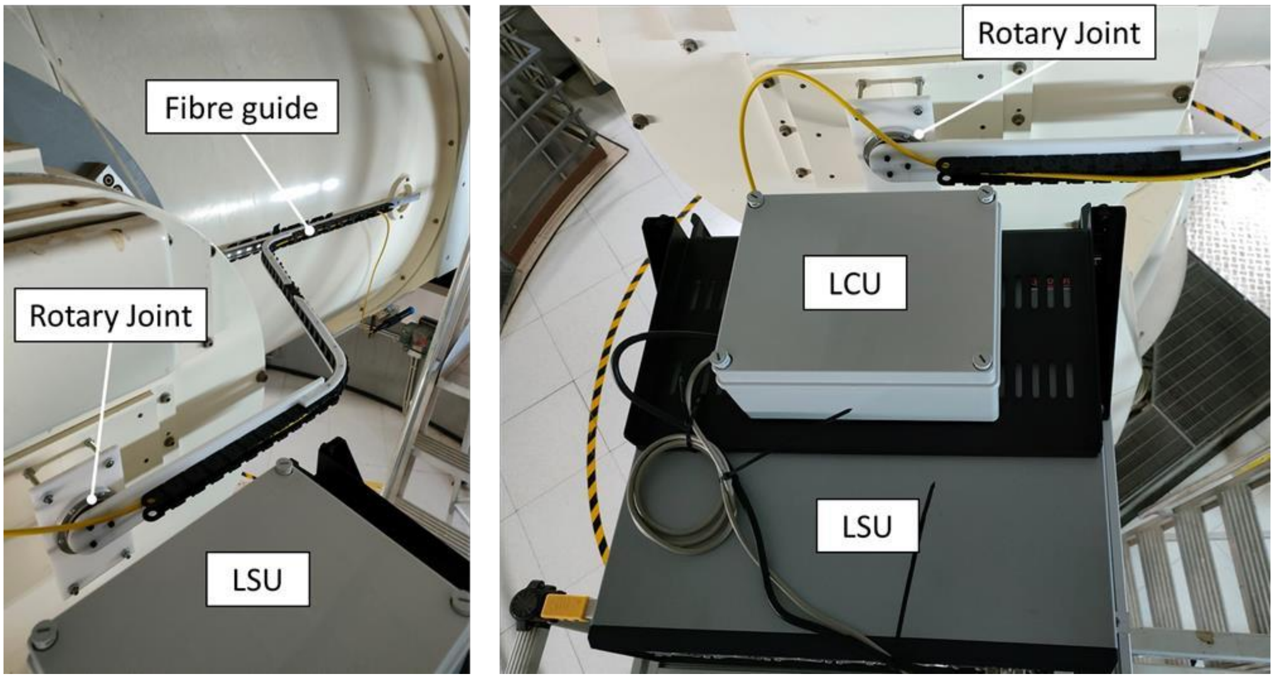

Figure 5-25: Rotary joint for fiber guide compliance with telescope movements.

UBC

The UBC collimates the laser beam generated by the LSU. The collimated beam has a diameter at the output of 10 mm and a nominal beam divergence <200 µrad, as required by the beacon link budget design. The UBC mounted on the telescope tube by means of the CAM is shown in Figure 5-26.

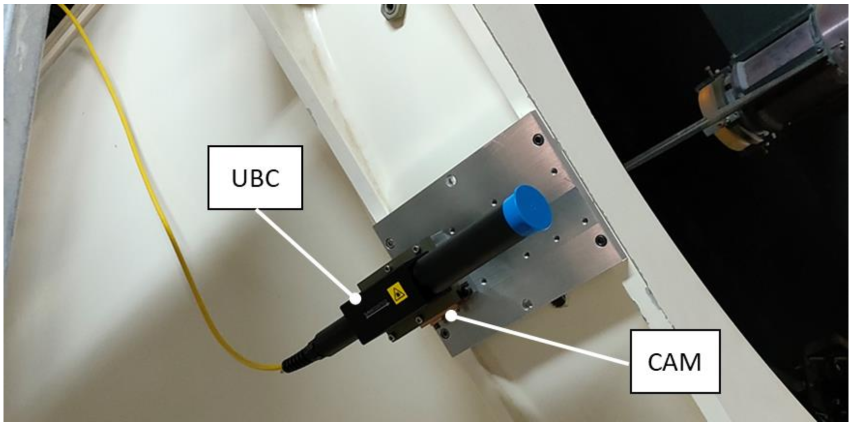

Figure 5-26: UBC mounted on the the telescope by means of the CAM.

CAM

The CAM (Figure 5-27) serves as mechanical interface between the UBC and the telescope tube, also allowing to finely adjust the UBC orientation for precise alignment of the beacon axis with the telescope optical axis. It is composed of Newport 9063-PY-MTilt/Rotation platform and of custom designed aluminum plates for mechanical interface with UBC. The CAM orientation with respect to the telescope can be adjusted by means of adjustment screws and fixed by means of locking screws. The main specifications of the CAM are presented in Table 5-8. The CAM is attached to the telescope tube through one aluminium plate directly fixed to the tube structure, as shown in Figure 5-28 and Figure 5-29.

Figure 5-27: Newport 9063-PY-M Tilt/Rotation platform.

Table 5-8: CAM main specifications.

Tip and rotation range [°]	±2
Sensitivity [µrad]	< 20
Load capacity [N]	50

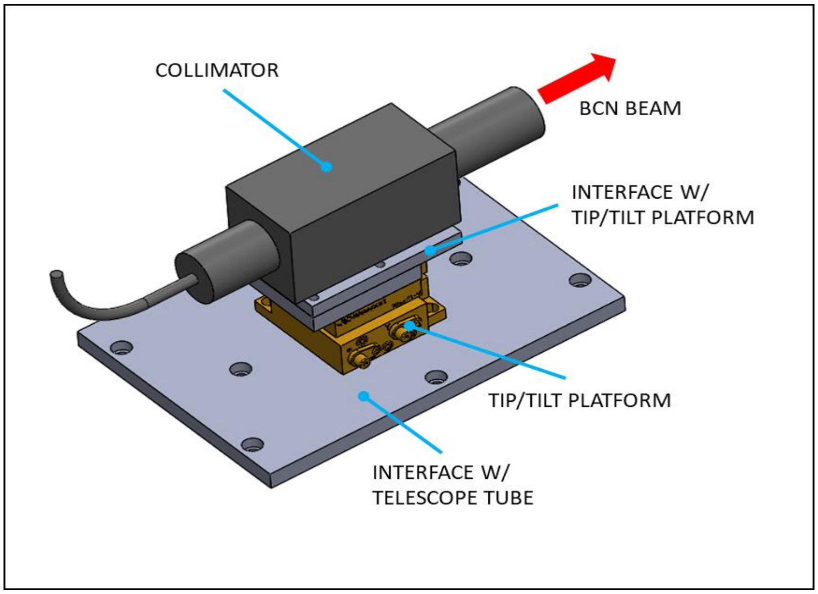

Figure 5-28. Assembly with uplink beacon collimator, tip/tilt platform for beacon pointing regulation and interface with the telescope tube.

Figure 5-29. Integration of uplink beacon mechanical interface on the telescope tube.

<ins>LCU</ins>

Due to limitations to the presence of personnel in the telescope dome during operations and for practicality reasons, the LSU activation and parameters are controlled by the LCU. The LSU and LCU mounted with a dedicated interface to the telescope's Nasmyth base is shown in Figure 5-30. The LCU mainly consists of a Raspberry Pi (Figure 5-31) remotely connected via wi-fi to the telescope control room.

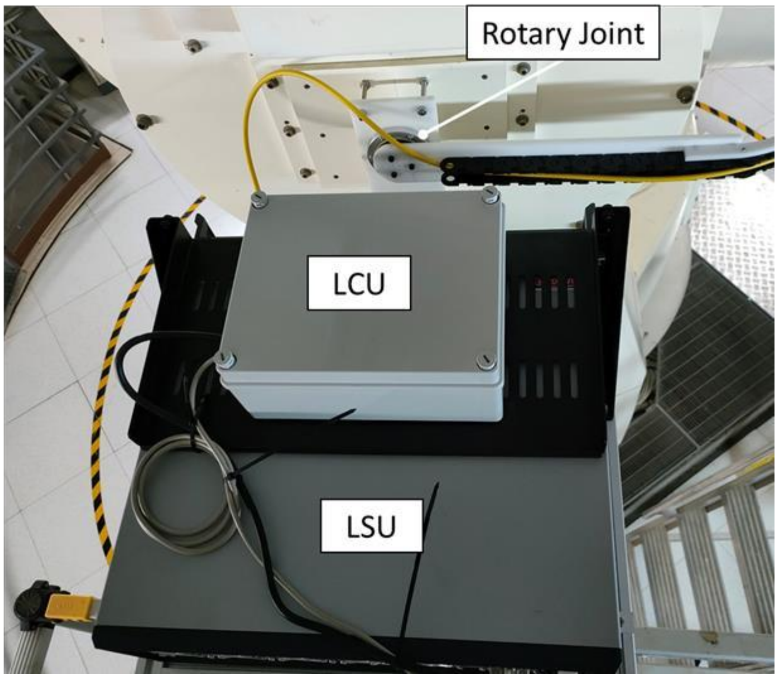

Figure 5-30: and LCU mounted on dedicated support.

Figure 5-31: Raspberry Pi.

5.3 System verification

In this chapter a description of the tests performed to assess the system compliance with project requirements is presented. The candidate has consistently contributed to the definition of the system verification test plan and has been the main responsible for test completion and analysis of results, with the constant interaction of ASI researchers, eGeos personnel and Stellar Project team.

5.3.1 FPA optical characterization and adjustment

The objective of this test was the optical characterization and adjustment of the collimated output beam divergence and diameter by means of the FPA. The aim of the test was to verify a beam reduction = 8 +/- 10% and a collimated beam divergence ≤ 10 mrad.

Test setup

Test setup consists in:

- MLRO telescope
- FPA beam reduction stage assembled on MLRO optical table (Figure 5-32). See Figure 5-5 for optical layout scheme)
- CMOS camera

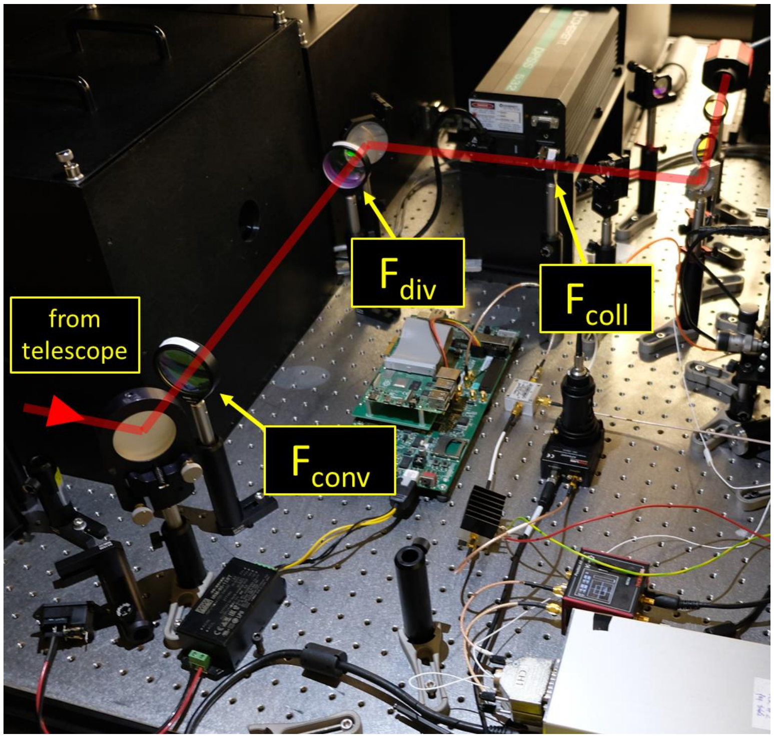

Figure 5-32: Path through beam reduction stage followed by light incoming from telescope.

Test procedure

The test consists in the acquisition of the optical image which is formed at several distances from the beam reducer exit while pointing the telescope at a reference star. The output beam diameter is measured using the CMOS camera. This allows to measure both the beam diameter and beam divergence at the exit of the beam reduce.

Test results

The acquired beam profiles at different distances from the beam reducer exit (‘F_{coll}’ in Figure 5-32) are shown in Figure 5-33. The beam diameter at each distance has been computed as the diameter encircling 86.5% of the total power incident on the CMOS sensor.

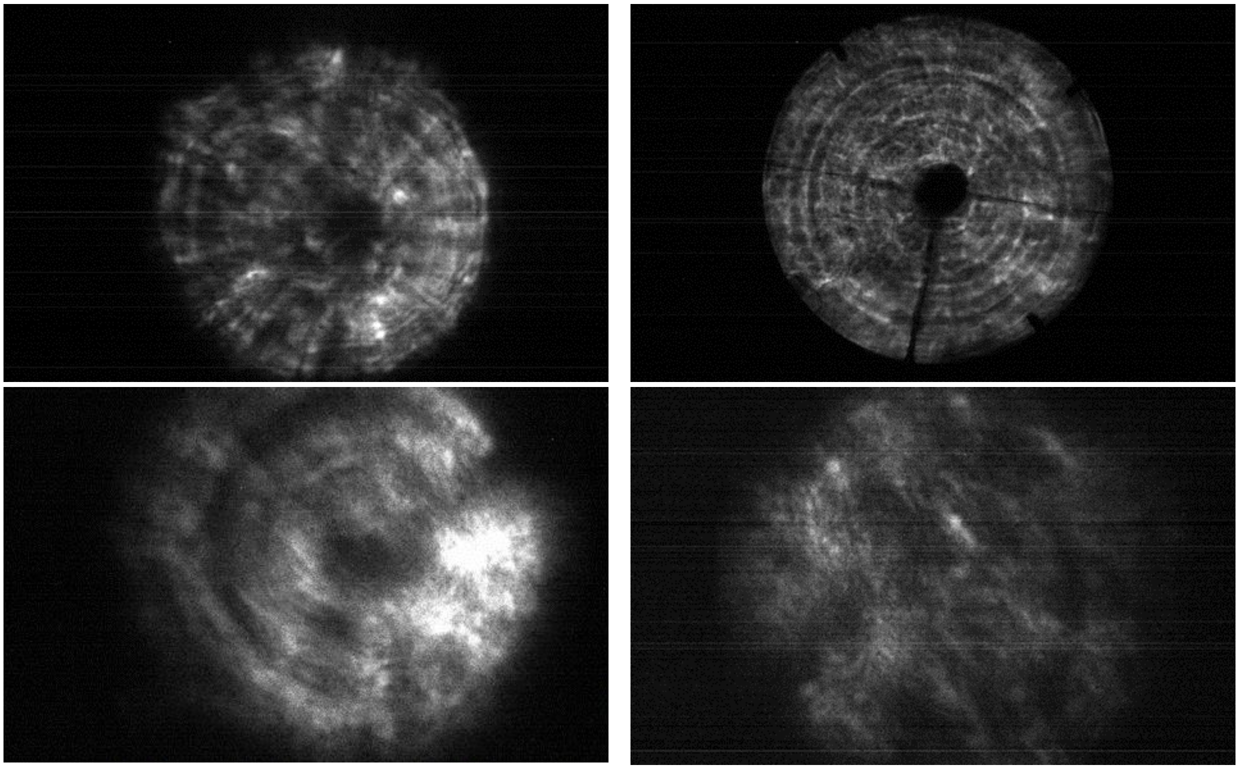

Figure 5-33: beam spot profile acquired at different distances from beam reducer exit with Kiralux cam. Distances from beam reducer exit are as following: 75 mm (top left); 170 mm, pupil (top right); 370 mm (bottom left); 410 mm (bottom right).

Table 5-9: measured beam diameter at different distances from beam reducer exit.

Distance from beam reducer exit [mm]	Beam diameter [mm]
75	6.1
170 (pupil)	6.5
370	7.0
410	7.3

The resulting beam reduction ratio is 8.2 (compliant with 8 ± 10% requirement).

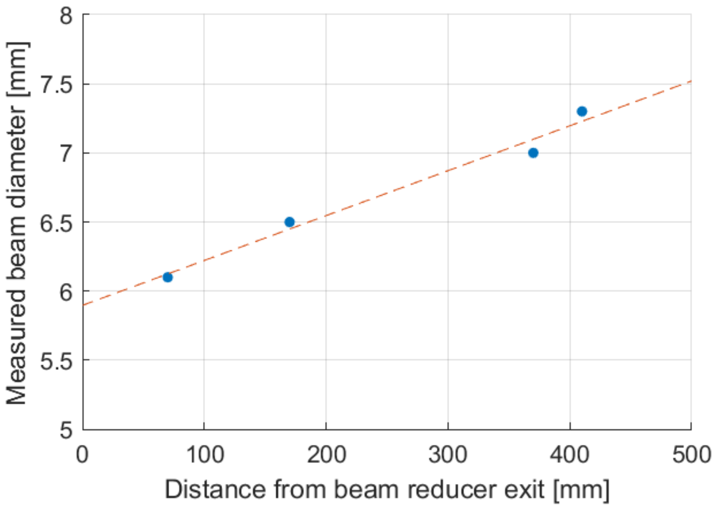

Figure 5-34: measured beam diameter at different distances from beam reducer exit.

Full beam divergence is computed as the angular coefficient of the linearly fitted data, resulting in 3.2 mrad. Although the resulting beam divergence is not strictly compliant with the initial required value derived from inherited design (< 1 mrad), further considerations have shown that the adoption of lenses with larger aperture with respect to previous design allows to relax the beam divergence requirement (≤ 10 mrad). For this reason, the exit beam divergence is compliant with system requirements.

5.3.2 FPA beam stabilization test

The objective of this test was the verification of the FPA beam stabilization capability. The aim of the test was to demonstrate that the residual rms angular deviation of the collimated beam at the FPA output is compatible with expected multimode optical fiber FoV (1.5 mrad).

Test setup description

Test setup consists in:

- Operational telescope
- Completely assembled FPA

Test procedure

The test procedure will consist in:

1. Telescope tracking of a reference star (Sirius, Vega)
2. Measurement of the beam spot position jitter on the CMOS camera sensor WITHOUT active beam stabilization stage
3. Measurement of the beam spot position jitter on the CMOS camera sensor WITH active beam stabilization stage

Test results

A sample frame of the CMOS camera is shown in Figure 5-35. The results of the CMOS camera acquisition with fine pointing system ON and OFF in terms of pointing error are both shown in Figure 5-36. While the pointing error is greater than requirement with the FSM off, the activation of the fine pointing system allows to consistently keep the pointing error below the 1.5 mrad threshold. This results in a pointing error RMS value of 0.8 mrad, which is below the 1.5 mrad requirement.

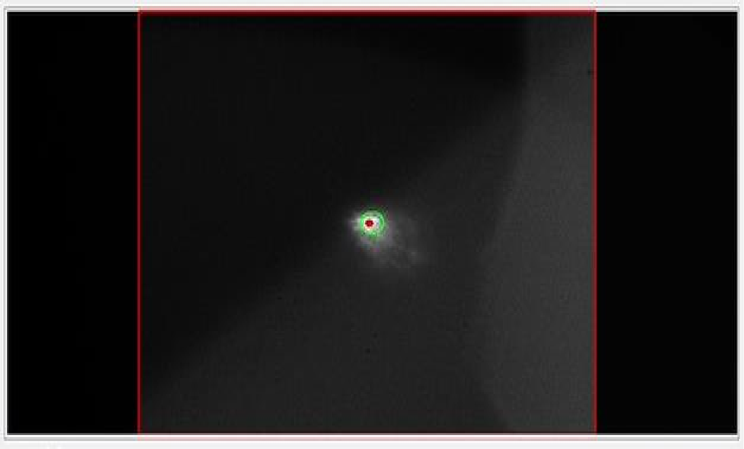

Figure 5-35: Sample frame of the camera acquisition while pointing at a reference star. The red dot represents the calculated star spot centroid. The green circle represents the target pointing error of 1.5 mrad.

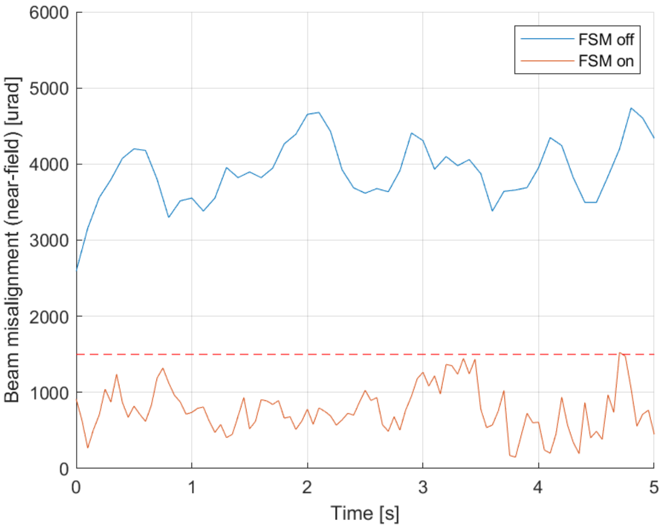

Figure 5-36: Pointing error obtained with FSM OFF and ON. X-axis shows time from camera acquisition start.

5.3.3 Receiver peak-to-peak sensitivity

The objective of this test was the measurement of the APD detector's achievable coupling efficiency. The aim of the test was to demonstrate a peak-to-peak sensitivity ≥ 90% nominal sensitivity from datasheet (≈45 kV/W).

<u>Test setup</u>

Test setup consists in:

- Modulated laser source
- Optical attenuator
- Collimator
- Adjustable mirror
- APD lens
- APD receiver
- Oscilloscope

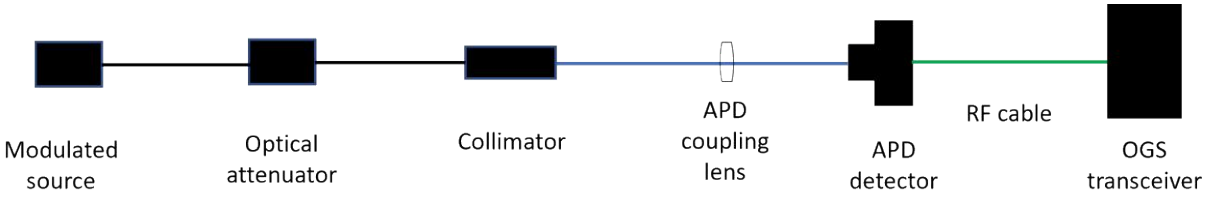

Figure 5-37: test setup layout.

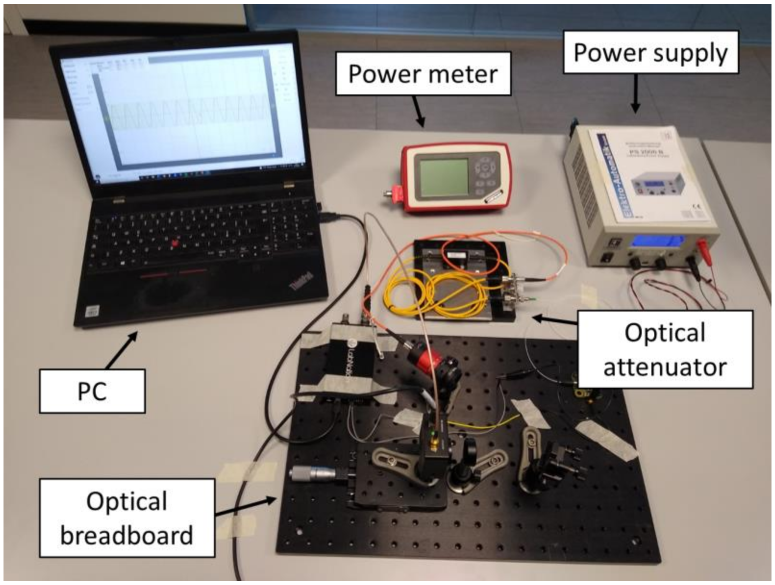

Figure 5-38: test setup, overall view.

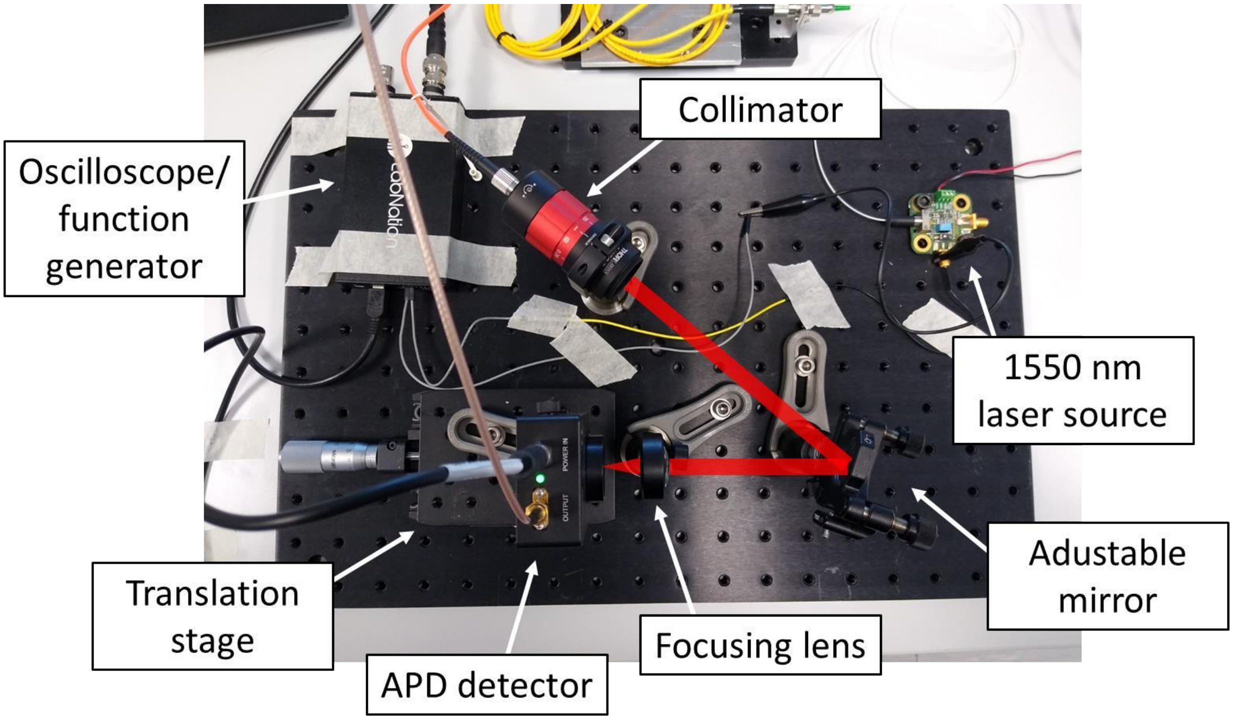

Figure 5-39: test setup, components on optical breadboard.

Test procedure

The test procedure will consist in:

1. Transmission of modulated optical signal
2. Adjustment of translation stage and adjustable mirror for APD coupling optimization
3. Attenuation of transmitted signal to reach desired input optical power at APD
4. Measurement of peak-to-peak output from the APD
5. Derivation of APD V/W sensitivity in terms of output/input peak-to-peak ratio

Test results

Test results at different attenuation levels using a single mode fiber patch cable can be found in Table 5-10 and Figure 5-40.

Table 5-10: Measured peak-to-peak voltage versus peak-to-peak optical power at APD input.

Peak-to-peak optical power at APD input [uW]	Measured peak-to-peak voltage at APD output [mV]
0	2.4
0.05	8.7
0.1	15.6
0.2	29
0.5	66
1	133
1.9	250
5	580
10	1050
20	1850

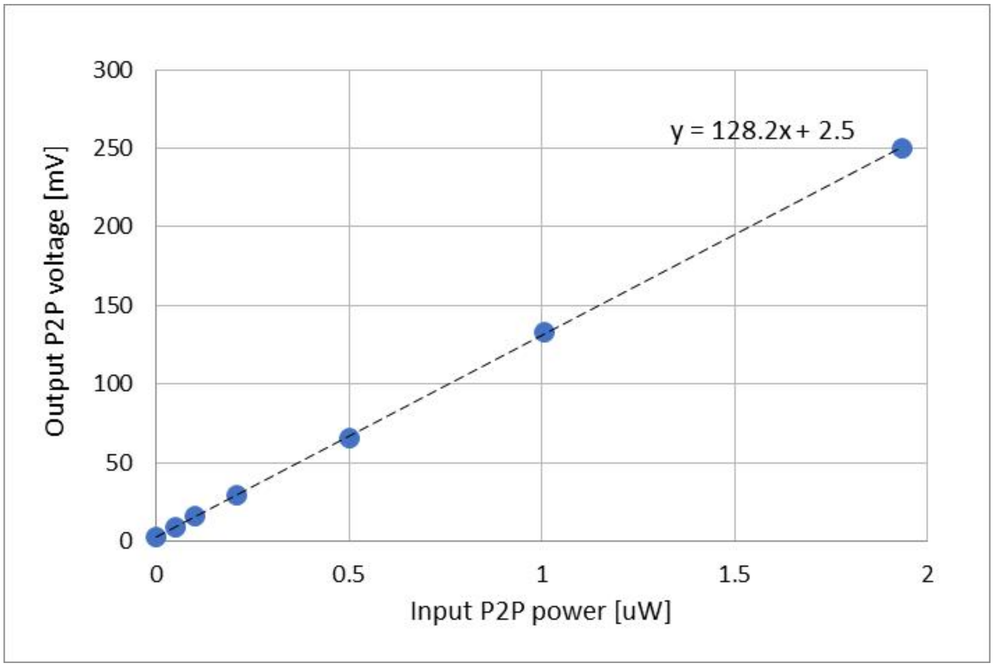

Figure 5-40: Measured peak-to-peak voltage versus peak-to-peak optical power at APD input.

Results show a peak-to-peak sensitivity of 128 kV/W, compatible with requirement (> 40 kV/W).
An additional coupling loss of 0.7 dB has been measured when using a 105 µm multimode patch cable instead of the single mode patch cable, corresponding to a sensitivity of 104 kV/W (still compatible with requirement).

Given that:

- measurements performed by the supplier indicate a flat frequency response of the detector in its operating range (0.3-1600 MHz), see Figure 5-41,
- the tests have been performed at a frequency (2 MHz) that lies within the detector's operating range

we expect the measured sensitivity to be a valid estimate of the detector coupling efficiency throughout its operating frequency range.

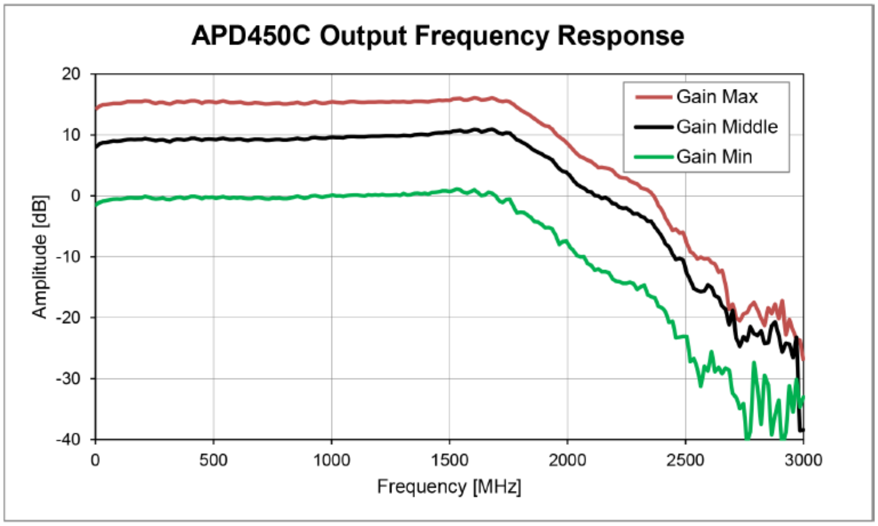

Typical Output Frequency Response APD450C

Figure 5-41: frequency response of the detector as measured by the supplier.

5.3.4 Receiver alignment and beam stabilization performance

The objective of this test was the verification of the receiver alignment and stabilization performance. The test aimed to show that the telecom beam is consistently detected by the APD receiver after FPA alignment.

Test setup

Test setup consists in:

- Representative beacon source
- Representative telecom source
- Beam combiner
- Collimator
- Tip/tilt mirror
- Dichroic mirror
- CMOS camera
- CMOS camera lens

- Fiber coupling lens
- Multimode optical fiber with connector mounted on 5-axis (xyz translation + tip/tilt) stage
- APD detector
- Oscilloscope

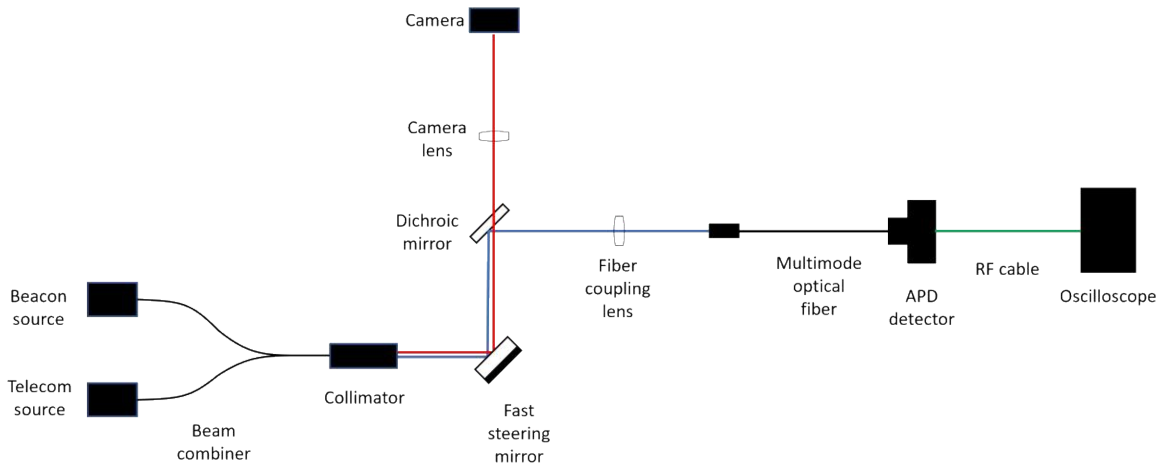

Figure 5-42: test setup layout.

Test procedure

The test procedure consists in:

1. Transmission of combined beacon and telecom beams through collimator.
2. Beacon spot alignment at center of camera sensor by means of FSM.
3. Adjustment of optical fiber input connector position by means of 3-axis translation stage until optical power at multimode fiber output is maximized.
4. Measurement of APD detector output after successive at multimode fiber misalignment and realignment cycles.

Test results

After completion of steps 1. and 2. of the procedure, the optical power at the multimode fiber input and output has been measured in order to derive the maximum coupling efficiency for the 105 µm and 200 µm core fibers, resulting in 72% (-1.4 dB) and 82% (-0.9 dB) respectively.

The optical power at the output of the multimode fiber has also been measured at different beam misalignment angles with respect to optimal alignment to characterize the system's fiber coupling loss profile and derive an equivalent FoV with a <1dB coupling loss (FoV_{-1dB}). The misalignment has been imposed by the FSM and measured by the beacon camera. The coupling loss has been computed with respect to the maximum measured coupling efficiency throughout the swept angular range. The measured horizontal and vertical profiles relative to the target 105 µm core fiber are shown in Figure 5-43. The horizontal and vertical profiles relative to the 200 µm core fibers have also been measured as a backup solution and are shown in Figure 5-44. Results show that a FOV_{-1dB} > ±1.5 mrad can be obtained with both fibers (in particular ±1.8 mrad with the 105 µm core fiber, ±4 mrad with the 200 µm core fiber). These values are compatible with the system RMS pointing error value resulting from test RX-T2 (800 µrad).

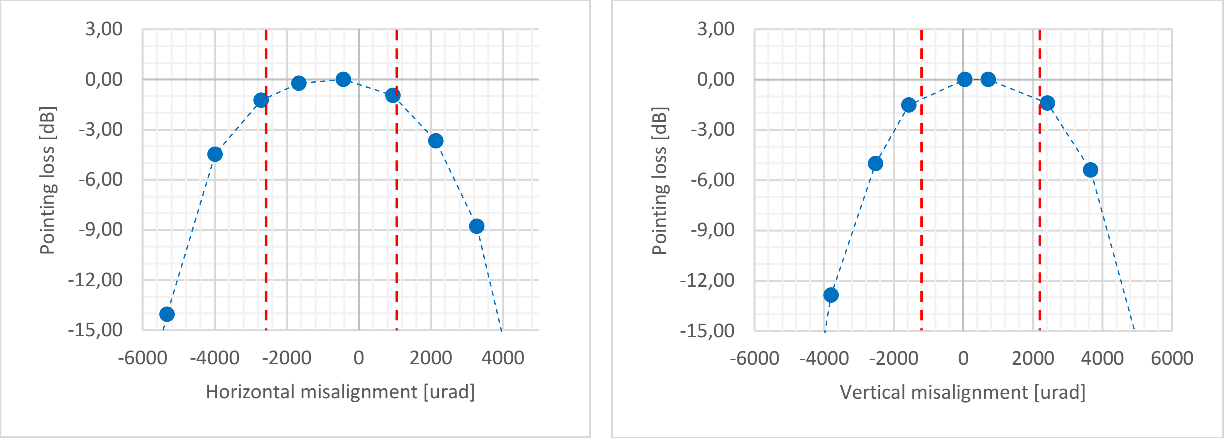

Figure 5-43: Horizontal (left) and vertical (right) fiber coupling efficiency profiles relative to the 105 µm core multimode fiber, expressed in terms of pointing loss. Vertical red dashed lines show the FoV_{-1dB} limits.

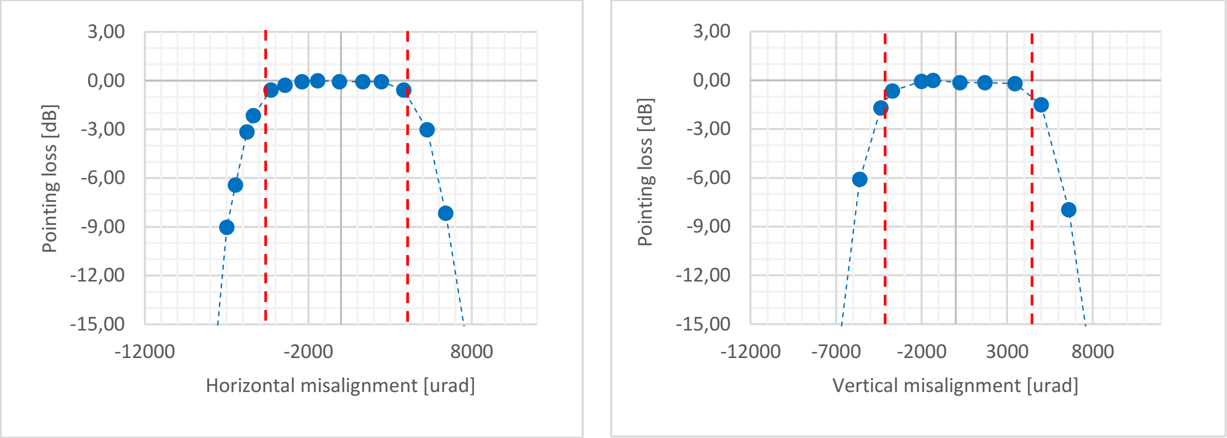

Figure 5-44: Horizontal (left) and vertical (right) fiber coupling efficiency profiles relative to the 200 µm core multimode fiber, expressed in terms of pointing loss. Vertical red dashed lines show the FoV_{-1dB} limits.

A similar measurement has been performed to derive the APD coupling efficiency profile, in order to rule out any unexpected problems specifically related to coupling with the APD detector. In this case the 1550 nm telecom signal has been modulated with a 2 MHz sine carrier (given the APD lower bandwidth limit of 0.3 MHz) and the resulting peak-to-peak voltage amplitude at the APD output has been measured at different misalignment errors. Results in terms of pointing loss with respect to peak-to-peak output at reference alignment using the 105 µm fiber are shown in Figure 5-45, confirming a FOV_{-1dB} > ±1.5 mrad.

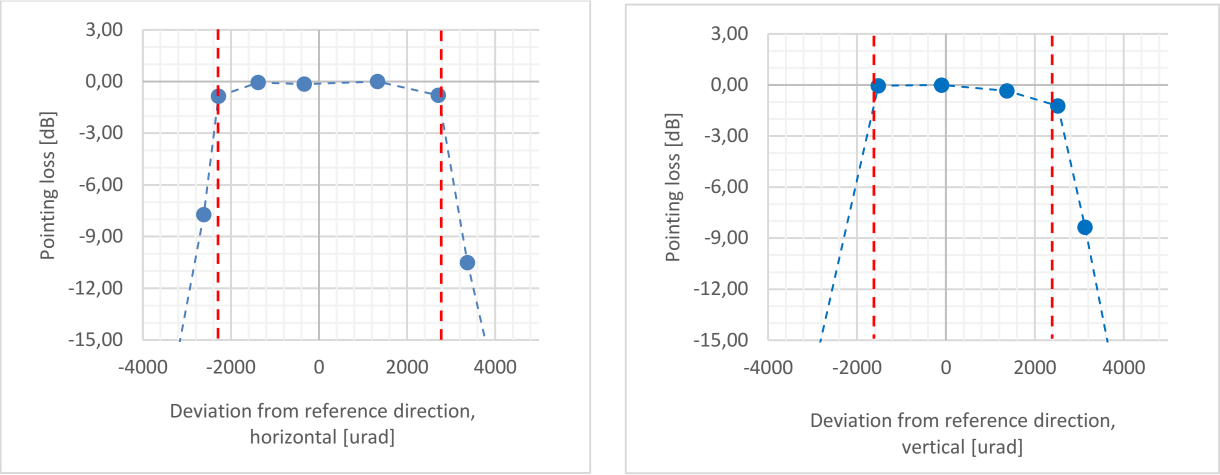

Figure 5-45: Horizontal (left) and vertical (right) APD detector coupling efficiency profiles (using 105 µm fiber), expressed in terms of pointing loss. Vertical red dashed lines show the FOV$_{-1dB}$ limits.

In the final part of the test, the system capability to restore coupling after misalignment has been tested. A series of arbitrary misalignment angles > 20 mrad have been imposed using the FSM and the output of the system (both at fiber output and at APD receiver) has been measured after the FPA system activation. Results in terms of normalized multimode fiber output optical power and APD detector peak-to-peak signal are shown in Figure 5-46 and Figure 5-47 respectively. Values greater than 100% are due to the fact that normalization is performed with respect to the highest values obtained during FOV profile determination, which could not provide a measurement of the highest possible coupling efficiency. Results show in both cases that the output power after system realignment by means of FPA is typically > 95 %. These results are in accordance with the FOV$_{-1dB}$ and RMS pointing error measurements described earlier in this paragraph.

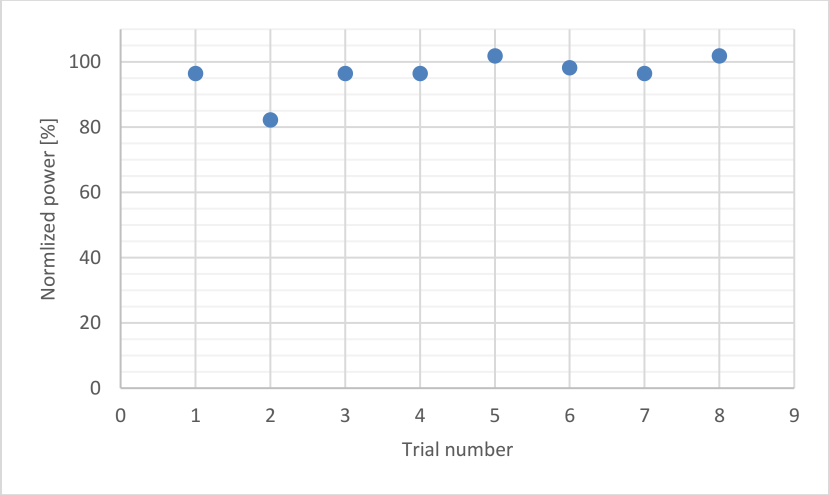

Figure 5-46: multimode fiber output optical power after FPA realignment, normalized with respect to highest value obtained during FOV$_{-1dB}$ profile determination.

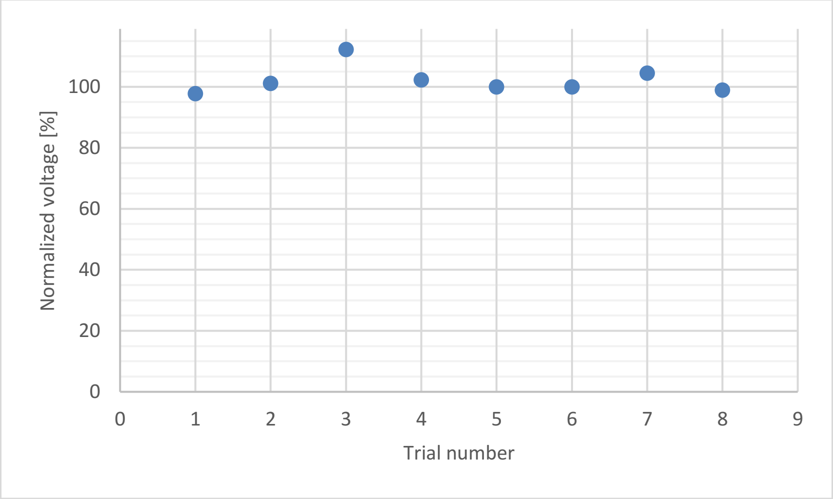

Figure 5-47: APD peak-to-peak output voltage amplitude after FPA realignment, normalized with respect to highest value obtained during FOV$_{-1dB}$ profile determination.

5.3.5 Receiver electronics demodulation test in loopback

The objective of this test was to verify the loopback telecommunication capabilities of the TX/RX electronics. A measured BER ≤ 10^{-5} was deemed sufficient, although no transmission errors were expected.

Test setup

- ELU-EM-DL
- 6 dB RF attenuator
- Balun board
- GS receiver

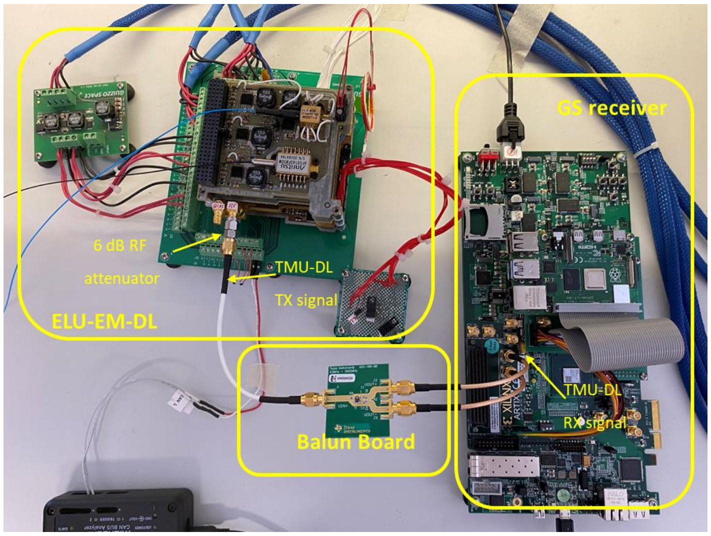

Figure 5-48: Test setup.

Test procedure

The test procedure consists in:

1. Transmission of a PRBS by ELU-EM-DL.
2. PRBS sequence identification and BER measurement by GS receiver.

Tested bitrates are 0.5, 1 and 2 Gbps.

Test results

No errors have been detected at any modulation bitrate. Considering the number of transmitted bits, a BER<10^{-9} is verified for all modulation rates. Detailed results are shown in Table 5-11.

Table 5-11: test results at different modulation rates.

Modulation rate [Gbps]	Transmitted bits	Error count	BER
0.5	7.93E10	0	<1.3e-11
1	7.94E9	0	<1.3e-10
2	2.86E10	0	<3.5e-11

5.3.6 Receiver electronics demodulation test with APD receiver

The objective of this test was to assess the system's end-to-end telecommunication performance, including the optical modulation and demodulation. The test aimed to demonstrate a BER of the received signal ≤10^{-5} at nominal bitrates and received optical power levels.

Test setup description:

- LaserCube ELU-EM-DL
- Optical modulator (OM)
- Optical attenuator
- APD detector
- Amplifier and balun
- GS transceiver

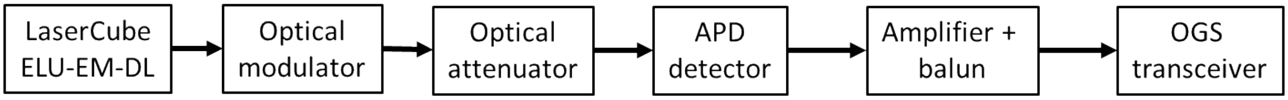

Figure 5-49: End-to-end telecommunication chain use to measure system BER at different bitrates and optical power attenuation levels.

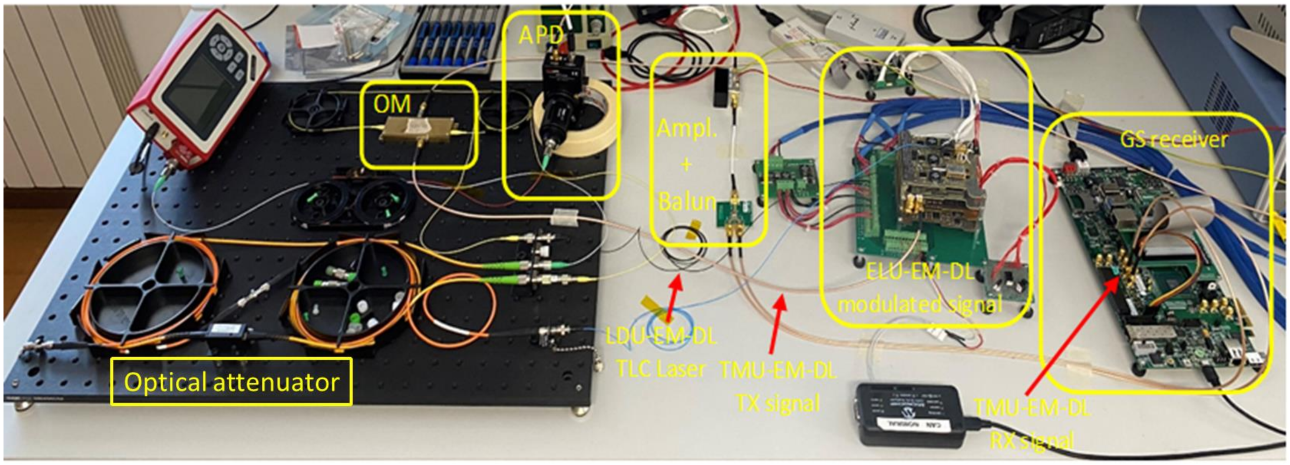

Figure 5-50: test setup.

Test procedure

The test procedure consists in:

1. Generation of modulated PRBS signal by means of LaserCube ELU-EM-DL
2. Attenuation of the generated signal to reach nominal input power at APD detector
3. Coupling of the signal on the APD detector
4. Demodulation of the received signal and measurement of BER by OGS transceiver

The laser is attenuated through a series of fixed and variable attenuators and the received optical power is measured.

The resulting BER is measured at different attenuation levels in order to:

1. Assess that the BER is ≤ 10^{-5} at the received power expected from LaserCube during the IOD.
2. Measure the lowest admittable received power which guarantees a BER ≤ 10^{-5}

Test results

The measured BER at different attenuation levels is shown in Figure 5-51 (500 Mbps modulation bitrate) and Figure 5-52 (1 Gbps modulation bitrate). No test has been performed at 2 Gbps bitrate due to optical modulator bandwidth limit.

For what concerns the 500 Mbps modulation bitrate test, the power level corresponding to the required BER of 10^{-5} is 2.5 µW. This is associated to a distance of 1200 km, which for the target 550 km altitude orbit corresponds to an elevation of approximately 20°.

For what concerns the 1 Gbps modulation bitrate test, the minimum power level corresponding to the required BER of 10^{-5} is 5 µW. This is associated to a distance of 800 km, which for the target 550 km altitude orbit corresponds to an elevation of approximately 40°.

In conclusion, results show that:

- A 500 Mbps link with BER <10^{-5} can be obtained at elevations >20°
- A 1 Gbps link with BER <10^{-5} can be obtained at elevations >40°

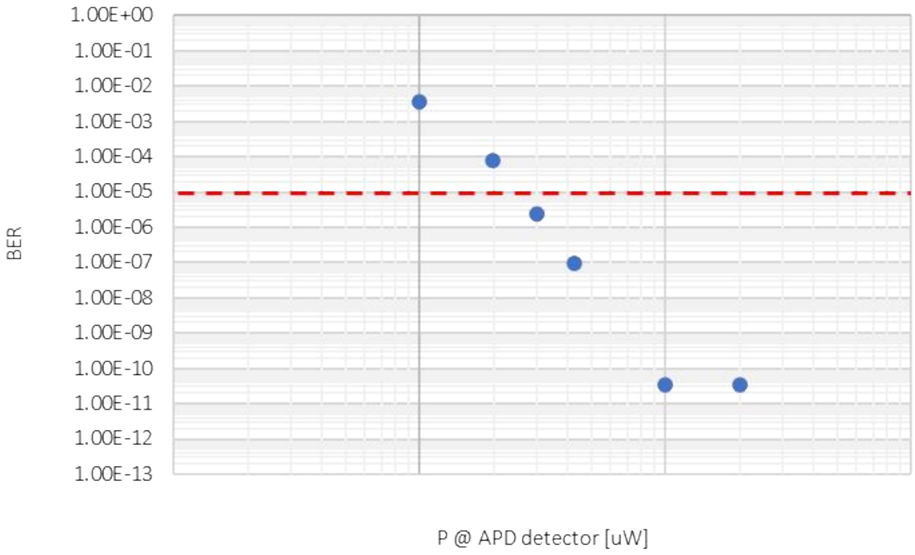

Figure 5-51: measured BER versus mean optical power at detector, 500 Mbps bitrate. X-axis values have been omitted for intellectual property reasons.

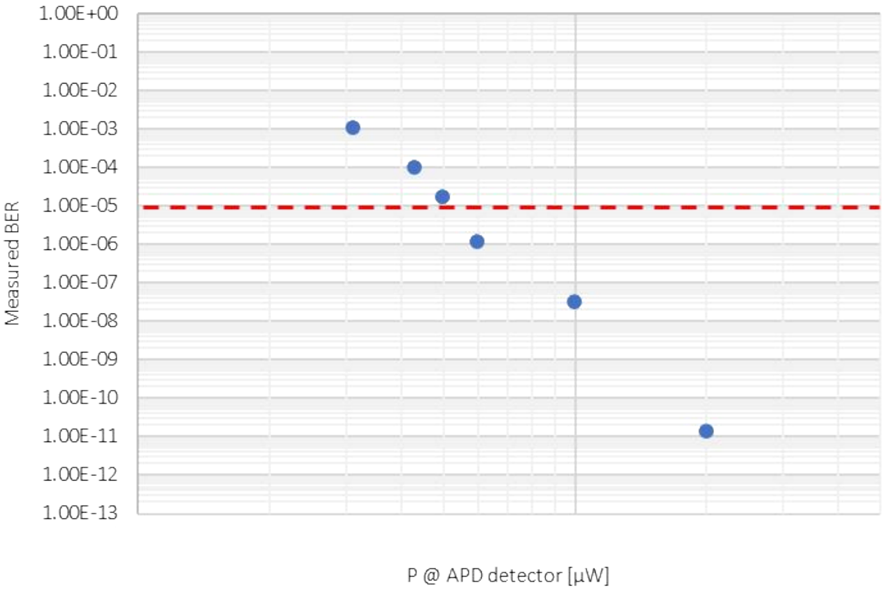

Figure 5-52: measured BER versus mean optical power at detector, 1 Gbps bitrate. X-axis values have been omitted for intellectual property reasons.

5.3.7 Uplink beacon alignment

The objective of this test was the alignment of the uplink beacon beam. A maximum beam alignment error requirement of 50 μrad has been derived from power budget analysis.

Test setup

Test setup consists in:

- MLRO telescope
- Beacon transmitter section
- Optical filters
- ConerCube Retroreflector (CCR) bar
- CCR bar support
- Beacon receiver section (FPA)

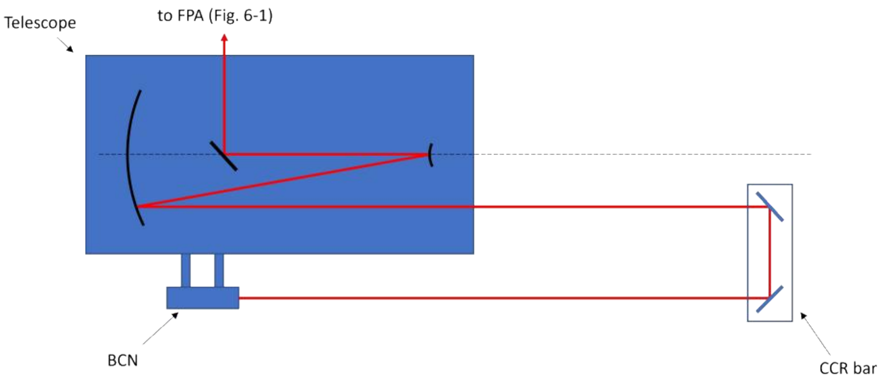

Figure 5-53: retroreflected beacon beam path.

Test procedure

The test procedure consists in:

1. Pointing of the telescope tube at elevation zero
2. Activation of uplink beacon laser source at minimum power, also attenuated by means of optical filters
3. Positioning of CCR bar so that beacon beam falls within CCR bar entrance surface
4. Change orientation of CCR bar so that beacon beam falls within both entrance and exit surface and is back-reflected towards the telescope primary mirror
5. Adjustment of beacon laser orientation by means of CAM micrometric screws until auxiliary beam spot is at the center of the beacon receiver camera FoV. This is the condition at which the telescope optical axis and beam axis are parallel

6. If during step 5 the beam falls outside CCR optical path and is not back-reflected to telescope primary mirror, repeat steps 3 to 5 iteratively until convergence (i.e. beam spot is at the center of the beacon receiver camera FoV)

Test results

Beacon camera acquisition of the retro-reflected uplink beacon spot after alignment is shown in Figure 5-54.

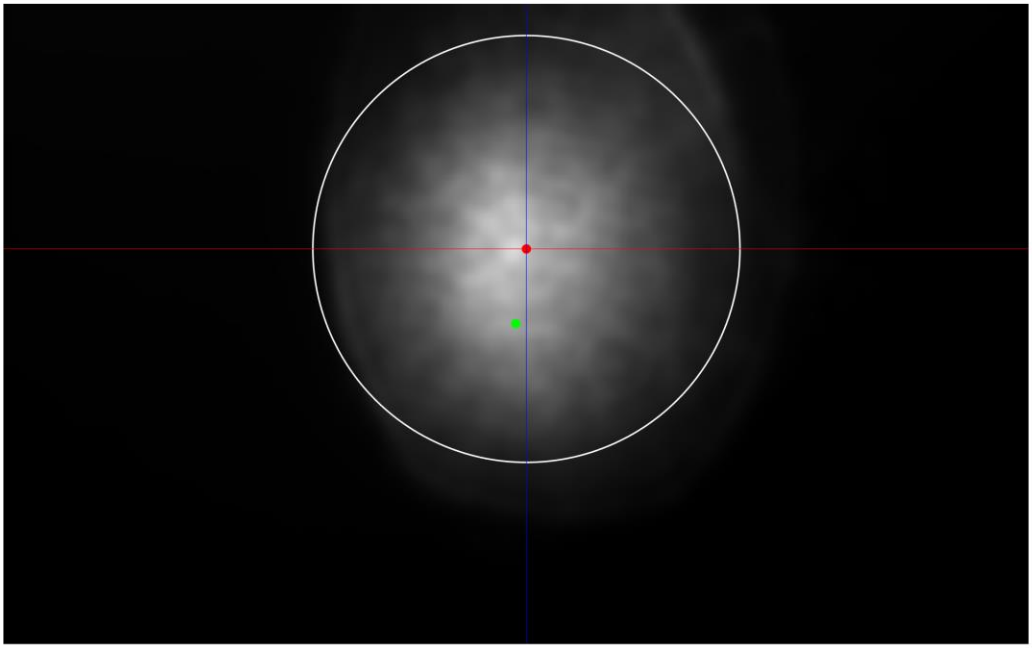

Figure 5-54: Beacon camera acquisition of the retro-reflected uplink beacon spot after alignment.

The barycentre of the spot, weighted upon pixel intensity $I_{i,j}$, is used as spot centroid:

$$C_{hor} = \frac{\sum_i i \sum_j I_{i,j}}{\sum_i \sum_j I_{i,j}}$$

$$C_{ver} = \frac{\sum_j j \sum_i I_{i,j}}{\sum_i \sum_j I_{i,j}}$$

Where *i* and *j* are horizontal and vertical pixel positions, respectively.

Spot decenter (in pixels) is computed as:

$$C_{err} = \sqrt{\left(C_{hor} - C_{hor,0}\right)^2 + \left(C_{ver} - C_{ver,0}\right)^2} = 142\ pixels$$

where $\boldsymbol{C_{hor,0}}$ and $\boldsymbol{C_{ver,0}}$ are the coordinates of the virtual central pixel of the camera sensor.
Considering the camera resolution of 0.19 µrad/pixel, the measured beam misalignment with respect to FPA reference optical axis is 27 µrad, i.e. < 50 µrad requirement.

5.3.8 Uplink beacon characterization

In this test, the characterization of the beam divergence was performed. A beam divergence comprised between 170 µrad and 250 µrad was expected.

Test setup

Test setup consists in:

1. MLRO telescope
2. Beacon transmitter section
3. Optical filters
4. CCR bar
5. CCR bar support
6. Beacon receiver section (FPA)

Test procedure

The test procedure consists in:

1. Activation of uplink beacon laser source at minimum power, also attenuated by means of optical filters
2. Positioning of CCR bar so that beacon beam is back-reflected towards the telescope primary mirror.
3. Measurement of beam spot size on FPA beacon camera.

This test approach assumes an incoming beacon with a diameter much lower than the telescope aperture. It also assumes that the FPA camera sensor is placed on the focal plane of the FPA (i.e. focused at infinity). In this condition, the divergence of the beam corresponds to the angular amplitude of the portion of FoV illuminated by the beam spot on the sensor.

Test results

The horizontal and vertical beam profiles across the calculated centroid are shown in Figure 5-55 and Figure 5-56, respectively. A gaussian fit of each profile has been performed to compute the respective $1/e^2$ divergence, yielding 740 pixels (141 µrad) and 860 pixels (163 µrad) respectively. This results in an average $1/e^2$ beam divergence of 152 µrad, which falls slightly below the 170-230 µrad requirement range. This is also confirmed by the computation of the power encircled within the measured $1/e^2$ radius, which yields 87% of the total power measured on the sensor, in good accordance with theoretical encircled power of a gaussian beam profile (86.5%).

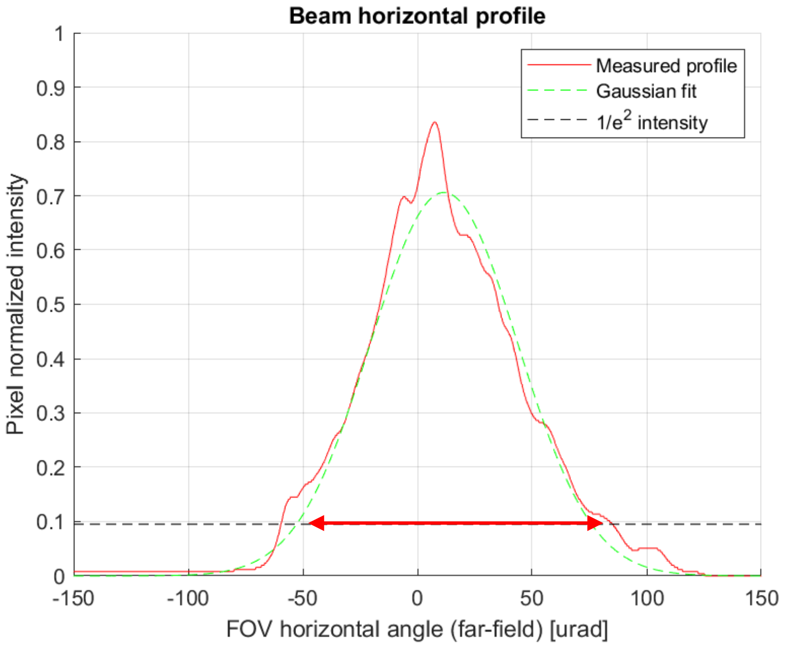

Figure 5-55: horizontal beam profile across the calculated beam centroid.

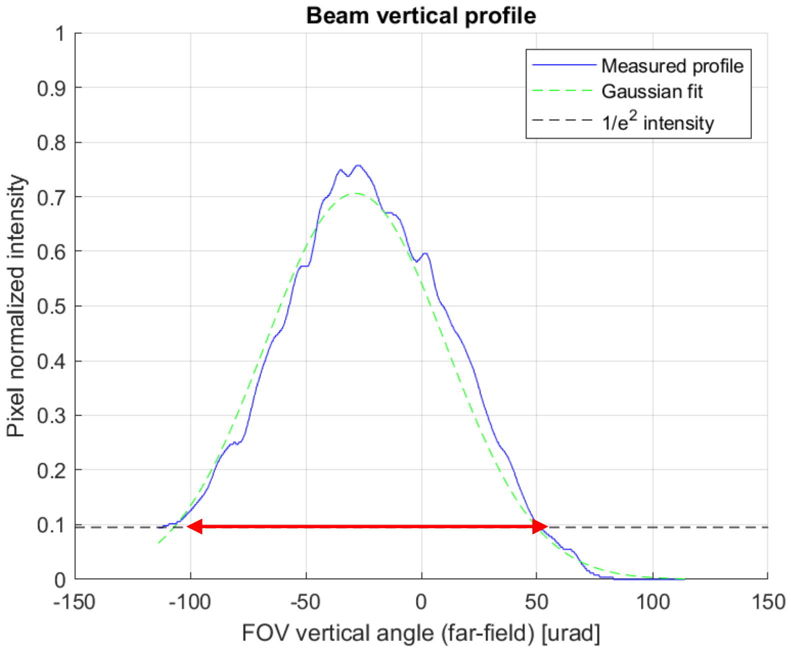

Figure 5-56: vertical beam profile across the calculated beam centroid.

The uplink beacon beam divergence target range of 170-230 µrad had initially been selected based on the optical power requirement of 500 nW, derived from the telecom signal pointing budget. Nevertheless, the acquisition phase only requires that the beacon signal be transmitted from the satellite to the ground station with a sufficient pointing accuracy, allowing the ground station to compensate for orbital prediction uncertainties. Since the LaserCube beacon beam divergence (1 mrad) is much larger than the telecom beam divergence (80 µrad), the initial requirement was too strict and a larger pointing error can be tolerated. Namely, a 100 µrad pointing error has been assumed for the downlink beacon power budget, as opposed to a 10 µrad pointing error for the telecom beam. Following these considerations, the impact of the lower-than-expected beam divergence has been experimentally evaluated, to assess that the uplink beacon power received at the QD detector is still sufficient to ensure a <100 µrad downlink beacon pointing error during acquisition phase and a <10 µrad downlink telecom pointing error during tracking phase.

In Figure 5-57 the expected received power at LaserCube QD during the acquisition phase (i.e. open-loop pointing based on orbital predictions) is plotted versus the spacecraft elevation above the horizon. A spacecraft position uncertainty of 50 m has been assumed, based on Global Positioning System (GPS) data propagation analysis. It can be seen that, with a beam divergence of 150 µrad, a beacon power >200 nW is provided throughout the elevation range of interest (>20°). Since the beacon beam pointing loss is only dependent on the coarse stage pointing error, the latter has been measured at different received power levels and results are shown in Figure 5-58. We can observe that a beacon power of 100 nW is sufficient to keep the coarse pointing error < 100 µrad. We then conclude that the measured beam divergence is compatible with acquisition phase requirements.

It should also be noticed that link budgets have been computed assuming a transmitted power of 80 W. A 25% margin is then available considering the uplink beacon laser maximum power of 100 W.

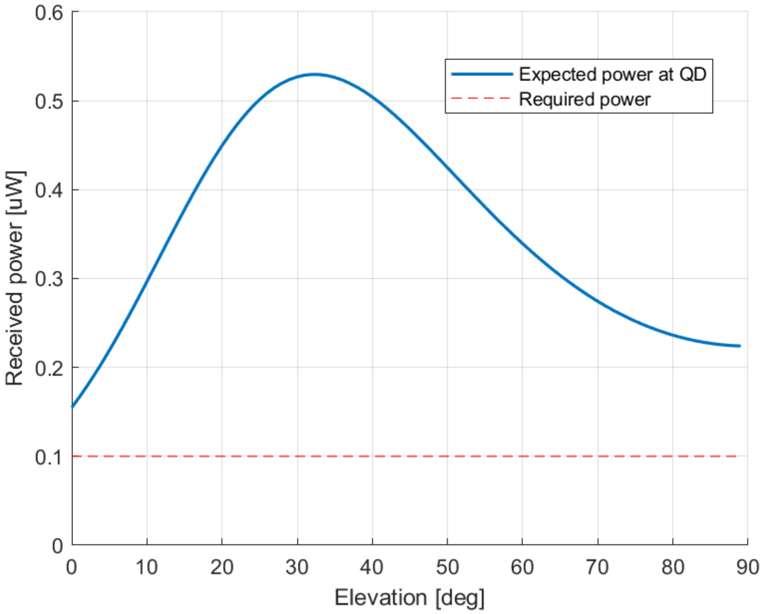

Figure 5-57: received beacon power at LaserCube QD during acquisition phase as a function of spacecraft elevation above horizon. Transmitted power: 80 W. We can see that at the measured beam divergence (150 urad) the received power is always above 200 nW for the elevation angles of interest (>20°).

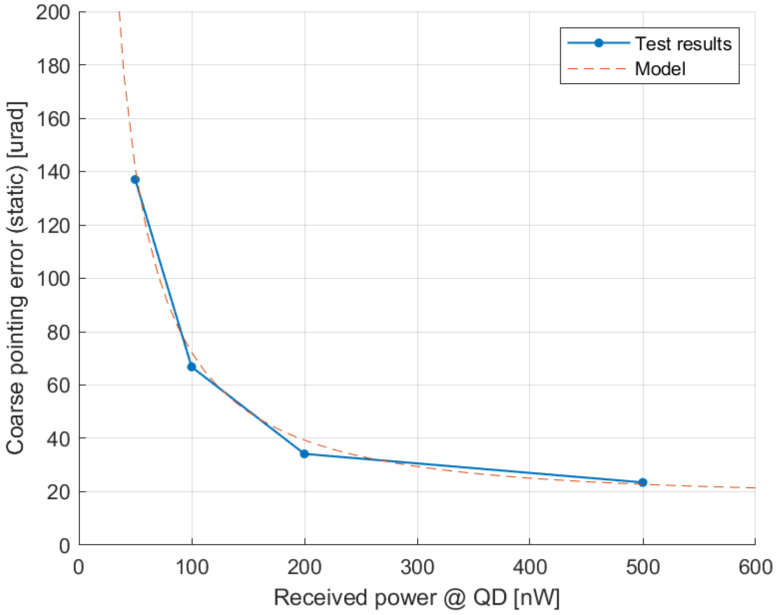

Figure 5-58: coarse pointing error as a function of received power at QD detector.

Once the satellite beacon has been acquired by the ground station, the uplink pointing error component associated to the spacecraft position uncertainty is eliminated and the tracking phase can be initiated. The resulting power budget is presented in Figure 5-59, showing that the 500 nW optical power at the satellite QD required for telecom transmission is met throughout the elevation range of interest (i.e. >20°) during the tracking phase.

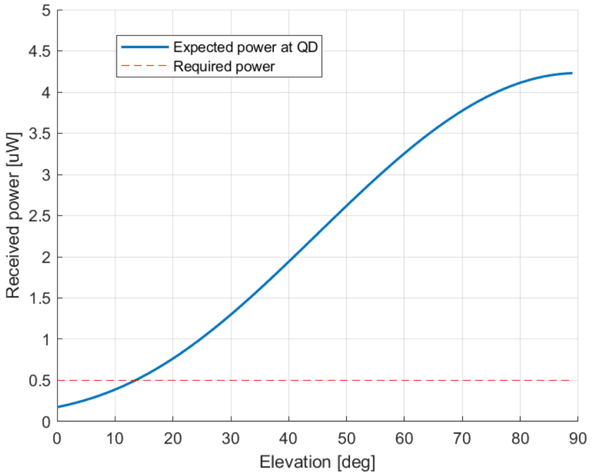

Figure 5-59: received beacon power at LaserCube QD during tracking phase as a function of spacecraft elevation above horizon. Transmitted power: 80 W. We can see that at the measured beam divergence (150 urad) the received power is expected to be always above 500 nW for the elevation angles of interest (>20°).

5.3.9 Verification of uplink beacon control and output power calibration

A specific test was performed to verify the capability to remotely control the laser actuation through LCU, for safety and operation optimization reasons.

Test setup

Test setup consists in:

- LCU
- LSU
- UBC
- Optical filters
- Projection screen
- Free-space optical power meter

Test procedure

The test procedure consists in:

1. Positioning of the power meter in front of collimator output
2. Activation of LSU by means of LCU
3. Verification of auxiliary beam spot presence on screen
4. Detection of beacon beam presence by means of free-space optical power meter

Test results

The remote control of the uplink beacon has been tested in situ (see Figure 5-60). Both the beacon laser and auxiliary laser activation have been verified with success. The relation between driving current and laser output power has also been measured by means of a high-power power meter. Results are presented in Figure 5-61.

Figure 5-60: Laser activation test and calibration setup.

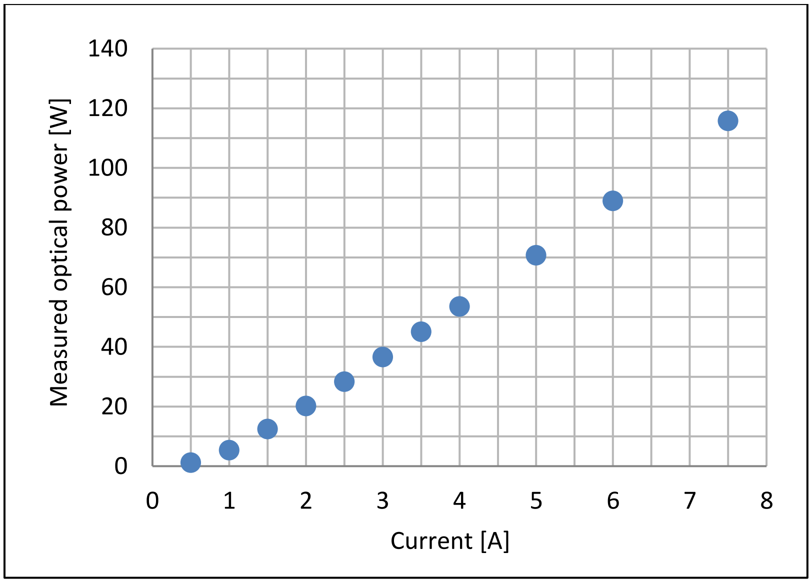

Figure 5-61: Laser calibration curve.

6. LASERCUBE IN-ORBIT DEMONSTRATION

In this chapter the main activities related to the launch and in-orbit demonstration of LaserCube are presented, namely: orbital determination analysis, preliminary ground-to-ground demonstration, space qualification tests and integration on host platform. Some preliminary results of the IOD are also presented.

6.1 Description of operations

Pointing of the telescope during LaserCube IOD test sessions are based on the expected satellite position (in terms of elevation and azimuth of the telescope mounting assembly) that are given by propagation of the latest available satellite orbital position / orbital parameters. In fact, during a test session the telescope will follow a pre-defined trajectory based on the satellite orbital predictions. This motion is executed with no feedback from the space segment until the beacon transmitted by LaserCube is detected; after that, trajectory corrections can be applied to better align the OGS telescope boresight with the received beam direction. In order to have a reasonable chance to point the telescope towards the actual position of the satellite, the orbital predictions uncertainty shall be lower than, or at least compatible with the uplink beacon divergence.

During the acquisition phase, the uplink beacon will be transmitted in order to illuminate the satellite. At the same time, the LaserCube model in orbit will scan its FoV looking for the uplink beacon and transmitting its own downlink beacon.

When the OGS detects the downlink beacon, the fine pointing stage will be activated and the operator will apply corrections to the pointing direction of the telescope tube with respect to the trajectory given by the orbital predictions, using as feedback the position of the fast-steering mirror in the fine pointing assembly. The more the FSM position will be off-nominal, the more the telescope tube pointing will be corrected in order to require less correction by the FSM, resulting also in lower pointing error of the uplink beacon, which is fixed to the telescope tube and is not actively pointing in other ways.

On the flight segment, once the uplink beacon is detected by LaserCube’s quadrant detector, the pointing system will shift from seeking to tracking, aligning the optical head with the uplink beacon. If the latter is lost for any reason, LaserCube goes back to seeking, scanning the field of uncertainty looking for the uplink beacon, and so on.

The flow of operations on both ground and flight segment is presented in Figure 6-1; the two segments operate independently, i.e., there are no direct feedbacks from one terminal to the other on the current status of operation.

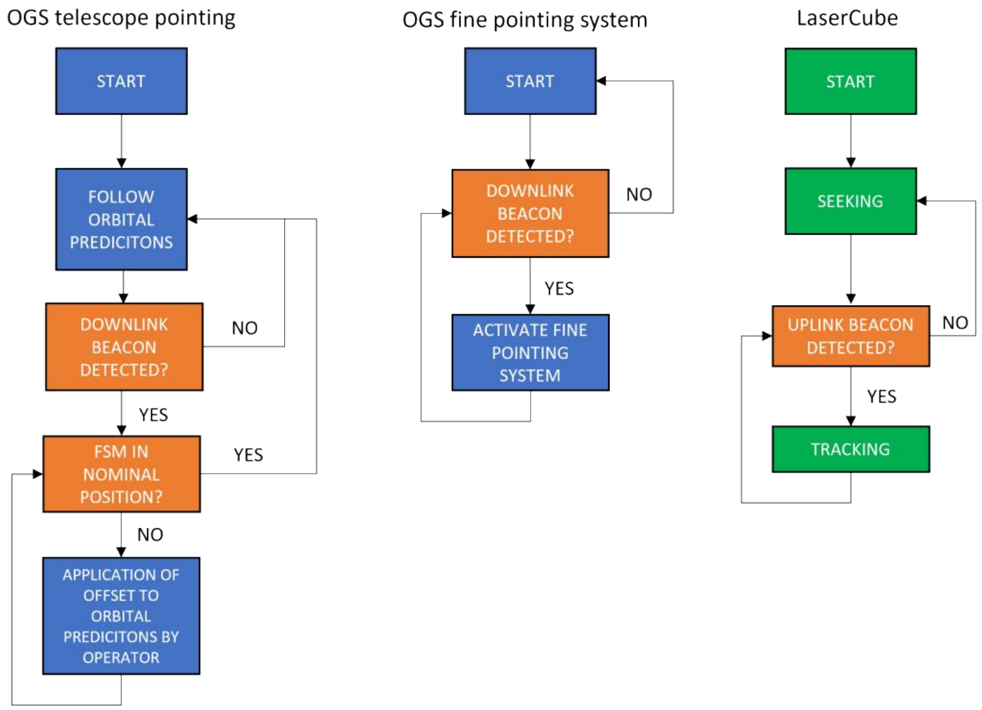

Figure 6-1. Flow of operations on both ground and flight segment.

6.2 Precise orbital determination analysis

Given the extremely narrow beamwidth of the transmitted beacon beam, an accurate estimate of the satellite’s orbital position is required for a sufficiently fast acquisition process. An orbital analysis was then performed by Stellar Project team using GMAT and Matlab with the purpose of defining the requirements on the GPS data acquisitions frequency given the azimuth and elevation accuracy requirement. The candidate contributed to this activity by supporting the definition of simulation conditions and the interpretation of results. The required angular accuracy is set at 100 µrad both for azimuth and elevation with respect to Matera ground station. The main choice for computing positions of one satellite in LEO is the use of the Two-Line Element (TLE) sets provided by the North American Aerospace Defence Command (NORAD) once per day. TLEs contain the mean Keplerian orbital elements of the spacecraft and the drag term, B*, at a specific point in time, the epoch. TLEs are the input for the Simplified General Perturbation Satellite Orbit Model 4 (SGP4) which allows the propagation of satellite states both in the past and future with respect to the epoch [71]. This model simplifies forces modelling, which means that errors increase rapidly during the propagation [72].

Another way to compute satellite state vector evolution is the propagation based on Global Positioning System (GPS) positions and velocities provided by spacecraft operators. The precise orbit determination requires to know the forces acting on the satellite, a least squares estimation algorithm and how to relate the observed parameters with the state vectors [72] [73], as described hereafter.

The forces acting on a satellite are both gravitational and non-gravitational. The following forces have been considered for the analysis:

- geopotential force due to the attraction of Earth's gravity field. It can be expressed as a spherical harmonic expansion of the gradient of the Earth's solid body mass distribution.
- atmospheric drag force. This force is one of the principal sources of error of the system because it depends on the atmospheric density, which is usually obtained by mathematical models, and the drag coefficient, which is difficult to estimate a priori.
- the force due to Solar Radiation Pression (SRP).

In addition to these forces, the relativistic correction due to difference of rate between two clocks placed one on the satellite and one in the terrestrial surface, is considered.

Regarding the least square estimation algorithm, two types are mainly used: the *batch least squares* approach, where data of a fixed period are collected and then processed together; and the *Kalman filter,* that analyses and processes data for each time span imposed to provide a better estimate at each epoch using process noise information. In particular, the Extended Kalman Filter (EKF) has been used, which allows to reduce the residual error between the observed and the propagated measures.

To validate the developed model, GRACE-FO mission data have been used. GRACE-FO is composed by two satellites at 220 km distance from each other and at about 500 km of altitude on the same orbital plane. Postprocessed data, Level 1B data, of each satellite are available by Jet Propulsion Laboratory's Physical Oceanography Distributed Active Archive Centre (PODAAC) [74]. For this work, GPS data have been used both for the EKF and for comparison with positions obtained at the end of the propagation. PODAAC also provides data about the attitude of the satellite, known as SCA1B, which have been integrated in the modelling of SRP. Finally, the geopotential force from the Joint Earth Gravity Model (JGM-3) has been used, while the MSISE-90, an empirical model of the temperature and composition of the atmosphere at heights between 0 and 700 km, provides atmospheric density.

The EKF algorithm has been applied to data sets separated by 12 hours from each other and each composed of GPS acquisitions spanning 90 minutes, sampled at 10-minute intervals. For each data set, a 24-hour orbital propagation has been generated. Considering a one-month period, a total of 60 24-hour propagations have been generated. Results are shown in Figure 6-2 in terms of difference between the estimated satellite position through orbit propagation and the measured position given by GPS data. Green, red, blue and yellow points represent respectively the radius of the error sphere computed with respect to GPS data after 6, 12, 18 and 24 hours of propagation. The dotted black line represents a 50-meter error threshold, which is the orbital prediction error considered for the beacon transmission power budget design. Results show that after 6 hours the error is always under 50 meters, while after 12 hours the limit is respected for 80% of points. It becomes 50% after 18 hours and around 15% after 24 hours.

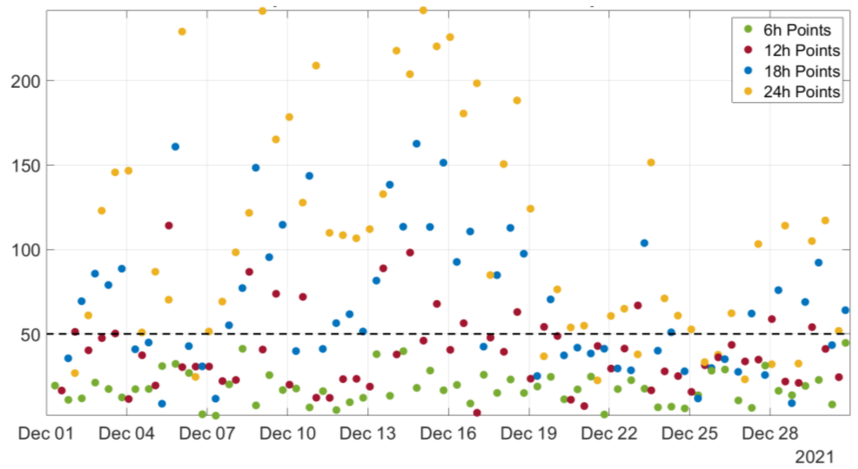

Figure 6-2: Error with respect to acquired GPS data of orbital propagation positions obtained using 10 GPS acquisitions from GRACE mission. This corresponds to a 90-minute acquisition period, i.e. a complete GRACE orbit. Points represent variations between GPS data and estimation obtained by the propagation after 6 hours (green points), 12 hours (red points), 18 hours (blue points), 24 hours (yellow points).

During the design phase of the beacon transmission section, an orbital prediction error of 50 m has been used for the power budget analysis, corresponding to the 80th percentile of the 12-hour orbital prediction simulations using EKF. This translates into a requirement in terms of GPS data download frequency; in other words, in order to obtain GPS-based orbital predictions with accuracy < 50 m, the GPS data shall be available no earlier than 12 hours before the satellite pass over the ground station.

Passes of Laser Cube over Matera ground station throughout the month of October 2021 have been considered to evaluate contact durations at 3 possible range of Laser Cube altitudes, 400, 500 and 600 km and with a minimum elevation of 15 degrees and a maximum elevation of 70 degrees. Over 70°, telescope is not able to track satellite and it starts again when the satellite returns below 70°. Figure D2 shows the number of accesses below 1 minute, including 1’ and 2’, 2’ and 3’, 3’ and 4’, 4’ and 5’ and above 5’ minutes. Anyway, we point out that only 10% of all passages over the MLRO result in elevation > 70°.

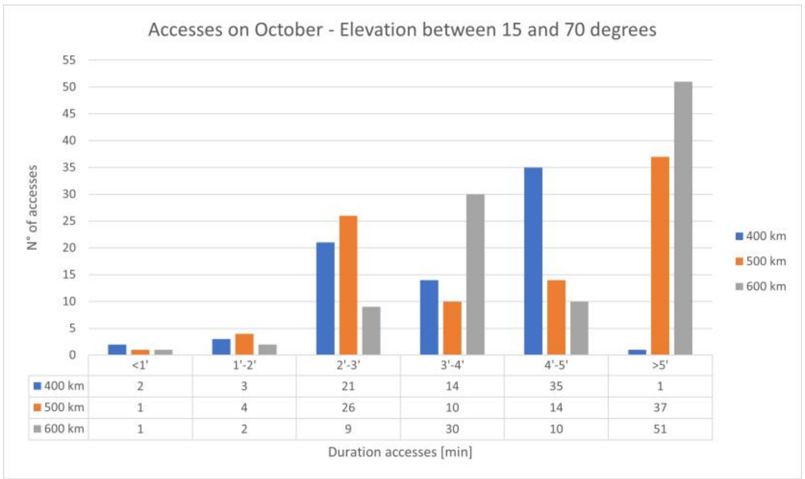

	<1'	1'-2'	2'-3'	3'-4'	4'-5'	>5'
■ 400 km	2	3	21	14	35	1
■ 500 km	1	4	26	10	14	37
■ 600 km	1	2	9	30	10	51

Figure 6-3: Contact duration at orbit altitudes of 400, 500 and 600 km.

Table 6-1 shows, at the varying of the height, the number of all accesses that LC has with Matera ground station for the entire month of October and the access with the maximum duration.

Table 6-1: Total number of accesses and maximum duration for each height.

Height	Total number of accesses	Maximum duration [sec]
400 km	76	300.58
500 km	92	361.31
600 km	103	417.68

6.3 Preliminary ground-to-ground demonstration

This section describes the experimental verification of an end-to-end optical communication link established between LaserCube qualification model and a small portable telescope. The main objective of the test was to familiarize with the challenges related to the establishment of a free space link between two distant terminals. The experiment was carried out in two operational scenarios: first in laboratory environment on a 20 m baseline between the two devices; then, between two university buildings 250 m apart. The candidate contributed with the support of both the design and realization of the tests and to a lesser extent to the analysis of test results. The tests demonstrated the lasercom terminal capability of acquiring and tracking the beacon signal sent by the telescope and of establishing a communication link at 50 Mbps with BER less than 10^{-5}. Please notice that the presented results are in general not representative of the current system performance, due to successive system developments. Some quantitative details have been omitted for intellectual property reasons.

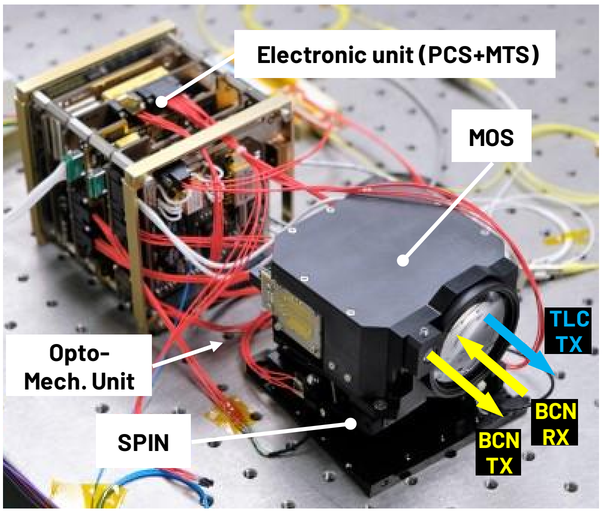

Figure 6-4. LaserCube-Downlink Proto-Flight Model.

The goal of this work is the validation of the LaserCube terminal in a scenario representative of operational conditions. In particular, the objectives are (1) the verification of LaserCube capability of acquiring and tracking the beacon signal transmitted by a remote terminal and (2) the verification of the establishment of a free-space optical communication link with performances that are compatible with commercial applications.

6.3.1 Test setup

First, the test was carried out at the Luxor laboratories of the Institute of Photonics and Nanotechnologies (IFN) in Padova, Italy. The test setup is shown in Figure 6-5 and Figure 6-8. It comprises, on one side, the LaserCube-ISL Qualification Model integrated in a 3U cubesat Structure, mounted on a light motorized mount for manual coarse alignment with the remote terminal. In addition, a power supply and a laptop PC are used to operate and monitor the LaserCube terminal. A pigtailed variable attenuator is used to impose the required attenuation to the 1550 nm telecom laser to get the desired optical power level at the receiver, simulating different link distances. On the other side, at a distance of 20 m, a compact, custom telescope receiver was placed on another light motorized mount. The telescope receiver features a 50 mm optical aperture, a beacon laser transmission path and a reception path that culminates to a fibre mount, as shown in Figure 6-5, bottom right. The latter is used to couple the received optical beam to different detectors through multi-mode fibre. The transmission and reception paths are separated through a dichroic mirror (see Figure 6-5). Two coaxial laser beams are transmitted: a 1064 nm beacon, which is coupled with the narrow-band (5 nm) filter mounted inside the LaserCube optical unit, and a 635 nm beam used for manual alignment purposes. At the receiver end, a 105 nm multi-mode fibre is used to couple the received 1550 nm beam with a commercial APD detector with 1.5 GHz bandwidth (Thorlabs APD450C), the same used on the developed ground segment receiver (see Paragraph 5.2.4). The output of the receiver is fed to a custom electronic receiver which transforms the APD analogue output voltage in a digitized signal and performs signal demodulation and automatic BER evaluation. A 350 MHz bandwidth, 1 GS/s oscilloscope is used to visualize the received modulated signal.

The test was then repeated between two buildings of the University of Padova; the LaserCube terminal was placed in an office of the Department of Industrial Engineering (DII) facing towards the DEI building. The receiver telescope was placed on the rooftop of DEI building.

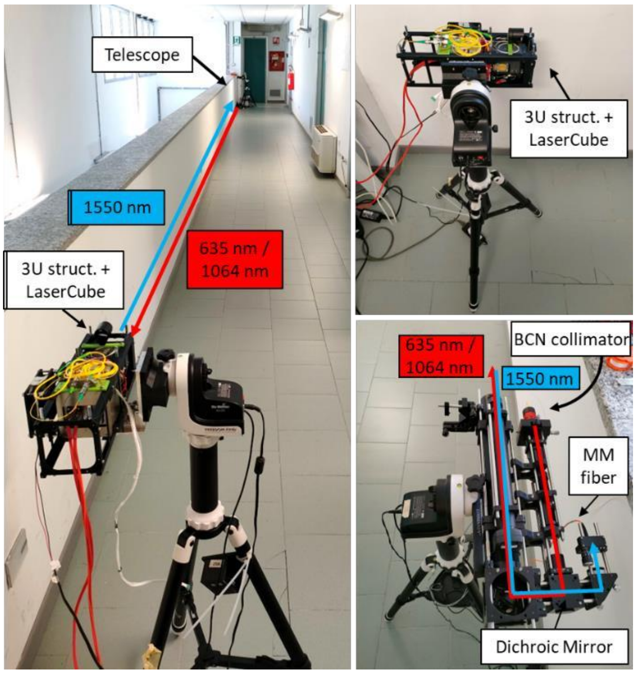

Figure 6-5. Left: test setup arranged on a 20 m laboratory corridor. Top right: 3U structure with LaserCube terminal on telescope mount. Bottom right: receiver telescope.

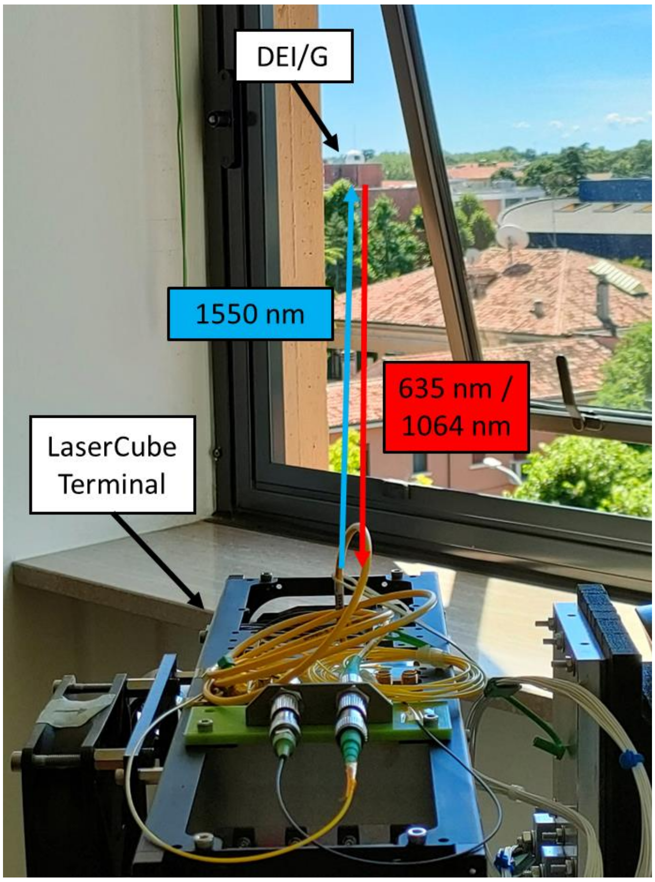

Figure 6-6. View from the DII office; DEI building is visible with no obstruction at a distance of 250 m.

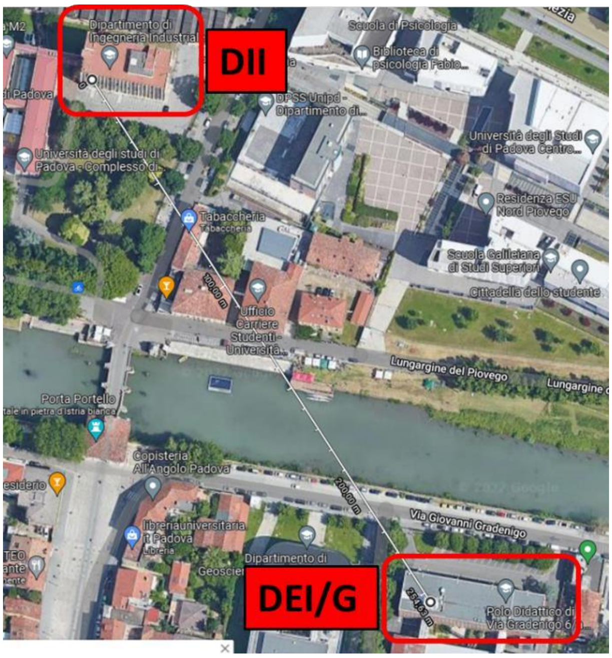

Figure 6-7. Location of the two sites in which the communicating terminals were positioned during the second part of the test.

6.3.2 Test Procedure

First, the telescope mount was manually oriented so that the 635 nm (red) laser spot was centred on the LaserCube main aperture; then, the beam divergence was adjusted by regulating the achromatic collimator so that the beacon spot covered the whole LaserCube aperture. After that, the red laser was turned off and the coaxial 1064 nm beacon was turned on. LaserCube was commanded the acquisition procedure that was completed with success after detection of the 1064 nm beacon, aligning the optical head with the incoming beacon sent by the telescope. Alignment was then checked by turning on the LaserCube 1550 nm telecom laser and verifying that its spot fell into the telescope aperture. The telecom laser was focussed by the telescope lenses and coupled with a 105 µm fibre. The telescope focus was manually finely adjusted by regulating a lens position along the optical path so that the coupling with the fibre was maximized. The optical power collected by the fibre was monitored with the power meter.

Then, RF modulation was applied to the LaserCube 1550 nm telecom laser; a PRBS code was used as modulation sequence, with bitrate of 50 Mbps. The telescope output fibre was connected to the receiver APD, which converts the modulated optical signal to an electrical signal. The latter was first visualized by means of an oscilloscope. Then, the APD was connected to the receiver electronics in order to perform BER measurements. The receiver acquires the modulated signal for 60 s, compares the received bitstream with the expected bit sequence and computes the BER as ratio between the detected bit errors and the total received bits.

The modulated optical signal was attenuated at the transmitter by means of a variable attenuator, so that different power levels were measured at the receiver.

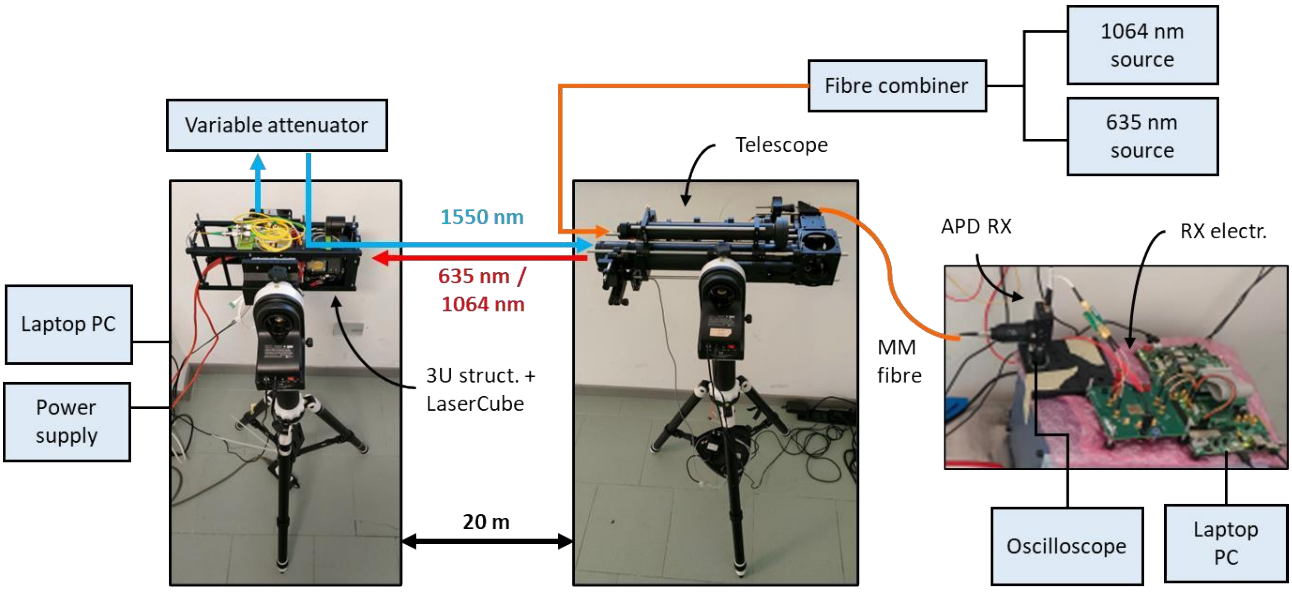

Figure 6-8. End-to-end test setup, comprising the LaserCube terminal on the left and the receiver portable telescope on the right.

6.3.3 Test Results

We present here the main results of the performed tests. Please notice that the presented results are in general not representative of the current system performance, due to successive system developments. Some quantitative details have been omitted for intellectual property reasons.

6.3.3.1 Laboratory Experiment

Measured fibre coupling efficiency at the receiver was 80% with the 105 µm multi-mode fibre, as shown in Figure 6-9; the use of a 200 µm fibre increased efficiency to 92% but the latter was not used since the coupling with the APD was better with the 105 µm fibre (coupling loss are 0.7 dB and 4.1 dB for the 105 µm and the 200 µm fibre, respectively).

Results from BER computation are shown Figure 6-9. Each BER figure is calculated on a sample of 3E9 received bits (50 Mbps for 60 seconds). From these results, a clear BER dependence on received power can be noticed, with BER increasing as received power decreases.. The value BER = 3.33E-10, which corresponds to the inverse of the total amount of received bits+1, was artificially assigned considering the worst case, i.e., the bit after the last received bit was wrong. An example of low received power PRBS signal visualized on the oscilloscope is presented in Figure 6-11.

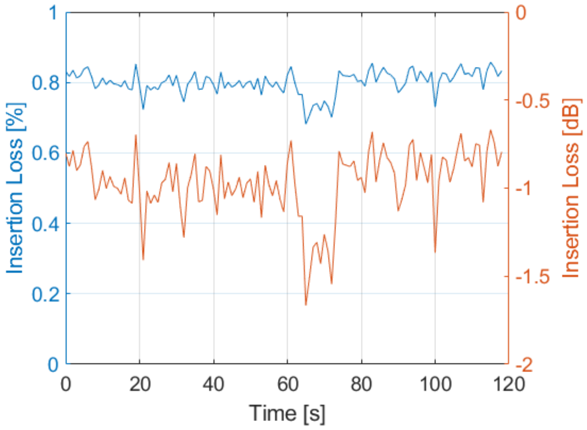

Figure 6-9. Fibre coupling efficiency/insertion loss at the receiver after LaserCube acquisition of telescope beacon.

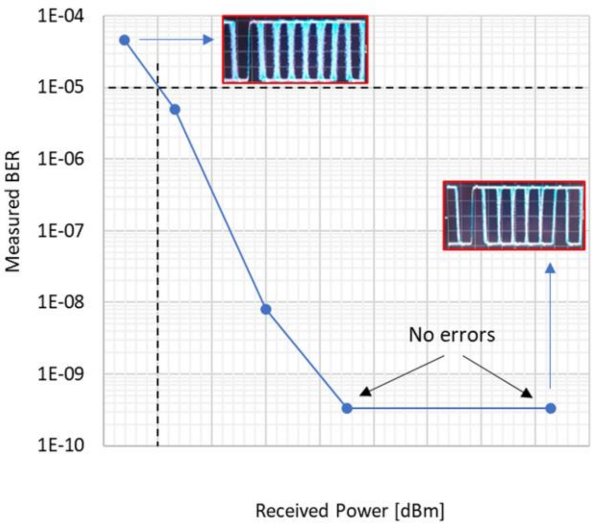

Figure 6-10. Measured BER versus received power. X-axis values have been omitted for intellectual property reasons.

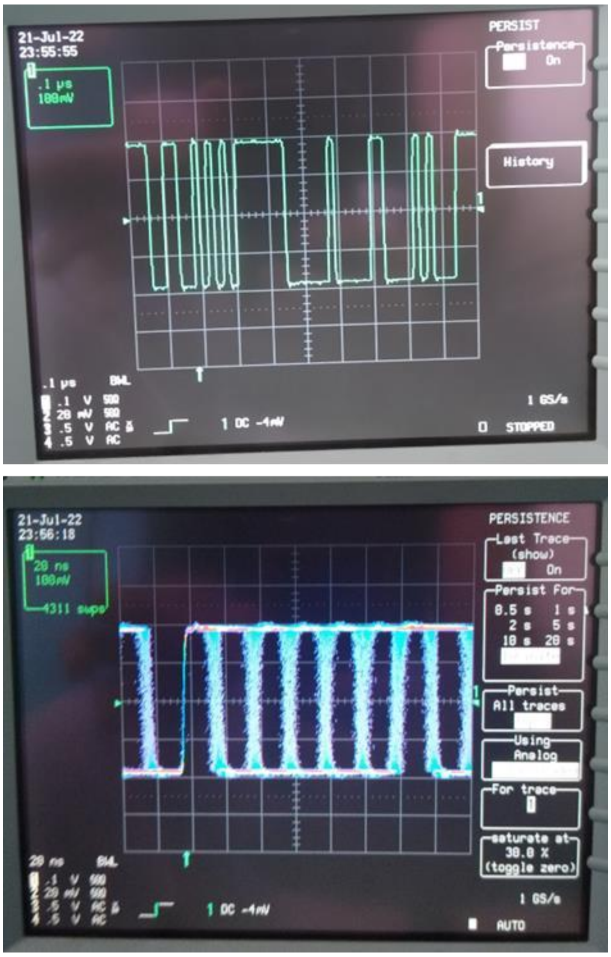

Figure 6-11. PRBS signa visualized on the oscilloscope during laboratory tests, 150 nW received power. Top: bit sequence. Bottom: signal persistence.

6.3.3.2 Field Experiment

In Figure 6-12, the results from the field experiment between DII and DEI buildings are reported, compared to the laboratory test results. The reasons of the minor discrepancy between laboratory and field results are under evaluation.

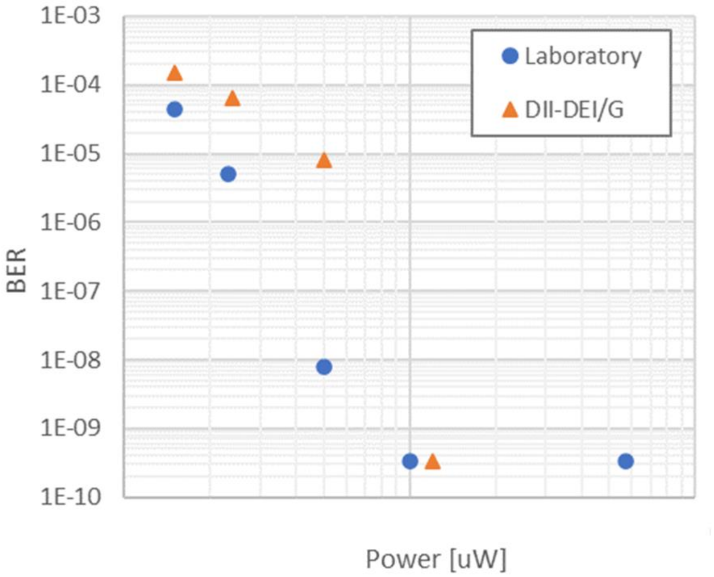

Figure 6-12. Comparison between laboratory test and field test results. X-axis values have been omitted for intellectual property reasons.

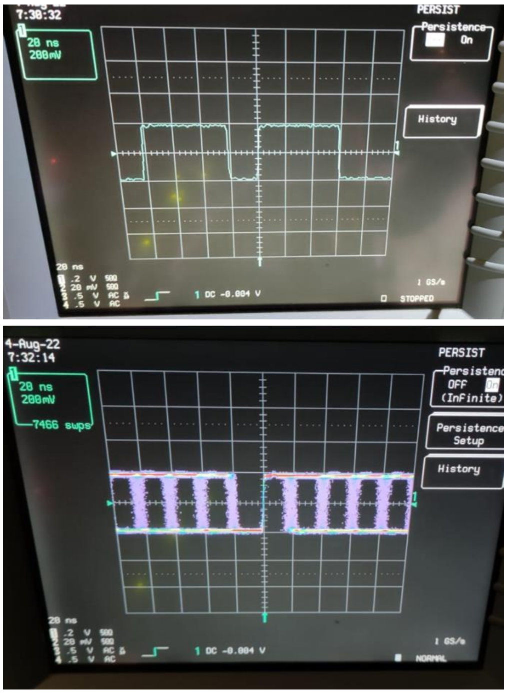

Figure 6-13. PRBS signa visualized on the oscilloscope during field tests, 250 nW received power. Top: bit sequence. Bottom: signal persistence.

6.4 Space qualification tests

6.4.1 Structural qualification

Structural qualification tests have been performed to verify the compliance of the mechanical natural frequencies of the system with mission requirements and to assess the capability of the system to withstand launch loads (random, quasi-static). System compliance is verified if frequency shift after tests remains < 10% and if nominal operation is verified after test completion. The candidate contributed with the support of both the design and realization of the tests.

Test Setup

For the purpose of these tests, LaserCube-DL PFM has been integrated into a 2U CubeSat mock-up structure. The CubeSat structure was fixed between two lateral supports that are used to connect the 2U structure to the test facility, as shown in Figure 6-14 and Figure 6-15. Accelerometers was placed on key spots, as shown in Figure 6-16.

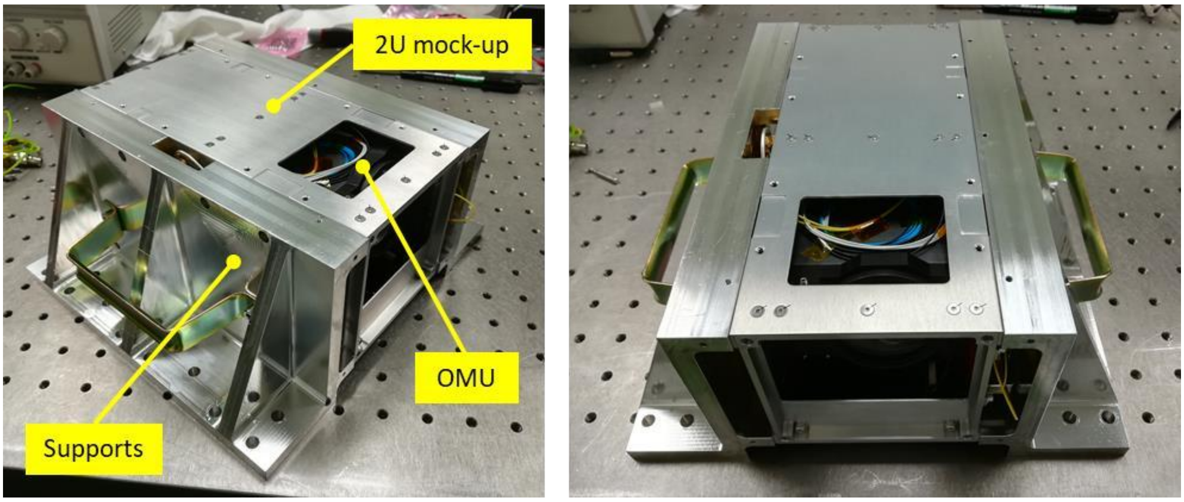

Figure 6-14: LaserCube-DL PFM integrated in the 2U CubeSat structure mock-up.

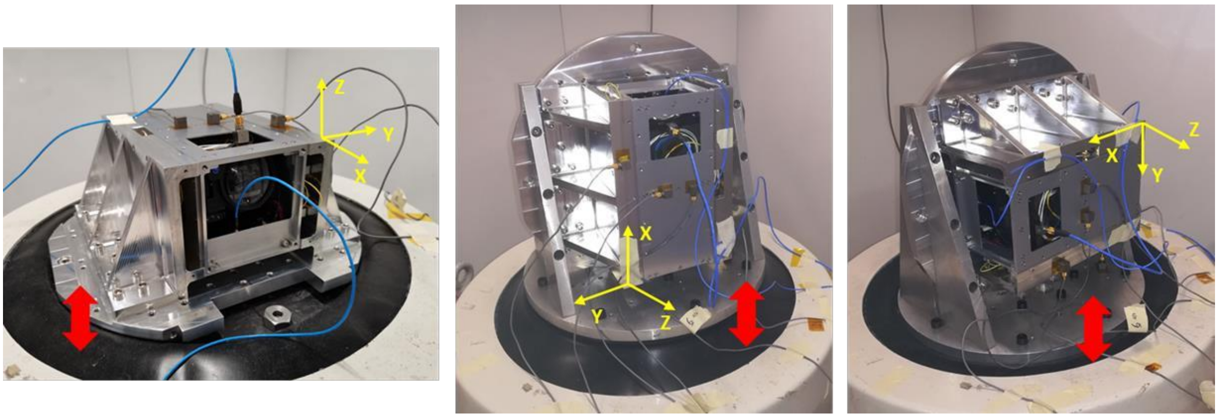

Figure 6-15: System mounted on the shaker facility on the three axes. Red arrow indicates shaking direction. Accelerometers mounted on the test setup are visible.

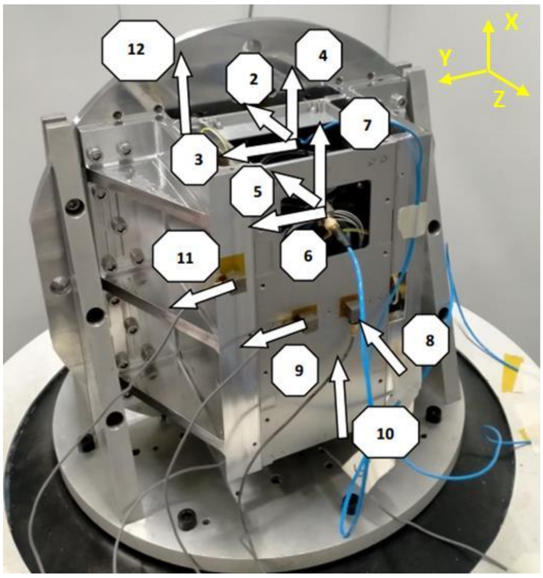

Figure 6-16: Position and labelling of accelerometers.

Test Procedure

The test procedure for each axis was the:

1. Perform modal search.
2. Perform random vibrations.
3. Perform modal search.
4. Perform quasi-static sine.
5. Perform modal search

Sine loads are not necessary since first natural frequency is higher than 150 Hz. However, quasi static tests have been carried out upon request from the candidate platform provider for the LaserCube-DL IOD mission. For quasi-static sine, the sine burst profile shown in Figure 6-15 was adopted; it features a fixed vibration frequency of 20 Hz with increasing acceleration from 0 to 12.5 g, which is kept constant for one second (20 cycles). For random vibration, the adopted profile is the same as described in Paragraph 4.2.4.

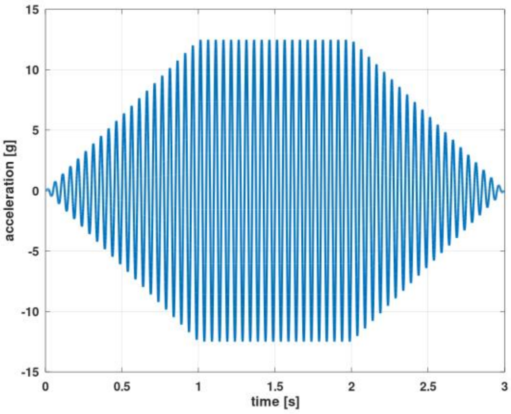

Figure 6-17. Sine burst used for quasi-static loads test.

Test results

The results of the tests showed complete system compliance to launch loads, with a first frequency shift <10% and nominal system operation after test completion. Quantitative results are omitted for intellectual property reasons.

6.4.2 Thermal vacuum chamber qualification

TVAC (Thermal Vacuum Chamber) tests have been performed on LaserCube-DL PFM model to assess system nominal operation in vacuum and in the temperature range -30 / +20 °C. The candidate contributed with the support of both the design and realization of the tests. The goal of the test was to verify that the temperatures of active elements remain within operational range, that peak power consumption is compatible with expected value and that the SMA actuator of the launch lock can be heated up to 200 °C in all operating conditions.

Test Setup

The LaserCube-DL PFM was mounted on an aluminium enclosure that simulates the thermal interface (conductive and radiative) of the satellite payload bay, as shown in Figure 6-18 and Figure 6-19. The enclosure surfaces are all made of transparent-anodized aluminium (emissivity ≈0.8). A dedicated copper thermal strap was mounted to connect the ELU thermal interface to the base of the thermal enclosure, simulating the conductive thermal link to the satellite heatsink. The thermal enclosure was connected to the thermo-mechanical interface of the thermal vacuum chamber by means of eight M5 screws, as shown in Figure 6-19; a graphite conductive thermal pad of thickness 0.07 mm was inserted between the chamber interface and the aluminium enclosure to increase the conductive thermal link between the two elements. Several Pt100 temperature sensors were applied on the payload and on the thermal enclosure to monitor the thermal response of the payload ad the temperature of the conductive and radiative elements of the thermal interface. Several Pt100 probes were also placed on the payload. The thermal enclosure was covered with multi-layer insulation foils. The LaserCube-DL PFM electrical interface was connected to the chamber internal electrical interface; on the exterior, the chamber electrical interface was connected to a power supply unit and a PC with the Graphical User Interface (GUI) used to operate and monitor the payload (see Figure 6-20).

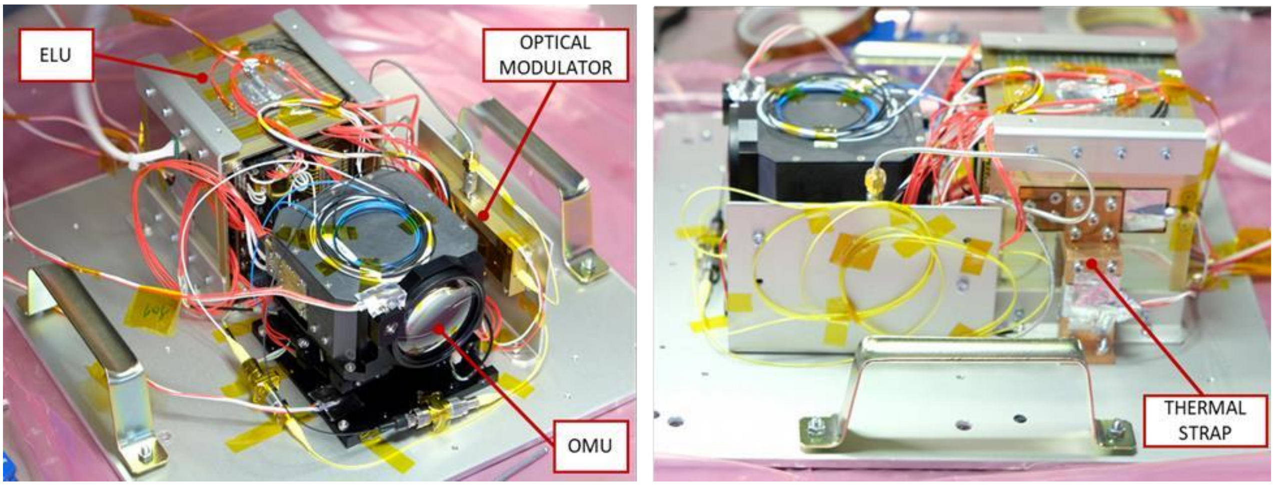

Figure 6-18: LaserCube-DL PFM mounted on the thermal interface for the TVAC tests, with Pt100s placed on OMU, ELU and optical modulator.

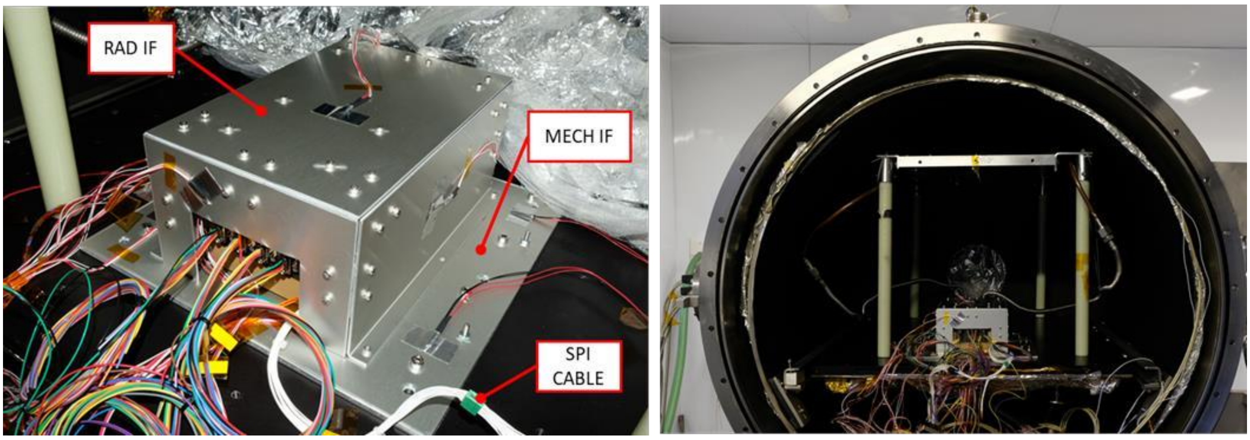

Figure 6-19: Right: thermal interface with enclosure simulating the radiative surfaces of the satellite. Pt100 temperature sensors were placed on all thermal enclosure surfaces. Left: thermal enclosure with LaserCube-DL PFM mounted on the thermal vacuum chamber thermomechanical interface.

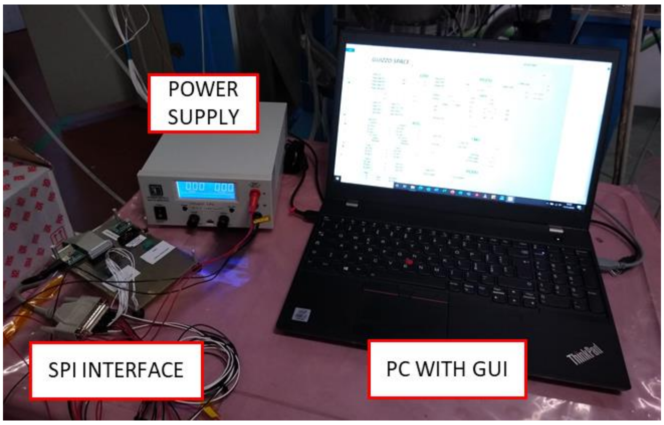

Figure 6-20: Workstation used to operate and monitor the LC-DL PFM during TVAC tests.

Test Procedure

Pressure in the chamber was lowered down to <5e-3 Pa (<5e-5 mbar). Four thermal cycles in the -30 / +20 °C range were applied to the payload, starting from the +20 °C plateau and then proceeding with the -30 °C plateau. The temperature rate used for transitions between temperature limits was set to the maximum achievable with the facility, which is ≈50 °C/h. When the temperature of the thermal enclosure mechanical interface simulating the satellite payload bay was stable at +20 °C with a tolerance of +4 °C or -30 °C with a tolerance of -4°C and with a variation lower than 2 °C/h, the test procedure was executed manually by the operator using the dedicated GUI. The test procedure replicates the sequence of operations of the state machine, simulating all the main system functions: launch lock disengage, system warm up, open loop seeking with coarse pointing stage, beacon and telecom laser activation. Internal temperatures and currents were recorded and saved at 1 S/s, while the Pt100 readings were saved at a lower rate (one sample every 30 s). The payload power consumption was monitored and recorded manually at each step of the procedure.

Test results

Tests results have been obtained in terms of:

- measured temperature of the thermal encloser surfaces (mechanical interface and radiative interface).
- measured temperature of critical elements of the payload during the test sequence.
- measured electrical current and power consumption of the payload.

The test allowed to assess that the system performs nominally at all temperature conditions. Most of the quantitative results are omitted here for intellectual property reasons. Figure 6-21 shows the temperature evolution of the launch lock SMA actuator upon controlled heating during test at +20 °C; the system was capable of heating the actuator up to 200 °C and then stabilize the temperature at that setpoint, confirming the behaviour expected from launch lock thermal analysis (see Section 4.3).

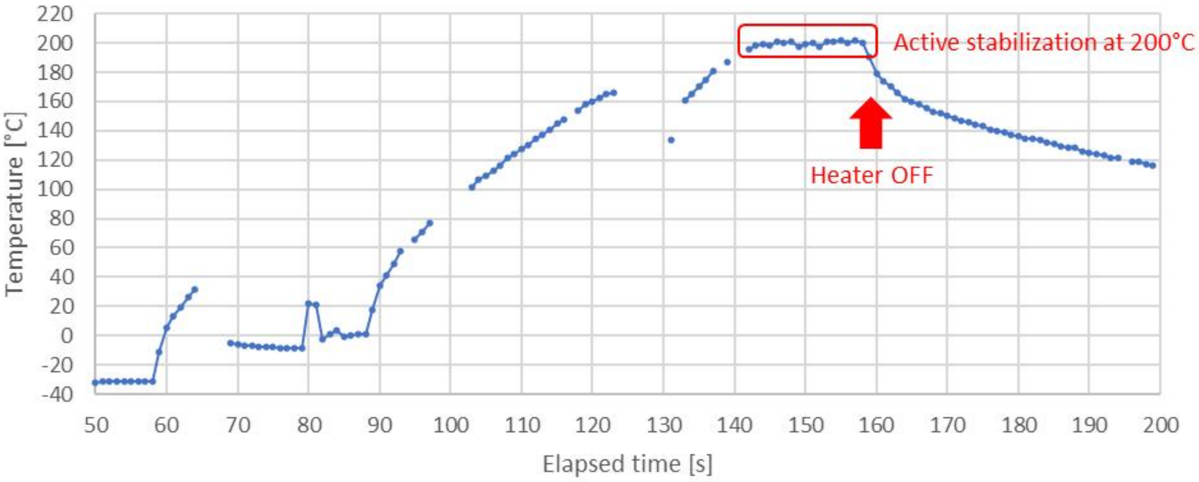

Figure 6-21: Launch Lock actuator temperature evolution during activation, starting from a temperature plateau of -30°C. The system was able to increase and stabilize the actuator temperature at 200 °C.

6.5 Integration on host platform and launch

Once the system passed all the required space qualification activities, the integration of LaserCube in the host platform was performed (Figure 6-22). LaserCube has been launched as a hosted payload on a satellite provided by D-Orbit in the context of the InOrbit NOW (ION) CubeSat deployer mission. The candidate has physically taken part to the integration activities at D-Orbit premises in Fino Mornasco, Italy supporting both the mechanical integration of the payload and the tests necessary to assess that the system functional performance presented no significant difference with respect to tests performed in laboratory.
After the successful payload integration, the satellite was transported to John F. Kennedy Space Center in Cape Canaveral, FL for the launch preparation activities. The launch into orbit took place on 30th of June 2021 onboard the Transporter-2 launcher provided by SpaceX (Figure 6-23).

Figure 6-22: Completion of integration activities on host satellite at D-Orbit premises.

Figure 6-23: SpaceX Transporter-2 launch that put LaserCube into orbit on the 30th of June 2021.

6.6 Preliminary IOD results

LaserCube IOD operations have officially started with launch. The results of the payload commissioning and in-orbit operations are still under analysis; some preliminary results of the in-orbit tests are provided in this section, focusing on the results that allow to assess the validity of the design and analysis activities to which the candidate has provided a direct contribution. Most of the quantitative results of in-orbit tests have been omitted due to intellectual property reasons.

6.6.1 Orbital prediction assessment

To assess the validity and performance of the orbital prediction analysis described in Section 6.2 in a real LaserCube operating scenario, the model has also been applied to GPS data collected during the LaserCube-DL in-orbit demonstration mission. The candidate has mainly contributed to this activity by supporting the definition of the simulation conditions and results interpretation.

The satellite is at a slightly higher altitude (550 km) with respect to GRACE-FO (500 km) and it is smaller in terms of size and mass. In this case, orbit propagation has been carried out using both GPS and TLE data, in order to compare the two methods. Considering the data available between the 18th and the 20th of July 2021, Figure 6-24shows the radius of error spheres obtained after propagation starting with TLE of 18th of July (orange circles), TLE of 19th of July (blue circles) and GPS data (black circles). For GPS data, the EKF was set using 18 GPS acquisitions with a time span of 5 minutes, which corresponds to a 90-minute acquisition period, i.e. a complete satellite orbit. Considering Figure 6-24, vertical lines represent the instant when TLE data are available, so the orange one is for the 18th of July, while the blue one is for the 19th of July. As it possible to see, the error obtained using TLE data is in the order of kilometres, while the error obtained using GPS data is under 50 metres until at least 11 hours after the starting point of propagation and under 150 meters after 24 hours. The validity of the developed orbital prediction analysis model is then confirmed by data acquired during the IOD mission.

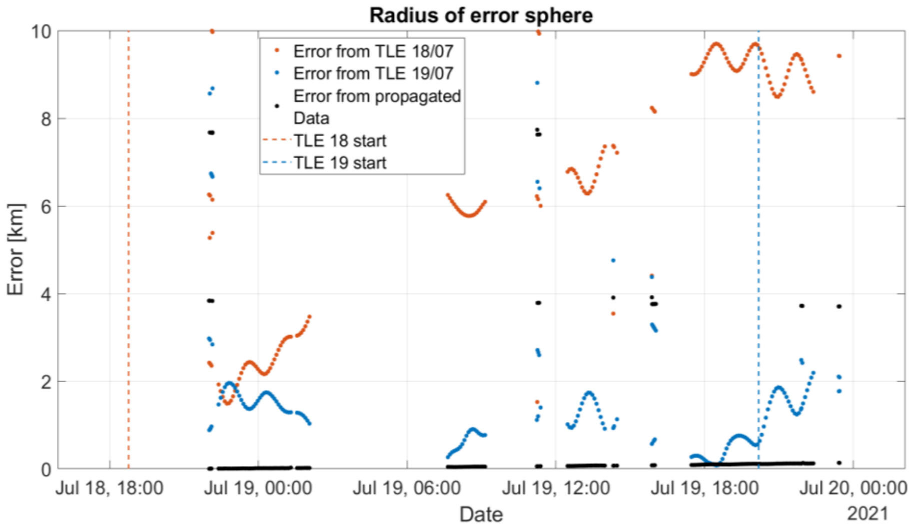

Figure 6-24: radius of sphere error between GPS data and data obtained by TLE of 18th propagation (orange points), data obtained by TLE of 19th propagation (blue points), data obtained from propagation of starting

data (black points). The dotted lines represent time where TLE were available, the orange one is for TLE of 18th of July, while the blue one is for the TLE of 19th of July.

6.6.2 Launch lock activation

A specific test has been dedicated to the assessment of correct launch lock disengage procedure. During the test, the payload correctly switched from Idle mode to Disengage mode and back. A dedicated power line feeds the launch lock SMA actuator; upon heating, current is turned on and off during temperature stabilization of the SMA actuator at 215 °C and finally falls to minimum value after the launch lock optical switch is triggered. Launch lock temperature evolution and trigger commutation of the optical switch are shown in Figure 6-25; the optical switch triggering means that the launch lock screw was successfully broken. In-orbit launch lock activation test results confirmed the thermal behaviour expected from numerical analysis (Section 4.3) and TVAC qualification tests performed on ground (Paragraph 6.4.2).

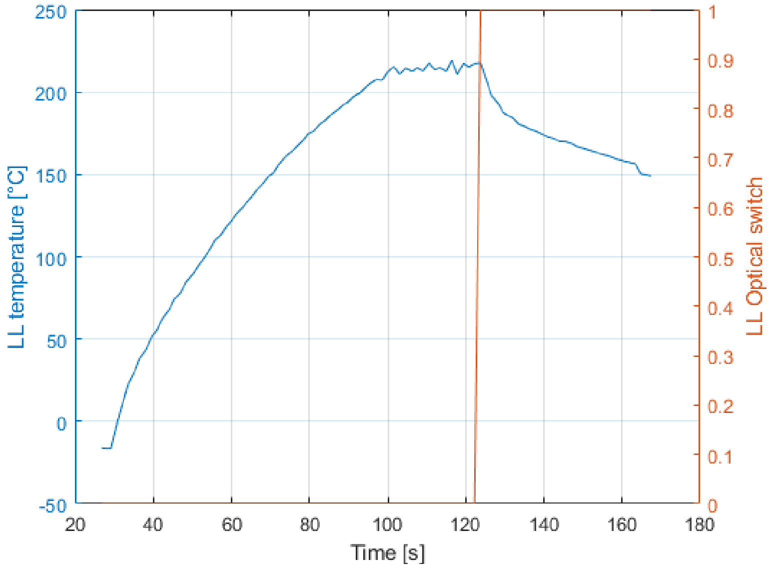

Figure 6-25: Blue plot (left): SMA actuator temperature increase and stabilization at 215 °C; red plot (right): launch lock optical switch triggering (0=untriggered, 1=triggered).

6.6.3 Coarse pointing actuation

When the optical switch is triggered upon disengage procedure completion, the launch lock heater is turned off and the linear actuators of the MPSS move to reach a predetermined setpoint, as shown in Figure 6-26. Both actuators reach their setpoint with error < 1.25 µm, indicating nominal functioning status and successful completion of the operation. An additional telecommand sequence was tested which comprises a manual forward movement of the linear actuators to complete the homing procedure and execution of the spiral trajectory to be performed during the link acquisition phase. Test results are presented in Figure 6-27 and show a good accordance between measured and expected coarse pointing spiral trajectory. The results of the test show that the coarse pointing mechanism has resisted to the launch loads as expected from FEM structural analysis (Section 4.2) and structural qualification tests (Paragraph 6.4.1).

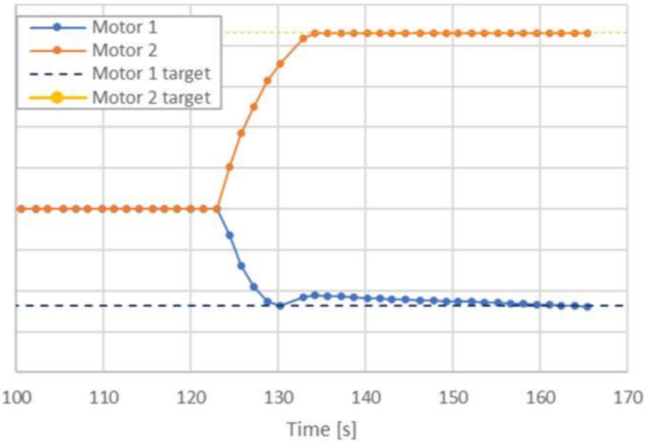

Figure 6-26: Motion of the MPSS linear actuators after triggering of the launch lock optical switch. Y-axis values have been omitted for intellectual property reasons.

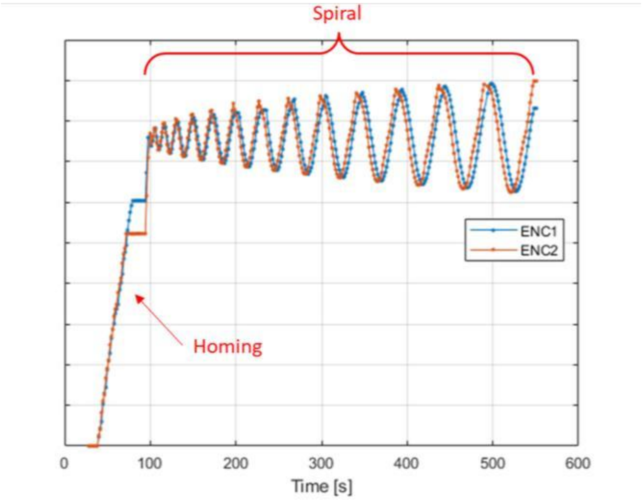

Figure 6-27: Measured elongation of the linear actuators by the encoders, showing the completion of the homing procedure and the subsequent execution of the spiral trajectory. Y-axis values have been omitted for intellectual property reasons.

7. CONCLUSIONS AND FUTURE WORK

We have described here the main activities performed by the candidate during the three years and the most significant scientific and technical achievements. The results obtained during the research project are numerous, both in terms of scientific and technical achievements and of professional education of the candidate. From a technical-scientific point of view, the followed approach has allowed to deeply investigate the challenges relative to satellite optical communications and to identify technical solutions that will benefit the future development of this technology, contributing to a substantial strengthening of the already solid competences of Stellar Project, the start-up company in which the project has been carried out. In particular, the research provides a valuable contribution to the development of the main building blocks that will enable the large-scale adoption of space optical communications in the short and medium term: the analysis and design of innovative applications based on satellite network configurations supported by optical communications; and the design and development of the optical communications space segment and ground segment. The research has also contributed to the development and launch of a technological demonstration mission, with the design, integration and testing of both space segment and ground segment hardware and the analysis of data collected during preliminary commissioning and operational phase of the mission. Finally, the project has led to the development of an optical communication network analysis software tool, that will enable and support the optimization of optical communication constellations.

Due to the peculiar nature of the project, a consistent part of the workload has been dedicated to the support of the start-up company in a wide range of activities, which has contributed to the technical and professional education of the candidate. This includes the delivery of formal documents reporting LaserCube design and test progress, which have been presented during the main development milestones of the system. In this regard, the start-up context has allowed to combine the acquisition of a solid research method with the peculiar soft skills required in an industrial environment, such as the effective interaction with clients, partners and suppliers.

This work will serve as a starting point to address several challenges and promising development directions emerged during the research period. From a satellite network perspective, the in-depth analysis of promising dedicated routing strategies shall be addressed, in order to upgrade the developed software with routing logic capabilities; this will include the analysis of Optical Transport Networks (OTN) based on WDM lightpath routing. Moreover, additional system constraints (such as link acquisition time, payload power and thermal management, data packets management, etc.) should be included in the simulation for more in-depth evaluation of the impact of payload and satellite design choices on the performance at network level. System interoperability at network level should also be investigated, following the guidelines provided by existing and ever-evolving satellite telecommunication standards, like the one devised the by Consultative Committee for Space Data Systems (CCSDS); this will also have an impact on system design both at space segment and ground segment level.

The space segment development shall be focused on the required system improvements suggested by the guidelines derived from application and network analysis, specifically in terms of link range increase at comparable SW&P. In this regard, the feasibility of coherent detection schemes implementation on payloads designed for small satellites shall be evaluated. Moreover, the convenience of pulsed beacon implementation shall be considered for background noise mitigation and beacon power reduction. The integration of QKD modules on CubeSat systems should also be considered a priority for future feasibility investigations.

The development of ground segment technologies shall focus in the first place on the optimization of the developed solutions for more compact, less costly and potentially transportable ground stations; this shall also include the industrialization of production for the reduction of development cost impact. A more in-depth analysis of the impact of atmospheric turbulence on system performance will allow to increase system performance and reduce fading issues, specifically in relation to uplink feeder link development; this may include the implementation of adaptive optics technologies. The development of fast and robust link acquisition strategies for link time maximization and reduction of fading impact on telecommunication performance should be carried out in parallel. Finally, the analysis of optimal ground station distribution will allow to optimize the financial resources dedicated to infrastructure design and construction.

Future in-orbit demonstrations will represent an unvaluable resource for the increase of TRL at component, system and infrastructure level and the consolidation of system design expertise in relation to the development of network, space segment and ground segment solutions.

APPENDIX I: OPTICAL LINK BUDGET

The theoretical background and analytical models used for the development of technologies performed during the project is described below. This includes the description of the link budget design methodology used throughout the doctoral activity and the mathematical models of the main components of the optical systems considered. The general approach and fundamental equations used for LaserCube's telecom and beacon link budget design are presented. Factors typically included in the design of optical fiber communications, such as signal dispersion, have not been taken into account, as fiber length is almost negligibile and free space propagation is not affected by this kind of phenomena.

Telecom

The telecom link budget design involves three main requirements: the distance *D* at which the link will be established, the bitrate R_b and the *Bit Error Ratio* (*BER*).

The selection of a desired *BER* automatically implies a requirement on the *SNR* of the received signal, by means of the equation:

$$BER = \frac{1}{2} erfc\left(\frac{1}{2\sqrt{2}}\sqrt{SNR}\right) \tag{1}$$

where *erfc* is the *complementary error function.*

The *SNR* is by definition the ratio between the power of the signal *S* and the noise power *n* at the detector:

$$SNR = \frac{S^2}{n} \tag{2}$$

Let us first deal with them separately.

If we neglect the components due to undesired optical sources (e.g. albedo, sun, backreflections), noise power can be divided into three main components:

$$n = n_{th} + n_{I0} + n_{sn} \tag{3}$$

Where:

- Thermal noise: $n_{th} = kTB$
- Dark current noise: $n_{I_0} = 2eG_2 I_0 B$
- Shot noise: $n_{sn} = 2eG_2 \mathfrak{R} P_{rx} B$

Here *k* is the Boltzmann constant, *T* is the temperature, G_2 is a statistical parameter describing the detector's gain behaviour, I_0 is the dark current and $\mathfrak{R}$ is the detector's responsivity.
As can be seen from these equations, noise components can be modelled as white noise, i.e. with a flat frequency content. The total noise is then directly proportional to the bandwidth *B* of the detector, which is strictly related to the required data rate R_b of the link. The detector's bandwidth *B* is then a fundamental parameter of the system. Depending on several factors, among which the modulation scheme, a bandwidth efficiency can be defined as the ratio between the data rate R_b and the minimum bandwidth of the detector required to correctly demodulate the bitstream. See e.g. Elganimi (2013) for the relationship between modulation scheme and bandwidth efficiency. In our case:

$$\eta_B = \frac{Rb}{B} = 1 \tag{4}$$

Once R_b has been chosen, a minimum *B* value is then fixed by means of Eq. 4. This value can possibly be increased by a margin factor, keeping in mind that increasing *B* increases the noise at the detector.
It must be highlighted that, in order to obtain the desired bandwidth, conditioning electronics must be used to low-pass filter the detector's output. Otherwise, the detector's bandwidth specified in the datasheet can be used as an adequate approximation, although this clearly does not correspond to an optimal solution.
We now have all the quantities necessary to compute the expected noise at the receiver.

The signal at the detector can be computed as:

$$S = G\mathfrak{R}\eta P_{\mathrm{rx}} \tag{5}$$

where *G* is the gain, $\mathfrak{R}$ is the responsivity and η is the quantum efficiency of the detector and P_{rx} is the received power. We can now combine equations 1 to 5 to compute the required P_{rx} at the detector. It is important to highlight that we refer here to P_{rx} as the peak power received at the detector.

Due to the nature of electromagnetic waves propagation and the non-ideality of components, only part of the transmitted power will reach the detector. The transmitted power P_{tx} required to obtain a received power P_{rx} at the detector can be computed by means of the so-called *radar equation*:

$$\frac{P_{\mathrm{rx}}}{P_{\mathrm{tx}}} = G_{\mathrm{tx}} + G_{\mathrm{rx}} + L_{\mathrm{l}} + L_{\mathrm{p}} + L_{\mathrm{s}} + L_a \tag{6}$$

Where, under the hypothesis of diffraction limited system and ideal gaussian beam:

$G_{\mathrm{tx}} = \frac{4\pi A_{TX}}{\lambda^2}$	*transmitter gain*	(6-a)
$G_{\mathrm{rx}} = \frac{4\pi A_{RX}}{\lambda^2}$	*receiver gain*	(6-b)
L_l	*line losses (from datasheet)*	(6-c)
$L_{\mathrm{p}}\|_{dB} = -12\,(\frac{\varepsilon_P}{FWHM})^2$	*pointing losses*	(6-d)
$L_{\mathrm{s}} = \left(\frac{\lambda}{4\pi D}\right)^2$	*space losses*	(6-e)
L_a	*Atmospheric losses*	(6-f)

Further considerations should be done when computing G_{tx} in case of non-diffraction limited beams. A brief outline is given in Appendix.

We now have a series of equations relating *D*, *R_b* and *BER* and the main system parameters. The output of the telecom link budget design is then the definition of the system parameters whose combination meets the fixed requirements. A general description of the design approach followed in order to converge on a solution is shown in Figure I-1.

Beacon

Although the transmission of the telecom and beacon beams follows similar physical principles, the digital and analogic nature distinguishing the information encoded in the two signals imply a different approach for the link budget design.

A first difference lies in the fact that, while in case of the telecom signal the SNR was derived through Eq. 1 following the BER requirement, no digital communication is involved in the beacon signal. For this reason, the SNR will be derived in this case by the tracking control requirements, as the minimum SNR necessary to compensate for the satellites motion and attitude jitter and perform mutual tracking with the required accuracy. This value is difficult to estimate *a priori* and should be verified experimentally. A preliminary SNR value of 10^4, derived by means of numerical simulations, has been assumed.

A second difference lies in the fact that the necessary detector's bandwidth is not derived from the digital signal demodulation but by the closed-loop tracking bandwidth requirement. In our case, the closed-loop tracking control operates at 1 ksps and is designed to reject disturbances up to about 100 Hz. This theoretically imposes a bandwidth of the QD of circa 100 Hz. Nevertheless, if no conditioning electronic is envisaged to reduce the effective bandwidth of the sensor, the entire sensor bandwidth specified in datasheet must be considered. The expected noise can then be computed from the QD’s bandwidth and noise figures, expressed as Noise Equivalent Power (NEP). Additional noise due to electronic hardware or environmental exposure should be taken into account as well.

Once the expected noise and required SNR are computed, the required received signal power can be immediately derived. The same approach described relatively to the telecom case can then be followed in order to compute the required transmitted beacon power, by means of Eq. 5. A general description of the design approach followed in order to converge on a solution is shown in Figure I-1

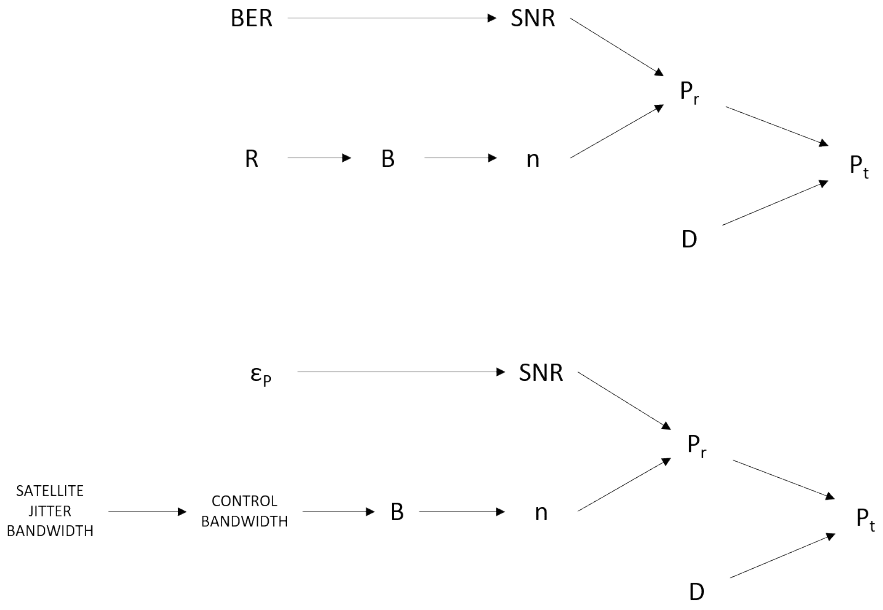

Figure I-1: Schematic representation of the procedure for the derivation of the main system parameters followed during the iterative design phase. Top: TLC; bottom: BCN.

APPENDIX II: LINK ACQUISITION ANALYSIS

A specific analysis has been performed to study the optical communications criticalities in terms of time of link acquisition. A quantitative analysis of the acquisition problem is given in [75]. In the present work, the problem of the beacon acquisition has been further analyzed numerically and experimentally, with focus on the small satellite case. The content of this work has been published in [76].

Acquisition problem definition

In order to establish a reliable optical cross–link, the lasercom terminals onboard two satellites must achieve Line of Sight (LOS), i.e. they must orient their optical aperture along the ideal line connecting the satellites so that the pointing error is lower than the transmit laser beamwidth. The required pointing accuracy is extremely challenging due to the narrowness of optical beams. Considering laser wavelengths in near infrared range between 800nm and 1550nm, which are commonly used, and main optical aperture of 50mm for a terminal suitable for small satellites, the transmit laser beamwidth is 20–50 µrad; on medium / large satellites the beamwidth decreases to 5–15 µrad, assuming an aperture of 150mm. Beacon laser used for pointing purposes are typically emitted through secondary optical apertures [70] [77], resulting in laser beamwidths in the order of 0.1–1 mrad. Required pointing accuracy is a fraction of the transmit laser beamwidth in order to minimize losses. Such accuracy is hardly feasible in open loop because of the limits of satellites Attitude Determination and Control System (ADCS). This is particularly true for small satellites, even if equipped with state-of-the-art technology [78] [79] [80].

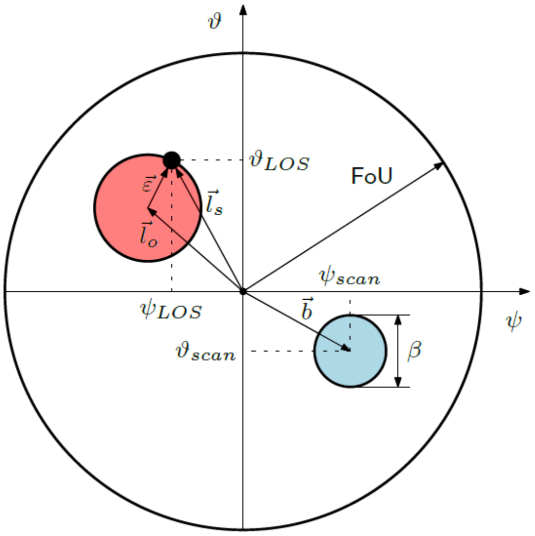

Figure II-1: Depiction of the beacon acquisition problem. The FoU is scanned by the beacon laser with beamwidth until it overlaps the current position of the partner satellite $\boldsymbol{\overrightarrow{l_s}}$.

In fact, the field of uncertainty (FoU), i.e. the uncertainty on the LoS direction in the reference frame fixed to the satellite, is typically larger than the transmit laser beamwidth. Thus, precise pointing is achieved by tracking a beacon laser that is transmitted by the partner satellite; mutual tracking is required in order to transmit and receive correctly over optical channel. Since the transmit laser beamwidth is smaller than the FoU, an acquisition procedure must be performed, during which the two terminals point towards each other in open loop relying on the predicted orbital positions of the satellites. Then, each terminal scans its beacon beam over the FoU, until the beam is detected by the partner satellite which can lock on it and start tracking. The process is complete when both satellites have acquired and are tracking the beacon beam coming from the partner satellite. The problem is pictured in Figure II-1, showing the FoU region in the satellite–fixed reference frame (ψ, θ), which correspond to azimuth and elevation, the current position of the transmit beacon beam scanning the FoU $\vec{b} = (\psi_{SCAN}, \theta_{SCAN})$ with beamwidth β, the current LoS vector $\overrightarrow{l_s} = (\psi_{LOS}, \theta_{LOS})$ in the satellite–fixed reference frame and the LoS vector in the orbital reference frame $\overrightarrow{l_o} = (\psi'_{LOS}, \theta'_{LOS})$. The vectors $\overrightarrow{l_0}$ and $\overrightarrow{l_s}$ do not coincide because of the attitude jitter $\vec{\varepsilon}$ of the transmitter satellite, that generates a dynamic discrepancy between the satellite-fixed and the orbital reference frames. Acquisition of the beacon beam by the partner satellite occurs when the blue circle, representing the beacon beam, overlaps the actual position $(\psi_{LOS}, \theta_{LOS})$ of the partner satellite. Both $\vec{b}$ and $\overrightarrow{l_s}$ vary with time. The main contributors to the FoU are: the uncertainty of the satellite ephemeris, the ADCS accuracy and stability, the mechanical/optical misalignments between the lasercom terminal and the satellite bus. Typical values for FoU contributions are summarized in Table II-1. Attitude pointing accuracy of small satellites is generally between 0.05 deg and 0.5 deg, depending on the ADCS hardware. Best performance are achieved with the use of star trackers (attitude knowledge accuracy 0.05 deg 3σ) and a full complement of reaction wheels and magnetorquers. The FoU represents the capability of pointing a given direction with a constant error. Satellite attitude is also subjected to jitter in the form oscillations along the pointing direction due to external disturbances and reaction wheels unbalance. Reference values of satellite jitter spectrum can be found in [81] [82] [83] [84].

Table II-1: Main contributors to FoU during acquisition phase for optical crosslinks.

FoU contribution	LEO–LEO small sats	LEO–GEO medium / large sats [13]
Ephemeris	0.050 deg	0.025 deg
ADCS accuracy	0.200 deg	0.150 deg
Misalignments	0.100 deg	0.050 deg
Total	0.229 deg	0.160 deg

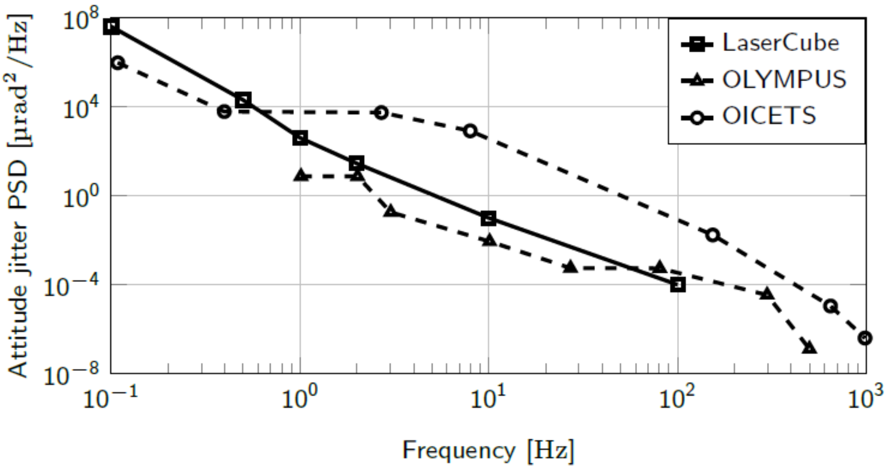

Figure II-2: Attitude jitter PSD of the satellite (data from the literature). The same PSD used for LaserCube **[83]** has been used in this work.

Acquisition approaches

In this work, two different approaches to scan the FoU with the beacon beam are defined: spiral search and snakelike search. They are shown in Figure II-3 and Figure II-4, respectively. In the first case, the transmit beacon beam follows a simple Archimedean spiral trajectory in the (ψ, θ), space starting from the FoU center. In polar coordinates, the current value of the spiral radius is proportional to the cumulative angle swept since the initial time. The pitch of the spiral is the radius increment occurred between two consecutive revolutions. In order to guarantee the full coverage of the FoU, the pitch is less than or equal to the beacon beamwidth.

In the second case, the scanning trajectory follows a repetitive linear sweep pattern along the elevation coordinate, with a movement equal to the FoU diameter and starting at one extreme point of the FoU. Once the opposite extreme position in elevation is reached, scanning direction is inverted after a step displacement in the azimuth direction. This base sequence is repeated until the whole FoU is covered. Also in this case, the azimuth step is less than or equal to the beacon beamwidth.

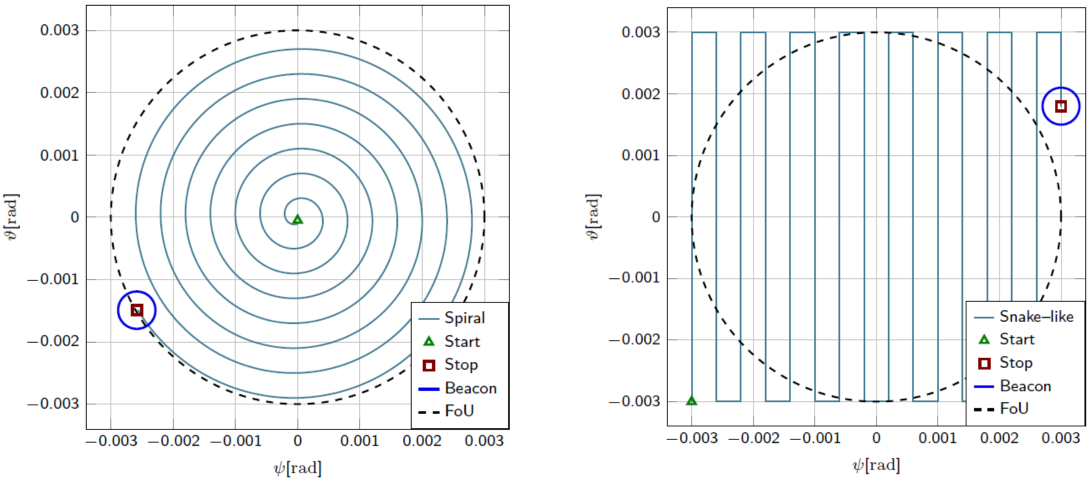

Figure II-3: Spiral (left) and snake-like (right) trajectories. The blue circle represents the beacon beamwidth.

Numerical analysis

Performance of each FoU scanning approach has been evaluated numerically. The dynamic process of FoU scanning has been simulated taking into account the parameters that play a key role in the process, namely the type of scanning path, the FoU radius, the satellite attitude jitter, the transmit beacon beamwidth. The simulation workspace is summarized in Table II-2. The LoS components $(\psi'_{LOS}, \theta'_{LOS})$ of the $\overrightarrow{l_0}$ vector are modeled as normal distributions with standard deviation σ_{LOS}. For each simulation, the initial LoS $\overrightarrow{l_0}$ of the partner satellite was randomly set within the FoU region and then it was perturbed adding the satellite jitter $\vec{\varepsilon}$ so that the true LoS in the satellite reference frame was $\overrightarrow{l_s} = \overrightarrow{l_0} + \vec{\varepsilon}$. The jitter time profile for each simulation was generated as a sum of sine waves combined with random phase, approximating the LaserCube jitter PSD shown in Figure II-2. FoU radius is set equal to $3\sigma_{LOS}$.

Table II-2: Space of parameters considered for the numerical simulations.

Parameter	Range
Scanning mode	spiral / snake–like
LOS uncertainty σ_{LOS}	0.5–5 mrad
FoU radius	$3\,\sigma_{LOS}$
Beacon beamwidth β	300 µrad
Trajectory step	$\frac{2}{3}\beta$
Scanning velocity	5 mrad/s

Two performance parameters have been identified: the probability of beacon acquisition Pacq and the average time required for acquisition Tavg. For evaluation of the performance parameters, a Monte Carlo approach was adopted: for each combination of trajectory profile and σ_{LOS}, a 20000– simulation batch was run. Then, for each simulation batch, the probability of acquisition was calculated as the ratio between the amount of runs for which the beacon beamwidth overlapped the current LoS and the total amount of runs. The average time required for this event was calculated considering only successful scanning sequences. The amount of Monte Carlo trials for each simulation was selected as a good compromise between computational time and uncertainty of the results. It was observed that 20000 trials were sufficient to reduce the results uncertainty below 1%. This was estimated by running ten 20000-trial simulations with a given set of parameters; then, the standard deviations σ_P and σ_T of P_{ACQ} and T_{AVG} were calculated and compared to the average values P_{ACQ} and T_{AVG}. The relative errors were calculated as

$$\varepsilon_P = \frac{\sigma_P}{P_{ACQ}} \qquad \varepsilon_T = \frac{\sigma_T}{T_{AVG}}$$

which are good indicators of the uncertainty of the results.

Table II-3: Evaluation of uncertainty of the results from numerical simulations. Selected set of parameters: spiral trajectory, FoU of 9 mrad, 20000 trials per simulation.

Simulation	P_{acq} [%]	T_{acq} [s]
1	78.89	51.40
2	78.15	50.93
3	78.16	51.51
4	77.85	51.41
5	77.16	51.51
6	78.20	51.35
7	77.78	51.40
8	77.46	50.77
9	77.40	51.88
10	77.90	51.31
Average	77.70	51.35
Standard deviation	0.52	0.20
Relative error [%]	0.67	0.39

The process is described in Table II-3. Results of the simulation campaign are reported in Figure II-5 and Figure II-6. The probability of beacon acquisition increases for larger values of σ_{LOS}, which correspond to larger values of FoU radius. From values of σ_{LOS} larger than 2 mrad (FoU radius larger than 6 mrad), which is the maximum jitter amplitude according to the adopted jitter PSD, the probability of acquisition stabilizes around 80%. This is because in these cases the satellite jitter is no more comparable with the FoU radius. The snake–like trajectory offers a slightly larger probability of acquisition for lower values of FoU radius. As regards the average time required for acquisition, it increases quadratically with FoU radius. The spiral trajectory is advantageous because of a significant lower T_{AVG} (one third with respect to the snake–like trajectory). The reason for this lies in the starting position of the scanning trajectory that, in the case of the spiral, is at the center of the FoU, where the probability of finding the target satellite is larger.

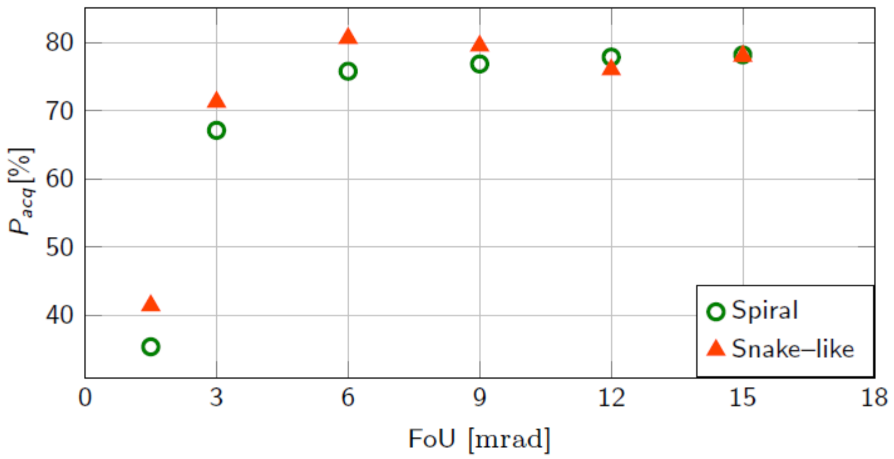

Figure II-4: Probability of beacon acquisition as a function of scan trajectory type (spiral vs snake-like) and FoU (set to 3 LOS).

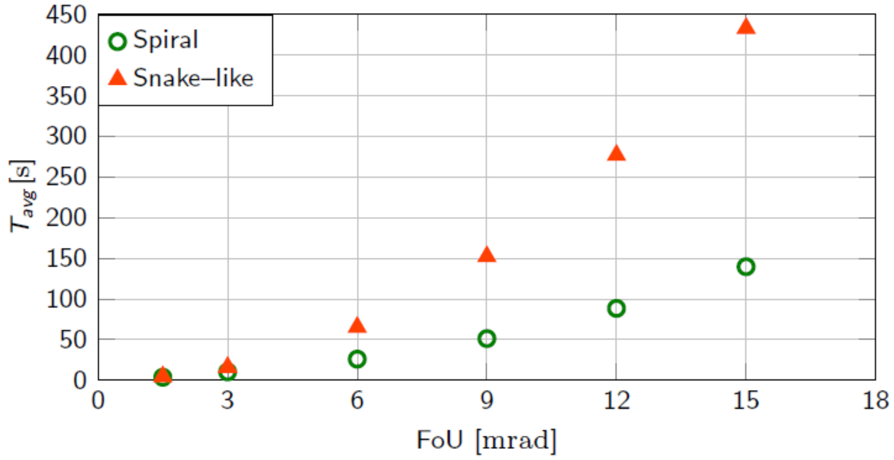

Figure II-5: Average acquisition time as a function of scan trajectory type (spiral vs snake-like) and FoU (set to 3 LOS).

Experiment

To validate the results of the numerical simulations, experimental tests have been designed and carried out in laboratory environment. The test setup (Figure II-7) is composed of an Optical Assembly (OA) mounted on a two degrees–of–freedom (i.e. azimuth and elevation) motorized gimbal (STANDA 8MR151- 1-MEn1, micro–step resolution 1.36 µrad), a 900nm pigtailed diode laser connected to a collimator, and a piezo–electric Fast Steering Mirror (FSM, PI S-330.2SH, resolution 0.05 µrad).

The collimated laser beam is aimed at the FSM which reflects it towards the OA; a manually adjustable mirror is used to fine adjust the laser direction before testing. The OA comprises a 50mm lens focusing the incoming beam on a Quadrant Detector (QD, First Sensor QP50-6-42u SD2), allowing to measure the direction of the incoming laser beacon with an uncertainty of 11 µrad rms. The gimbal–mounted OA represents the lasercom terminal scanning its FoU, while the collimator represents the remote partner terminal; the laser beam is used to measure with the QD the current misalignment of the OA with respect the true LoS connecting the two terminals. When such misalignment is lower than half of the beamwidth β of the laser ideally transmitted by the OA, the scanning procedure is considered successful and it is interrupted. The time required for this event to occur is recorded with a resolution of 0.1 s. At the start of each scanning sequence, a random misalignment between the laser and the OA optical axis is imposed, with a normal distribution equal to σ_{LOS} as described previously. The purpose of the FSM is to simulate the satellite attitude jitter by imposing a controlled deviation to the laser beam, since the effect of jitter is equivalent to a deviation of the incoming beam direction. An example of jitter imposed by the FSM in the time domain is shown in Figure II-8. Both the motorized gimbal and the FSM are controlled by microcontroller boards (STM NUCLEO-L476RG board and STM X-NUCLEO-IHMO2A1 stepper motor driver) programmed via MATLAB/Simulink autocoding tools.

The FoU scanning procedures have been performed replicating the conditions simulated in the numerical analysis described but covering only a subset of the space of parameters presented in Table II-2 because of the long time required to perform an amount of test trials that gives a decent statistical coverage. Probability of acquisition and average acquisition time have been measured for the selected scenarios and compared to numerical results.

The experimental results are presented in Table II-4 and Figure II-8 shows a typical test result: the OA pointing error with respect to the true LoS is plotted along with a flag which is raised only when the pointing error is below the $\beta/2$ threshold. The FoU values covered are 6 mrad and 9 mrad for both trajectory types. The experiments qualitatively confirm the results obtained with the simulations, in that the snake-like trajectory requires a considerably longer time for the beacon acquisition, with respect to the spiral trajectory. This can be explained by the fact the spiral trajectory starts from the direction of highest estimated probability of acquisition. A quantitative discrepancy can instead be observed with respect to the simulations, which show an approximately constant ratio between the acquisition time obtained through the two types of trajectory. This difference could be explained by the lower number of scanning sequences (up to 15) for each FoU number, due to the higher time required to perform the experiments, which may not allow to reach complete statistical convergence. Results concerning the probability of acquisition also highlight a slightly different behavior with respect to simulations, since no difference emerged between the two types of trajectory. The same observations concerning the relatively low number of scanning sequences can be made in this respect.

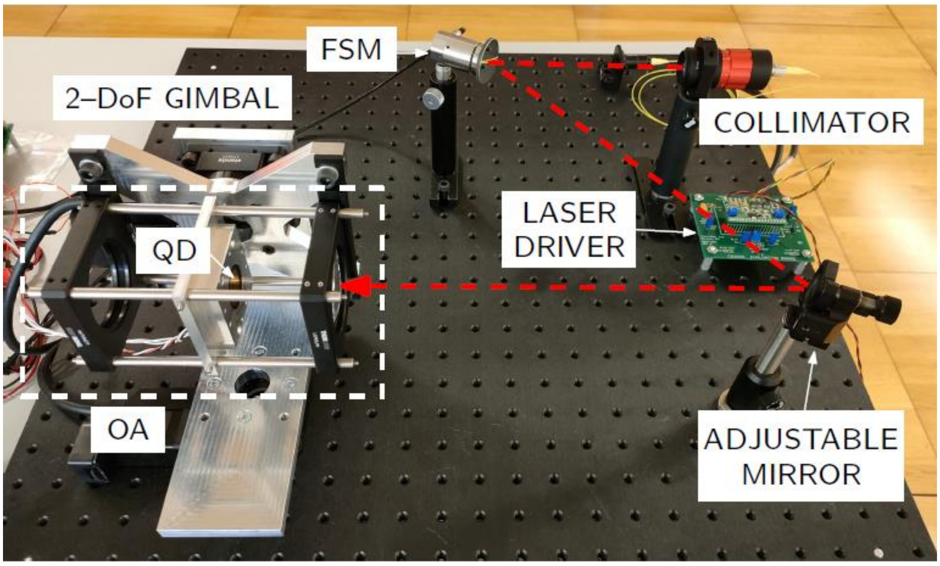

Figure II-6: Test setup.

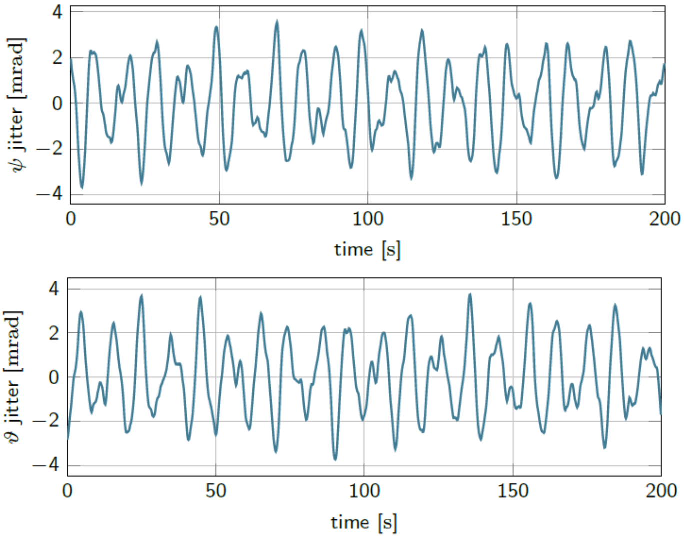

Figure II-7: Example of random jitter generated according to the profile shown in Figure II-2.

Conclusions

This work analyses the beacon acquisition problem for the establishment of mutual tracking between two satellites, which is required for optical crosslinks. Each satellite sends a beacon laser towards the direction of the partner satellite, which is known with a given uncertainty; scan of the field of uncertainty (FoU) is required since the beacon beamwidth is typically smaller than the FoU. The analysis focuses on small satellites inLEO. Two different techniques to scan the FoU are quantitatively compared in terms of probability of acquisition and mean time required for acquisition, taking into account the typical pointing accuracy and attitude jitter of small satellites. Comparison is carried out first through numerical simulations, with a Monte Carlo approach. Then, a simplified, yet representative laboratory experiment is performed and the results are compared to the numerical simulations. According to the results, a spiral trajectory is more time efficient than a snake-like one, but the latter can provide a slight advantage in terms of probability of acquisition in case the satellite jitter is comparable with the FoU radius.

Future work shall include the continuation of the experimental campaign, in order to cover the entire space of parameters and to improve the statistical significance of the results. An interesting extension of the analysis could address the mutual acquisition of two terminals, for which the optimization of the scanning approach may be required, or other types of scanning trajectory (e.g. random walk).

Table II-4: Average acquisition time and probability from experiments with comparison to simulation results.

FoU [mrad]	Trajectory	T_{avg} [s]		P_{acq} [%]	
		Exp.	Sim.	Exp.	Sim.
6	Spiral	28.5	26.1	86.7	75.8
	Snake–like	73.1	65.5	93.3	80.7
9	Spiral	37.9	51.4	71.4	76.9
	Snake–like	218.1	152.3	71.4	79.5

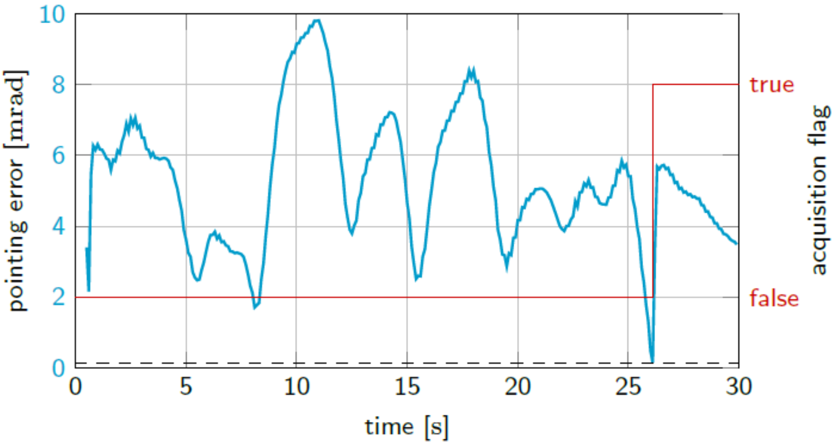

Figure II-8: Example of successful beacon acquisition. When the pointing error (blue plot) is below the threshold of half beacon beamwidth (=2), a flag is raised (red plot) and the acquisition process is considered successful. This particular example is referred to snakelike trajectory and FoU of 6 mrad.

REFERENCES

[1] S. -. S. E. Academy, «New Space Economy,» 2022. [Online]. Available: https://seac-space.com/new-space-economy/#:~:text=New%20Space%20Economy%202022%20represents,Space%20Race%2C%20together%20with%20new. [Consultato il giorno 30 November 2022].

[2] OECD, Handbook on Measuring the Space Economy, 2nd Edition, 2022.

[3] K. Devaraj, «Planet high speed radio: crossing Gbps from a 3U CubeSat,» in *33rd AIAA/USU Small Satellite Conference*, Logan, USA, 2019.

[4] K. Leveque, «Unlocking the next generation of nano-satellite missions with 320 Mbps Ka-band downlink: on-orbit results,» in *33rd AIAA/USU Small Satellites Conference*, Logan, USA, 2019.

[5] H. Hemmati, Near-Earth Laser Communications, 2nd edition, CRC Press, 2021.

[6] Euroconsult, «Prospects ofr the Small Satellite Market,» 2019.

[7] Northern Sky Research, «Small Satellite Markets 5th Edition,» 2019.

[8] Fortune Business Insights, «Small Satellite Market, 2021-2028.,» 2022.

[9] Valuates Reports, «Small Satellite Market, 2021-2030,» 2021.

[10] Allied Market Research, «Small Satellite Market, 2021-2030,» 2021.

[11] Institute for Defense Analyses, «Global Trends in Small Satellites,» 2017.

[12] Allied MArket Research, «Satellite-Based Earth Observation Market, 2021-2030,» 2022.

[13] EUSPA, «EO and GNSS Market Report,» 2022.

[14] European Commission, «Big Data in Earth Observation,» 2017.

[15] Data Center Frontier, «Terabytes From Space: Satellite Imaging is Filling Data Centers,» April 2020. [Online]. Available: https://datacenterfrontier.com/terabytes-from-space-satellite-imaging-is-filling-data-centers/. [Consultato il giorno 29 September 2022].

[16] Data Center Frontier, «BigData From Space: How Satellite Launches Power Cloud Growth,» 2021. [Online]. Available: https://datacenterfrontier.com/bigdata-from-space-how-satellite-launches-power-cloud-growth/. [Consultato il giorno 29 September 2022].

[17] The Economic Times, «Satellites are generating tonnes of data in space. Beaming it back to earth is a problem,» 2022. [Online]. Available: https://economictimes.indiatimes.com/small-biz/entrepreneurship/satellites-are-generating-tonnes-of-data-in-space-beaming-it-back-to-earth-is-a-problem/articleshow/89631138.cms. [Consultato il giorno 29 September 2022].

[18] Northern Sky Research, «Space Traffic Study, 2nd edition,» 2022.

[19] Acumen Research and Consulting, «Satellite Internet Market Share, Analysis Report and Region Forecast, 2022 - 2030,» 2022.

[20] M. S. Ville, «Laser Communication Terminals Market 2022: Industry Size, Regions, Emerging Trends, Growth Insights, Opportunities, and Forecast By 2030,» 2022.

[21] Planet Labs, "Planet Labs Specifications: Spacecraft Operations & Ground Systems," 2015.

[22] Iceye, “SAR Product Guide v4,” 2021.

[23] ESA, «How space data are transforming the global food system,» 2022. [Online]. Available: https://earth.esa.int/eogateway/news/how-space-data-are-transforming-the-global-food-system. [Consultato il giorno 29 September 2022].

[24] B. Systems, «SAT100 Satellite Modems Provides Improved Real-Time Groundwater Monitoring,» [Online]. Available: https://www.scadalink.com/products/satscada/hydrology-and-hydrogeology-applications/groundwater-monitoring/. [Consultato il giorno 29 September 2022].

[25] J. d. Leeuw, A. Vrieling, A. Shee, C. Atzberger, K. M. Hadgu, C. M. Biradar, H. Keah and a. C. Turvey, “The Potential and Uptake of Remote Sensing in Insurance:,” *MDPI Remote Sensing,* vol. 6, pp. 10888-10912, 2014.

[26] W. Vroege, T. Dalhaus and R. Finger, “Index insurances for grasslands – A review for Europe and North-America,” *Agricultural Systems,* vol. 168, pp. 101-111, 2019.

[27] H. Greatrex, J. Hansen, S. Garvin, R. Diro, S. Blakeley, M. L. Guen, K. Rao and D. Osgood, “Scaling up index insurance for smallholder farmers: Recent evidence and insights,” CGIAR Research Program on Climate Change, Agriculture and Food Security (CCAFS), 2015.

[28] International Fund for Agricultural Development (IFAD), “Remote sensing for index insurance - Findings and lessons learned for smallholder agriculture,” 2017.

[29] O. Insights, «The fastest and easiest way to use location data to answer your organization’s questions.,» [Online]. Available: https://orbitalinsight.com/. [Consultato il giorno 29 September 2022].

[30] R. Metrics. [Online]. Available: https://rsmetrics.com/. [Consultato il giorno 29 September 2022].

[31] E. D. Analytics, «Real-estate management,» [Online]. Available: https://eos.com/industries/real-estate-management/. [Consultato il giorno 29 Septembr 2022].

[32] Starlab, «Stalab Space,» [Online]. Available: https://www.starlab.es/space. [Consultato il giorno 29 September 2022].

[33] A. Khan, S. Gupta and S. Gupta, “Multi-hazard disaster studies: Monitoring, detection, recovery, and management, based on emerging technologies and optimal techniques,” *International journal of disaster risk reduction,* no. 47, p. 101642, 2020.

[34] P. C. Oddo and J. D. Bolten, “The value of near real-time Earth observations for improved flood disaster response,” *Frontiers in Environmental Science,* no. 7, p. 127, 2019.

[35] ESA, “European quantum communications network takes shape,” [Online]. Available: https://www.esa.int/Applications/Telecommunications_Integrated_Applications/European_quantum_communications_network_takes_shape. [Accessed 29 September 2022].

[36] D. A. Fritz, “Military satellite communications: Space-based communications for the global information grid,” *Johns Hopkins APL Technical Digest,* vol. 27, no. 1, pp. 32-40, 2006.

[37] Eutelsat, «6 Industry Use Cases for Satellites,» [Online]. Available: https://www.eutelsat.com/en/blog/6-industry-use-cases-for-satellite.html. [Consultato il giorno 29 September 2022].

[38] S. D. Ilcev, Global Mobile Satellite Communications Applications: For Maritime, Land and Aeronautical Applications Volume 2, 2nd edition, Springer, 2018.

[39] H. Hemmati, Deep Space Optical Communications, Jet Propulsion Laboratory, California Institute of Technology, 2005.

[40] SpaceNews.com, “All future Starlink satellites will have laser crosslinks,” 2021. [Online]. Available: https://spacenews.com/all-future-starlink-satellites-will-have-laser-crosslinks/. [Accessed 29 September 2022].

[41] Telesat, “Affordable, Quality Internet Everywhere,” [Online]. Available: https://www.telesat.com/leo-satellites/. [Accessed 29 September 2022].

[42] eoPortal, “OneWeb Minisatellite Constellation for Global Internet Service,” 2015. [Online]. Available: https://www.eoportal.org/satellite-missions/oneweb#eop-quick-facts-section. [Accessed 29 September 2022].

[43] eoPortal, “Astrocast CubeSats,” [Online]. Available: https://www.eoportal.org/satellite-missions/astrocast#astrocast-commercial-iot-network-service. [Accessed 29 September 2022].

[44] C.-H. F. Fung, K. Tamaki, H.-K. Lo and M. Xiongfeng, “Security proof of quantum key distribution with detection efficiency mismatch,” *Quantum Information and Computation,* vol. 9, pp. 131-165, 2009.

[45] P. Jianwei, “Progress of the Quantum Experiment Science Satellite (QUESS) "Micius" Project,” 2020.

[46] T. Jennewein, J. P. Bourgoin, B. Higgins, C. Holloway, E. Meyer-Scott, C. Erven, B. Heim, Z. Yan, H. Hübel, G. Weihs, E. Choi, I. D'Souza, D. Hudson and R. Laflamme, “QEYSSAT: a mission proposal for a quantum receiver in space,” in *Advances in Photonics of Quantum Computing, Memory, and Communication VII*, SPIE OPTO, 2014, San Francisco, California, United States, 2014.

[47] ESA, “European quantum communications network takes shape,” 2019. [Online]. Available: European quantum communications network takes shape. [Accessed 29 September 2022].

[48] C. E. DeVoe, A. D. Pillsbury, F. Khatri, J. M. Burnside, A. C. Raudenbush, L. J. Petrilli and T. Williams, “Optical overview and qualification of the LLCD space terminal,” in *International Conference on Space Optics*, Tenerife, Canary Islands, Spain, 2014.

[49] B. Rödiger, M.-T. Hahn, C. Fuchs and C. Schmidt, “OSIRIS4CubeSat - System Engineering with new Space approach from the development of a high data-rate optical communication payload to the demonstrator in a quasi-operational mission,” in *SECESA, the 9th International Systems & Concurrent Engineering for Space Applications Conference*, Delft, Netherlands, 2020.

[50] J. R. Nonay, C. Fuchs, D. Orsucci, C. Schmidt and D. Giggenbach, “SelenIRIS: a Moon-Earth Optical Communication Terminal for CubeSats,” in *IEEE International Conference on Space Optical Systems and Applications (ICSOS)*, Kyoto City, Japan, 2022.

[51] J. Breidenthal, C. Edwards, E. Greenberg, G. Kazz and G. Noreen, “End-to-end information system concept for the Mars Telecommunications Orbiter,” in *IEEE Aerospace Conference*, Big Sky, MT, USA, 2006.

[52] C. Heese, Z. Sodnik and I. Carnelli, “Design of the optical communication system for the asteroid impact mission,” in *International Conference on Space Optics — ICSO*, Biarritz, France, 2017.

[53] A. Biswas, M. Srinivasan, R. Rogalin, S. Piazzolla, J. Liu, B. Schratz, A. Wong, E. Alerstam, M. Wright, W. T. Roberts, J. Kovalik, G. Ortiz, A. Na-Nakornpanom, M. Shaw, C. Okino, K. Andrews and M. Peng,

"Status of NASA's deep space optical communication technology demonstration," in *IEEE International Conference on Space Optical Systems and Applications (ICSOS)*, Naha, Japan, 2017.

[54] A. Vettor, F. Sansone e A. Francesconi, «Benefits of intersatellite connectivity for backhaul networks based on small satellites,» in *International Astronautical Congress (IAC)*, 2020.

[55] I. d. Portillo, B. Cameron and E. Crawley, "Ground Segment Architectures for Large LEO Constellations with Feeder Links in EHF-band," in *IEEE Aerospace Conference*, Big Sky, MT, USA, 2018.

[56] G. Pandolfi, R. Albi, J. Puglia and Q. Berdal, "Solution for a ground station network providing a high bandwidth and high accessibility data link for nano and microsatellites," in *67th International Astronautical Congress (IAC)*, Guadalajara, Mexico, 2016.

[57] L. Wu, Y.-J. Xu, Q. Wang and F. Wang, "Mapping Global Shipping Density from AIS Data," *The Journal of Navigation,* vol. 70, no. 1, pp. 67-81, 2017.

[58] SEDAC, "Gridded Population of the World (GPW) v4," [Online]. Available: https://sedac.ciesin.columbia.edu/data/collection/gpw-v4. [Accessed 29 September 2022].

[59] A. Kosta, N. Pappas and V. Angelakis, "Age of Information: A New Concept, Metric, and Tool," *Now Foundations and Trends,* 2017.

[60] E. Polehampton, C. Cox, D. Smith, D. Ghent, M. Wooster, W. Xu, J. Bruniquel and S. Dransfeld, "Copernicus Sentinel-3 SLSTR Land User Handbook," 2021.

[61] A. Goffi, D. Stroppiana, P. A. Brivio, G. Bordogna and M. Boschetti, "Towards an automated approach to map flooded areas from Sentinel-2 MSI data and soft integration of water spectral features," *International Journal of Applied Earth Observation and Geoinformation,* no. 84, 2019.

[62] S. Nasery e K. Kalkan, «Burn Area Detection and Burn Severity Assessment Using Sentinel-2 MSI Data: The Case of Karabağlar District,» *2 MSI Data: The Case of Karabağlar District,* vol. 1, n. 2, 2020.

[63] SUHET, «Sentinel-2 User Handbook, ESA Standard Document,» 2013.

[64] A. Vettor, D. Scelsa, A. Bettio, F. Sansone and A. Francesconi, "Advantages of inter-satellite connectivity for Earth observation constellations," in *72nd International Astronautical Congress (IAC)*, Dubai, United Arab Emirates, 2021.

[65] W. Sanderson, C. Tierceline and J. Villanueva, "Accident of the oil tanker Jessica off the Galàpagos Islands (Ecuador), January 16th, 20012001, Report to European Commission DG Environment ENV.C.3, Civil Protection.," 2001.

[66] I. C. f. H. A. (ICHA), "Use of earth observation products to enhance humanitarian disaster response," 2020.

[67] Atlas Space Operations, "Global Antenna Network," [Online]. Available: https://atlasground.com/antenna-network/. [Accessed 29 September 2022].

[68] J. Wertz, Mission Geometry; Orbit and Constellation Design and Management, Dordrecht, Netherlands: Springer, 2001.

[69] T. Elganimi, "Performance Comparison between OOK, PPM and PAM Modulation Schemes for Free Space Optical (FSO) Communication Systems: Analytical Study," *International Journal of Computer Applications,* vol. 79, no. 11, 2013.

[70] F. Sansone, A. Francesconi, R. Corvaja, G. Vallone, R. Antonello, F. Branz and P. Villoresi, "LaserCube optical communication terminal for nano and micro satellites," *Acta Astronautica,* vol. 173, pp. 310-319, 2020.

[71] X.-l. Xu and Y.-q. Xiong, "Orbit error characteristic and distribution of TLE using CHAMP orbit data," *Astrophysics and Space Science,* vol. 363, no. 2, 2018.

[72] D. Hobbs and P. Bohn, "Precise orbit determination for Low Earth Orbit satellites," *Annals of the Marie Curie Fellowships,,* no. 4, pp. 128-135, 2006.

[73] Y. Yang, X. Yue and A. G. Dempster, "GPS-based onboard real-time orbit determination for LEO satellites using consider Kalman filter," *IEEE Transactions on Aerospace and Electronic Systems,* vol. 52, no. 2, pp. 769-777, 2016.

[74] D. A. Vallado, Fundamentals of Astrodynamics and Applications, Springer, 2001.

[75] J. Ma, G. Lu, S. Yu, L. Tan, Y. Fu and F. Li, "Acquisition performance analysis for intersatellite optical communications with vibration influence," *Chinese Physics B,* vol. 29, no. 1, p. 014205, 2020.

[76] F. Sansone, F. Branz, A. Vettor and A. Francesconi, "Acquisition Analysis for Small–Satellite Optical Crosslinks," in *IEEE 8th International Workshop on Metrology for AeroSpace (MetroAeroSpace)*, Naples, Italy, 2021.

[77] T. S. Rose, D. W. Rowen, S. LaLumondiere, N. I. Werner, R. Linares, A. Faler, J. Wicker, C. Coffman, G. Maul and D. Chien, "Optical communications downlink from a 1.5 u cubesat: Ocsd program," in *International Conference on Space Optics (ICSO)*, Crete, Greece, 2018.

[78] C. Pong, "On-orbit performance & operation of the attitude & pointing control subsystems on asteria," in *32nd Annual AIAA/USU Conference on Small Satellites*, Logan , Utah, USA, 2018.

[79] J. P. Mason, M. Baumgart, B. Rogler, C. Downs, M. Williams, T. N. Woods, S. Palo, P. C. Chamberlin, S. Solomon and A. Jones, "Minxss-1 cubesat on-orbit pointing and power performance: the first flight of the blue canyon technologies xact 3-axis attitude determination and control system," *Journal of Small Satellites,* vol. 6, no. 3, pp. 651-662, 2017.

[80] W. Weiss, S. Rucinski, A. Moffat, A. Schwarzenberg-Czerny, O. Koudelka, C. Grant, R. Zee, R. Kuschnig, J. Matthews and P. Orleanski, "Brite-constellation: nanosatellites for precision photometry of bright stars," *Publications of the Astronomical Society of the Pacific,* vol. 126, no. 940, p. 573, 2014.

[81] Y. Fujiwara, M. Mokuno, T. Jono, T. Yamawaki, K. Arai, M. Toyoshima, H. Kunimori, Z. Sodnik, A. Bird and B. Demelenne, "Optical inter-orbit communications engineering test satellite (OICETS)," *Acta Astronautica,* vol. 61, no. 1-6, pp. 163-175, 2007.

[82] M. E. Wittig, L. V. Holtz, D. E. L. Tunbridge and H. C. Vermeulen, "In-orbit measurements of microaccelerations of ESA's communication satellite Olympus," *Free-Space Laser Communication Technologies,* vol. 1218, no. 2, pp. 205-214, 1990.

[83] R. Antonello, F. Branz, F. Sansone, A. Cenedese and A. Francesconi, "High-precision dual-stage pointing mechanism for miniature satellite laser communication terminals," *IEEE Transactions on Industrial Electronics,* vol. 68, no. 1, pp. 776-785, 2020.

[84] G. Baister and P. V. Gatenby, "Pointing, acquisition and tracking for optical space communications," *Electronics & Communication Engineering,* vol. 6, no. 1994, pp. 271-280, 1994.

ABBREVIATIONS

Abbreviation	Definition
ADCS	Attitude Determination and Control System
ADS-B	Automatic Dependent Surveillance - Broadcast
AIM	Asteroid Impact Mission
AIS	Automatic Identification System
ALASCA	Advanced Laser Guide Star Adaptive Optics for Satellite Communication Assessments
AOGSN	Australian Optical Ground Station Network
APD	Avalnche Photodiode
ASI	Agenzia Spaziale Italiana - Italian Space Agency
BCN	Beacon
BER	Bit Error Ratio
BPSK	Binary Phase Shift Keying
CAGR	Compound Annual Growth Rate
CAM	Collimator Adjustable Mount
CCR	CornerCube Retroreflector
CCSDS	Consultative Committee for Space Data Systems
CISAS	Centro di Ateneo di Study e Attività Spaziali
CMOS	Complementary Metal-Oxide Semiconductor
COTS	Commercial Off The Shelf
CTTIC	China Transport Telecommunication Information Group Company Limited
DEI	Department of Information Engineering
DII	Department of Industrial Engineering
DLR	German Aerospace Agency
dNBR	Deutsches Zentrum für Luft- und Raumfahrt - German Aerospace Center
DSN	Deep Space Network
DSOC	Deep-Space Optical Communication
DSTG	Defense Science and technology Group
ECEF	Earth-Centered Earth-Fixed
EKF	Extended Kalman Filter
ELU	ELectronic Unit
EM	Engineering Model
EONN	European Optical Nucleu Network
ESA	European Space Agency
ESO	European Southern Observatory
EuroQCI	European Quantum Communication Infrastructure
FEM	Finite Element Model

FM	Flight Model
FoR	Field of Regard
FoV	Field of View
FPA	Fine Pointing Assembly
FSM	Fast Steering Mirror
FSOC	Free Space Optical Communications
GEO	Geostationary Earth Orbit
GEVS	General Environmental Verification Standard
GPS	Global Positioning System
GS	ground station
GUI	Graphical User Interface
IAT	Inter-Acquisition Time
IOD	In-Orbit Demonstration
ION	InOrbit NOW
IoT	Internet of Things
ISL	Inter-Satellite Link
ISRO	Indian Space research Organisation
ISS	International Space Station
ITU	International Telecommunication Union
JAXA	Japan Aerospace Exploration Agency
LCT	Laser Communication Terminal
LCU	Laser Control Unit
LDU	Laser Driver Unit
LEO	Low Earth Orbit
LL	Launch Lock
LLCD	Lunar Laser Communication Demonstration
LoS	Line of Sight
LSU	Laser Source Unit
LVTTL	Low Voltage Transistor-Transistor Logic
MLRO	Matera Laser Ranging Observatory
MOS	Miniature Optical Subsystem
MPSS	Miniature Pointing and Stabilization Subsystem
MSI	MultiSpectral Instrument
MTO	Mars Telecommunication Orbiter
MWIR	Middle Wavelength Infrared
NASA	National Aeronautics and Space Administration
NDWI	Normalized Difference Water Index
NEP	Noise Equivalent Power
NGSO	Non-GeoStationary Orbit
NICT	National Institute of Information and Communications
NIR	Near Infrared
NORAD	North American Aerospace Defence Command
NRT	Near Real Time
NRZ-OOK	Non-Return to Zero - On Off Keying

NSR	Northern Sky Research
O4C	OSIRIS4CubeSat
OGS	Optical Ground Station
OGS-OFL	Optical Ground Station for Terabit Feeder Link
OMU	Opto-Mechanical Unit
OOK	On Off Keying
OTN	Optical Transport Network
PAA	Point Ahead Angle
PAT	Pointing Acquisition and Tracking
PCB	Printed Circuit Board
PFM	Proto-Flight Model
PPM	Pulse-Position Modulation
PSD	Position Sensitive Device
QAM	Quadrature Amplitude Modulation
QEYSSat	Quantum Encryption and Science Satellite
QKD	Quantum Key Distribution
QM	Qualification Model
QPSK	Quadrature Phase Shift Keying
QUANGO	QUANtum and 5G cOmmunication
QUESS	Quantum Experiments at Space Scale
RF	Radio Frequency
SAGA	Security And CryptoGrAphic Mission
SAR	Synthetic Aperture Radar
SEAQUE	Space Entanglement and Annealing QUantum Experiment
SEDAC	Socioeconomic Data and Applications Center
SLSTR	Sea and Land Surface Temperature Radiometer
SMA	Shape Memory Alloy
SNR	Signal to Noise Ratio
SRP	Solar Radiation Pressure
SWIR	Short-Wavelength Infrared
T-AOGS	Transportable-Adaptive Optics Ground Station
TBIRD	Terabyte Infrared Delivery
TIR	Thermal Infrared
TLC	telecom
TLC-RX	Telecom-Receiver
TLE	Two-Line Elements
TMU	Telecommunication Management Unit
TOGS	Transportable Optical Ground Station
TREU	Transmitter-Receiver Electronic Unit
TRL	Technology Readiness Level
TTL	Transistor-Transistor Logic
TVAC	Thermal Vacuum Chamber
TX/RX	Transmitter-Receiver
UBC	Uplink Beacon Collimator

VIS	VISible
VoI	Value of Information
WDM	Wavelength Division Multiplexing

LIST OF FIGURES

LIST OF TABLES

END OF DOCUMENT